Geochemistry, petrogenesis and tectonic setting of ophiolites and mafic-ultramafic complexes in the Northeastern Aegean Region: New trace-element, isotopic and age constraints.

Dissertation
zur Erlangung des Grades
"Doktor der Naturwissenschaften"
im Promotionsfach Geologie/Paläontologie

am Fachbereich Chemie, Pharmazie und Geowissenschaften
der Johannes Gutenberg-Universität

Nikola Koglin
geb. in Halle/Saale

Mainz, 2008

Erklärung

Ich versichere hiermit, die vorliegende Arbeit selbständig und nur unter Verwendung der angegebenen Quellen und Hilfsmittel verfasst zu haben.

Mainz, Januar 2008

Abstract

In this study two ophiolites and one mafic-ultramafic complex of the northeastern Aegean Sea, Greece, have been investigated to re-evaluate their petrogenetic evolution and tectonic setting. These complexes are: the mafic-ultramafic complex of Lesvos Island and the ophiolites of Samothraki Island and the Evros area. In order to examine these complexes in detail whole-rock major- and trace-elements as well as Sr and Nd isotopes, and minerals were analysed and U-Pb SHRIMP ages on zircons were determined.

The mafic-ultramafic complex of Lesvos Island consists of mantle peridotite thrusted over a tectonic mélange containing metasediments, metabasalts and a few metagabbros. This succession had previously been interpreted as an ophiolite of Late Jurassic age. The new field and geochemical data allow a reinterpretation of this complex as representing an incipient continental rift setting that led to the subsequent formation of the Meliata-Maliac-Vardar branches of Neotethys in Upper Permian times (253 ± 6 Ma) and the term "Lesvos ophiolite" should be abandoned. With proceeding subduction and closure of the Maliac Ocean in Late Jurassic times (155 Ma) the Lesvos mafic-ultramafic complex was obducted. Zircon ages of 777, 539 and 338 Ma from a gabbro strongly suggest inheritance from the intruded basement and correspond to ages of distinct terranes recently recognized in the Hellenides (e.g. Florina terrane). Geochemical similar complexes which contain rift associations with Permo-Triassic ages can be found elsewhere in Greece and Turkey, namely the Teke Dere Thrust Sheet below the Lycian Nappes (SW Turkey), the Pindos subophiolitic mélange (W Greece), the Volcanosedimentary Complex on Central Evia Island (Greece) and the Karakaya Complex (NW Turkey). This infers that the rift-related rocks from Lesvos belong to an important Permo-Triassic rifting episode in the eastern Mediterranean.

The 'in-situ' ophiolite of Samothraki Island comprises gabbros, sparse dykes and basalt flows as well as pillows cut by late dolerite dykes and had conventionally been interpreted as having formed in an ensialic back-arc basin. The results of this study revealed that none of the basalts and dolerites resemble mid-ocean ridge or back-arc basin basalts thus suggesting that the Samothraki ophiolite cannot represent mature back-arc basin crust. The age of the complex is regarded to be 160 ± 5 Ma (i.e. Oxfordian; early Upper Jurassic), which precludes any correlation with the Lesvos mafic-ultramafic complex further south (253 ± 6 Ma; Upper Permian). Restoration of the block configuration in NE Greece, before extensional collapse of the Hellenic hinterland and exhumation of the Rhodope Metamorphic Core Complex (mid-Eocene to mid-Miocene), results in a continuous ophiolite belt from Guevgueli

in the NW to Samothraki in the SE, thus assigning the latter to the Innermost Hellenic Ophiolite Belt. In view of the data of this study, the Samothraki ophiolite represents a rift propagation of the Sithonia ophiolite spreading ridge into the Chortiatis calc-alkaline arc.

The ophiolite of the Evros area consists of a plutonic sequence comprising cumulate and non-cumulate gabbros with plagiogranite veins, and an extrusive sequence of basalt dykes, massive and pillow lavas as well as pyroclastic rocks. Furthermore, in the Rhodope Massif tectonic lenses of harzburgites and dunites can be found. All rocks are spatially separated. The analytical results of this study revealed an intra-oceanic island arc setting for the Evros ophiolitic rocks. During late Middle Jurassic times (169 ± 2 Ma) an intra-oceanic arc has developed above a northwards directed intra-oceanic subduction zone of the Vardar Ocean in front of the Rhodope Massif. The boninitic, island arc tholeiitic and calc-alkaline rocks reflect the evolution of the Evros island arc. The obduction of the ophiolitic rocks onto the Rhodope basement margin took place during closure of the Vardar ocean basins. The harzburgites and dunites of the Rhodope Massif are strongly depleted and resemble harzburgites from recent oceanic island arcs. After melt extraction they underwent enrichment processes by percolating melts and fluids from the subducted slab. The relationship of the peridotites and the Evros ophiolite is still ambiguous, but the stratigraphic positions of the peridotites and the ophiolitic rocks indicate separated origin. The harzburgites and dunites most probably represent remnants of the mantle wedge of the island arc of the Rhodope terrane formed above subducted slab of the Nestos Ocean in late Middle Jurassic times. During collision of the Thracia terrane with the Rhodope terrane thrusting of the Rhodope terrane onto the Thracia terrane took place, whereas the harzburgites and dunites were pushed between the two terranes now cropping out on top of the Thracia terrane of the Rhodope Massif.

Zusammenfassung

Im Rahmen dieser Doktorarbeit wurden zwei Ophiolithe und ein mafisch-ultramafischer Komplex in der nordöstlichen Ägäis in Griechenland, untersucht und ihre petrogenetische Entwicklung sowie ihr tektonischer Rahmen neu bewertet. Dabei handelt es sich um den mafisch-ultramafischen Komplex der Insel Lesvos und um die Ophiolithe der Insel Samothraki sowie der Evros Region. Um die bestehenden Modelle für diese Komplexe im Detail zu überprüfen, wurden die Gesamtgesteinschemie der Haupt- und Spurenelemente sowie die Sr- und Nd-Isotopengeochemie und die Mineralchemie analysiert und die Gesteine mit der SHRIMP-Methode an Zirkonen datiert.

Der mafisch-ultramafische Komplex der Insel Lesvos besteht aus Decken von Mantel Peridotit, welche über eine tektonische Mélange geschoben wurden, die aus Metasedimenten, Metabasalten und wenigen Metagabbros besteht. Diese Abfolge wurde bisher als Spät-Jurassischer Ophiolith interpretiert. Die neuen Feld- und Geochemiedaten erlauben eine Neuinterpretation dieses Komplexes als beginnendes kontinentales Rift, welches im Folgenden zur Bildung des Meliata-Maliac-Vardar Arms der Neotethys im Oberen Perm (253 ± 6 Ma) führte. Der Begriff “Lesvos Ophiolith” sollte daher nicht mehr verwendet werden. Mit fortschreitender Subduktion und Schließung des Maliac Ozeans im Späten Jura wurde der mafisch-ultramafische Komplex der Insel Lesvos obduziert. Einige Zirkone aus Gabbros zeigen Alter von 777, 539 und 338 Ma und deuten somit auf ererbtes Material aus dem von ihnen intrudierten Grundgebirge. Sie entsprechen den Altern verschiedener Terranes, welche kürzlich in den Helleniden entdeckt wurden (z.B. Florina Terrane). Geochemisch ähnliche Komplexe, welche Permo-Triassische Rift-Gesteine enthalten, können an mehreren Stellen in Griechenland und der Türkei gefunden werden. Dabei handelt es sich um die Teke Dere Überschiebungsdecken unterhalb der Lykischen Decken (SW Türkei), die subophiolithische Mélange des Pindos Ophioliths (W Griechenland), der vulkanisch-sedimentäre Komplex im Zentrum der Insel Evia (Griechenland) and der Karakaya Komplex (NW Türkei). Dies zeigt, daß die riftbezogenen Gesteine von Lesvos zu einer bedeutenden und überregionalen, permo-triassischen Rifting-Episode im östliche Mittelmeerraum gehören.

Der ‘in-situ’ Ophiolith der Insel Samothraki besteht aus Gabbros, mafischen Gängen und Basaltflüssen sowie basaltischer Kissenlava, welche von Dolerit-Gängen durchschlagen werden. Nach den Interpretationen verschiedenen Autoren soll sich dieser Ophiolith in einem ensialischen Backarc-Becken gebildet haben. Die Ergebnisse dieser Untersuchung haben ergeben, dass keine der Basalte und Dolerite Mittelozeanischen-Rücken- oder Backarc-

Becken-Basalten ähneln, weshalb der Samothraki Ophiolith kein reifes Backarc-Becken repräsentieren kann. Das Alter des Komplexes ist 160 ± 5 Ma (d.h. Oxford; frühes Ober Jura) was jegliche Korrelation mit dem mafisch-ultramafischen Komplex der Insel Lesvos weiter südlich (253 ± 6 Ma; Oberes Perm) ausschließt. Eine Rekonstruktion der Konfiguration der tektonischen Blöcke in NE Griechenland für die Zeit vor dem Extensions-Kollaps des Hellenischen Hinterlandes und der Exhumierung des "Rhodope Metamorphic Core Komplexes" im Mittel-Eozän bis Mittel-Miozän zeigt einen fortlaufenden Ophiolith-Gürtel, von Guevgueli Ophiolith im NW bis zum Samothraki Ophiolith im SE. Deshalb kann letzterer zum Innersten Griechischen Ophiolith-Gürtel gezählt werden. Nach den Daten dieser Studie repräsentiert der Samothraki Ophiolith ein propagierendes Rift des Meeresarmes des Sithonia Ophioliths, welcher sich in den kalk-alkalinen Chortiatis Bogen hinein fortpflanzt.

Der Ophiolith der Evros Region besteht aus einer plutonischen Sequenz von lagigen und isotropen Gabbros mit Plagiogranitgängen, Basaltgängen und einer extrusiven Sequenz massiver Laven und Kissen-Laven sowie pyroklastischen Gesteinen. Außerdem sind im Rhodope Grundgebirge tektonische Linsen bestehend aus Harzburgiten und Duniten aufgeschlossen. Die Ergebnisse dieser Arbeit ergaben, dass die ophiolithischen Gesteine der Evros Region in einem ozeanisches Inselbogen gebildet wurden, der sich im späten Mitteljura (169 ± 2 Ma) über der vor dem Rhodope-Grundgebirge gelegenen, nordwärts gerichteten Subduktionszone des östlichen Ausläufers des Vardar Ozeans bildete. Die boninitischen, tholeiitischen und kalkalkalinen Gesteine spiegeln die Entwicklung des Inselbogens wider. Obduziert auf den Südrand des Rhodope Grundgebirges wurde der Evros Ophiolith während der Schließung des Vardar Ozeans. Die Harzburgite und Dunite des Rhodope Grundgebirges sind stark verarmt und ähneln Harzburgiten von heutigen ozeanischen Inselbögen. Sie unterliefen Anreicherungsprozessen durch perkolierende Schmelzen und Lösungen aus der subduzierten Platte. Eine Verbindung zum Evros Ophiolith ist unklar, aber die stratigraphische Trennung der Peridotite und der mafischen Gesteine deutet auf eine getrennte Entstehung. Die Peridotite representieren sehr wahrscheinlich Reste des Mantelkeils unter dem Inselbogen des Rhodope Terranes, welcher über der subduzierten Platte des Nestos Ozeans im späten Mitteljura gebildet wurde. Die Kollision des südlichen Thracia Terranes mit dem nördlichen Rhodope Terrane resultierte in der Überschiebung des Rhodope Terranes über den Thracia Terrane wobei die Harzburgite und Dunite zwischen die zwei Terranes gepresst wurden und nun oberhalb des Thracia Grundgebirges aufgeschlossen sind.

Table of Contents

Abstract i

Zusammenfassung iii

Introduction to the thesis 1

Chapter 1 The Lesvos mafic-ultramafic complex, Greece: ophiolite or incipient rift?

Abstract 5
1. Introduction 6
2. Geological setting 8
3. Analytical methods 10
    3.1. X-ray fluorescence analysis (XRF) 10
    3.2. Laser ablation with inductively coupled plasma mass spectrometry (LA-ICPMS) 11
    3.3. Thermal ionisation mass spectrometry (TIMS) 11
    3.4. Sensitive high resolution ion microprobe (SHRIMP) 11
    3.5. Scanning electron microprobe (EMS) 12
4. Whole rock major and trace elements 12
    4.1. Basalts 12
    4.2. Mantle peridotites 21
        Mineral chemistry of the mantle peridotites *24*
5. Sr and Nd isotopic ratios 27
    5.1. Basalts 27
    5.2. Mantle peridotites 27
6. Zircon ages 29
7. Discussion and conclusions 34

Chapter 2 Geochemistry, petrogenesis and tectonic setting of the Samothraki ophiolite, NE Greece: Trace-element, isotopic and zircon age constraints

Abstract 40
1. Introduction 41
2. Geological setting 44
3. Analytical methods 46

3.1. X-ray fluorescence analysis (XRF) 46
3.2. Laser ablation with inductively coupled plasma mass spectrometry (LA-ICPMS) ... 46
3.3. Thermal ionisation mass spectrometry (TIMS) 46
3.4. Sensitive high resolution ion microprobe (SHRIMP) 47
4. Whole rock major and trace element geochemistry 47
4.1. Basalts and dolerites 47
4.2. Diorites 58
5. Sr and Nd isotopic characteristics 59
5.1. Basalts and dolerites 59
5.2. Diorites 60
6. Zircon geochronology 61
7. Discussion and conclusions 63

Chapter 3 New constraints on the ophiolitic rocks of the Evros Area, NE Greece: zircon ages, trace-element and isotope geochemistry

Abstract 69
1. Introduction 70
2. Geological setting 72
3. Analytical methods 74
3.1. X-ray fluorescence analysis (XRF) 74
3.2. Laser ablation with inductively coupled plasma mass spectrometry (LA-ICPMS) ... 74
3.3. Thermal ionisation mass spectrometry (TIMS) 74
3.4. Sensitive high resolution ion microprobe (SHRIMP) 75
3.5. Scanning electron microprobe (EMS) 75
4. Whole rock major and trace element geochemistry 75
4.1. Volcanic rocks 75
4.2. Gabbros 89
4.3. Mantle peridotites 94
5. Mineral chemistry 97
5.1. Pyroxenes of the gabbros 97
5.2. Amphiboles of the gabbros 98
5.3. Spinels of the mantle peridotites 99
6. Sr and Nd isotopic ratios 101

6.1. Volcanic rocks 101
6.2. Gabbros 102
6.3. Mantle peridotites 102
7. Geochronological results 104
8. Discussion 107
8.1. Volcanic rocks 107
8.2. Gabbros 108
8.3. Mantle peridotites 109
9. Conclusion 110
9.1. The mafic complex of the Evros area (Evros ophiolite) 110
9.2. The mantle peridotites of the Rhodope Massif 112

Synthesis 115
References 120

Appendices

Introduction to the thesis

This PhD study represents the results of geochemical and petrogenetic investigations and re-evaluations of ophiolites and mafic and ultramafic complexes of three different areas, namely Lesvos Island, Samothraki Island and the Evros Area.

The Greek orogenic system, also called Hellenides, is part of the Dinaride-Tauride branch of the Mesozoic-Cenozoic Alpine-Himalayan system in the Eastern Mediterranean. They are subdivided in several geotectonic zones (e.g. Jacobshagen, 1986; Papanikolaou, 1986) using lithological, geotectonic and structural features. There are three main zones: I) the External Hellenides, II) the Internal Hellenides and III) the Hellenic Hinterland. The subdivision of these zones is visible from Fig. 1. The External Hellenides are mainly made up of thick platform carbonate successions. The Internal Hellenides as well as the Hellenic Hinterland comprise several distinct crustal units consisting of metamorphic rocks of pre-Alpine protoliths, alpine sediments and igneous rocks of magmatic events from Mesozoic to Paleogene times which have been discovered by recent geochronological data (e.g. Anders et al., 2006). Therefore, the Internal Hellenides and the Hellenic Hinterland can be described as tectonic collage of several exotic terranes. There are two main ophiolite belts in Greece which are located in the Vardar Zone and in the Pelagonian Zone, the eastern ophiolite belt in the Vardar Zone consists of the Vardar ophiolites and those of the Innermost Hellenic Ophiolite Belt (Bébien et al., 1986), namely the Guevgueli, Oraeokastro, Thessaloniki and Chalkidiki ophiolites, the latter comprising the Thessaloniki-Metamorphosis and Kassandra-Sithonia occurrences. Further east the ophiolites of Samothraki Island and the Evros Area also are included. The western ophiolite belt in the Pelagonian Zone contains the ophiolites of Vourinos, Pindos, Koziakas, Othris and Argolis. The position of the mafic-ultramafic complex on Lesvos Island (E Greece) remained unclear. Some authors (e.g. Katsikatsos et al., 1986) counted this complex among the Pelagonian Zone (Internal Hellenides) while for example Pe-Piper et al. (2001) suggested that Lesvos is part of the Sakarya microcontinental block (NW Turkey).

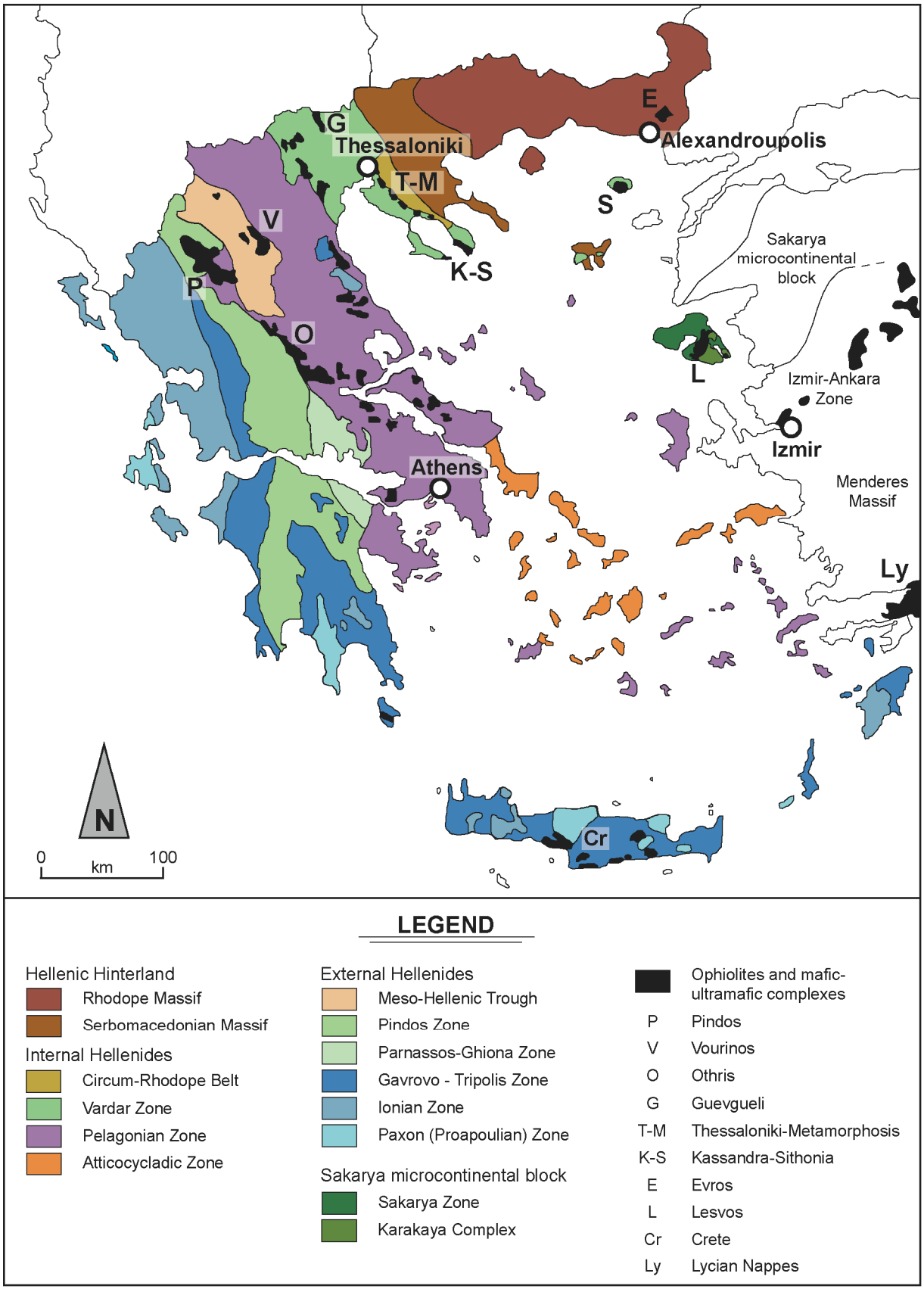

Fig. 1: Simplified geological map of Greece (modified after IGME, 1983; Beccaletto & Jenny, 2004; Zachariadis, 2007).

Before moving to the results there are some explaining words on the term “ophiolite”. The term “ophiolite” derived from the words “οφις” (ofis) for snake and “λιθος” (lithos) for rock and was used by Brongniart (1827) to describe serpentinites. Steinmann (1927) extended the term to describe a whole rock association of peridotites, diabases and others, the so-called “Steinmann Trinity”. In 1972 during the international conference of the Geological Society of Americas Penrose Conference the participants constituted the term “ophiolite” to describe a distinct assemblage of mafic and ultramafic rocks containing from bottom to top:

- Ultramafic complex (mainly harzburgites, lherzolites and dunites, serpentinised in varying degrees, exhibiting tectonic fabrics).
- Gabbro complex (Cumulate and massive gabbros, while the cumulate part also contains some peridotites).
- Mafic sheeted dyke complex.
- Mafic volcanic complex (massive and pillow lavas).

Associated rocks are:

- Sediments on top of the mafic complex (e.g. cherts, shales, limestones).
- Podiform ore bodies, usually chromites, associated with dunites.
- Sodic felsic intrusive and extrusive rocks, the so-called plagiogranites.

Moores (1982) proposed also to include the metamorphic sole and the tectonic mélange in the term “ophiolite”.

Moores (1969) and Moores & Vine (1971) discovered many similarities of ophiolite stratigraphy to oceanic lithosphere. Compared to regions of recent formation of oceanic lithosphere (e.g. Mariana, Izu-Bonin, Scotia, Atlantic) many conclusions can be drawn concerning the magmatism and the hydrothermal alteration processes in ancient oceanic lithospheres as well as their the tectonic setting (e.g. mid-ocean ridge [Atlantic], island arc [Mariana], back-arc basin [East Scotia Ridge], forearc [Izu-Bonin Forearc]). Since ophiolites are obducted due to the closure of oceans or basins, investigations on them, furthermore, provide findings about suture zones what is important for paleogeographic reconstructions. In summary ophiolites can be used as indicators of ocean spreading processes, plate reorganisations and collision tectonics.

Chapter 1 of this thesis reports on the geochemistry, petrogenesis and tectonic setting of the Lesvos mafic-ultramafic complex, NE Greece. Using whole-rock geochemistry, mineral chemistry, Sr and Nd isotopic ratios and new zircon ages the existing petrogenetic and tectonic models for the Lesvos mafic-ultramafic complex have been re-evaluated and a

new model has been proposed. This chapter is mainly identical with the manuscript: "The Lesvos mafic-ultramafic complex, Greece: ophiolite or incipient rift?", which is under review for publication in *Lithos, Special Issue: Balkan Ophiolites*. Co-authors are D. Kostopoulos (Department of Mineralogy and Petrology, National and Kapodistrian University of Athens, Greece) and T. Reischmann (Max Planck Institute for Chemistry, Mainz, Germany). The geochronological analyses were carried out by D. Kostopoulos, P. Zachariadis and T. Reischmann at VSEGEI in St. Petersburg. Further analyses, data interpretation and preparation of the manuscript were done by N. Koglin.

Chapter 2 discusses the geochemistry, petrogenesis and tectonic setting of the Samothraki ophiolite, NE Greece. Whole-rock geochemistry as well as Sr and Nd isotopic ratios and new zircon ages were used to review the present petrogenetic and tectonic models for this ophiolite and a new model has been proposed. This chapter is mainly identical with the manuscript: "Geochemistry, petrogenesis and tectonic setting of the Samothraki ophiolite, NE Greece: Trace-element, isotopic and zircon age constraints", which is under review for publication in *Tectonophysics, Special Issue: Tectonics of the Eastern Mediterranean*. Co-authors are D. Kostopoulos (Department of Mineralogy and Petrology, National and Kapodistrian University of Athens, Greece) and T. Reischmann (Max Planck Institute for Chemistry, Mainz, Germany). The geochronological analyses were carried out by D. Kostopoulos and T. Reischmann at VSEGEI in St. Petersburg. Further analyses, data interpretation and preparation of the manuscript were done by N. Koglin.

Chapter 3 deals with the geochemistry, petrogenesis and tectonic setting of the mafic and ultramafic rocks in the Evros area, NE Greece. Whole-rock geochemistry, mineral chemistry, isotopic ratios and new zircon ages were used to examine the existing petrogenetic and tectonic models for these rocks and a new model has been recommended. This chapter is considered to be submitted as manuscript: "New constraints on the ophiolitic rocks of the Evros area, NE Greece: zircon ages, trace-element and isotope geochemistry", for publication in an international journal in the near future. Co-authors are D. Kostopoulos (Department of Mineralogy and Petrology, National and Kapodistrian University of Athens, Greece) and T. Reischmann (Max Planck Institute for Chemistry, Mainz, Germany). The geochronological analyses were carried out by D. Kostopoulos and T. Reischmann at VSEGEI in St. Petersburg. Further analyses, data interpretation and preparation of the manuscript were done by N. Koglin.

Chapter 1

The Lesvos mafic-ultramafic complex, Greece: ophiolite or incipient rift?

Abstract

On the island of Lesvos in the northeastern Aegean Sea, thrust sheets of mantle peridotite override a tectonic mélange containing metasediments, metabasalts and a few metagabbros. Previous workers have collectively called the above rock types the "Lesvos ophiolite" and suggested it represents Neotethyan (Jurassic) oceanic crust of N-MORB and IAT affinities. However, the complete absence of a sheeted dyke complex and of a layered cumulate sequence, in turn overlain by isotropic gabbros does not support the ophiolite description. The basalts of the mélange define two distinct groups on the basis of Nb/Y values: the Vatera (low Nb/Y) and the Mélange (high Nb/Y) groups. The Vatera basalts show multi-element profiles and REE patterns lying well within the field of N-MORB with the exception of Y and HREE abundances that are lower than those of N-MORB and match those of E-MORB. They originated by ~10% melting of depleted MORB mantle that carried a small amount (~3%) of an enriched (OIB-like) component, corroborated by moderate initial εNd values (+4.6 - +6.2). The Mélange basalts, in contrast, have multi-element profiles and REE patterns typical of within-plate compositions, transitional between E-MORB and OIB. They originated by <5% melting of spinel (and occasionally garnet) lherzolite that carried a small amount (~3%) of recycled crustal component, supported by low initial εNd values (+3.8 - +5.1).

The Lesvos peridotites comprise both spinel lherzolites and harzburgites. Using mineral compositions and calculations of temperature and oxygen fugacity, the lherzolites plot in the fields of alpine-type and continental peridotites. Trace-element modelling suggests they have experienced anhydrous melting in the stability field of spinel but also garnet lherzolite; calculated degrees of melting are generally small and never exceed 14%. There is no evidence for refertilisation-hydrous melting in a supra-subduction zone environment for the lherzolites. The harzburgites, despite being considerably more altered than the lherzolites, also display evidence of anhydrous melting in the stability field of spinel. However, they also display spoon- and dish-shaped REE patterns that can be produced by contamination of the

harzburgites by a percolating OIB-like component with an inherent recycled sedimentary component, necessary to explain their isotopic shift towards EM2 compositions.

SHRIMP dating of gabbro zircons revealed an Upper Permian (253 ± 6 Ma) crystallization age and a Middle Triassic (236 ± 8 Ma) resetting of the zircon rims, compatible with the coeval and widespread rift-related intrusion of A-type granites in the eastern Mediterranean. Gabbro zircon ages of 777, 539 and 338 Ma strongly suggest inheritance from the basement into which the gabbros intruded and correspond to ages of distinct terranes recently recognized in the Hellenides.

We propose that the Lesvos mélange and ultramafics best represent an incipient continental rift setting that led to the subsequent formation of the Meliata-Maliac-Vardar branches of Neotethys, and that the term Lesvos ophiolite should be abandoned.

1. Introduction

Ophiolites traditionally mark suture zones between crustal blocks that were initially separated by an oceanic tract and eventually collided. Greece is a classical ophiolitic country. Type localities on the Greek mainland include the sizeable Pindos, Vourinos, Othris, Guevgueli, and Evros massifs, whereas smaller outcrops are known from the islands of Crete, Samothraki and Lesvos. Most of these bodies have been studied petrologically and geochemically by several workers for a number of years (see review by Robertson 2002 and references therein). However, the petrogenesis and tectonic setting of the mafic-ultramafic complex on the island of Lesvos have not yet been documented in detail. Lesvos is situated in the northeastern Aegean Sea, some 13 km south of the Turkish Biga Peninsula (Fig. 1-1) and along the western continuation of the Sakarya microcontinent. The latter is delineated to the north by the intra-Pontide Suture (iPS) and to the south by the Izmir-Ankara Suture (IAS) (Fig. 1-1) (Okay & Göncüoglu, 2004, Barr et al., 1999, Robertson, 2002). The Karakaya Complex is an integral part of the Sakarya microcontinent (Fig. 1-1). It contains highly deformed and partly metamorphosed clastic and volcanic series of Permian and Triassic age and has been interpreted as a subduction-accretion complex formed during the collision of two small continental fragments in Triassic times (Pickett & Robertson, 1996, 2004; Okay & Göncüoglu, 2004). The Denizgören ophiolite occurs along strike the Lesvos complex on Biga Peninsula at the northwestern edge of the Sakarya Zone (see Fig. 1-1).

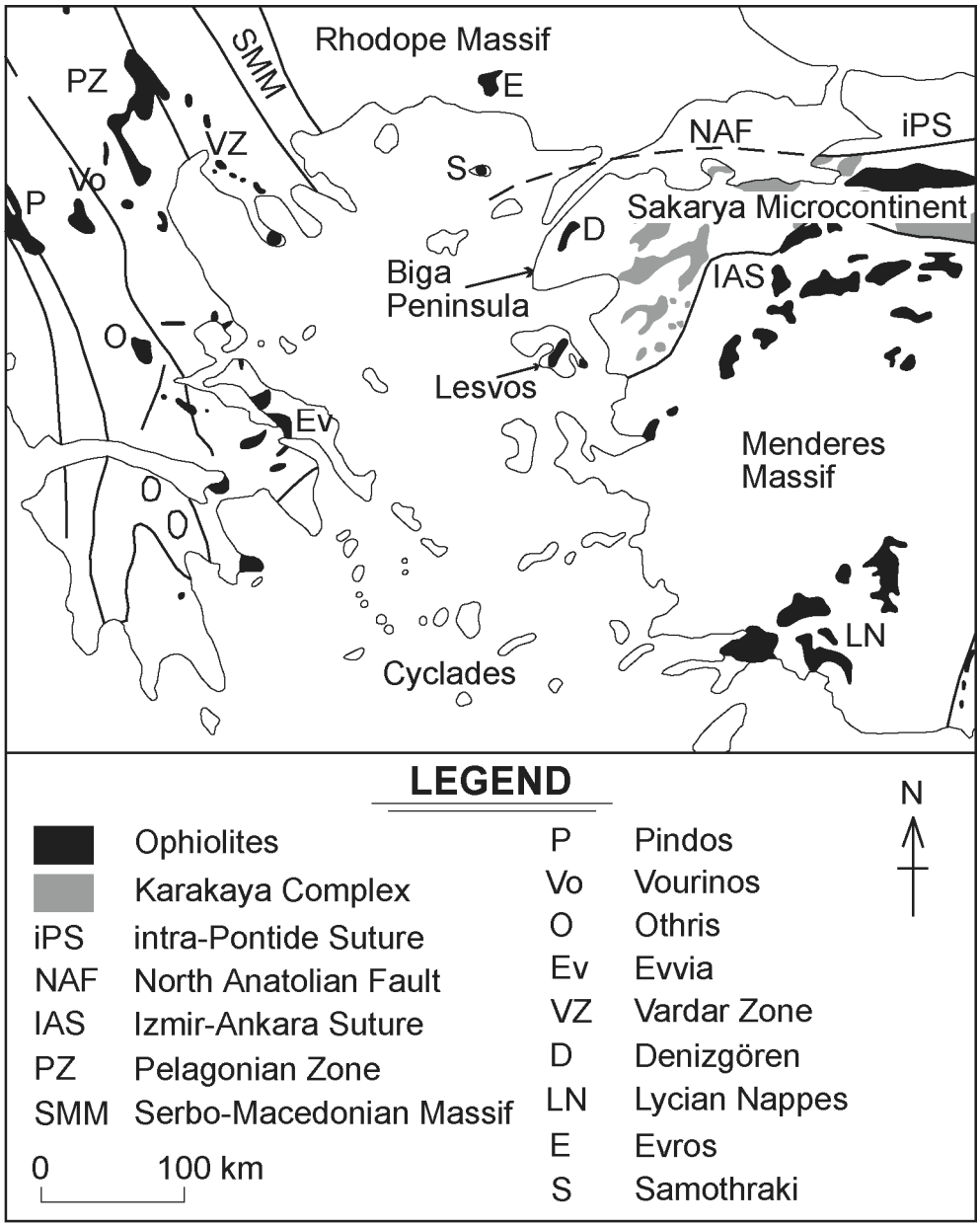

Fig. 1-1: Generalized map of the Aegean region sowing the main ophiolitic occurrences and suture zones (modified after Robertson 2002, Barr et al. 1999 and Beccaletto & Jenny 2004).

The Lesvos mafic-ultramafic complex does not fit the classical Penrose conference definition of an ophiolite (Anonymous, 1972). Nor does it fit the idea of a dismembered ophiolite body. Nowhere on the island is there any trace of a sheeted dyke complex or of a layered cumulate sequence in turn overlain by isotropic gabbros. The rocks that comprise what is known as the Lesvos ophiolite belong to two separate thrust sheets: the structurally overlying ultramafic thrust sheet, chiefly composed of mantle lherzolite with an amphibolitic metamorphic sole at its base, and the structurally underlying volcanosedimentary thrust sheet, termed ophiolitic or tectonic mélange, chiefly composed of metasediments, metabasalts and a few metagabbros. Likewise, the Denizgören ophiolite does not fit the ophiolite definition

proper. It is exclusively composed of serpentinised ultramafics with a partly amphibolitic metamorphic sole at their base and the crustal section is totally missing (Beccaletto & Jenny, 2004). The Lesvos mafic-ultramafic units described above have been correlated with the Karakaya Complex and the Denizgören ophiolite respectively by several authors (e.g. Pickett & Robertson, 1996, Beccaletto & Jenny, 2004). Both the Denizgören ophiolite and the Karakaya Complex tectonically overlie Permian platform carbonates and contain a mélange similar to the tectonic mélange of Lesvos (Beccaletto & Jenny, 2004). However, the timing of amphibolite sole formation at Denizgören (118-117 Ma, Okay et al., 1996, 125 Ma, Beccaletto & Jenny, 2004) and Lesvos (153-158 Ma, Hatzipanagiotou & Pe-Piper, 1995) is significantly different, and there are no ultramafic rocks in the Karakaya Complex (Pickett & Robertson 2004, Okay & Göncüoglu 2004). In this study we use trace-element and isotope geochemistry in conjunction with geochronological determinations to place tight constraints on the petrogenesis and tectonic setting of the Lesvos mafic-ultramafic complex and establish whether it can be correlated to ophiolites and/or subduction/accretion complexes in mainland Greece and western Turkey.

2. Geological setting

The geology of Lesvos Island can be subdivided into four major units: (a) a schist-marble unit, (b) a tectonic mélange unit, (c) an ultramafic unit, and (d) a Cenozoic cover unit (Fig. 1-2).

(a) Schist-marble unit: This unit consists of clastic sediments (shales, phyllites, metapsammites, conglomerates) intercalated with marbles, marble breccias and dolomites. All rocks have undergone low-grade metamorphism (Hecht 1970, 1972, Hatzipanagiotou & Pe-Piper 1995, Papanikolaou 1999). Its age ranges from Carboniferous to Triassic and was determined by fossils (Hecht 1970, 1972, Papanikolaou 1999). This unit is subdivided into several subunits that are described in detail by Hecht (1970).

(b) Tectonic mélange unit: This unit is also known as the Volcanosedimentary unit (Hatzipanagiotou & Pe-Piper, 1995) and is built up of metabasalts and metagabbros together with schists, crystalline limestones and psammites of greenschist facies metamorphism (Hecht 1970, 1972, Hatzipanagiotou & Pe-Piper 1995). It is located east of the major ultramafic body of the island in the area north of Plomari village, with one small outcrop situated southwest of

the major ultramafic body in the area west of Vatera village (Fig. 1-2). The rocks of this unit are strongly deformed except for the Vatera outcrop where the basalts show only slightly deformed to undeformed pillow structures. Pe-Piper et al. 2001 subdivided the basalts of the tectonic mélange unit of Lesvos into two groups: a high-Ti MORB group and a MORB-IAT transitional basalt group. The age of the tectonic mélange is considered to be Permian to Middle Triassic as determined by conodonts in sediments (Hatzipanagiotou & Pe-Piper 1995, Papanikolaou 1999).

(c) The Ultramafic unit: This unit is thrust over the previous unit and is exposed in two areas of the eastern part of the island: I) in the area stretching between Ambeliko and Komi villages, where it forms a single elongated body (ca. 30 x 8 km) striking NE-SW, and II) in the area east of Loutra village where the outcrop is much smaller (Fig. 1-2). Both bodies are mineralogically similar and strongly serpentinised (Hecht 1970, 1972). Dominant rock types are lherzolite with minor harzburgite and dunite (Hatzipanagiotou & Pe-Piper 1995, Pe-Piper et al. 2001). At the base of the ultramafic rocks there are amphibolites and amphibolitic schists that belong to the so-called amphibolitic sole, with N-MORB and WPB affinities (Pe-Piper et al. 2001). The age of the amphibolitic sole and by implication the obduction age of the ultramafic unit was determined by K/Ar on hornblende separates as being 153-158 ± 5 Ma (Hatzipanagiotou & Pe-Piper 1995).

(d) The Cenozoic cover unit: This unit covers almost two thirds of the area of the island (Fig. 1-2) and consists mainly of Miocene to Pliocene high-K andesitic volcanic rocks with minor clastic sediments and marls (Hecht 1970, 1972, Hatzipanagiotou & Pe-Piper 1995). They have been studied in detail by Pe-Piper (1980) and Pe-Piper & Piper (1992). It is within this unit that the famous “Petrified Forest” is preserved east of Sigri village.

For the purpose of this study we sampled basalts and gabbros from the tectonic mélange west of Plomari and Charamida villages as well as basalts from the area west of Vatera village. Peridotite samples were taken along sections southwest of Komi, north of Ambeliko and southeast of Loutra villages.

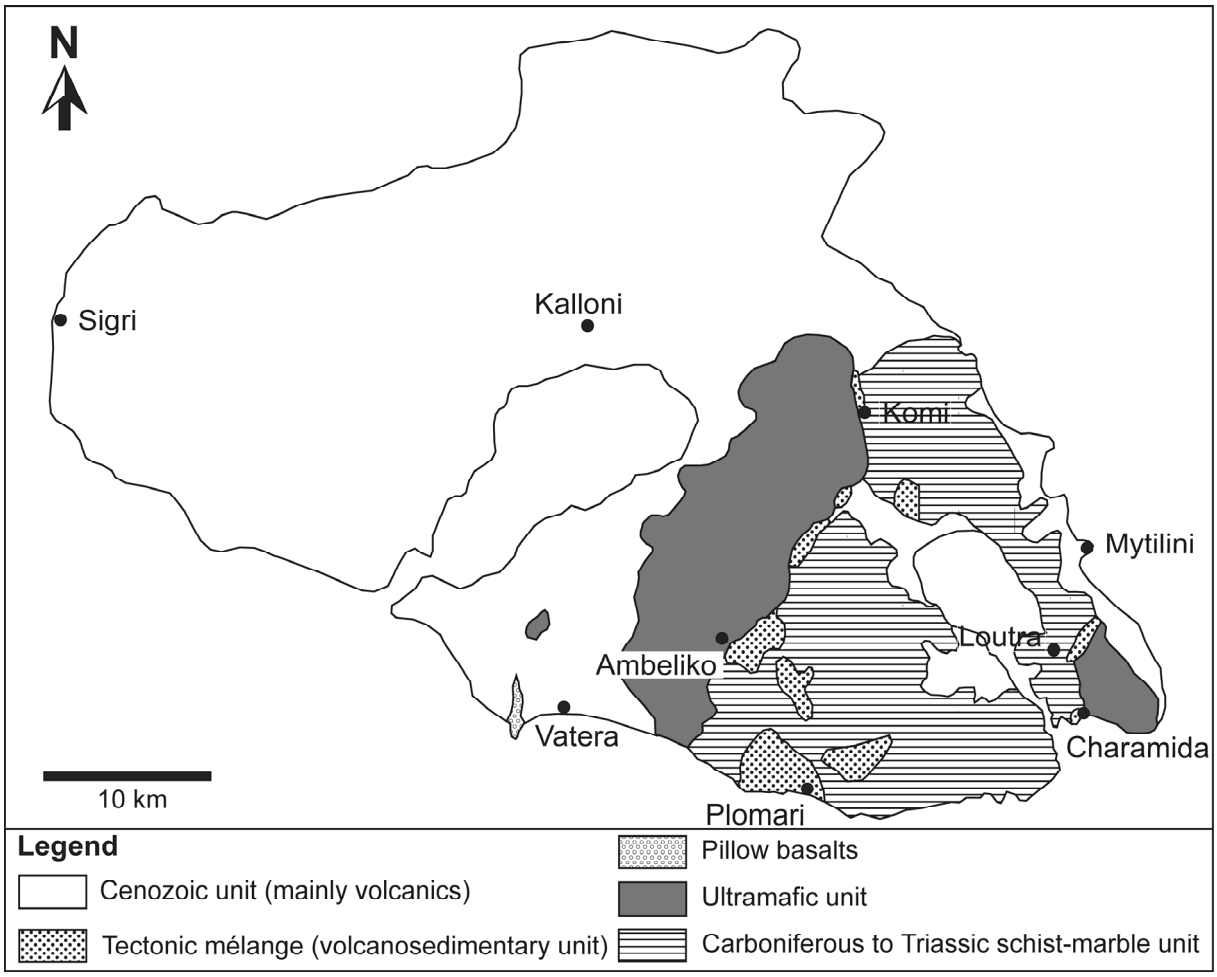

Fig. 1-2: Simplified geological map of Lesvos Island (after Hecht 1972, 1974).

3. Analytical methods

3.1. X-ray fluorescence analysis (XRF)

The samples were crushed and milled to a powder with a grain size of less than 50 µm. 6 g sample powder was mixed with Scandiplex A (resin) + B (hardener) and pressed with 7 t to pellets for trace element measurement. For major element measurement 0.8 g sample powder was mixed with 4.8 g flux material ($LiBO_4$). This mixture was molten in platinum pots and cooled down to glass pellets in a platinum platter. The glass and powder pellets were measured in a Philips PW1404 XRF spectrometer with an Rh X-ray tube with a maximum stimulation of 100kV (3kW) at the Johannes Gutenberg-University, Mainz, Germany. AGV-1, BCR-1, BHVO-1, JP-1 and others were used as standard materials.

3.2. Laser ablation with inductively coupled plasma mass spectrometry (LA-ICPMS)

The rare-earth element measurements were carried out using LA-ICPMS at the Max Planck Institute for Chemistry in Mainz, Germany. 40 mg sample powder was molten for 10 seconds on an Ir-strip at 1500°C and by rapid cooling we produced homogeneous glass chips for measurement. A solid-state New Wave UP213 Nd:YAG laser operating at a wavelength of 213 nm and a frequency of 10 Hz was used to produce ablation pits of 120 μm in diameter. The ablated material was carried by Helium and measured on a ThermoFinnigan Element2 sectorfield ICPMS in the low-resolution mode. Three laser spots were set on every sample with a measuring time of 20 s on the background and 110 to 130 s on the sample. NIST612, KL2G, BHVO-2 and JP-1 were used as standard materials.

3.3. Thermal ionisation mass spectrometry (TIMS)

The isotope measurements were performed at the Max Planck Institute for Chemistry in Mainz, Germany. 50mg sample powder was dissolved in Teflon Savilex beakers using 24M HF and 7M HClO4. The separation of Sr and REE was carried out using 5 ml AG50W-X12 (200-400 mesh) ion exchange resin, following standard ion exchange resin procedures ad using 2.5M HCl for Sr and 6M HCl for the REE. The REE fraction was further separated on a 2 ml column of Teflon powder coated with di-2-ethylhexyl phosphoric acid. Neodymium was eluted with 0.18M HCl. The ratios of Sr and Nd were determined on a Finnigan MAT 261 Thermal ionisation mass spectrometer (TIMS) equipped with a multicollector. Sr was loaded with TaF_5 on a single W filament, while Nd was loaded on double Re filaments. Both elements were analysed as metals. 200 ratios were measured on average for each sample. Mass fractionations were corrected to $^{86}Sr/^{88}Sr = 0.1194$ and $^{146}Nd/^{144}Nd = 0.7219$. Measurements for the NBS 987 Sr and La Jolla Nd standards gave $^{87}Sr/^{86}Sr = 0.710289 \pm 11$ (n=17, 2σ) and $^{144}Nd/^{143}Nd = 0.511840 \pm 6$ (n=33, 2σ), respectively.

3.4. Sensitive high resolution ion microprobe (SHRIMP)

For the separation of the zircons the material was crushed and the mineral fraction that contained the zircons was separated using the Wilfley shaking table, the Frantz magnetic separator and a heavy liquid (methylene iodide). Zircons were separated from the remaining mineral fraction under a binocular and fixed on a mount for SHRIMP measurement.

The U-Th-Pb SHRIMP (Sensitive High Resolution Ion Microprobe) technique allows in-situ spot dating of individual domains within single zircon grains. Combined with a thorough cathodoluminescence imaging study, it permits the dating of zircons with complex structure.

The U-Pb ion microprobe data were obtained using the SHRIMP II instrument at the Centre of Isotopic Research (VSEGEI) in St. Petersburg, Russian Federation. Five scans over the critical mass were carried out using a spot size of 20 μm. The intensity of the primary beam was set at 4 nA. Temora 1 was used as a standard zircon (Black et al., 2003). The data were reduced and visualised using the SQUID and ISOPLOT/ex add-in for Excel (Ludwig 2005a, 2005b).

3.5. Scanning electron microprobe (EMS)

Mineral analyses on chromium spinels were carried out on polished thin sections using a Jeol JXA 8900 RL electron microprobe at the University in Mainz, Germany. The mineral measurements run at an accelerating voltage of 20kV and a beam current of 12 nA, with a beam diameter of 2 μm. Natural and synthetic materials were used as standard. To calculate the concentration units the PRZ correction procedure was used. Cations of chromium spinel were calculated stoichiometric based on 4 oxygens per formula unit.

4. Whole rock major and trace elements

4.1. Basalts

Whole-rock geochemical analyses for the Lesvos basalts are given in Appendix B-1. The volcanic rocks are metamorphosed in low-grade conditions ranging from pumpellyite-prehnite to greenschist facies. Clinopyroxene is partly converted to actinolite while plagioclase is completely replaced by albite. Secondary minerals are mainly epidote, quartz and chlorite and minor amounts of pumpellyite and calcite.

In order to assess the effect of alteration on whole-rock geochemistry we plotted each element analysed against Zr, the latter having long been established as an immobile element during hydrothermal alteration (Kostopoulos 1988 and references therein). It is evident from Fig. 1-3 that most of the major elements, TiO_2 and P_2O_5 excepted, are more or less disturbed

by alteration as are some of the trace elements. Certain trace elements however (e.g. Nb, Ta, Hf, Th, Y, REE) are immobile, and only they are used for rigorous petrogenetic modelling. Some elements (Th, La) show both positive and negative trends against Zr, the former corresponding to the Vatera basalts and the latter to the remainder of the Mélange basalts (see below).

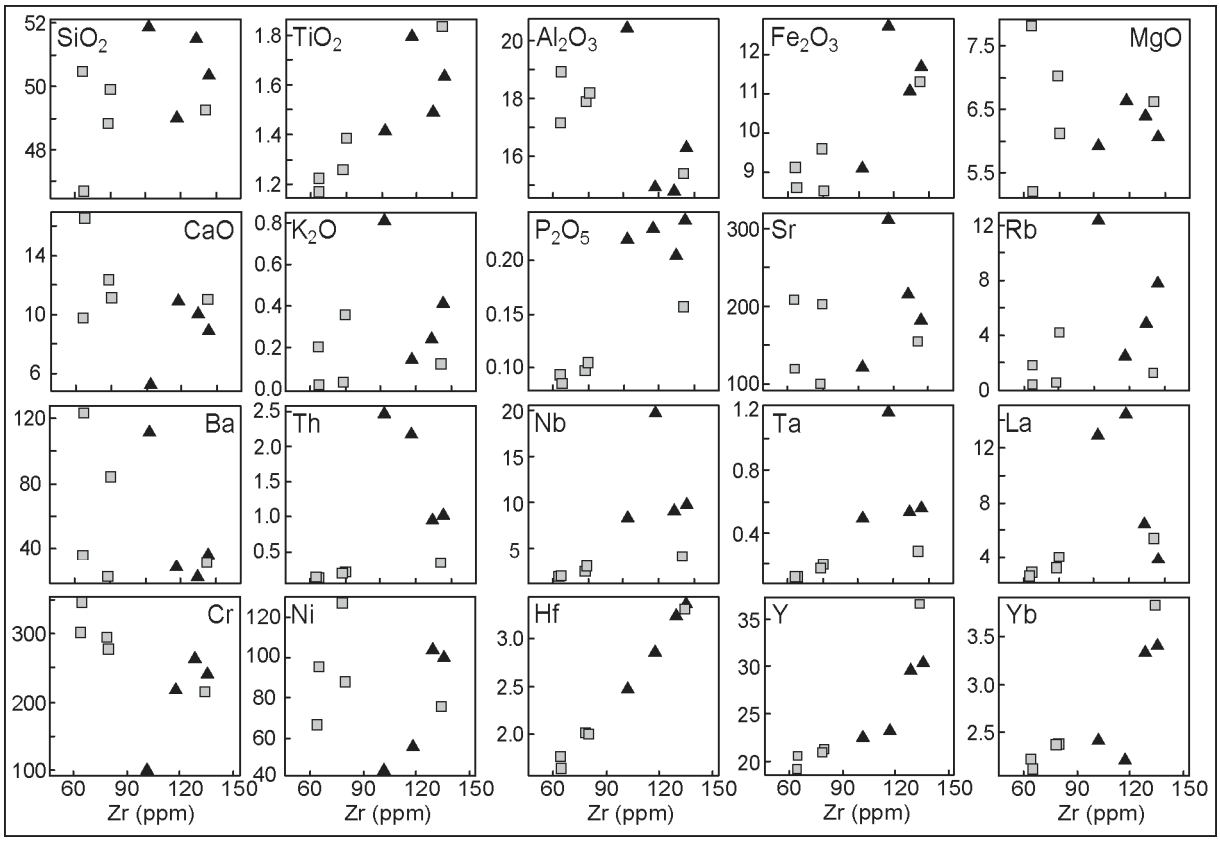

Fig. 1-3: Covariation diagrams of Zr against major (in wt%) and trace elements (in ppm). Grey boxes: Vatera basalts; black triangles: Mélange basalts.

In the Zr/Ti – Nb/Y classification diagram of Winchester & Floyd (1977) (Fig. 1-4) all but one of the Lesvos ophiolitic volcanic rocks fall in the field of subalkaline basalts with only one sample plotting in the field of alkali basalts. In this diagram the basalts form two distinct clusters, one with low Nb/Y ratio values (0.09 – 0.14), the other with high Nb/Y ratio values (0.31 – 0.85). Interestingly, all basalts with low Nb/Y ratio values come exclusively from the Vatera area, whereas all basalts with high Nb/Y ratio values come from the tectonic mélange east of the ultramafic unit (see Fig. 1-2 and description of the tectonic mélange above). Therefore, in the ensuing discussion, we will refer to the low Nb/Y group basalts as the "Vatera basalts" and to the high Nb/Y group basalts as the "Mélange basalts". Inspection of Appendix B-1 reveals that the two basalts groups mentioned above have comparable Y

contents but quite distinct Nb contents. The low Nb/Y group is also characterized by low Nb contents (1.7 – 4.1 ppm), whereas the high Nb/Y group is characterized by high Nb contents (8.4 – 19.8 ppm). The differences in Nb between the two basalt groups are also paralleled by differences in P_2O_5 with the low Nb/Y group showing lower concentrations in this element compared to the high Nb/Y group (P_2O_5: 0.09 – 0.16 wt% vs. 0.21 – 0.24 wt%, respectively).

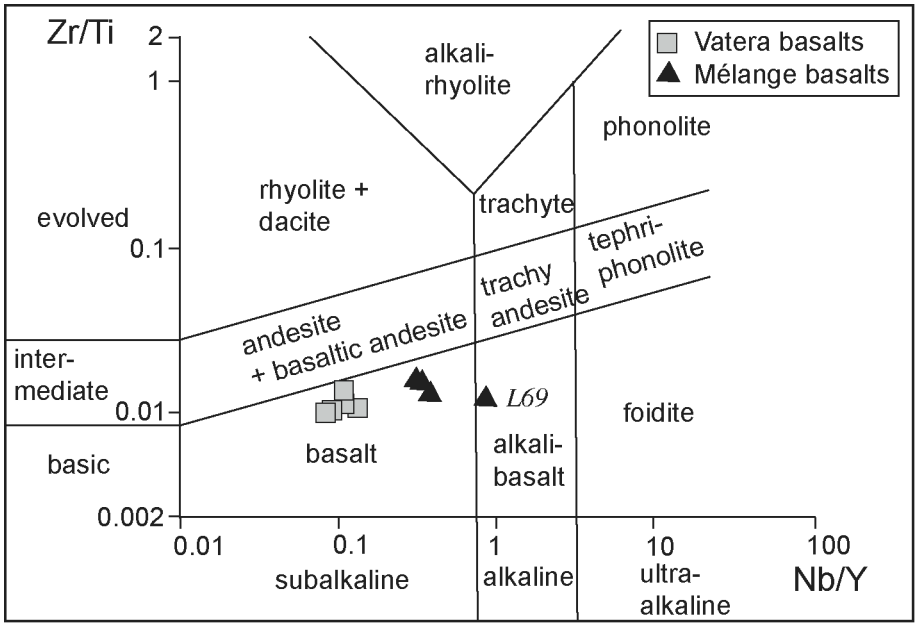

Fig. 1-4: Discrimination diagram for rock types (after Winchester & Floyd 1977). The basalts can be subdivided into a low Nb/Y group (Vatera basalts) and a high Nb/Y group (Mélange basalts). All basalts plot in the subalkaline basalt field except for sample L69, which plots in the alkali-basalt field.

Figure 1-5 depicts N-MORB normalized multi-element patterns for the Vatera and the Mélange basalts. The Vatera basalts show flat HFSE profiles lying well within the field of N-MORB subtypes (Nb_N/Yb_N = 1.0 – 1.6; see also Viereck et al. 1989) and variable LFSE profiles; Sr and Th have N-MORB-like values, Ba is constantly enriched while K and Rb can be either enriched or depleted compared to N-MORB (Fig. 1-5a). Taking into account the covariation of these elements, Th excepted, with Zr (Fig. 1-3), their variable behaviour can be attributed to hydrothermal alteration rather than to reflecting a primary source feature. Sample L30 shows a flat pattern parallel to N-MORB but at somewhat elevated values suggesting that it may represent a more fractionated composition.

The N-MORB normalized multi-element patterns of the Mélange basalts depict a continuous and progressive enrichment from the HFSE towards the LILE (Th_N/Yb_N = 7.3 – 26.1) with no negative Nb-Ta anomaly (except for sample L33) and a characteristic hump in

the LILE part (Fig. 1-5b). Such profiles, coupled with the often smaller than unity normalised values for Y and the HREE, are typical of within-plate basalts that were generated by melting partly within the stability field of garnet lherzolite. The absence of a Nb-Ta anomaly indicates that a subduction component was not involved in the enrichment process. In the case of sample L33 the slight negative Nb-Ta anomaly could be caused either by a subduction component or by assimilation of continental crust.

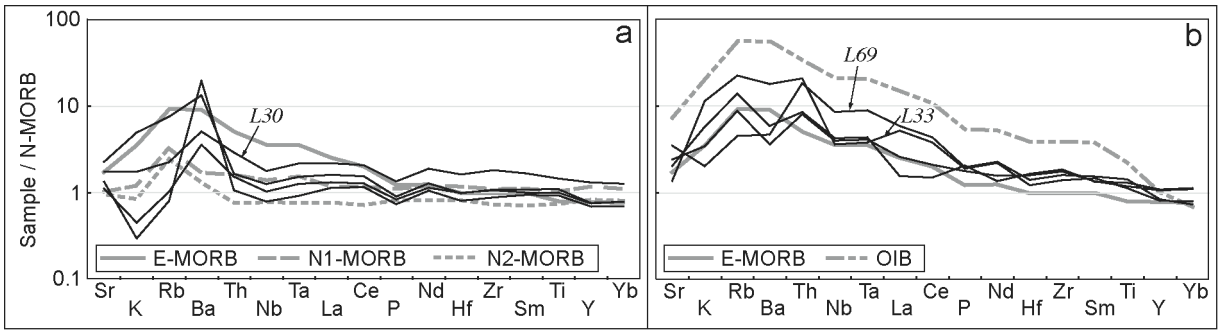

Fig. 1-5: N-MORB normalized multi-element profiles for the Vatera (a) and Mélange basalts (b). E-MORB and N-MORB normalizing values after Sun & McDonough (1989), N1-MORB and N2-MORB values after Viereck et al. (1989). N-MORB: normal mid-ocean ridge basalt; E-MORB: enriched mid-ocean ridge basalt; OIB: ocean island basalt.

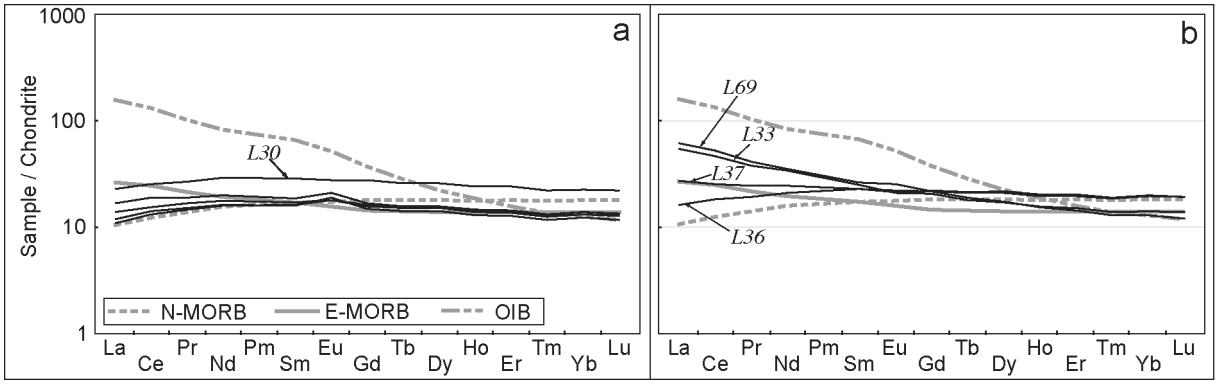

Fig. 1-6: Chondrite-normalised REE patterns for the Vatera (a) and Mélange basalts (b). Values for N-MORB, E-MORB, OIB and normalizing values after Sun & McDonough (1989).

Chondrite-normalized REE patterns for the Lesvos basalts are shown in Fig. 1-6. The REE patterns of the Vatera basalts are generally flat ($La_N/Yb_N \sim 1$) with a LREE depleted part ($La_N/Sm_N < 1$) and a slight positive Eu anomaly in some samples (Fig. 1-6a), the latter indicating accumulation of plagioclase phenocrysts. The depletion in the LREE is similar to that of N-MORB but the HREE are more depleted than N-MORB and resemble those of E-

MORB compositions. As was the case with the multi-element patterns, sample L30 is more enriched in REE compared to the other Vatera basalts but with a pattern parallel to theirs, again suggesting the possibility of a more fractionated composition.

The Mélange basalts show two distinct patterns. The patterns of samples L36 and L37 are flat (La_N/Yb_N ~1), similar to N-MORB, but with elevated LREE content. The patterns of samples L33 and L69 are enriched in LREE and depleted in HREE compared to N-MORB, showing features transitional between E-MORB and OIB (Fig. 1-6b).

The widely used tectonomagmatic discriminant diagram of Wood (1980) that employs the elements Th, Ta and Hf is shown in Fig. 1-7. Thorium is a good indicator of subduction-zone enrichment and is known for its immobility up to 600°C (Wood 1979). Furthermore, Th and Ta are enriched in intra-plate settings because of less melting taking place there and enriched mantle compositions.

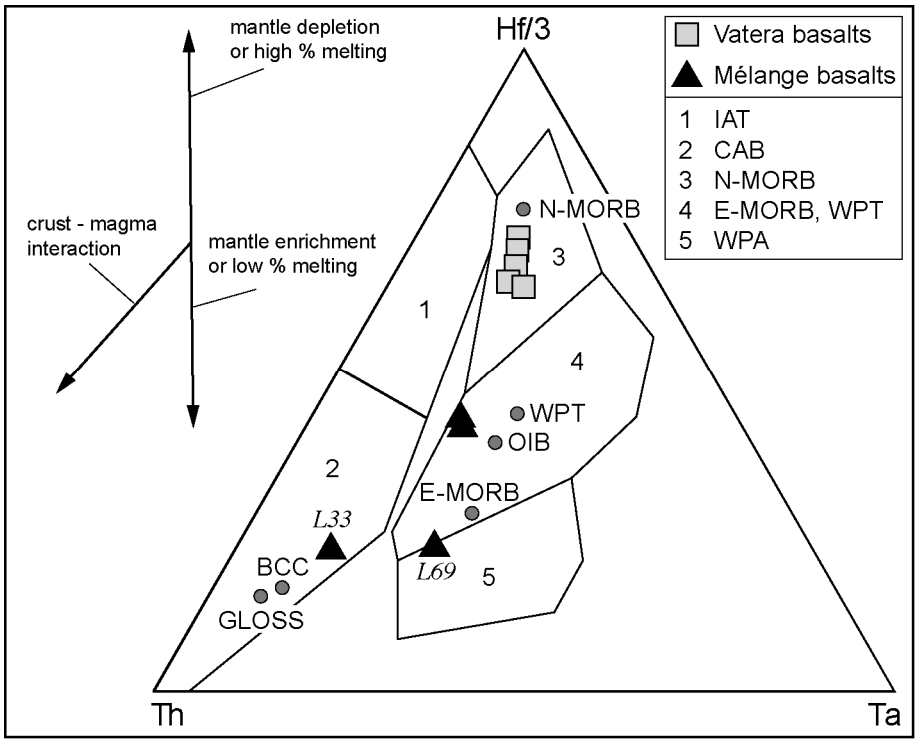

Fig. 1-7: Hf/3-Th-Ta tectonomagmatic discriminant diagram (Wood 1980, with modifications after Pearce [unpublished]). Values for N-MORB, OIB and E-MORB after Sun & McDonough (1989), DMM after Workman & Hart (2005), WPT after Pearce (1982), BCC after Rudnick & Gao (2003) and GLOSS after Plank & Langmuir (1998). IAT: island-arc tholeiite; CAB: calc-alkaline basalt; WPT: within-plate tholeiite; WPA: within-plate alkalic; IAB: island-arc basalt; GLOSS: global subducting sediment; BCC: bulk continental crust; DMM: depleted MORB mantle.

This diagram supports the MORB nature of the Vatera basalts with both low Th and Ta values. The Mélange basalts are enriched in Th and Ta similar to E-MORB/WPT and OIB compositions. Sample L33 displays a significant Th enrichment indicating crust-magma interaction (Fig. 1-7).

Plank (2005) introduced the Th/La vs. Sm/La diagram as a simple means to identify sediment recycling at subduction zones and to quantify mantle-sediment mixing calculations. Th/La is generally low in MORB (~0.05), OIB (~0.11) and primitive mantle and chondrites (~0.13, Hofmann 1988, Sun & McDonough 1989; Lyubetskaya & Korenaga 2007). Even if intra-plate basalt samples with anomalously high Th/La ratios are included, the mantle has Th/La < 0.2, whereas global subducting sediment and the upper continental crust have high Th/La ratios of ~0.24 and 0.34 respectively (Plank & Langmuir, 1998; Plank 2005; Rudnick & Gao, 2003). In general, mantle-derived melts do not have high Th/La, except when sediment subduction / crustal contamination is independently implicated (Plank 2005). On the other hand, the Sm/La ratio is a measure of the extent of LREE depletion or enrichment. When considered together with the Th/La ratio one can evaluate the proportion of sedimentary/crustal components and the extent of depletion of the mantle source using the geochemical signature of basalt.

Figure 1-8 shows Th/La vs. Sm/La systematics for the Lesvos basalts. The Vatera basalts show both low Th/La (0.045 – 0.063) and Sm/La ratios (0.71 – 0.96) similar to N-MORB (e.g. Hess Deep, Stewart et al. 2002; see Fig. 1-8). The variation in Sm/La can be explained by adding up to 5% of an enriched component like ocean-island basalt (OIB; i.e. a low-degree partial melt) to a depleted mantle source (DMM) (Fig. 8, DMM – OIB mixing line).

The Mélange basalts display Th/La ratios (0.149 – 0.192), which are in the range of the lower (LCC) and bulk continental crust (BCC) (0.15 and 0.26, respectively, Rudnick & Gao, 2003). Their low Sm/La ratios (0.27 – 0.55) point to an enriched source comparable to that of enriched mid-ocean ridge basalts (E-MORB) and OIB (Fig. 1-8). These basalts strongly resemble intraplate basalts from several localities worldwide (e.g. Central Europe, Ehrenberg et al., 1982; Arabian Plate, Weinstein et al., 2006; Central Africa, Dostal et al., 1985; East African Rift, Furman et al., 2006).

Sample L36 displays a high Sm/La ratio similar to that of N-MORB (0.91) but its Th/La ratio (0.26) is similar to that of BCC. This composition can be best explained by

mixing a depleted mantle source (DMM) with deep-sea sediments similar to those dredged from the Indian Ocean (Ben Othman et al., 1989).

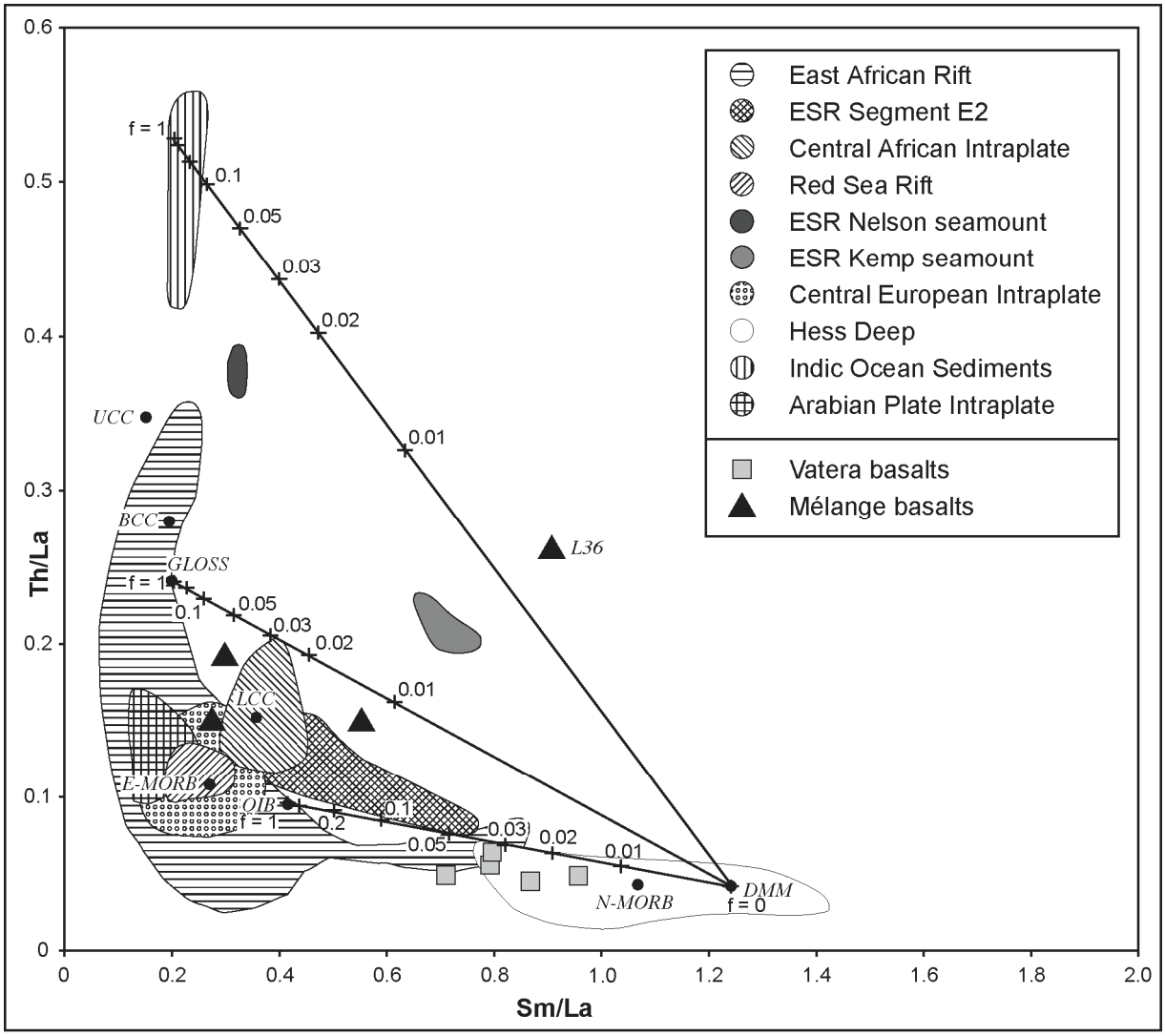

Fig. 1-8: Th/La against Sm/La for the Lesvos basalts (after Plank 2005). The Vatera basalts plot in the field of N-MORB, similar to the Hess Deep basalts (Stewart et al. 2002). The Mélange basalts show higher Th/La and lower Sm/La ratios, which are similar to the rift basalts of Central Africa (Dostal et al., 1985). Also shown for reference are values for basalts from Segment E2 of the East Scotia Ridge (ESR) and Kemp and Nelson seamounts (Leat et al. 2004), N-MORB, E-MORB and OIB (Sun & McDonough 1989), DMM (Workman & Hart 2004), GLOSS (Plank & Langmuir 1998) and UCC, CC and LCC (Rudnick & Gao 2003), Indian Ocean sediment (Ben Othman et al. 1989), basalts from the East African Rift (Furman et al., 2006), the Red Sea Rift (Moghazi et al., 2003), intraplate basalts from Central Africa (Dostal et al., 1985), Central Europe (e.g. Ehrenberg et al., 1982) and the Arabian Plate (Weinstein et al., 2006). UCC: upper continental crust; LCC: lower continental crust.

It has long been established that plotting a compatible element against an incompatible element is a useful technique to determine the processes responsible for the geochemical variations in a certain lava suite (Pearce 1975, 1980, 1982; Pearce et al. 1984, 1986; Kostopoulos 1988). In such plots, partial melting trends will be subparallel to the incompatible element axis because partial melting will rapidly extract the incompatible element from the source (Kostopoulos 1988). By contrast, fractional crystallisation trends will initially be vertical to the incompatible element axis because early precipitation of mafic minerals (e.g. Ol, Cr-Sp) will cause rapid depletion of the compatible element in the derivative melts (Kostopoulos 1988).

Figure 1-9 is a plot of Ti (incompatible element) vs. Cr (compatible element) for the Lesvos basalts with partial melting and crystallisation vectors taken from Kostopoulos (1988) and Kostopoulos and Murton (1992). Assuming that a Fertile Spinel Lherzolite (FSL), compositionally equivalent to DMM, is the source peridotite, the Vatera basalts would require ~10% melting (Fig. 1-9a) followed by early removal of minimal amounts of chromite, in turn followed by ~20% fractionation of olivine, plagioclase and clinopyroxene in proportions similar to those of experimental MORB eutectics (Fig. 1-9c, vector B). On the other hand, the Mélange basalts would require only ~5% melting (Fig. 1-9b) of the same source but larger amounts of early crystallising phases.

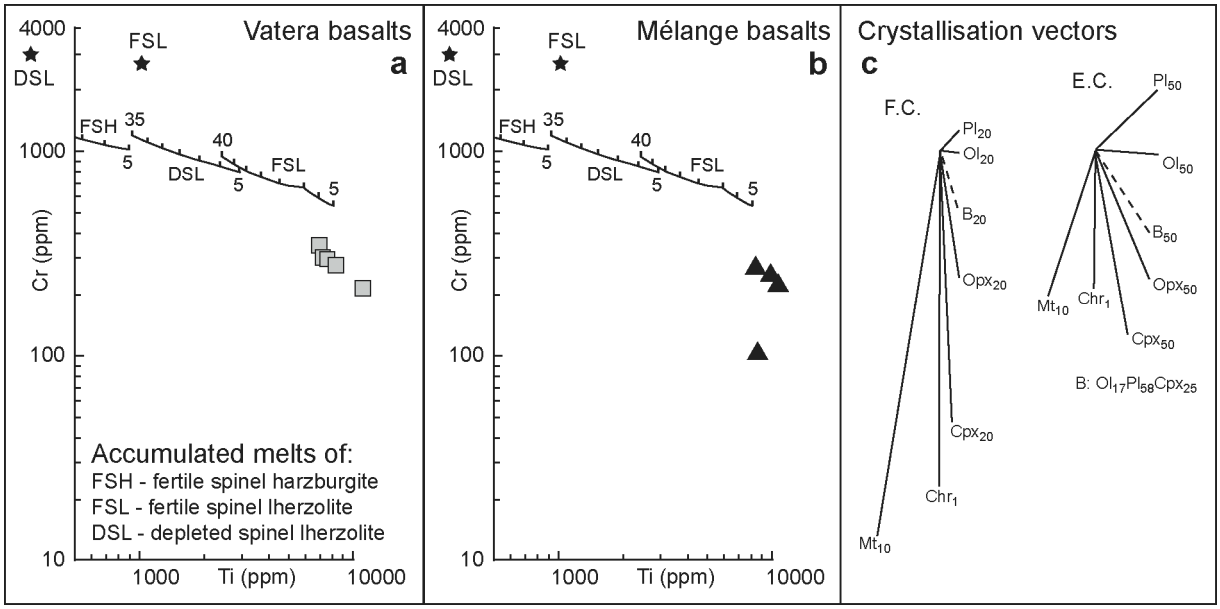

Fig. 1-9: Ti-Cr diagram with melting trends after Kostopoulos & Murton (1992). Crystallisation vectors after Kostopoulos (1988). E.C.: Equilibrium crystallisation; F.C.: Fractional crystallisation.

Pearce et al. (2005) used amongst others Ba, Th, and Nb for identification of the subduction component in the arc lavas of the Marianas arc-basin system. These elements are all highly incompatible and behave in a similar manner during melting and fractional crystallization. However, they are decoupled by subduction processes. Ba and Th are significantly partitioned into siliceous melts, but only Ba is also extensively partitioned in aqueous fluids derived from the subducted slab. Nb is possibly mobilized only in deep melts at the highest temperatures or by very low degrees of melting. In order to reduce the effect of fractional crystallization and accumulation of phenocrysts Pearce et al. (2005) used trace elements that are incompatible and highly conservative in subduction systems like Yb and Ta. Yb is useful as it is one of the most subduction-immobile incompatible elements and it varies only during partial melting in the presence of residual garnet. Ta is only slightly less incompatible than Ba, Th and Nb, but Ta might be concentrated in a mantle enrichment component. Therefore, the most useful diagram is the Th/Yb against Ta/Yb diagram after Pearce (1982) (Fig. 1-10). While the enrichment or depletion of the mantle source is shown by a high or low Ta/Yb ratio, respectively, the addition of a siliceous subduction melt is indicated by high Th/Yb ratios.

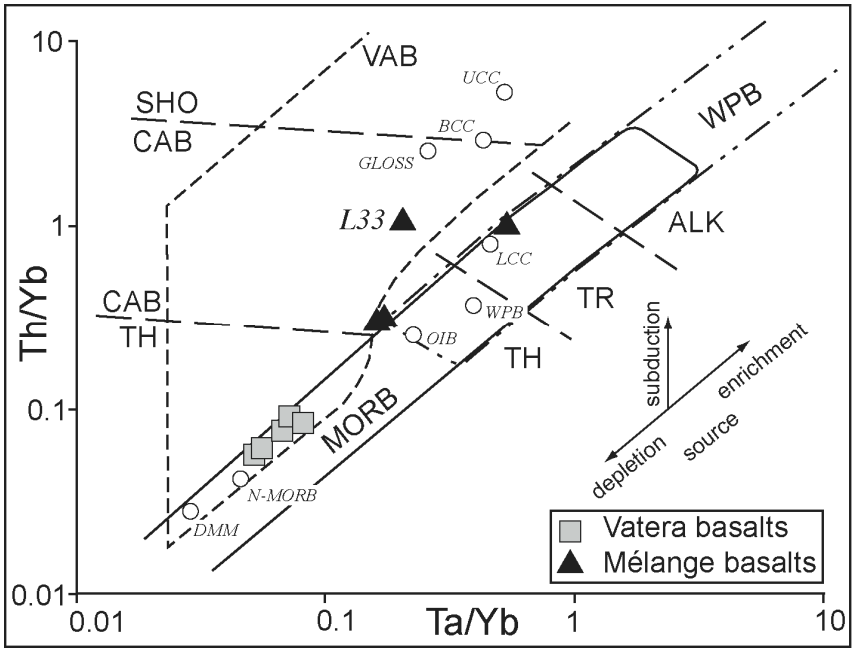

Fig. 1-10: The diagram Th/Yb against Ta/Yb after Pearce (1982) indicates a depleted mantle source for the Vatera basalts. The Mélange basalts are more enriched in Ta which supports an enriched mantle source with a within-plate component and partial enrichment in Th which might be caused by additional siliceous melt. SHO: shoshonitic; TH: tholeiitic; TR: transitional; ALK: alkaline.

Figure 1-10 depicts that the Vatera basalts are in the range of mid-ocean ridge basalts with low Th/Yb and Ta/Yb ratios that indicates a depleted mantle source. The Mélange basalts are shifted towards higher Ta/Yb and Th/Yb ratios along the upper edge of the MORB array that suggests enrichment in the mantle source or low degrees of melting. The Mélange basalts are similar to the range of within-plate basalts (WPB). The enrichment of Th in sample L33 indicates an addition of siliceous melt (Fig. 1-10).

4.2. Mantle peridotites

Major and trace element analyses for the mantle peridotites are given in Appendix B-2. The peridotites of the Lesvos mafic-ultramafic complex have been classified using the Ol – Opx – Cpx ternary diagram (Fig. 1-11). The modal amounts of olivine (Ol), clinopyroxene (Cpx) and orthopyroxene (Opx) were determined following Hutchinson (1975). According to Fig. 1-11, the majority of the ultramafic rocks classify as lherzolites and only a few peridotites plot in the field of harzburgites.

On bivariate diagrams of element vs. MgO (recalculated volatile-free; Fig. 1-12) the concentration of Al_2O_3, CaO, TiO_2, Y and Cr decreases, whereas that of Fe_2O_3 and Ni increases as MgO increases. The lherzolites with MgO < 40 wt.% exhibit similarities with published estimates of the composition of the primitive upper mantle (PUM), with the exception of the concentrations of TiO_2 and Fe_2O_3 which are somewhat lower and higher respectively than in PUM.

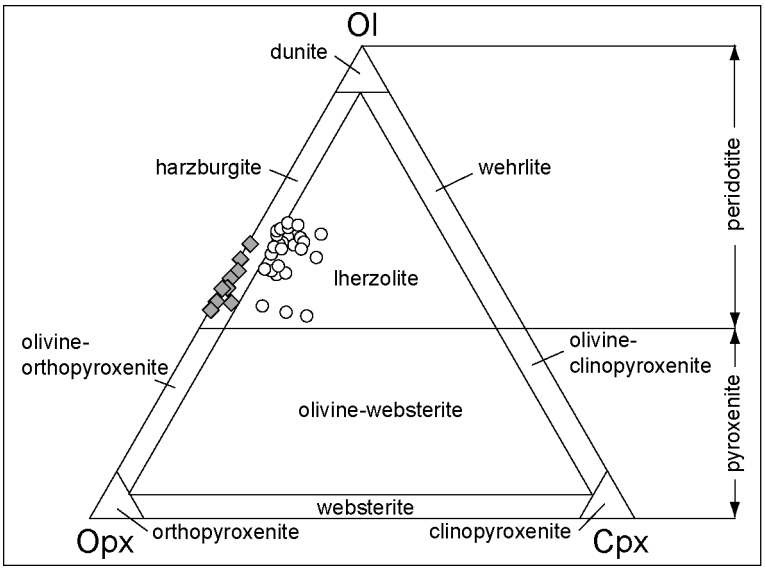

Fig. 1-11: Ol – Opx – Cpx ternary diagram. Mineral modal abundances calculated following Hutchinson (1975). Ol: olivine; Opx: orthopyroxene; Cpx: clinopyroxene.

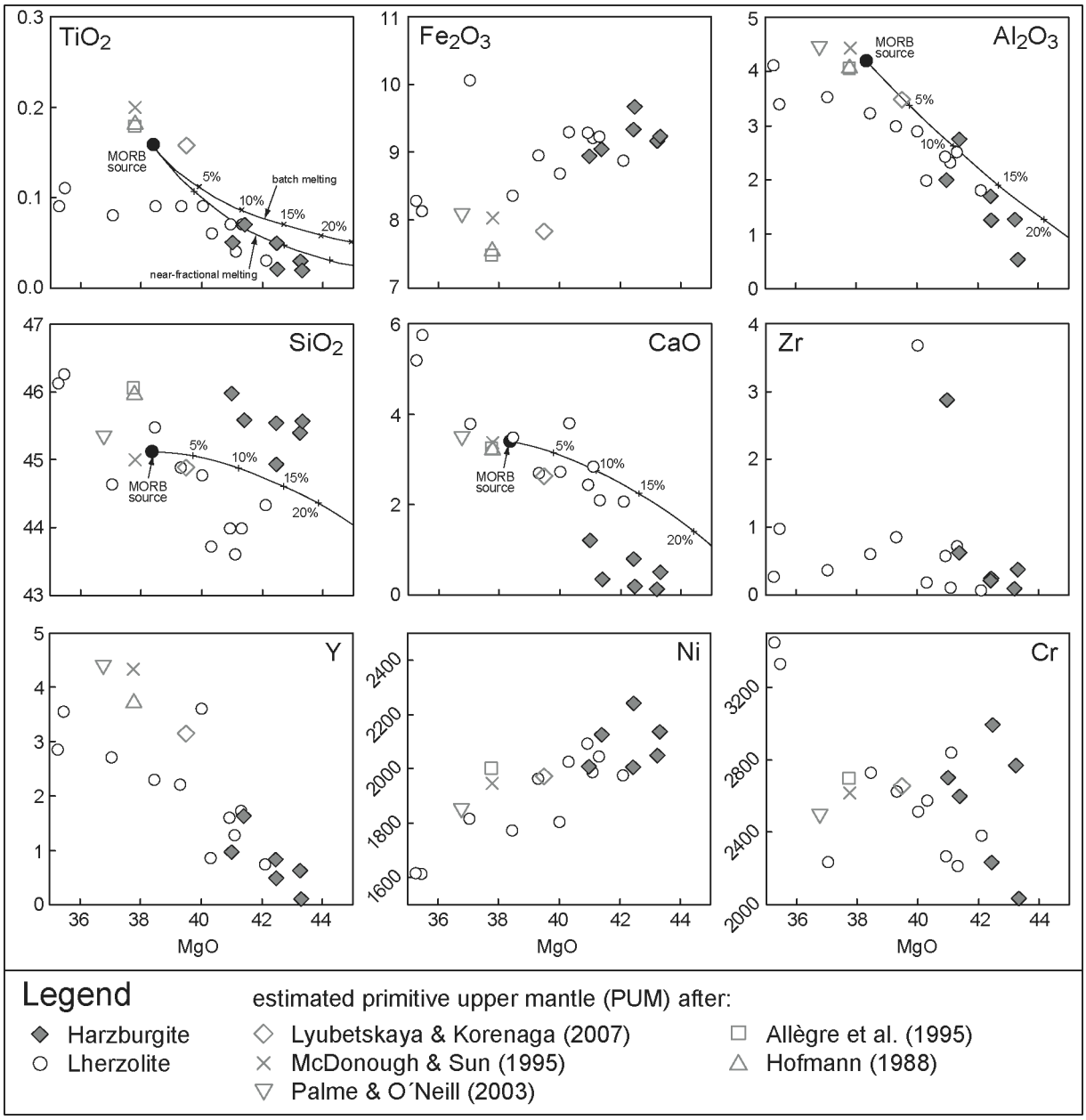

Fig. 1-12: Element vs. MgO bivariate plots for the ultramafic rocks of Lesvos Island (major elements in wt.%; trace elements in ppm). Primitive upper mantle estimates from the literature are given for comparison. Polybaric near-fractional and isobaric batch partial melting trends after Barth et al. (2007).

DMM-normalized patterns for the Lesvos harzburgites and lherzolites are displayed in Fig. 1-13. The patterns are similar with a well-developed hump at their LILE part and a trough over their HFSE part with a distinct negative Zr anomaly. The harzburgites display slightly higher abundances in the elements Nb to Nd but lower abundances in the elements Hf to Yb and a less well-defined Zr anomaly than the lherzolites. The Zr anomaly in both the

harzburgites and lherzolites may reflect changes in the partition coefficient of Zr during the melting process (Rampone et al., 1991; Rampone et al., 1996).

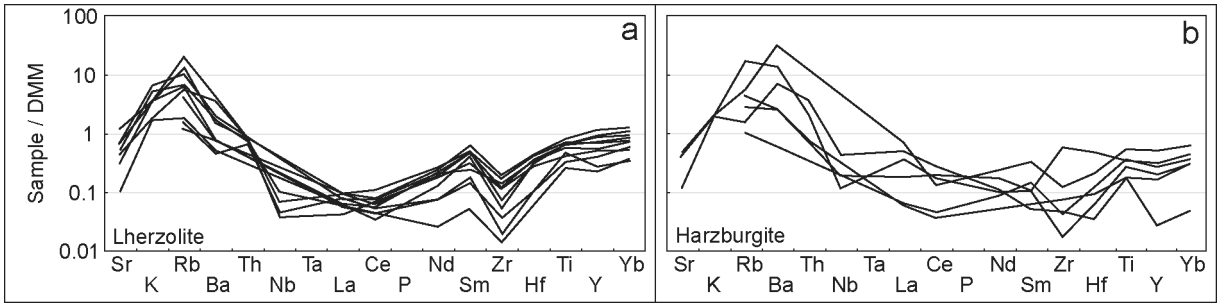

Fig. 1-13: DMM normalized multi-element diagrams for the Lesvos lherzolites (a) and harzburgites (b). Normalizing values after Workman & Hart (2005).

In chondrite-normalised REE plots, the lherzolites exhibit flat HREE patterns ($Dy_N/Yb_N \sim 0.8$) and strongly depleted LREE patterns ($La_N/Dy_N \sim 0.05$) most of which, however, show a slight enrichment in La over Ce (Fig. 1-14a). The harzburgites, by contrast, show a continuous depletion from the HREE towards the MREE ($Dy_N/Yb_N \sim 0.6$) and a variable enrichment in LREE resulting in typical spoon- or dish-shaped patterns or patterns with a marked negative Ce anomaly (Fig. 1-14b) reminiscent of boninites (Cameron, 1985; Kostopoulos, 1988). Such patterns can be produced by contamination of the harzburgites by a percolating OIB-like component as demonstrated by Kostopoulos and Murton (1992). The patterns with a negative Ce anomaly indicate an additional source for La, probably from a (subduction-related?) hydrous fluid (Cameron, 1985; Taylor & Nesbitt, 1988; Kostopoulos, 1988).

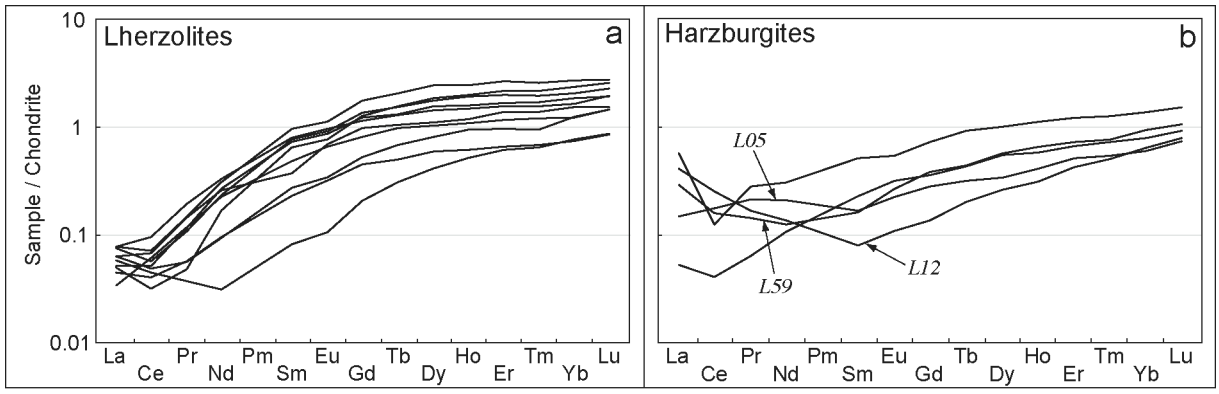

Fig. 1-14: Chondrite normalized REE patterns of the lherzolites (a) and harzburgites (b). Normalizing values after Sun & McDonough (1989).

On a Sm/Yb vs. Yb diagram (chondrite-normalized values; Fig. 1-15) the lherzolites as well as the harzburgites clearly plot in the array calculated for anhydrous melting of spinel peridotite (light grey band labelled "MORB") and away from the array calculated for refertilisation hydrous melting of spinel peridotite (dark grey band labelled "supra-subduction zone"; see Barth et al. 2007, for details). Furthermore, for some of the lherzolites with high Yb_N values, melting within the garnet stability field can also be assumed.

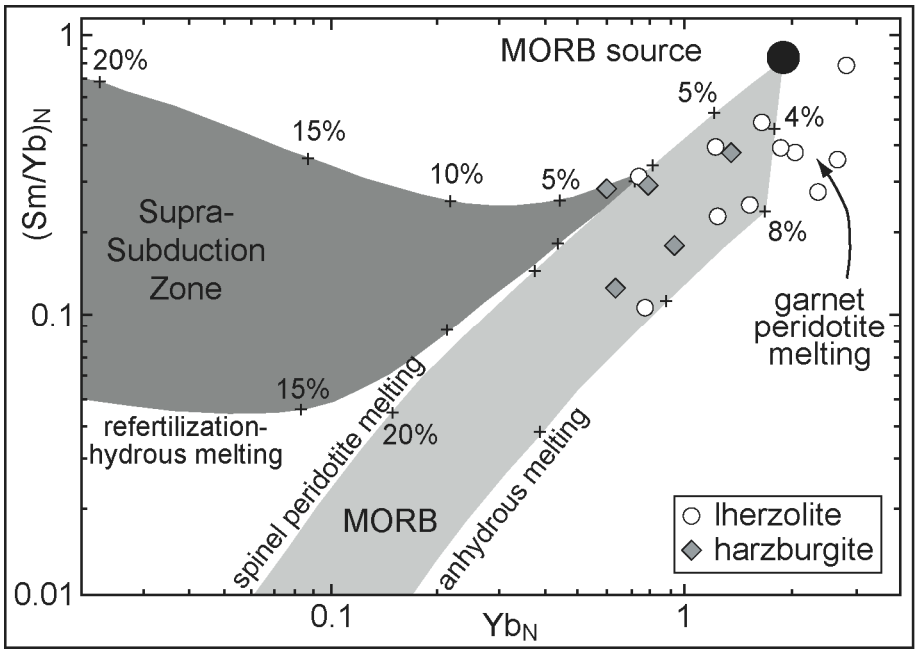

Fig. 1-15: $(Sm/Yb)_N$ against Yb_N for the lherzolites and harzburgites of Lesvos Island. Fields and melting models after Barth et al. (2007). See text for discussion.

Mineral chemistry of the mantle peridotites

In a pioneering paper, Dick & Bullen (1984) used spinel chemistry [Cr/(Cr+Al)) vs. $Mg/(Mg+Fe^{2+})$ or Cr# vs. Mg#] to classify spinel peridotites from different settings. In such a diagram (Fig. 1-16), spinels from abyssal (i.e. MORB-type) and a significant population of Alpine-type peridotites are characterized by high Al and Mg and low Cr and Fe^{2+} contents which results in low Cr# and high Mg# values.

The Lesvos lherzolite spinels are rich in Al, low in Fe and contain moderate amounts of Cr and Mg (see Appendix C-1). They exhibit low Cr# values (0.11-0.37), similar to those of abyssal and some Alpine-type peridotites (Fig. 1-16), which indicate only minor depletion. Their Mg# (0.57-0.77) is slightly higher than that of abyssal peridotites but similar to that of Alpine-type peridotites, suggesting an Alpine-type affinity. Hellebrand et al. (2001) used the

Cr# of spinel to calculate the degree of melting of spinel peridotites using the formula: F = 10ln(Cr#)+24. Upon application of the above formula to the spinels of the Lesvos lherzolites, degrees of melting between 2.3 and 14.1% can be calculated.

With regard to the Lesvos harzburgites, the strong serpentinisation has transformed the original spinel compositions to nearly pure ferrit-chromite ones, thus precluding any inferences to be made about peridotite setting and meaningful calculations of the degree of melting.

Kamenetsky et al. (2001) used TiO_2 vs. Al_2O_3 content of spinel to discriminate between peridotites from different tectonic settings (Fig. 1-17). The spinels from the Lesvos lherzolites plot at very low TiO_2 and very high Al_2O_3 values, partly overlapping with the MORB field and clearly indicating a fertile character.

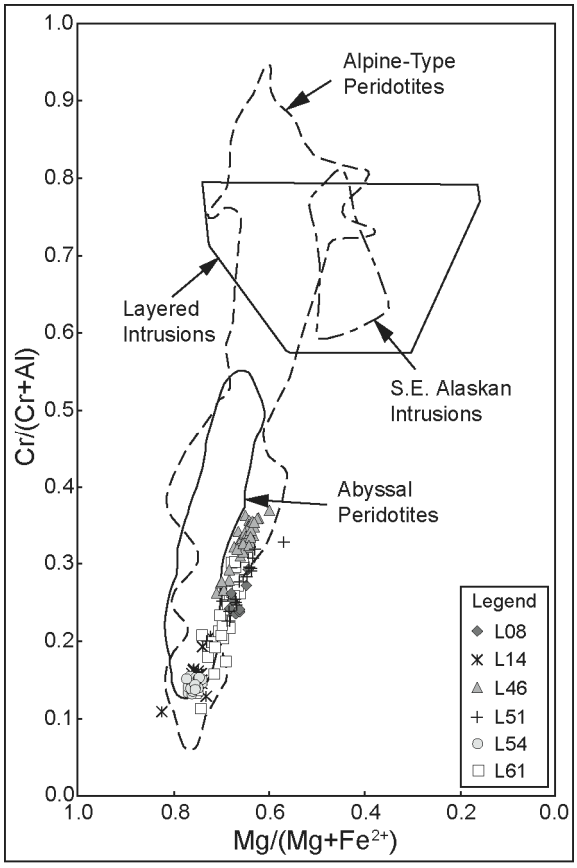

Fig. 1-16: Cr# against Mg# for spinels from the Lesvos lherzolites (after Dick & Bullen 1984). An Alpine-type affinity is clearly indicated.

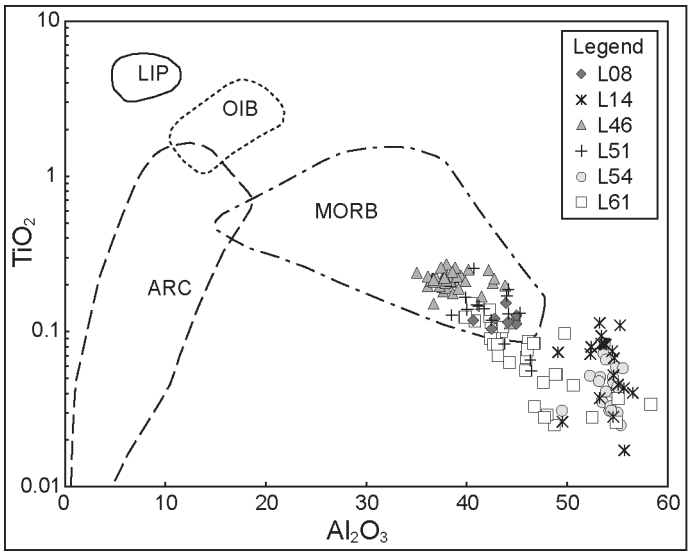

Fig. 1-17: TiO_2 against Al_2O_3 content of spinel from lherzolite after Kamenetsky et al. (2001). Low TiO_2 and high Al_2O_3 indicate a fertile character for the lherzolites. LIP: large igneous provinces.

Calculations of temperature and oxygen fugacity for the Lesvos lherzolites using equilibrium olivine-spinel pairs yielded values of 688 – 744°C and –0.82 - +0.38 log units relative to the QFM buffer respectively, at a nominal pressure of 10 kbar (formalisms of Ballhaus et al. 1990, 1991 were employed). On a plot of $\Delta \log fO_2$ (re:QFM) against spinel Cr# (Pearce et al. 2000; see Fig. 1-18) the Lesvos lherzolites fall exclusively into the field for continental peridotites.

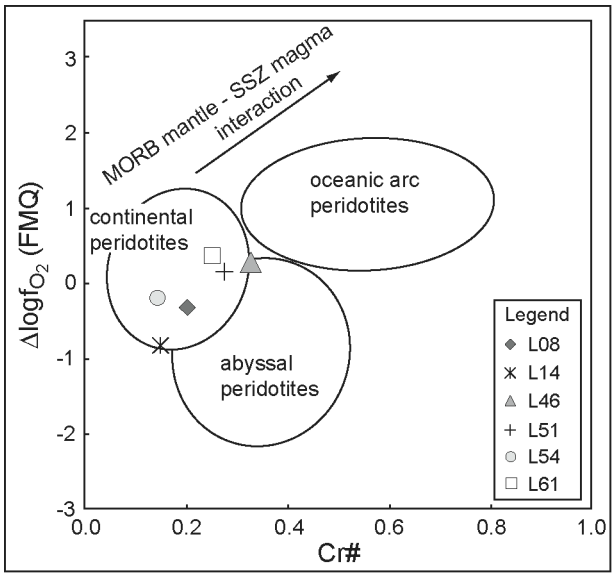

Fig. 1-18: Spinel Cr# against $\Delta \log fO_2$ (re:QFM) for the Lesvos lherzolites (after Pearce et al., 2000). A continental affinity is clearly indicated.

5. Sr and Nd isotopic ratios

In this section the Sr and Nd isotopic results for the Lesvos basalts and peridotites are presented. Sr initial ratios and epsilon Nd values are calculated to an age of 253 Ma, which is the age obtained from zircon geochronology of the gabbros (see Section 6).

5.1. Basalts

The pillow basalts of the Vatera area show εNd_{253} values (+4.6 to +6.2) that are higher than those of the basalts from the tectonic mélange west of Plomari village (+3.8 to +5.1) (see also Appendix D-1). The lowest εNd_{253} value (+1.3) was obtained for one basalt from the tectonic mélange south of Ambeliko village; this sample also shows the highest $^{87}Sr/^{86}Sr_{253}$ ratio value (0.7056) (Fig. 1-19). Except for this high-Sr Ambeliko basalt, the $^{87}Sr/^{86}Sr_{253}$ ratio values of the Mélange basalts (~ 0.7045) are virtually similar to the Sr initial ratios of the Vatera basalts (0.7044 – 0.7051).

Most of the Lesvos basalt samples plot within the mantle array (Fig. 1-19) suggesting that metamorphism has not affected the isotopic systems considered, especially that of Sr which is much more susceptible to seawater alteration than Nd and shifts to higher $^{87}Sr/^{86}Sr$ values. In a diagram of Nb/Th vs. εNd_{253} (Fig. 1-20) the Lesvos basalts form a linear array between DMM and crustal compositions with the Mélange basalts showing lower Nb/Th ratios and more non-radiogenic Nd values than the Vatera basalts. These findings corroborate the inferences made earlier about the presence of a recycled crustal component in the source of all Lesvos tectonic mélange basalts (Fig. 1-20, DMM – GLOSS mixing line).

5.2. Mantle peridotites

The harzburgites and lherzolites of Lesvos can be well distinguished by their initial εNd values and $^{87}Sr/^{86}Sr_{253}$ ratios (Fig. 1-19 and Appendix D-1). While the lherzolites are less depleted with high εNd_{253} values of +6.0 – +6.6, the harzburgites show clearly lower εNd_{253} values of around +2.1. The Sr initial ratios of the lherzolites are in the range: 0.7050 – 0.7053, significantly lower than those of the harzburgites (0.7067 – 0.7083).

Both, the lherzolites and the harzburgites, plot outside the mantle array (Fig. 1-19). If one assumes alteration by Sr-bearing fluids or seawater, then one can explain the horizontal shift of the lherzolites towards higher Sr initial ratios. In the case of the harzburgite however,

seawater cannot be the reason for the high $^{87}Sr/^{86}Sr_{253}$ value because seawater has a lower, time-corrected, Sr initial ratio value than that of the harzburgite. It is then plausible, according to Fig. 1-19, to assume that some other enriched component has played an important role in the isotopic shift of the harzburgite sample under consideration, most probably an OIB-like melt with an inherent recycled sedimentary component. Such an interpretation is in accord with the REE profiles of the harzburgites discussed earlier and moreover suggests the involvement of an EM2 reservoir which has a strong similarity with upper continental crust or continentally-derived sediment (Zindler & Hart, 1986).

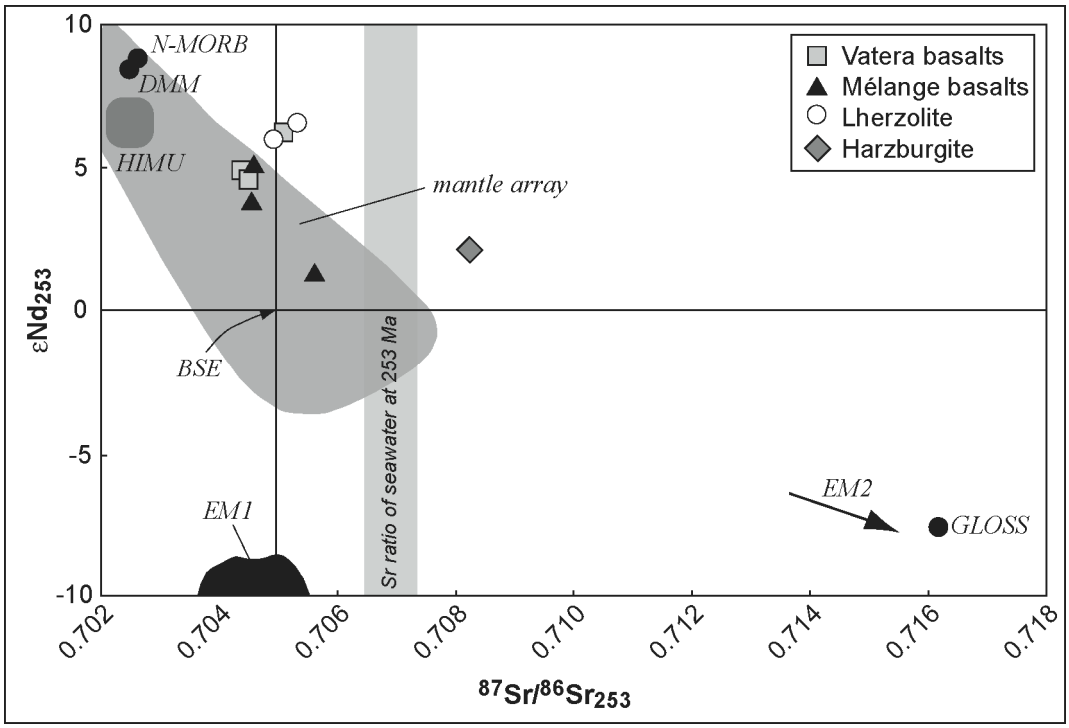

Fig. 1-19: εNd_{253} vs. $^{87}Sr/^{86}Sr_{253}$ for the different rock types of Lesvos Island. Mantle array after White (1998). Fields for HIMU, BSE, EM1 and EM2 after Zindler & Hart (1986). Data sources: GLOSS (global subducted sediment, Plank & Langmuir, 1998), N-MORB (Sun & McDonough, 1989), DMM (Workman & Hart, 2005), Sr Seawater (Burke et al., 1982). All reference values are recalculated to 253 Ma. HIMU: high-μ mantle reservoir; BSE: bulk silicate earth; EM: enriched mantle.

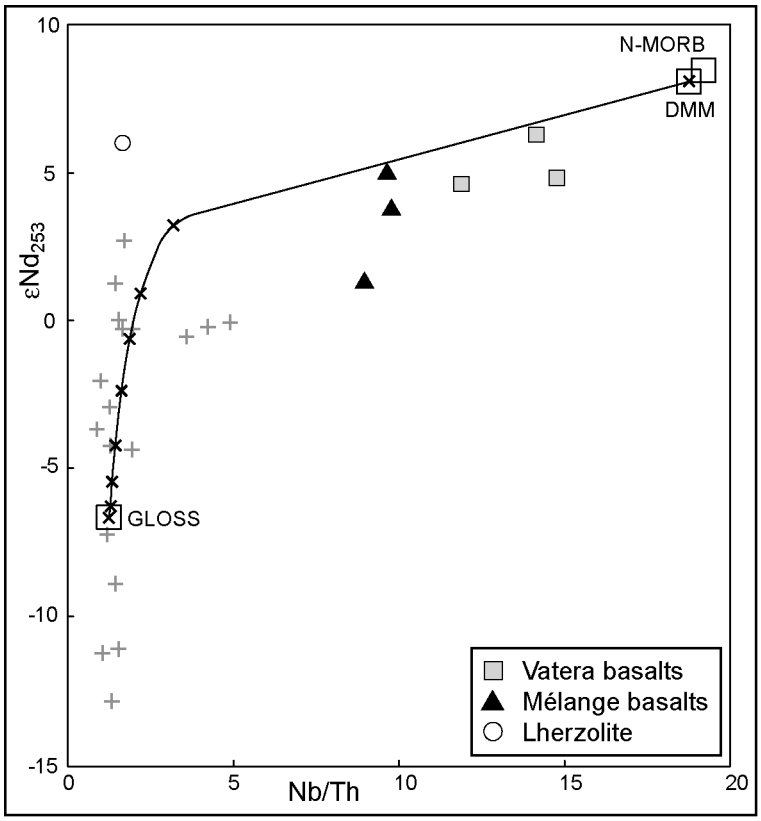

Fig. 1-20: Nb/Th versus εNd_{253} for the basalts and lherzolite from Lesvos Island. Data sources: DMM (Workman & Hart, 2005), N-MORB (Sun & McDonough, 1989), GLOSS (global subducted sediment, Plank & Langmuir, 1998). Grey crosses: bulk compositions of different sediment columns subducting at trenches (after Plank & Langmuir, 1998). All reference values are recalculated to 253 Ma.

6. Zircon ages

For the purpose of the age determination of the Lesvos mafic-ultramafic complex, zircons have been separated from gabbros and analysed by SHRIMP II. The gabbros were collected from the tectonic mélange at the western entrance of Charamida village (sample L02) and at the eastern entrance of Plomari village from an outcrop within the village itself (L40).

The zircons of gabbro L02 have prismatic and mostly idiomorphic shape and their size varies between 100-200 µm. Cathodoluminescence imaging revealed homogeneous growth and well- developed oscillatory zoning (Fig. 1-21). The Th/U ratio of the zircons ranges between 0.5 and 1.6 suggesting a clear magmatic origin (Fig. 1-25, Appendix E-1). On a Tera-Wasserburg diagram they are low in common Pb (Fig. 1-23a). Most of the zircon ages

are consistent with a $^{238}U/^{206}Pb$ weighted mean age of 253.1 ± 5.6 Ma (Uppermost Permian) (Fig. 1-23a). This age is interpreted as the crystallization age of the gabbro and is consistent with fossil ages from the sediments in the ophiolitic mélange obtained by Papanikolaou (1999). Three grains show slightly younger $^{238}U/^{206}Pb$ weighted mean ages of 235.9 ± 7.7 Ma at their rims (see Figs. 1-21C & 1-23b), suggesting new growth during a Middle Triassic tectonothermal event. It is proposed that this event can be directly linked to the recently recognised widespread rift-related intrusion of A-type granites in eastern Greece (SMM: Himmerkus et al. 2004; the Cyclades: Reischmann, 1998; Tomaschek et al., 2001), Bulgaria (SMM [Ograzhden]: Zidarov et al., 2004) and southwestern Turkey (Menderes Massif: Dannat & Reischmann, 1997; 1998; Koralay et al., 2001).

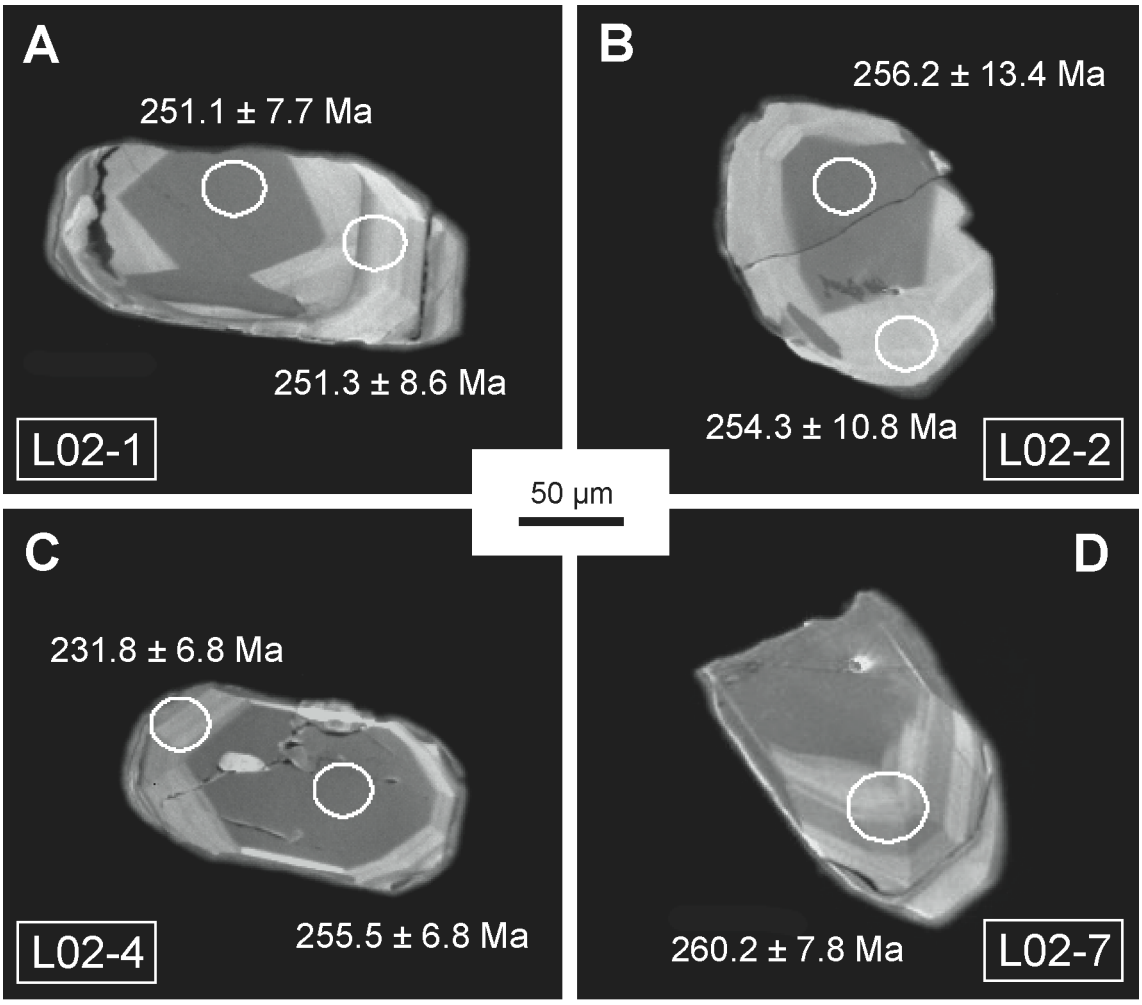

Fig. 1-21: Cathodoluminescence (CL) images of zircon crystals from gabbro L02. The euhedral shape and oscillatory zoning are well visible (A, C and D). In B the zircon crystal shows oscillatory zoning but also a rounded shape, possibly the result of resorption in a fluid phase. White circles indicate the points analysed by SHRIMP. $^{238}U/^{206}Pb$ ages are given with 1σ errors.

Zircons in gabbro L40 are rare and generally small in size. They display prismatic and variably rounded shape. Their sizes vary between 70-120 µm. Cathodoluminescence images reveal oscillatory zoning, occasionally very well developed (Fig. 1-22). The Th/U ratio points to a metamorphic origin for grain L40.3 and to a magmatic one for grain L40.1; grain L40.2 possesses a Th/U ratio that lies in between magmatic and metamorphic values (Fig. 1-25, Appendix E-2). The zircons of gabbro L40 yield different $^{206}Pb/^{238}U$ concordia ages (Fig. 1-24). Grain L40.1 yielded an age of 538.8 ± 7.5 Ma that is similar to ages obtained from granitic gneisses of the Menderes massif (Loos & Reischmann, 1999). Grain L40.2 yielded an age of 776.9 ± 11 Ma which is slightly older than that established for granitic gneisses of the Florina Terrane within the Pelagonian Zone (western Greece) discovered by Anders et al. (2006). Grain L40.3 yielded the youngest age obtained for this sample (337.5 ± 4.5 Ma) that corresponds to the well-known Permo-Carboniferous ages of basement rocks of the Pelagonian Zone (Anders et al., 2006).

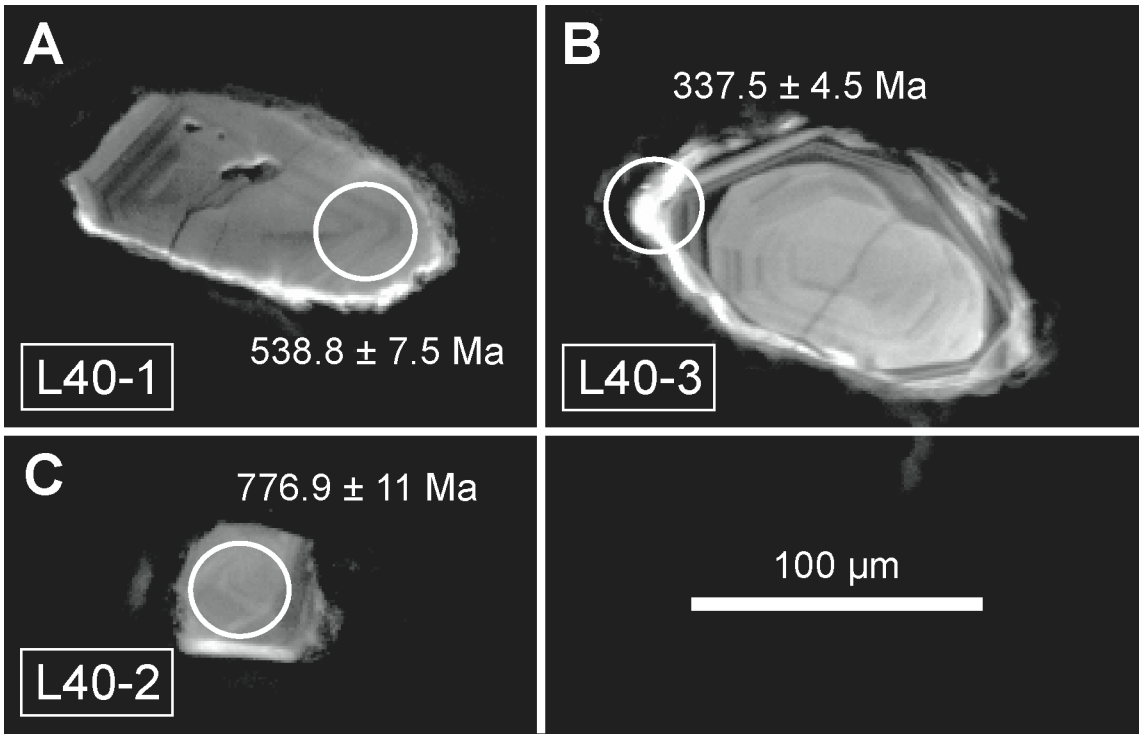

Fig. 1-22: Cathodoluminescence (CL) images of zircon crystals from gabbro L40. The oscillatory zoning is best seen in images A and B. The zircons are rounded, possibly as a result of resorption in a fluid. White circles indicate the points analysed by SHRIMP. $^{206}Pb/^{238}U$ ages are given with 1σ errors.

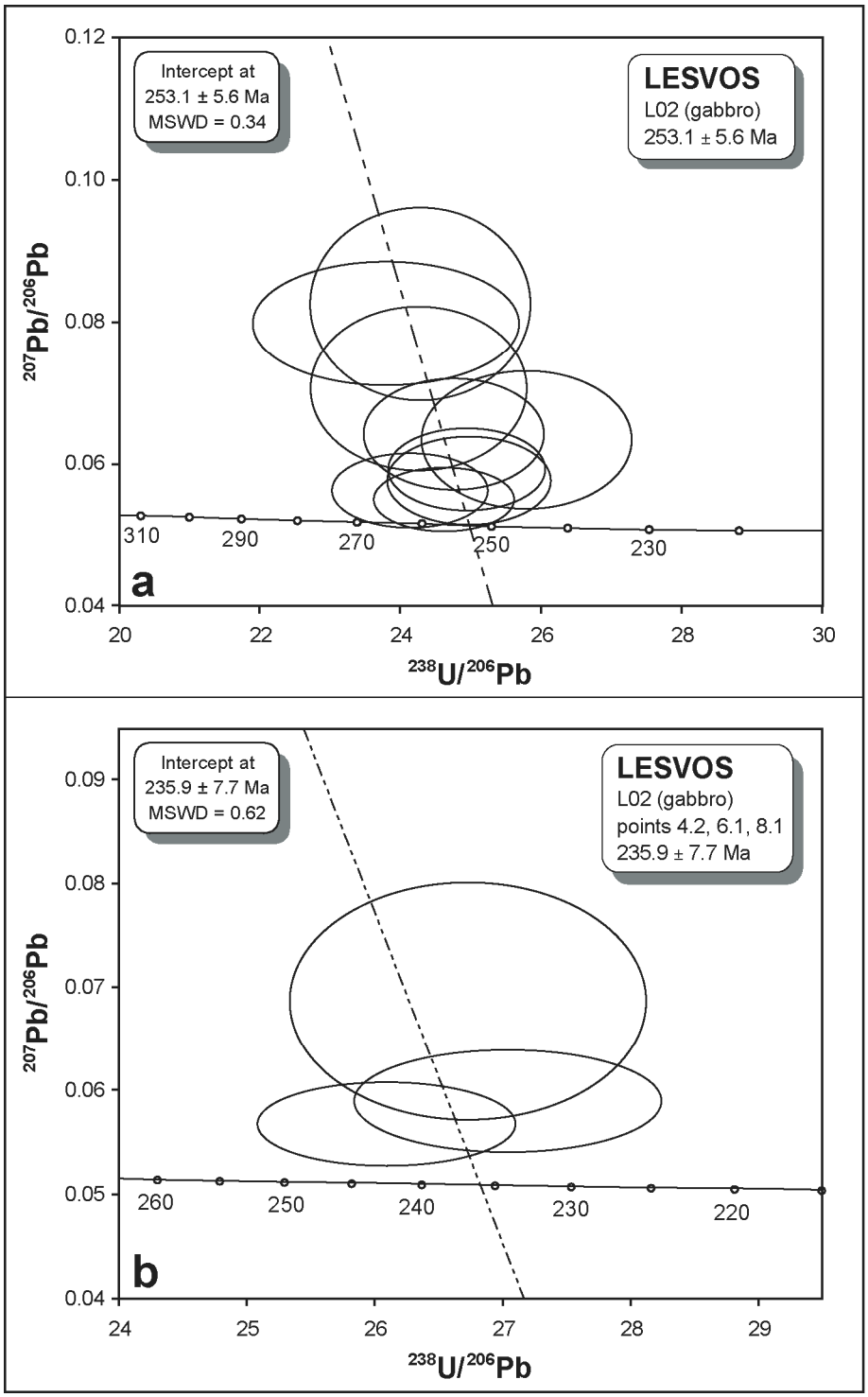

Fig. 1-23: Tera-Wasserburg diagrams for measured zircons from gabbro sample L02. The vast majority of the measured spots yield an intercept on the concordia at 253.1 ± 5.6 Ma that is interpreted as the crystallisation age of the gabbro (a). Some zircon grains (e.g. L02-4) show slightly younger ages at the rims with an intercept at 235.9 ± 7.7 Ma (b). Errors of the ellipses are 2σ.

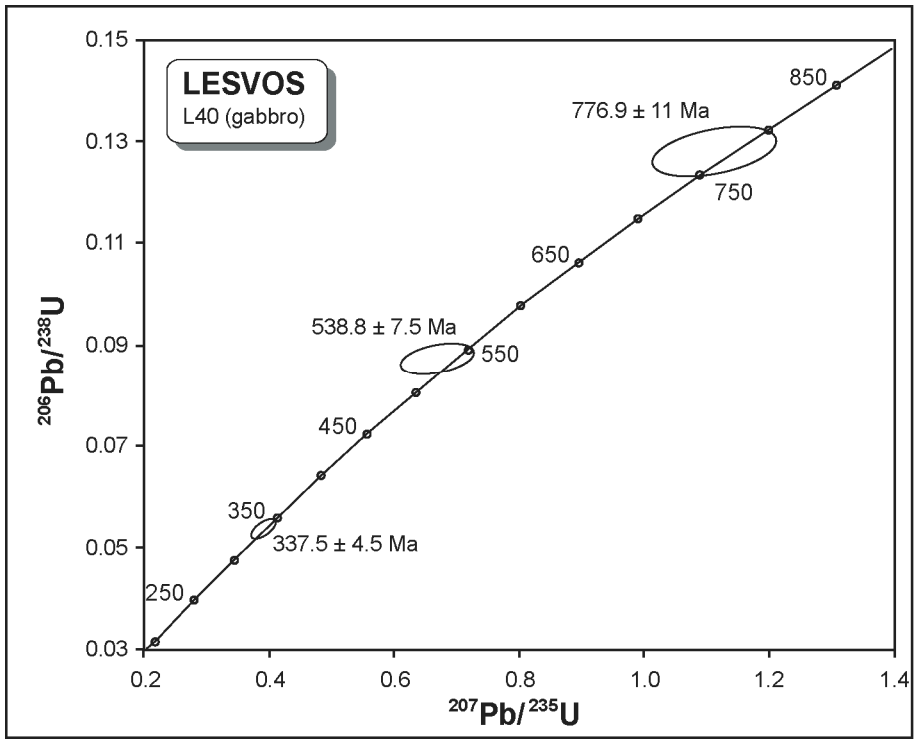

Fig. 1-24: Concordia diagram for measured zircons from gabbro sample L40. All three grains show inheritance from the basement into which the gabbro intruded and their ages correspond to those of three distinct terranes of the Internal Hellenides. See text for details.

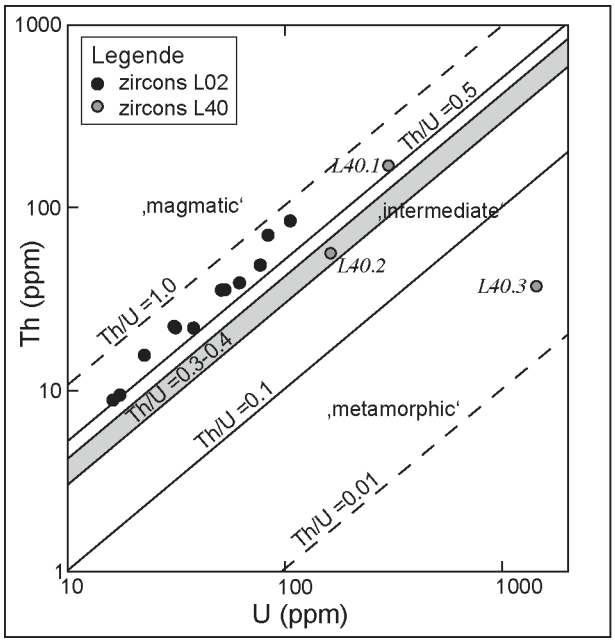

Fig. 1-25: Th and U concentrations of all measured zircons. The Th/U ratios of the zircons from gabbro L02 are ≥ 0.5 which indicates a magmatic origin. The zircons from gabbro L40 show Th/U ratios between 0.03 and 0.58. Diagram after Teipel et al. (2004).

7. Discussion and conclusions

On the island of Lesvos in the northeastern Aegean Sea, thrust sheets of mantle peridotite override a tectonic mélange containing metasediments, metabasalts and a few metagabbros. Previous workers have collectively called the above rock types the "Lesvos ophiolite" and suggested it represents Neotethyan (Jurassic) oceanic crust of N-MORB and IAT affinities. However, the complete absence of a sheeted dyke complex and of a layered cumulate sequence, in turn overlain by isotropic gabbros does not support the ophiolite description. The basalts of the mélange define two distinct groups on the basis of Nb/Y values: the Vatera (low Nb/Y) and the Mélange (high Nb/Y) groups. The Vatera basalts show multi-element profiles and REE patterns lying well within the field of N-MORB with the exception of Y and HREE abundances that are lower than those of N-MORB and match those of E-MORB. They originated by ~10% melting of depleted MORB mantle that carried a small amount (~3%) of an enriched (OIB-like) component, corroborated by moderate initial εNd values (+4.6 - +6.2). The Mélange basalts, in contrast, have multi-element profiles and REE patterns typical of within-plate compositions, transitional between E-MORB and OIB. They originated by <5% melting of spinel (and occasionally garnet) lherzolite that carried a small amount (~3%) of recycled crustal component, supported by low initial εNd values (+3.8 - +5.1).

The Lesvos peridotites comprise both spinel lherzolites and harzburgites. Using mineral compositions and calculations of temperature and oxygen fugacity, the lherzolites plot in the fields of alpine-type and continental peridotites. Trace-element modelling suggests they have experienced anhydrous melting in the stability field of spinel but also garnet lherzolite; calculated degrees of melting are generally small and never exceed 14%. There is no evidence for refertilisation-hydrous melting in a supra-subduction zone environment for the lherzolites. The harzburgites, despite being considerably more altered than the lherzolites, also display evidence of anhydrous melting in the stability field of spinel. However, they also display spoon- and dish-shaped REE patterns that can be produced by contamination of the harzburgites by a percolating OIB-like component with an inherent recycled sedimentary component, necessary to explain their isotopic shift towards EM2 compositions.

SHRIMP dating of gabbro zircons revealed an Upper Permian (253 ± 6 Ma) crystallization age and a Middle Triassic (236 ± 8 Ma) resetting of the zircon rims, compatible with the coeval and widespread rift-related intrusion of A-type granites in the eastern Mediterranean. Gabbro zircon ages of 777, 539 and 338 Ma strongly suggest inheritance from

the basement into which the gabbros intruded and correspond to ages of distinct terranes recently recognized in the Hellenides.

Similar succession can be found frequently in the adjacent areas of Greece and Turkey. In strike direction of the ultramafic unit of Lesvos the Denizgören ophiolite can be found on the Biga Peninsula. This ophiolite is composed of serpentinised harzburgites with an amphibolitic metamorphic sole at their base (Pickett & Robertson, 1996, Beccaletto & Jenny, 2004) what is similar to the Lesvos ultramafic unit. However, within the succession of the Denizgören ophiolite no mafic members are preserved and the age of the amphibolitic sole is very different. While the hornblendes of the Lesvos amphibolitic sole yield a mean K-Ar age of 155 ± 5 Ma (Hatzipanagiotou & Tsikouras, 1995) the metamorphic sole of the Denizgören ophiolite displays hornblende Ar-Ar ages of 125 Ma (Beccaletto & Jenny, 2004).

SE of Lesvos Island, as an integral part of the Sakarya microcontinent, the Karakaya Complex can be found. Similar to Lesvos this complex contains highly deformed and partly metamorphosed clastic and volcanic series of Permian to Triassic age with within-plate and mid-ocean ridge affinity (Pickett & Robertson, 1996, 2004; Göncüoglu et al., 2004). One significant difference to the Lesvos complex is the absence of ultramafic rocks. Furthermore, the Karakaya Complex is interpreted by Pickett & Robertson (1996) to be formed by the collision of two small continental fragments during the closure of the Paleotethys already in Triassic times, while the Lesvos rocks have been obducted in Jurassic times.

In northern Turkey the Küre ophiolite (Central Pontides) displays a Triassic age (Robertson, 2002; Cakir et al., 2006) similar to that determined in this work for the Lesvos complex. However, the Küre ophiolitic rocks have been interpreted as being of supra-subduction zone origin (Robertson, 2002; Cakir et al., 2006), while the Lesvos complex does not show any subduction component involved.

A complex with similar rocks, namely the Lycian Nappes, can be found in the SW part of Turkey within the Taurides. Those nappes contain a mélange and a peridotite sheet of Late Jurassic to Early Cretaceous age and supra-subduction affinity (Robertson, 2002, Celik & Delaloye, 2003) what precludes further comparison with Lesvos. Below the mélange and peridotite sheet the Karadag and Teke Dere Thrust Sheets are situated. The Karadag Thrust Sheet records Late Carboniferous to Upper Permian continental shelf deposition and the overlying Teke Dere Thrust Sheet comprises a Late Permian rift succession including within-plate basalts (Collins & Robertson, 1999). These thrust sheets are comparable to the Lesvos schist-marble unit and the tectonic mélange, respectively.

The adjacent to the Lycian Nappes Antalya ophiolites contain ophiolitic rocks with mainly lower crustal and upper mantle members. They two are regarded of Cretaceous age (Rojay et al., 2001; Önen, 2003) what precludes them for further comparison with the Lesvos complex.

The Ankara Complex in Central Turkey comprises many mafic-ultramafic rocks mainly of Late Jurassic to Cretaceous in age. Furthermore, they display a supra-subduction zone signature (Tankut et al., 1998; Gökten & Floyd, 2007). Hence they are entirely different from the Lesvos mafic-ultramafic rocks.

On the Greek mainland there are several ophiolites and mafic-ultramafic complexes. Many of them were formed in Jurassic times, e.g. the Vardar ophiolites in NW Greece (Zachariadis, 2007) or the Evros ophiolite in NE Greece (Koglin et al., 2007; Bonev & Stampfli, 2007), and are therefore much younger than the Lesvos mafic-ultramafic complex.

The Pindos ophiolite in western Greece, which is described in detail by Kostopoulos (1988), contains ophiolitic rocks and a subophiolitic mélange. While the ophiolitic rocks display MORB to IAT and boninitic affinities, the subophiolitic mélange of Triassic age contains within-plate basalts similar to the Mélange basalts of Lesvos as well as T- and N-MORB basalts comparable to the Vatera basalts. The presence of N-MORB type basalts within the subophiolitic mélange of Triassic age suggest that spreading in Pindos was already on the way in Triassic times.

On Evia Island, Greece, Katzir et al. (2000) described mafic and ultramafic rocks from the ophiolitic mélange of the Cycladic Blueschist Unit of supra-subduction zone affinity. De Bono (1998) mentioned basalts of Middle Triassic age within the Volcanosedimentary Complex of Central Evia, which exhibit within-plate characteristics similar to the Mélange basalts of Lesvos Island.

In order to explain the origin and evolution of the Lesvos mafic-ultramafic complex within the Neotethyan context we used the paleogeographic maps of Stampfli & Borel (2002). In Permo-Triassic and Late Triassic times (250 – 240 Ma) the Lesvos complex is situated within the Meliata-Maliac rift at the northern margin of the Pelagonian basement (Fig. 1-26a, b). Between 240 Ma and 230 Ma the Maliac rift started to open due to Paleotethyan slab rollback. During Triassic and Jurassic the Maliac Ocean broadens and the Lesvos complex together with the Pelagonian basement moves towards south (Fig. 1-26c, d). Intra-oceanic subduction started at 180 Ma to create the Vardar Ocean (Fig. 1-27a) and with proceeding subduction of the Maliac Ocean in Late Jurassic (155 Ma) WPB and MORB basalts together

with slivers of lherzolite and harzburgite get obducted (Fig. 1-27b). The northwards movement of the African plate during Cretaceous times and closure of the ocean basins causes the movement of the Lesvos complex as well as the Pelagonian basement towards north until they reach their present position (Fig. 1-27c, d).

We propose that the Lesvos mélange and ultramafics best represent an incipient continental rift setting that led to the subsequent formation of the Meliata-Maliac-Vardar branches of Neotethys, and that the term "Lesvos ophiolite" should definitively be abandoned.

Complexes containing rift associations with Permo-Triassic ages can be found elsewhere in Greece and Turkey, namely the Teke Dere Thrust Sheet of the Lycian Nappes (SW Turkey), the Pindos subophiolitic mélange (W Greece), the Volcanosedimentary Complex on Central Evia Island (Greece) and probably the Karakaya Complex (NW Turkey).

Fig. 1-26 (next page): Paleogeographic maps of the Paleo- and Neotethyan region (250 – 200 Ma) (after Stampfli & Borel, 2002).

Legend: AA, Austro-Alpin; Ab, Alboran; Ad, Adria s.str.; Ag, AladaEuro-BolkardaEuro; An, Antalya, Alakir Cay; Ap, Apulia s.str.; Ar, Arna accretionary complex; As, Apuseni-south, ophiolites; At, Attika; Av, Arvi; Ay, Antalya upper units; Ba, Balkanides, external; Bd, BeydaEurolari; BH, Baer Basit-Hatay ophiolites; Bk, Bozdag-Konya fore-arc; Bl, Bitlis; Bn, Bernina; Br, Briançonnais; BS, Bator-Szarvasko ophiolites; Bu, Bucovinian; Bü, Bükk; Bv, Budva; Ca, Calabria autochton; cB, central Bosnia; cD, central Dinarides ophiolites; Ci, Ciotat flysch; CL, Campania-Lucania; Co, Codru; Cn, Carnic-Julian; cR, circum-Rhodope; Cv, Canavese; Da, Dacides; Db, Dent Blanche; Dg, Denizgören ophiolite; Do, Dobrogea; Ds, Drimos, Samothace ophiolites; Du, Durmitor; eA, east Albanian ophiolites; Eç, Eriç ophiolite; El, Elazig, Guleman ophiolites+arc; eP, east Pontides; Er, Eratosthen; Fa, Fatric; gC, Great-Caucasus; Gd, GeydaEuro-Anamas-Akseki; Ge, Gemeric; GT, Gavrovo-Tripolitza; Gt, Getic; Gü, Gümüshane-Kelkit; He, Helvetic rim basin; Hg, HuEurolu-Boyalitepe; hK, high karst; HM, HuEurolu-Mersin; Hr, Hronicum; Hy, Hydra; IA, Izmir-Ankara ocean; Ig, Igal trough; Io, Ionian; Is, Istanbul; Ja, Jadar; Jo, Jolfa; Jv, Juvavic; Ka, Kalnic; Kb, Karaburun; Ke, Kotel flysch; Ki, Kirshehir; Kk, Karakaya forearc; Ko, Korab; Kp, Karpinski; Kr, Kermanshah ophiolite; KS, Kotel-Stranja rift; Ku, Kura; Kü, Küre ocean; La, Lagonegro; Lb, Longobucco; Le, Lesbos ophiolites; Li, Ligurian; Lo, Lombardian; Ma, Mani; Mc, Maliac rift/ocean; Me, Meliata rift/ocean; Mi, Mirdita autochton; Mm, Mamonia accretionary complex; Mn, Menderes; Mo, Moesia; MP, Mersin, Pozanti ophiolites; Mr, Mrzlevodice fore-arc; MS, Margna-Sella margin; Mt, Monte Amiata fore-arc; Mz, Munzur daEuro-Keban; nC, north Caspian; Ni, Nilüfer seamount; Ns, Niesen flysch; Ot, Othrys-Evia-Argolis ophiolites; Oz, Otztal-Silvretta; Pa, Panormides; Pd, Pindos rift/ocean; Pi, Piemontais ocean; Pk, Paikon island arc; Pl, Pelagonian; Pn, Pienniny rift; Px, Paxi; Rh, Rhodope; Sc, Scythian platform; Sd, Srednogorie rift-arc; Se, Sesia (western Austroalpine); Si, Sicanian; Sj, Strandja; Sk, Sakarya; sK, south-Karawanken fore arc; Sl, Slavonia; SM, Serbo-Macedonian; Sn, Sevan ophiolites; Sr, Severin ophiolites; SS, Sanandaj-Sirjan; St, Sitia_E_Crete; TB, Tirolic-Bavaric; tC, Transcaucasus; TD, Transdanubian; Tg, Tuz Gölü, Haimana; Tl, Tavsenli; To, Talea Ori; Tp, Troodos ophiolite; Tt, Tatric; TT, Toros transform margin; Tu, Tuscan; Tv, Tavas+Tavas seamount; Ty Tyros fore arc; Tz, Tizia; UM, Umbria-Marches; Va, Valais trough; Vd, Vardousia; Ve, Veporic; Vo, Vourinos (Pindos)-Mirdita ophiolites; Vr, Vardar ocean; wC, western-Crete (Phyl-Qrtz) accr. complex; WC, West-Carpathian; Zl, Zlatibar ophiolites; Zo, Zonguldak.

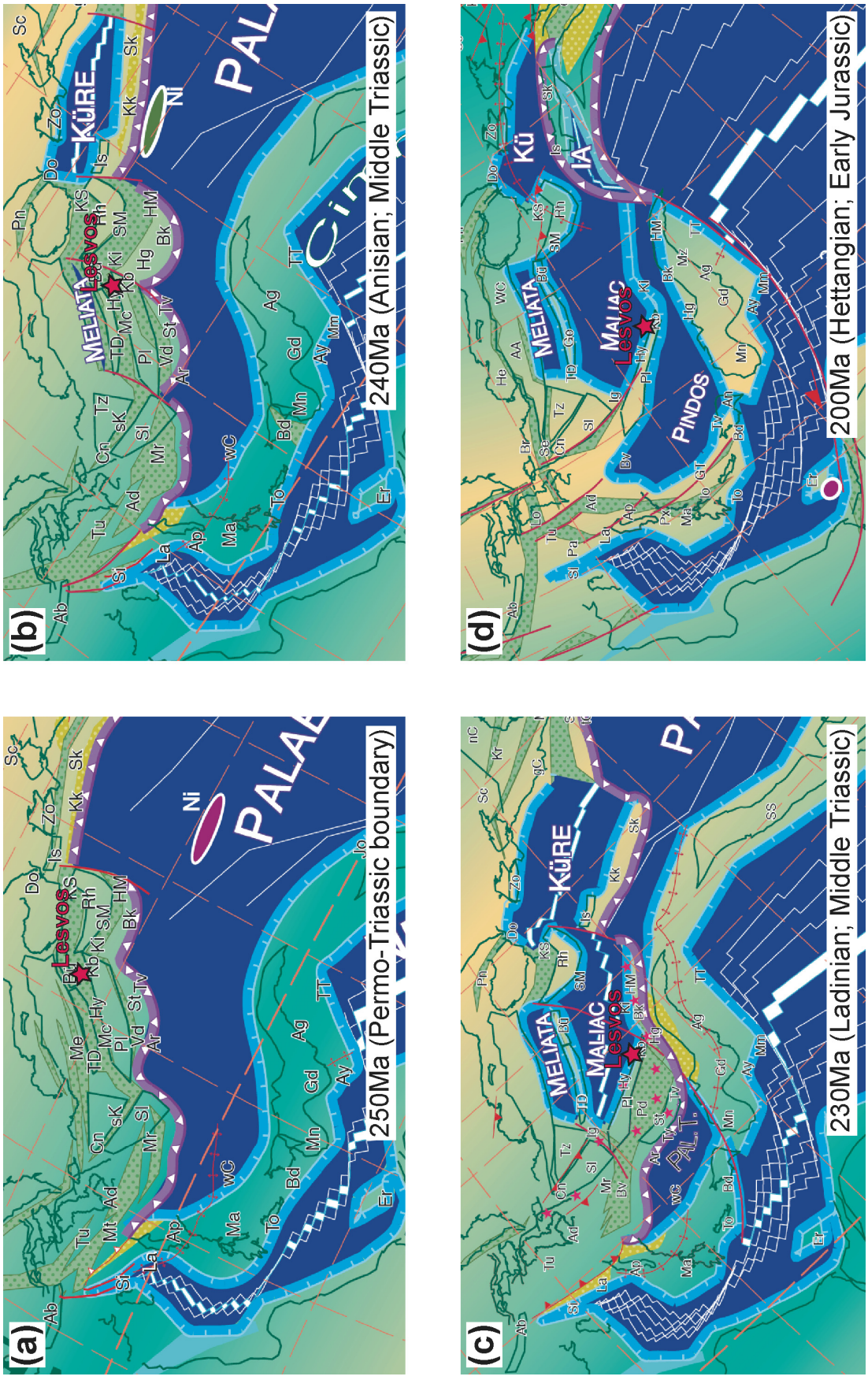
(a)
250Ma (Permo-Triassic boundary)
(b)
240Ma (Anisian; Middle Triassic)
(c)
230Ma (Ladinian; Middle Triassic)
(d)
200Ma (Hettangian; Early Jurassic)
Lesvos
MELIATA
MALIAC
KÜRE
PINDOS
PALAEOTETHYS
Ni

Fig. 1-27: Paleogeographic maps of the Paleo- and Neotethyan region (180 – 46 Ma) (after Stampfli & Borel, 2002); for Legend see Figure 26.

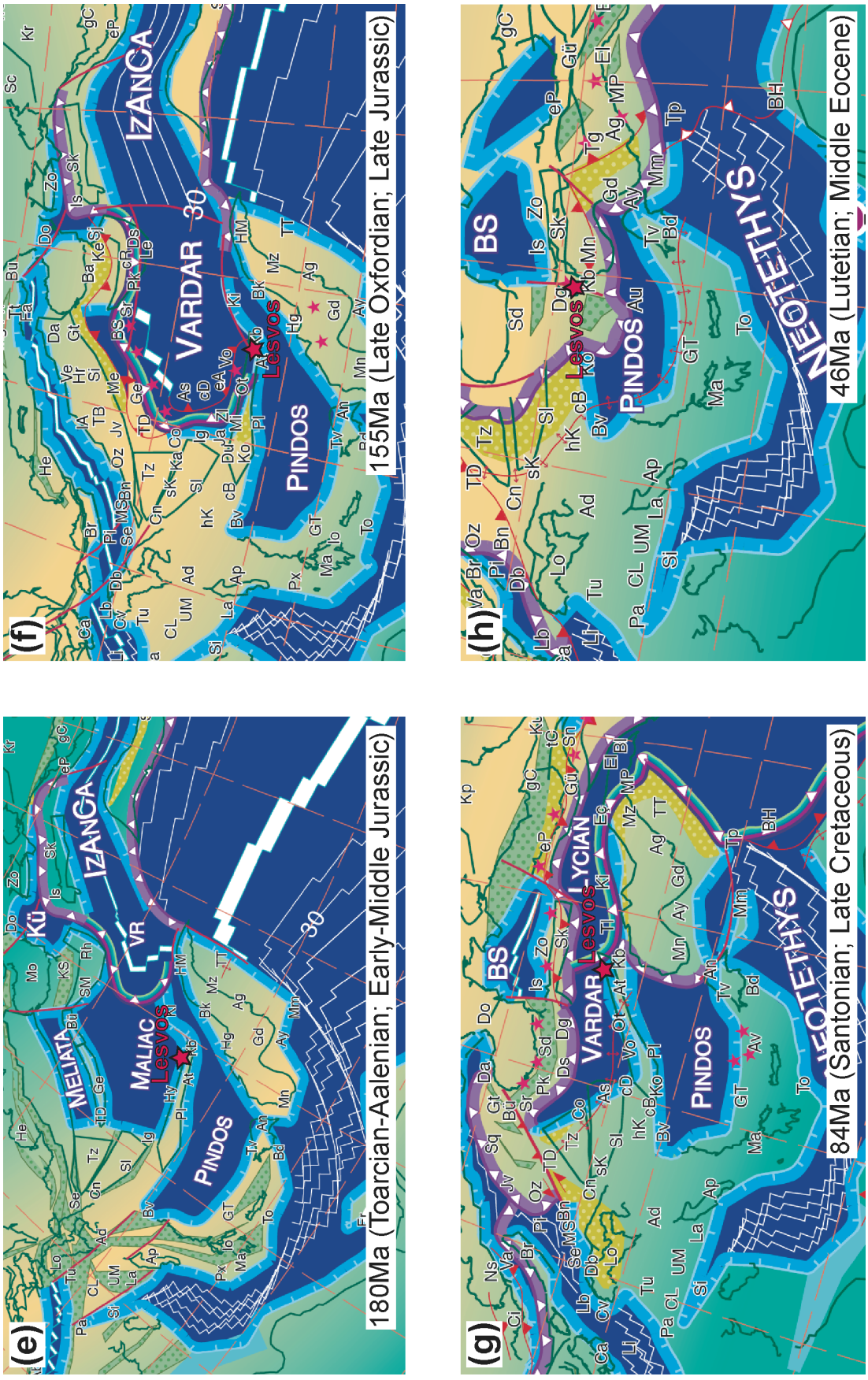

Chapter 2

Geochemistry, petrogenesis and tectonic setting of the Samothraki ophiolite, NE Greece: Trace-element, isotopic and zircon age constraints

Abstract

The Samothraki ophiolite in the north-eastern Aegean Sea, Greece, is an 'in situ' mafic suite comprising gabbros, sparse dykes and basalt flows and pillows cut by late dolerite dykes. We have determined the age of the complex by SHRIMP zircon geochronology of a gabbro as 159.9 ± 4.5 Ma (i.e. Oxfordian; early Upper Jurassic), which precludes any correlation with the so-called Lesvos ophiolite further south (253.1 ± 5.6 Ma; Uppermost Permian).

Six distinct, hitherto unrecognised, geochemical groups have been identified among the basalts and dolerites of the Samothraki ophiolite on the basis of trace-element and Nd-Sr isotopic characteristics. All groups show the presence of an enriched component in their source region, be that a long-term enriched mantle reservoir or an enriched melt. They also invariably show evidence of the addition of subduction-related hydrous fluids. Some groups testify to recent depletion events of long-term enriched mantle, some to the involvement of strongly depleted, recently refertilised mantle, whereas others to significant addition of melts either from subducted sediments or continental crust. None of the groups bear resemblance to mid-ocean ridge or back-arc basin basalts thus suggesting that the Samothraki ophiolite cannot represent mature back-arc basin crust.

In view of recent advances in back-arc basin geology and the data collected here, the Samothraki ophiolite could represent a slab-edge segment of an evolved back-arc basin near the trench, a situation that satisfies the inflow of fertile mantle, the strong signature of sediment melts and the rare occurrence of boninite-like melts. Alternatively, it could represent the embryonic stages of back-arc basin formation either by a propagating rift tip into continental crust or by oblique subduction causing back-arc rifting of continental crust and creation of nascent transtensional basins.

Restoration of block configuration in NE Greece before extensional collapse of the Hellenic hinterland and exhumation of the Rhodope Metamorphic Core Complex (mid-Eocene to mid-Miocene), results in a continuous ophiolite belt from Guevgueli to Samothraki, thus assigning the latter to the Innermost Hellenic Ophiolite Belt. We propose that the Samothraki ophiolite originated via rift propagation of the Sithonia ophiolite spreading ridge into the Chortiatis calc-alkaline arc (and its basement), which was partly assimilated. Our model does not favour southward intra-oceanic subduction of the Meliata–Maliac Ocean under the Vardar Ocean whereby Samothraki is located in the back-arc spreading centre.

1. Introduction

Ophiolites traditionally mark suture zones between crustal blocks that were initially separated by an oceanic tract and eventually collided. Greece is a classical ophiolitic country. Type localities on the Greek mainland include the sizeable Pindos, Vourinos, Othris, Guevgueli, Chalkidiki (comprising the Thessaloniki-Metamorphosis and Kassandra-Sithonia occurrences) and Evros massifs, whereas smaller outcrops are known from the islands of Crete and Samothraki (Fig. 2-1). Most of these bodies have been studied petrologically and geochemically by several workers for a number of years (see review by Robertson 2002 and references therein).

Samothraki is situated in the northeastern Aegean Sea, some 45 km south of the Greek coastal city of Alexandroupolis (see Fig. 2-1), and is considered by several authors to be part of the Circum-Rhodope Belt (Kotopouli et al., 1989; Tsikouras et al., 1990; Tsikouras & Hatzipanagiotou, 1998a, b). The Circum-Rhodope Belt (originally defined by Kauffmann et al., 1976) is a NW-SE trending zone along the eastern border of the Vardar Zone and the western border of the Serbo-Macedonian Massif (Fig. 2-1). It mainly comprises Lower to Middle Jurassic continental slope and rise sediments (turbidites; Svoula or Melissochori flysch Formation) draping the western edge of the Serbo-Macedonian Massif; Permo-Triassic continental rift sediments and associated rhyolitic volcanics (known as the Examili Formation and the Nea Santa Unit respectively), Triassic shelf carbonates, ophiolites (known as the Oraeokastro, Thessaloniki-Metamorphosis and Kassandra-Sithonia ophiolites), and low-K dioritic to tonalitic/trondhjemitic intrusives (known as the Chortiatis magmatic suite) are also assigned to this belt. Ricou et al. (1998), however, discarded the term “Circum-Rhodope Belt” and suggested that the Thessaloniki-Metamorphosis ophiolites and the Chortiatis magmatic

suite form a klippe of Rhodopian origin, whereas the Svoula turbidites are in fact Cretaceous flysch deposits that accumulated in the closing Vardar ocean basin.

The Samothraki ophiolite is regarded as having originated in an ensialic back-arc basin setting (e.g. Tsikouras, 1992; Tsikouras and Hatzipanagiotou, 1998a). This, in conjunction with the reported total absence of pillow lavas in the complex, the ultrahigh Th abundance (of lamproitic levels; 26-44 ppm) of massive basalts and dolerites otherwise interpreted as MORB, occasionally with a subduction-zone imprint, and the resemblance of the complex with the so-called "Lesvos ophiolite" further south (Tsikouras & Hatzipanagiotou, 1998a, b), have prompted us to revisit the island and undertake a detailed study of this controversial ophiolitic body.

In this paper we use trace-element and isotope geochemistry combined with geochronological determinations in order to place tight constraints on the petrogenesis and tectonic setting of the Samothraki mafic complex and to establish whether it can be correlated to ophiolites in NE Greece.

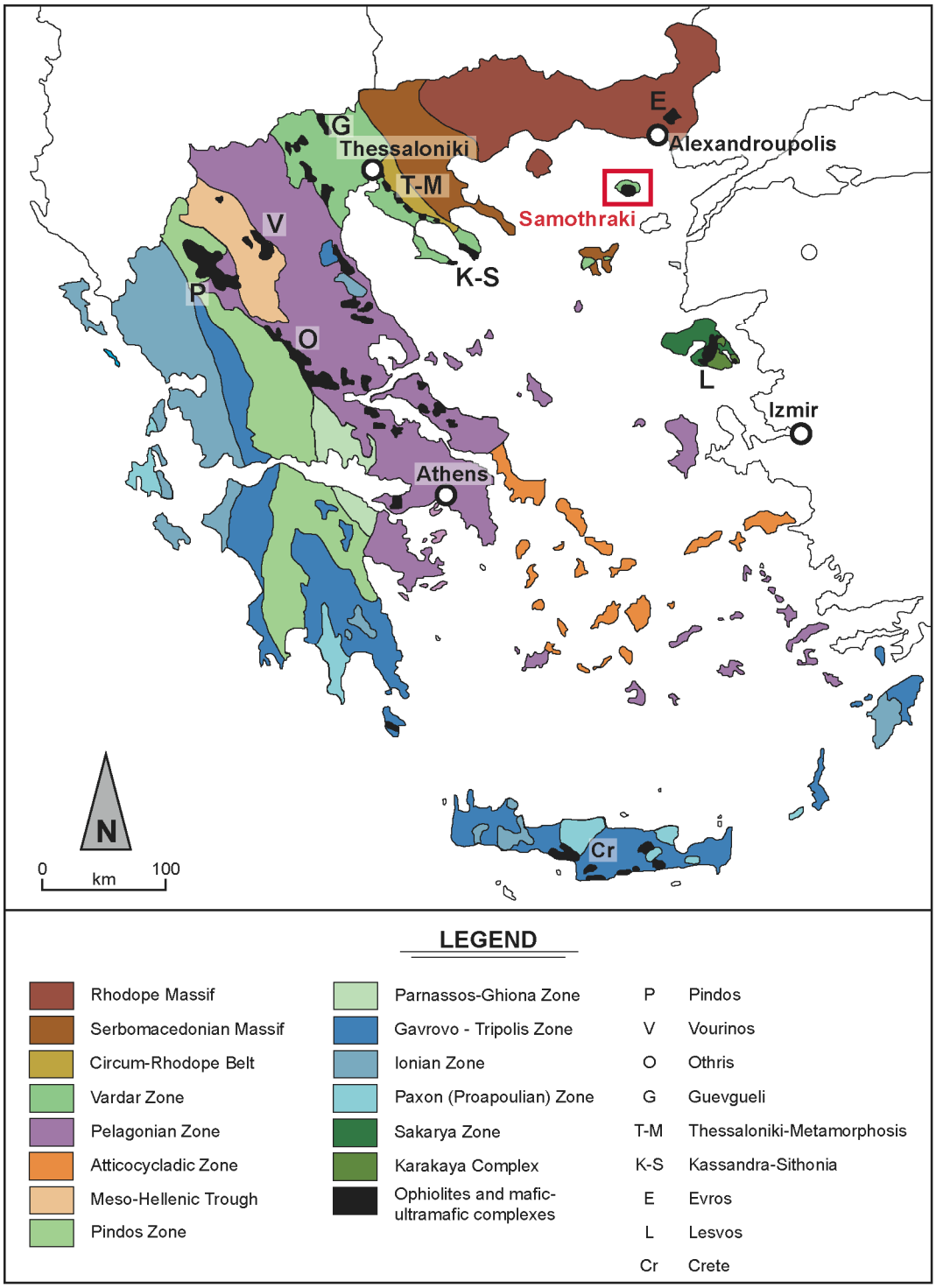

Fig. 2-1: Simplified geological map of Greece (modified after IGME, 1983 and Zachariadis, 2007).

2. Geological setting

The geology of Samothraki Island can be subdivided into four major units: (a) a Basement unit, (b) an Ophiolitic unit, (c) a Tertiary unit and (d) a Quaternary unit (Fig. 2-2).

(a) Basement unit: This unit, also known as "Schieferserie" (Heimann et al., 1972), consists of low-grade metamorphosed sedimentary and volcanic rocks. The sedimentary formations predominate in the series and comprise shallow marine to terrestrial conglomerates, limestones, sandstones and shales of Late Jurassic age (Heimann et al., 1972; Tsikouras & Hatzipanagiotou, 1998a). Coarse-grained metaconglomerates occupy the bottom part of the sequence whereas fine-grained schists prevail at the top. Syndepositional intercalations of rhyodacitic to andesitic metavolcanic rocks are confined to the lower parts of the Basement unit which represent Alpine flyschoid series accumulated in a continental-rift setting (Tsikouras & Hatzipanagiotou, 1998a). The sedimentary lithologies of the Basement unit display fining upwards possibly suggesting decreasing tectonic activity or deepening of deposition.

(b) Ophiolitic unit: This unit overlies the Basement unit with faulted contacts. It consists, from bottom to top, of cumulus gabbros overlain by isotropic gabbros carrying sparse dykes that pass upwards into massive basalt flows and pillow lavas. Although declared missing from the complex (Tsikouras and Hatzipanagiotou, 1998a), the latter are present at several localities (e.g. Paleopoli and Kipos; see Appendix F-1 and Fig. 2-2). All rock types mentioned above are intruded by dolerite dykes. More fractionated rock types like diorites can be found in the SW of the island. They do not belong to the ophiolite as Tsikouras et al. (1990) have suggested but strongly resemble the calc-alkaline diorites described in detail by Schünemann (1985) from the Chortiatis magmatic suite. K-Ar dating on hornblende separated from a diorite yielded a Late Jurassic age (154-155 ± 7 Ma; Tsikouras et al., 1990). This age is in good agreement with the SHRIMP zircon age of a Chortiatis diorite (159.1 ± 4.2Ma; Zachariadis, 2007). The relationship between the ophiolite and the diorites of Samothraki is further explored in a later section. Ultramafic rocks are virtually absent from the island.

(c) Tertiary unit: This unit unconformably overlies the Ophiolitic unit. It is built of conglomerates, sandstones, shales, and (numulitic) limestones as well as basaltic to rhyodacitic volcanic rocks of Upper Oligocene to Lower Miocene age (Heimann et al., 1972;

Eleftheriadis et al., 1994; Vlahou et al., 2006). These rocks occupy the western and eastern part of Samothraki Island and developed in an extensional, post-collisional setting (Vlahou et al., 2006). The central part of the island is occupied by a large granite intrusion of Miocene age (Rb-Sr on biotite and whole rock, Christofides et al., 2000) that thermally affected both the Ophiolitic and the Basement units. The Tertiary unit is described in detail by Esson et al. (1990), Eleftheriadis et al. (1994), Seymour et al. (1996) and Vlahou et al. (2006).

(d) Quaternary unit: This unit is composed of very young clastic sedimentary rocks that occur at the peripheral parts of Samothraki Island.

For the purpose of this study we sampled basalts and dolerites from the Ophiolitic Unit at different places (Paleopoli, Therma, Kipos, Profitis Ilias, SE Dafnes, SE Samothraki, Isomata), as well as dioritic samples from the SW part of the island near Profitis Ilias village (see Fig. 2-2 for localities).

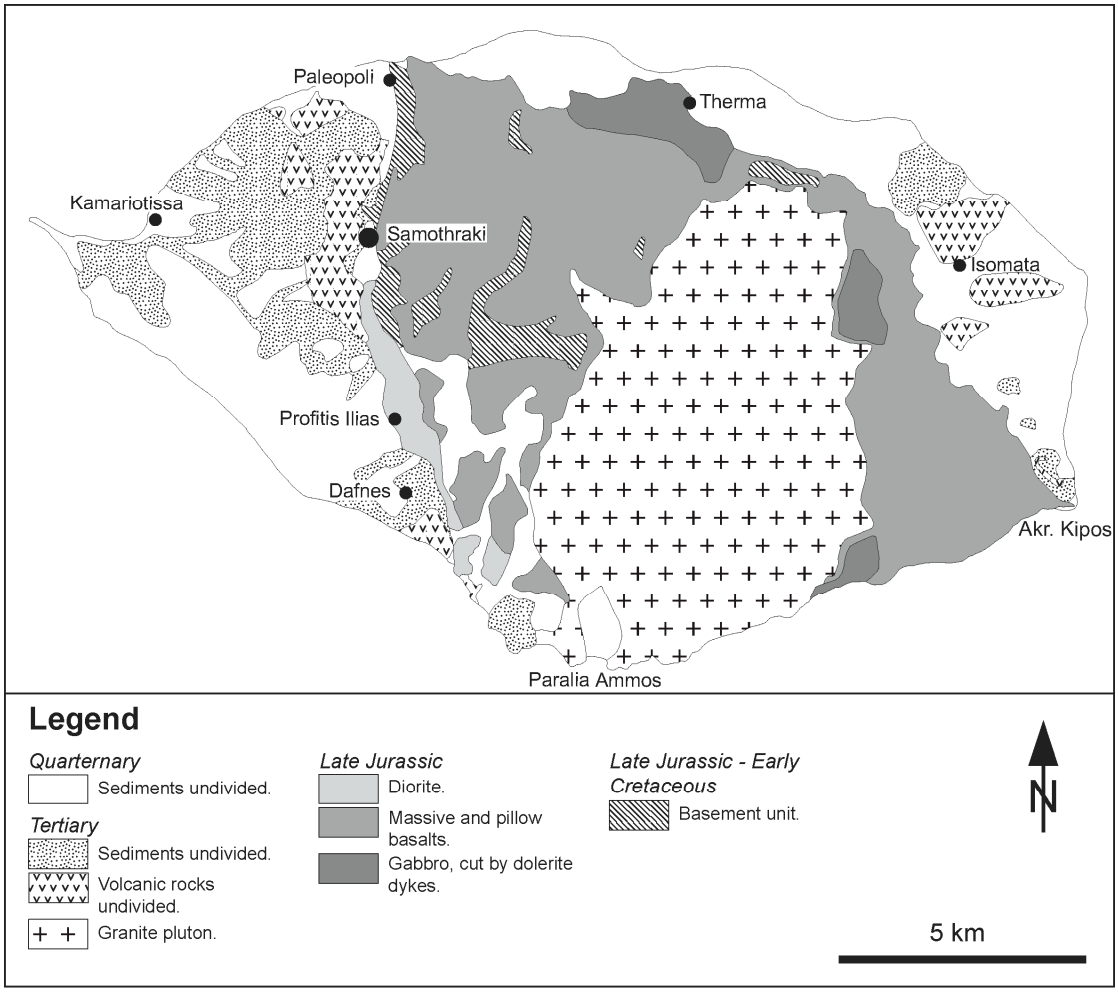

Fig. 2-2: Simplified geological map of Samothraki Island (after Heimann et al., 1972).

3. Analytical methods

3.1. X-ray fluorescence analysis (XRF)

The samples were crushed and milled to a powder with a grain size of less than 50 µm. 6 g sample powder was mixed with Scandiplex A (resin) + B (hardener) and pressed with 7 t to pellets for trace element measurement. For major element measurement 0.8 g sample powder was mixed with 4.8 g flux material ($LiBO_4$). This mixture was molten in platinum pots and cooled down to glass pellets in a platinum platter. The glass and powder pellets were measured in a Philips PW1404 XRF spectrometer with an Rh X-ray tube with a maximum stimulation of 100kV (3kW) at the Johannes Gutenberg-University, Mainz, Germany. AGV-1, BCR-1, BHVO-1, JP-1 and others were used as standard materials.

3.2. Laser ablation with inductively coupled plasma mass spectrometry (LA-ICPMS)

The rare-earth element measurements were carried out using LA-ICPMS at the Max Planck Institute for Chemistry in Mainz, Germany. 40 mg sample powder was molten for 10 seconds on an Ir-strip at 1500°C and by rapid cooling we produced homogeneous glass chips for measurement. A solid-state New Wave UP213 Nd:YAG laser operating at a wavelength of 213 nm and a frequency of 10 Hz was used to produce ablation pits of 120 µm in diameter. The ablated material was carried by Helium and measured on a ThermoFinnigan Element2 sectorfield ICPMS in the low-resolution mode. Three laser spots were set on every sample with a measuring time of 20 s on the background and 110 to 130 s on the sample. NIST612, KL2G, BHVO-2 and JP-1 were used as standard materials.

3.3. Thermal ionisation mass spectrometry (TIMS)

The isotope measurements were performed at the Max Planck Institute for Chemistry in Mainz, Germany. Strontium (Sr) and Nd ratios were determined on a Finnigan MAT 261 thermal ionisation mass spectrometer (TIMS) equipped with a multicollector. Strontium (Sr) was loaded with TaF_5 on a single W filament, while Nd was loaded on double Re filaments. Both elements were analysed as metals. Two hundred (200) ratios were measured on average for each sample. Mass fractionations were corrected to $^{86}Sr/^{88}Sr = 0.1194$ and $^{146}Nd/^{144}Nd =$

0.7219. Measurements for the NBS 987 Sr and La Jolla Nd standards gave $^{87}Sr/^{86}Sr$ = 0.710289 ± 11 (n=17, 2σ) and $^{144}Nd/^{143}Nd$ = 0.511840 ± 6 (n=33, 2σ), respectively.

3.4. Sensitive high resolution ion microprobe (SHRIMP)

The U-Th-Pb SHRIMP (Sensitive High Resolution Ion Microprobe) technique allows in-situ spot dating of individual domains within single zircon grains. Combined with a thorough cathodoluminescence imaging study, it permits the dating of zircons with complex structure.

The U-Pb ion microprobe data were obtained using the SHRIMP II instrument at the Centre of Isotopic Research (VSEGEI) in St. Petersburg, Russian Federation. Five scans over the critical mass were carried out using a spot size of 20 μm. The intensity of the primary beam was set at 4 nA. Temora 1 was used as a standard zircon (Black et al., 2003). The data were reduced and visualised using the SQUID and Isoplot/Ex add-in for Excel (Ludwig 2005a, 2005b).

4. Whole rock major and trace element geochemistry

4.1. Basalts and dolerites

Whole-rock geochemical analyses for the Samothraki basalts and dolerites are given in Appendix B-3. In order to assess the effect of alteration on whole-rock geochemistry we plotted each element analysed against Zr, the latter having long been established as an immobile element during hydrothermal alteration (Kostopoulos 1988 and references therein). These plots are available as supplementary data (Appendix F-2). It is evident from Appendix F-2 that most of the major elements, TiO_2 and P_2O_5 excepted, are more or less disturbed by alteration as are some of the trace elements. Certain trace elements however (e.g. Nb, Ta, Hf, Th, Y, REE) are immobile, and only they are used for rigorous petrogenetic modelling.

Figure 2-3 depicts normal mid-ocean ridge basalt- (N-MORB-) normalised multi-element patterns for the Samothraki basalts and dolerites. Such diagrams allow first-order geochemical interpretations that can further be elaborated by consideration of specifically designed ratio-ratio plots and diagrams involving isotopes. Six geochemical groups can be distinguished and are discussed separately below.

Group I rocks are characterised by nearly flat HFSE segments lying between those of N2-MORB (as originally defined by Viereck et al., 1989) and enriched mid-ocean ridge basalt (E-MORB) (Zr_N/Yb_N = 0.9 – 1.2), a continuous and progressive enrichment from Zr to Th (Zr_N/Th_N ~ 0.3; Nb_N/Yb_N = 1.5 – 3.6) and a "hump" in the LILE part of variable height; Sr and Th display E-MORB-like values (Fig. 2-3A). To facilitate the reader, N2-MORB is interpreted as deep (compared to N1-MORB), small degree partial melts of spinel lherzolite (Viereck et al., 1989). On the other hand, E-MORB are interpreted as products of melting of enriched upper mantle domains formed either at depth in subduction zones where the mantle wedge is enriched by the addition of low-degree melts of subducted crust (Donnelly et al., 2004) or by subduction and recycling of alkalic ocean islands and seamounts (Hémond et al., 2006). Some samples show an additional enrichment in K, Rb and Ba, which can be explained by contamination of their mantle source region by subduction-related hydrous fluids. The N-MORB-normalised value of Yb is greater than unity suggesting a spinel-lherzolite mantle source. Group I resembles Type 2 volcanics (oceanic island tholeiites) from the Mamonia Complex (SW Cyprus) described by Lapierre et al. (2007) as the early stage of intra-oceanic within-plate volcanism.

Group II shows the same pattern as Group I from Yb to Th lying also between N2-MORB and E-MORB but displaying a strong enrichment in K, Rb and Ba ascribed here to aqueous fluid addition from dehydrating subducting crust (Fig. 2-3B).

Group III rocks have patterns parallel to that of E-MORB but at somewhat lower absolute abundances of all trace elements. These patterns are steeper (crossing at Ce) and characterised by lower P, Y and HREE contents compared to those of Group I rocks (P_N = 0.91 – 1.07; Y_N = 0.60 – 0.73) suggesting melting in the garnet stability field (Fig. 2-3C).

The N-MORB-normalised multi-element patterns of Group IV rocks depict a strong enrichment in LILE and a continuous and progressive enrichment from the HFSE towards the LILE (Th_N/Yb_N = 17 – 90) with a well pronounced Nb-Ta and P negative anomaly similar to global subducting sediment (GLOSS) and/or upper continental crust (UCC) (Fig. 2-3D). Such profiles of basaltic rocks can be generated either by melting of a depleted mantle source fluxed by a subduction-zone component (sediment melt or supercritical aqueous fluid) or by crust – magma interaction when basalts erupt in rift settings and assimilate crust. The patterns of Group IV rocks readily compare with that of Nelson seamount from the South Sandwich arc-basin system that exhibits enhanced subduction fluxes and has the isotope (low Nd and high Sr isotope ratios) and elemental (ultra-high Th and Ba and high Hf/Nd ratios) characteristics of a sediment melt (Leat et al., 2004).

Group V is represented by a dyke showing a concave-upward pattern at low absolute abundances of both the HFSE and REE (Fig. 2-3E). The strong depletion in HFSE suggests melting of a depleted peridotite source such as harzburgite. The continuous and progressive enrichment from P towards the LILE can be the result of mixing the depleted source with an enriched component (e.g. E-MORB, OIB). Furthermore, the enrichment in K, Rb, and Ba is likely the result of addition of hydrous fluids to the source in a subduction-related environment. This sample is geochemically comparable to Group II upper pillow lavas of the Troodos ophiolite, Cyprus which are described as transitional between island-arc tholeiites (IAT) and boninites and originated by melting of the residue after 20% melt extraction of an IAT source to which small amounts of an enriched component had been added in a supra-subduction zone setting (Cameron, 1985).

Group VI is a dolerite with a flat pattern from Th to Yb at N-MORB levels and a strong enrichment in LILE (K, Rb, Ba) suggesting derivation from a depleted mantle source affected by subduction-zone fluid percolation (Fig. 2-3F). The negative P and positive Ti anomalies are the result of apatite fractionation and Fe-Ti oxide accumulation respectively. This group is similar to Type 1 volcanics (depleted olivine tholeiites) of the Mamonia Complex (SW Cyprus) marking the very beginning of intra-oceanic within-plate volcanism and interpreted as having derived from a depleted MORB mantle (DMM) source contaminated by an Enriched Mantle Type 2 (EM2) component (Lapierre et al., 2007). The EM2 reservoir has a strong similarity with upper continental crust or continentally derived sediment (Zindler & Hart, 1986).

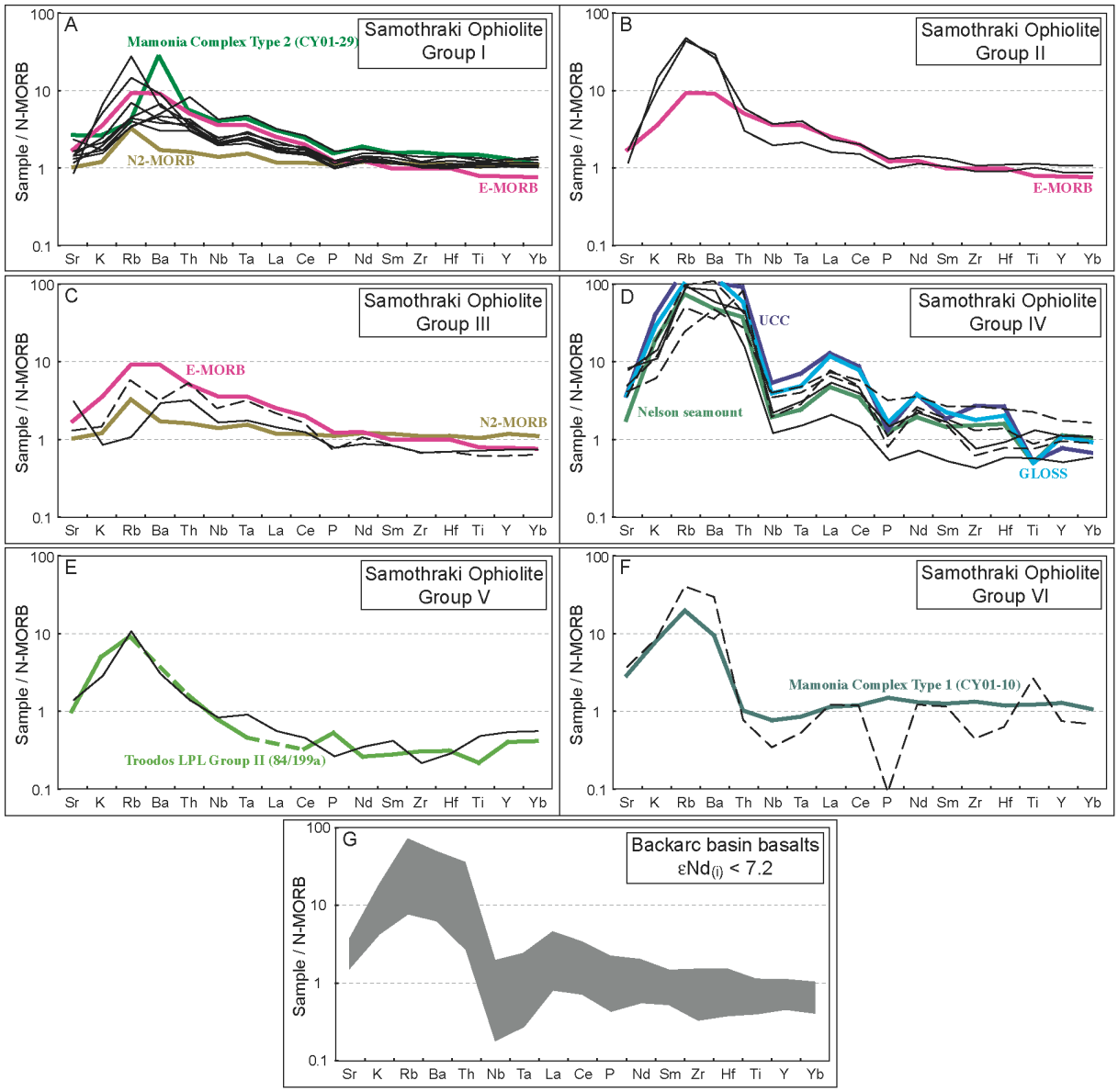

Fig. 2-3: N-MORB-normalised multi-element profiles for the different groups of the Samothraki basalts and dolerites and selected BABB (see text for discussion). Solid lines: basalts; dashed lines: dolerites. Data sources: N-MORB (normalising values) and E-MORB (Sun & McDonough, 1989); N2-MORB sub-type (Viereck et al., 1989); GLOSS (Plank & Langmuir, 1998); UCC (Rudnick & Gao, 2003); Mamonia Complex (Lapierre et al., 2007); Troodos Ophiolite (Cameron, 1985); Nelson seamount (Leat et al., 2004); Back-arc basin basalts (see text). Abbreviations: N-MORB: normal mid-ocean ridge basalt; E-MORB: enriched mid-ocean ridge basalt; BABB: Back-arc basin basalts; GLOSS: global oceanic subducted sediment; UCC: upper continental crust; UPL: upper pillow lavas.

It is important to emphasise here that the Samothraki ophiolitic volcanics have been interpreted as back-arc basin basalts (BABB) having N-MORB chemistry with an IAT imprint (Tsikouras & Hatzipanagiotou, 1998a, b). Figure 2-3G shows the field of back-arc basin basalts (BABB) constructed using selected analyses from the existing BABB database (North Fiji Basin [Nohara et al., 1994]; Okinawa Trough [Shinjo et al., 1999]; East Scotia Ridge [Leat et al., 2004]; Mariana Trough [Pearce et al., 2005]; Lau Basin [e.g. Fretzdorff et al., 2006]). Care was taken to choose only those samples for which Nd isotopic analyses were available and the $\varepsilon Nd_{(i)}$ value of which fell in the range of that of the Samothraki basalts. It becomes very clear that none of the studied samples match the BABB pattern; the absence, in particular, of a strong enrichment in LILE coupled with the absence of a prominent negative Nb-Ta anomaly strongly support the view, despite previous assertions, that the Samothraki ophiolite does not represent mature back-arc basin crust. We were also unable to confirm the previously reported lamproite-like ultrahigh Th levels (determined by XRF), attributed to contributions from subduction-related fluids (Tsikouras & Hatzipanagiotou, 1998a).

Chondrite-normalised REE patterns for the different geochemical groups of the Samothraki basalts and dolerites are available in Fig. 2-4.

Groups I and II generally show flat patterns ($La_N/Yb_N \sim 1$) with HREE abundances similar to those of N-MORB and a slight enrichment in LREE similar to that of E-MORB compositions indicating the presence of an enriched component in their mantle source. Slight negative Eu anomalies in some samples indicate plagioclase fractionation (Fig. 2-4A and B).

Group III patterns are LREE-enriched and MREE- and HREE-depleted compared to N-MORB (Fig. 2-4C). Sample SA10 shows a slight enrichment in LREE ($La_N/Sm_N = 1.6$) similar to that of E-MORB, while sample SA04 shows a rather flat profile ($La_N/Yb_N = 1.1$).

Group IV rocks exhibit REE contents similar to those of GLOSS and BCC compositions with patterns directly comparable ($La_N/Sm_N = 1.7 – 3.0$) to that of the Nelson seamount strongly suggesting the presence of subducting sediment/crustal melts in their mantle source region. Sample SA29 is particular in that it displays enrichment in LREE ($La_N/Sm_N = 2.4$) but is highly depleted relative to N-MORB and the remainder of Group IV samples. Sample SA33 shows a pattern parallel to that of E-MORB but much more elevated possibly suggesting fractionation (Fig. 2-4D).

The strong depletion of Group V mentioned earlier is supported by a highly depleted REE pattern (Fig. 2-4E). The enrichment in LREE is the result of addition of an LREE-enriched component to an already depleted mantle source. Plagioclase accumulation is

indicated by a positive Eu anomaly. Such patterns are known from Group II upper pillow lavas of the Troodos ophiolite, Cyprus (Cameron, 1985) although the pattern of the Samothraki sample is relatively more fractionated than the Troodos sample.

Group VI displays LREE and MREE abundances similar to those of N-MORB and Type 1 volcanics (depleted olivine tholeiites) of the Mamonia Complex (SW Cyprus) discussed above. The HREE are depleted and thus resemble E-MORB compositions (Fig. 2-4F).

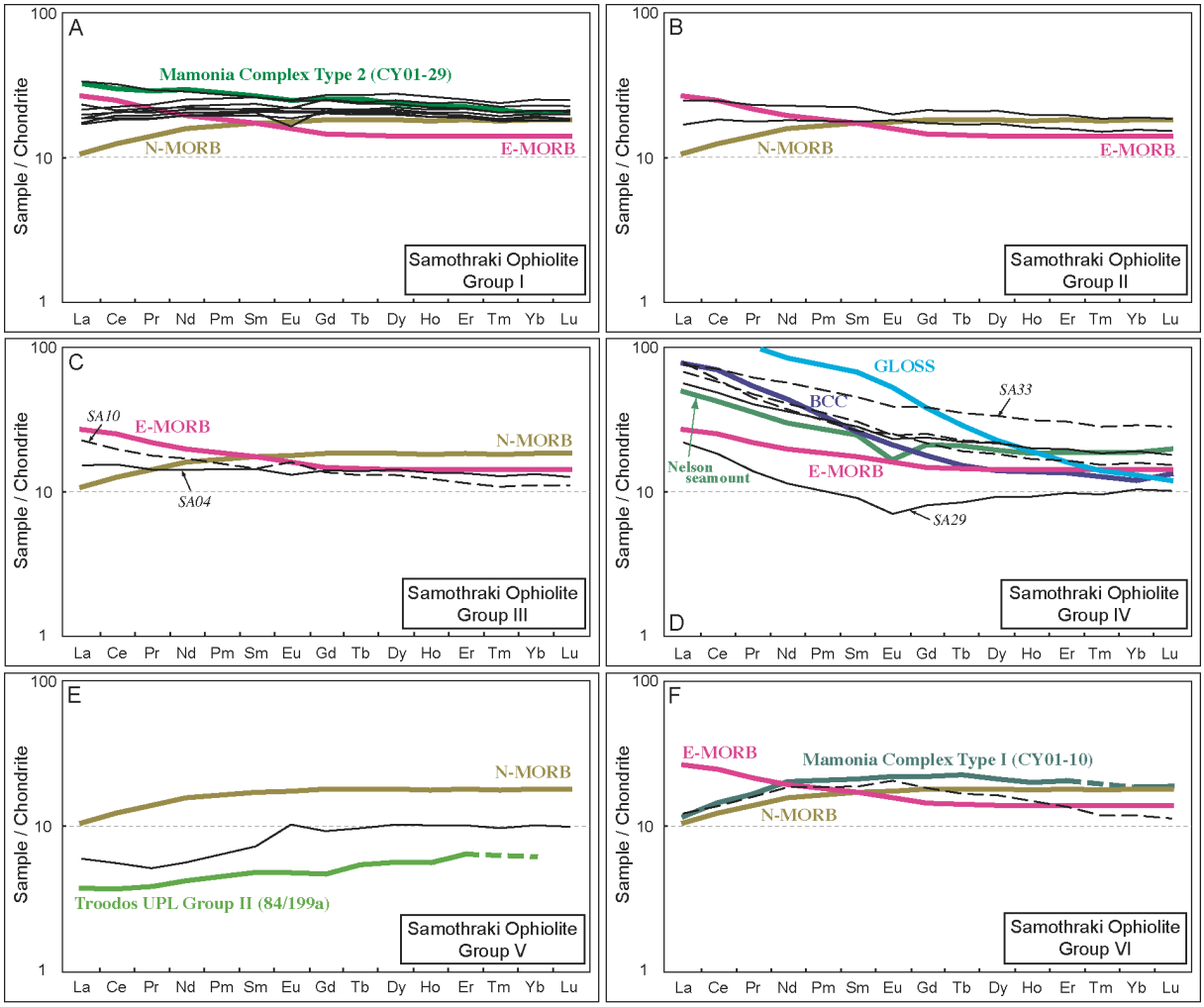

Fig. 2-4: Chondrite-normalised REE profiles for the different groups of the Samothraki basalts and dolerites. Solid lines: basalts; dashed lines: dolerites. For data sources and abbreviations of terms see also captions to Fig. 2-3: Additional data sources: Chondrite (normalising values; Sun & McDonough, 1989); BCC (Rudnick & Gao, 2003). Additional abbreviations: BCC: bulk continental crust.

The widely-used tectonomagmatic discriminant diagram of Wood (1980) that employs the elements Th, Ta and Hf is shown in Fig. 2-5. Thorium is a good indicator of subduction-zone enrichment and is known for its immobility up to 600°C (Wood 1979). Furthermore, these elements show higher concentrations in intra-plate magmas because of enriched mantle compositions and often lower degrees of melting in such settings.

This diagram strongly supports the previously inferred involvement of an enriched mantle component in the source of the Samothraki volcanics that belong to Groups I, II, III and V with both elevated Th and Ta values. Group VI dyke displays depletion in Th and Ta indicating a depleted mantle source. The basalts and dolerites of Group IV are enriched in Th but depleted in Ta and Hf similarly to GLOSS and BCC which reinforces their proposed mode of formation either by melting of a mantle source fluxed by a subduction-zone component (sediment melt or supercritical aqueous fluid) or by crust – magma interaction when basalts erupt in rift settings and assimilate crust. The vector of Th enrichment for this group resembles that of crust-magma interaction rather than that of subduction-zone fluxing (Fig. 2-5). Interestingly, Group IV rocks define an array stretching from an average WPT composition to that of diorite SA46 near the Th apex of the diagram. The importance of this point is discussed later on in this paper. Figure 2-5 also shows the fields for typical BABB (e.g. Okinawa Trough [Shinjo et al., 1999]; Lau Basin [Pearce et al., 1995; Fretzdorff et al., 2006]; East Scotia Ridge [Leat et al., 2000, 2004; Fretzdorff et al., 2002]; Mariana Trough [Pearce et al., 2005]) and basalts from extensional rift basins behind the Izu-Bonin arc (Hochstaedter et al., 2001) constructed using selected analyses from the existing literature. It is clearly evident that BABB plots in the field of MORB, IAT and CAB basalts along the trend of subduction-zone enrichment and differ significantly from the Samothraki ophiolitic basalts.

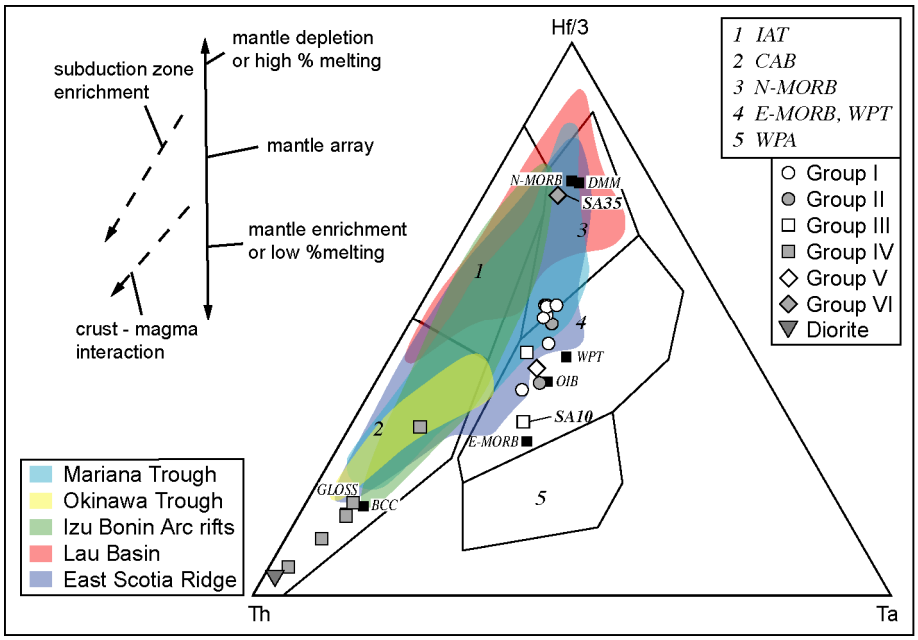

Fig. 2-5: Hf/3-Th-Ta tectonomagmatic discriminant diagram for the Samothraki ophiolitic volcanic rocks (Wood 1980, with modifications after Pearce [unpublished]). Data sources and abbreviations of terms as in captions to Fig. 2-3. Additional data sources: DMM (Workman & Hart, 2005); WPT (Pearce, 1982); Lau Basin (e.g. Pearce et al., 1995; Fretzdorff et al., 2006); Okinawa Trough (e.g. Shinjo et al., 1999); rift basins behind the Izu-Bonin Arc (Hochstaedter et al., 2001); East Scotia Ridge (Leat et al. 2000; 2004; Fretzdorff et al., 2002); Mariana Trough (Pearce et al., 2005). Additional abbreviations: IAT: island-arc tholeiite; CAB: calc-alkaline basalt; WPT: within-plate tholeiite; WPA: within-plate alkalic; DMM: depleted MORB mantle.

In the Th/Yb vs. Ta/Yb diagram of Pearce (1982) (Fig. 2-6) the enrichment or depletion of the mantle source is generally indicated by higher or lower than N-MORB Ta/Yb ratio values respectively, whereas the addition of a subduction-related siliceous melt component is indicated by high Th/Yb ratios (see also Pearce and Stern, 2006).

In Fig. 2-6 all Samothraki groups but IV fall in the mantle array and along its upper boundary; the elevated, compared to N-MORB, Ta/Yb ratios coupled with the slightly elevated Th/Yb ratios testify to an enriched mantle source. The increased Th/Yb ratios of Group IV basalts and dolerites can be explained by mixing with a subducting sediment/crustal melt component with diorite SA46 being the best candidate (Fig. 2-6). Group VI exhibits low Th/Yb and low Ta/Yb ratios pointing to a depleted mantle source similar to DMM.

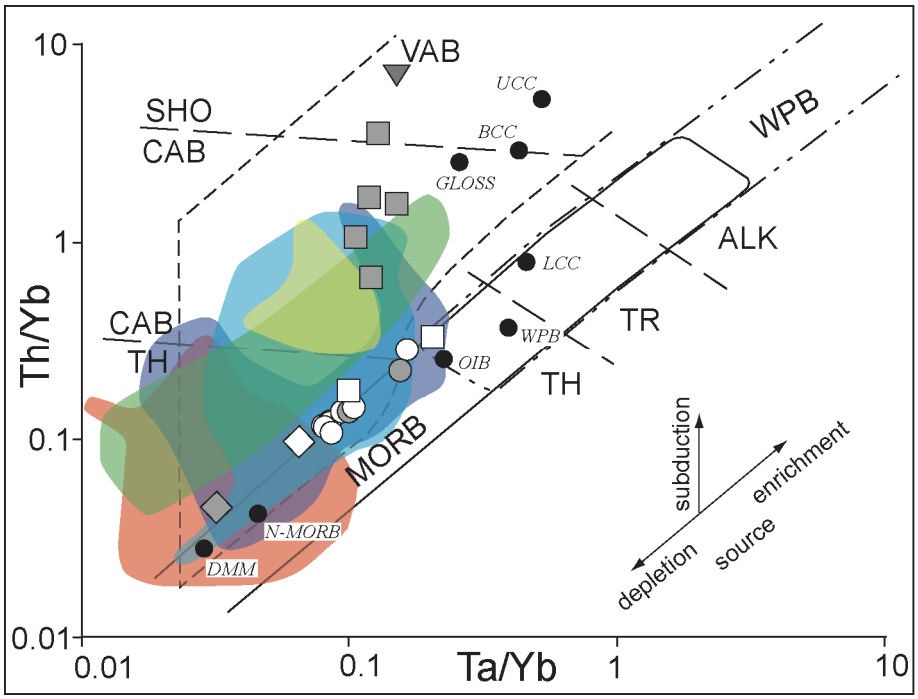

Fig. 2-6: Th/Yb vs. Ta/Yb for the Samothraki ophiolitic basalts and dolerites indicating an enriched mantle source. Group IV rocks are significantly more enriched in Th due to mixing with an enriched component (assimilated crustal material or melts from subducted sediments). Symbols, fields, data sources and abbreviations as in captions to Fig. 2-3 and 2-5. Additional abbreviations: SHO: shoshonitic; TH: tholeiitic; TR: transitional; ALK: alkaline; LCC: lower continental crust.

Plank (2005) introduced the Th/La vs. Sm/La diagram as a simple means to identify sediment recycling at subduction zones and to quantify mantle-sediment mixing calculations. In general, mantle-derived melts do not have high Th/La, except when sediment subduction/crustal contamination is independently implicated (Plank 2005). On the other hand, the Sm/La ratio is a measure of the extent of LREE depletion or enrichment. When considered together with the Th/La ratio one can evaluate the proportion of sedimentary/crustal components and the extent of depletion of the mantle source using the geochemical signature of basalts.

Figure 2-7 shows Th/La vs. Sm/La systematics for the Samothraki basalts and dolerites. Rocks from Groups I, II, III and V show moderate Th/La (0.08 – 0.13) and low Sm/La ratios (0.41 – 0.78) similar to those of back-arc basin/rift basalts (see captions to Fig. 2-3 – 2-6 for data sources). The variation in Sm/La at nearly constant Th/La values can be explained by adding up to 5% of an enriched component like E-MORB to a depleted mantle source (DMM) (Fig. 6, DMM – E-MORB mixing line).

Group IV basalts and dolerites display Th/La ratios in the range 0.18 – 0.51. Their low Sm/La ratios (0.22 – 0.39) point to an enriched source comparable to that of E-MORB or ocean island basalts (OIB) (Fig. 2-7). The enrichment in Th resulting in a high Th/La ratio can be ascribed to mixing between variable amounts (5 – 50%) of crustal material or melts from subducted sediments and an already enriched mantle source or melts thereof (e.g. E-MORB, OIB; see also Fig. 2-7, OIB – Samothraki diorite mixing line).

Group VI displays high Sm/La (0.99) and low Th/La (0.031) similar to N-MORB (e.g. basalts from Hess Deep; Stewart et al., 2002) pointing to a depleted mantle source.

Assuming that a Fertile Spinel Lherzolite (FSL), compositionally equivalent to DMM, is the source peridotite, the Samothraki ophiolitic basalts of Groups I and II would require less than about 10% melting and attendant fractionation of MORB-like eutectic compositions, whereas dyke SA17 (Group V) would require ~25% melting of the same source or smaller degrees of melting of a more depleted source (Ti-Cr modelling from Kostopoulos, 1988; Kostopoulos and Murton, 1992). Group III basalts have low Ti and high Cr contents and qualify for near primary melts from garnet-lherzolite at small to moderate extent of melting (see Kostopoulos and James, 1992). Dolerite SA35 (Group VI) is fractionated with respect to Cr and Ni but extremely rich in Ti and V indicating titanomagnetite accumulation. The melting/crystallization history of Group IV dolerites cannot be evaluated directly using Ti-Cr systematics because of the inferred assimilation of considerable amounts of crustal material. If sources more enriched than DMM are involved in the genesis of basalts then the above estimated degrees of melting should be augmented by ca. 2-3%.

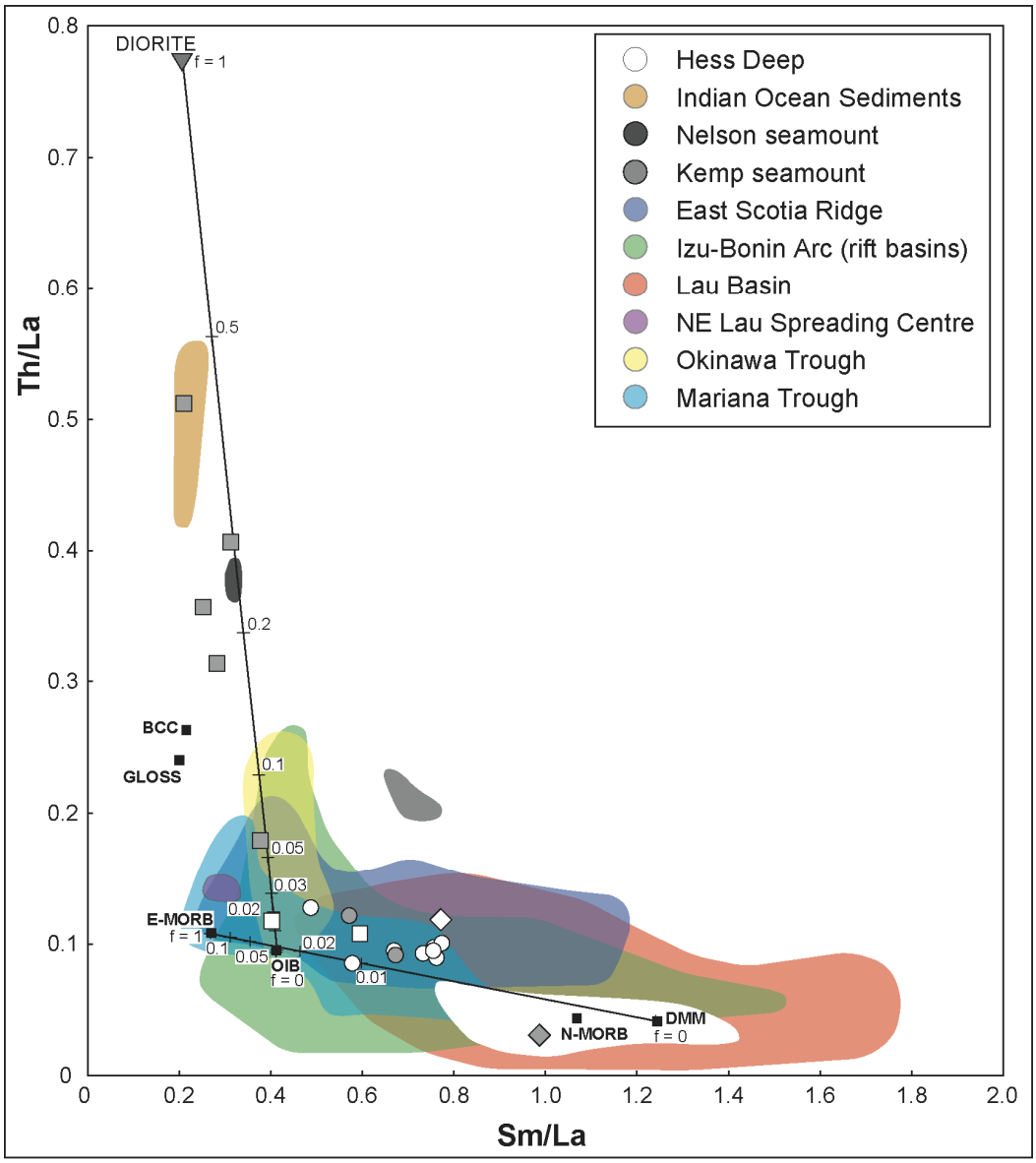

Fig. 2-7: Th/La vs. Sm/La for the different groups of the Samothraki ophiolitic basalts and dolerites (after Plank, 2005). Groups I, II, III and V mainly plot in the field of enriched mantle compositions, similar to the East Scotia Ridge back-arc basin basalts of segment E2 (Leat et al., 2000, 2004; Fretzdorff et al., 2002). Group IV rocks show high and variable Th/La at nearly constant but low Sm/La ratios, similar to basalts from enriched mantle sources additionally fluxed with variable amounts of crustal material or melts from subducted sediments. Group VI has very low Th/La and high Sm/La ratios and plots within the field of N-MORB (e.g. Hess Deep, Stewart et al., 2002). Mixing lines between DMM and E-MORB, and OIB and Samothraki diorite are indicated. Numbers next to the tic marks on the mixing lines indicate amount of melt fraction of sediment added to the mixture. Symbols, data sources and abbreviations as in captions to Fig. 2-3 – 2-6. Additional data sources: Hess Deep (Stewart et al., 2002); Kemp and Nelson seamounts (Leat et al., 2004); Northeast Lau Spreading Centre (Falloon et al., 2007); Indian Ocean sediments (Ben Othman et al., 1989).

4.2. Diorites

Dioritic rocks occur in the form of an SE-NW striking elongated body at the SW margin of the Samothraki ophiolite. Major- and trace-element analyses of a representative sample are tabulated in Appendix B-3. The age of this dioritic body has been determined by K-Ar dating of hornblende by Tsikouras et al. (1990) as Upper Jurassic age (154-155 ± 7 Ma). This age is identical within error to the Upper Jurassic age (159.1 ± 4.2 Ma) of a Chortiatis magmatic suite diorite 25 km SE of Thessaloniki (see Fig.1) obtained by Zachariadis (2007) by SHRIMP dating of zircons.

DMM-normalised multi-element pattern of the diorite (Fig. 2-8A) exhibits a continuous enrichment from the HFSE (Yb) towards the LILE (Th) with an LILE 'hump' and significant negative Nb-Ta and P anomalies thus mimicking the profile of continental crust or of melts derived from subducting sediments. The pattern of the Chortiatis diorite (Schünemann, 1985) is shown for reference and corresponds well with that of the Samothraki diorite.

The chondrite-normalised pattern of the diorite is illustrated in Fig. 2-8B. This pattern is nearly chondritic and flat in HREE with a continuous enrichment from the MREE towards the LREE. The diorite pattern is parallel to that of BCC but at somewhat lower absolute abundances of all rare earth elements.

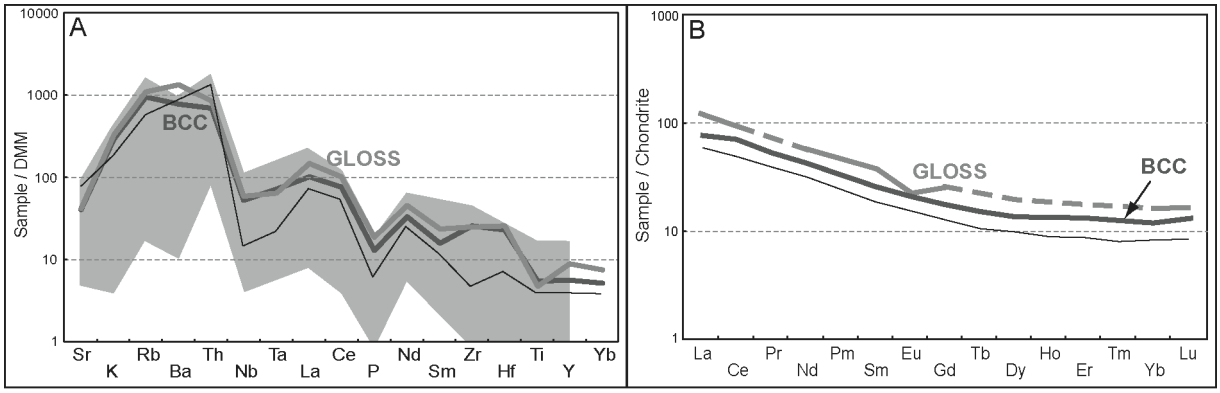

Fig. 2-8: DMM-normalised multi-element profile (A) and chondrite-normalised REE pattern (B) for the Samothraki diorite. Grey shade in 2-8A: Chortiatis Magmatic Suite (Schünemann, 1985). Data sources and abbreviations as in captions to Fig. 2-3 & 2-4.

5. Sr and Nd isotopic characteristics

In this section the Sr and Nd isotopic results for the Samothraki ophiolitic rocks are presented. Strontium (Sr) initial ratios and epsilon Nd values are back-projected at an age of 160 Ma, which is the age obtained from zircon geochronology of the gabbros (see Section 6).

5.1. Basalts and dolerites

Age-corrected epsilon Nd (εNd_{160}) values calculated for basalts and dolerites from Groups I to III vary only slightly ranging from +4.7 to +6.6 (Group I), +7.2 (Group II; single determination) and +4.1 to +5.2 (Group III); age-corrected Sr initial ratios ($^{87}Sr/^{86}Sr_{160}$) span between 0.7034 and 0.7050. Group IV differs by having lower εNd_{160} (+3.0 - +3.4) and higher $^{87}Sr/^{86}Sr_{160}$ ratio (0.7034 – 0.7058) values (see also Appendix D-2 and Fig. 2-9). Group VI shows the lowest εNd_{160} (+1.1) value and an elevated $^{87}Sr/^{86}Sr_{160}$ ratio value of 0.7049 indicating the presence of a component enriched in non-radiogenic Nd. Most of the Samothraki basalts and dolerites plot within the mantle array (Fig. 2-9) suggesting that metamorphism has not affected the isotopic systems considered, especially that of Sr which is much more susceptible to seawater alteration than Nd. Some basalts are affected by seawater alteration that is shown by shifts to higher $^{87}Sr/^{86}Sr_{160}$ values at a given εNd_{160}.

In a diagram of εNd_{160} vs. Ce/Sm (Fig. 2-10) it is evident that the component responsible for the enrichment in LREE was also responsible for the enrichment in non-radiogenic Nd (low εNd_{160}). The isotopic and elemental composition of diorite SA46 certainly meets the requirements of this component and provides an easy explanation for the observed variability in most of the Samothraki ophiolitic rocks in Fig. 2-10 through mixing in different amounts (up to 15%). This by no means excludes the additional presence of an enriched mantle reservoir in the source region of the basalts. Group VI shows a low initial εNd_{160} value together with depletion in LREE suggesting mixing with an enriched end-member different to diorite SA46 (e.g. subducted sediments from the Kamchatka Trench; Plank & Langmuir, 1998 – see also Section 6 below). These findings corroborate the inferences made earlier about the presence of a (recycled) crustal component or sediment melt in the source of all Samothraki basalts and dolerites.

5.2. Diorites

Diorite SA46 displays a low εNd_{160} value of +1.9 and an $^{87}Sr/^{86}Sr_{160}$ of 0.7044 and plots amidst Groups IV and VI (Fig. 2-9, Appendix D-2). In the εNd_{160} vs. Ce/Sm diagram (Fig. 2-10) the diorite plots at low εNd_{160} values and high Ce/Sm ratios typical of crustal material. This rock type represents one of the enriched components necessary to explain the chemistry of the Samothraki basalts and dolerites, especially those of Group IV, by providing non-radiogenic Nd and LREE.

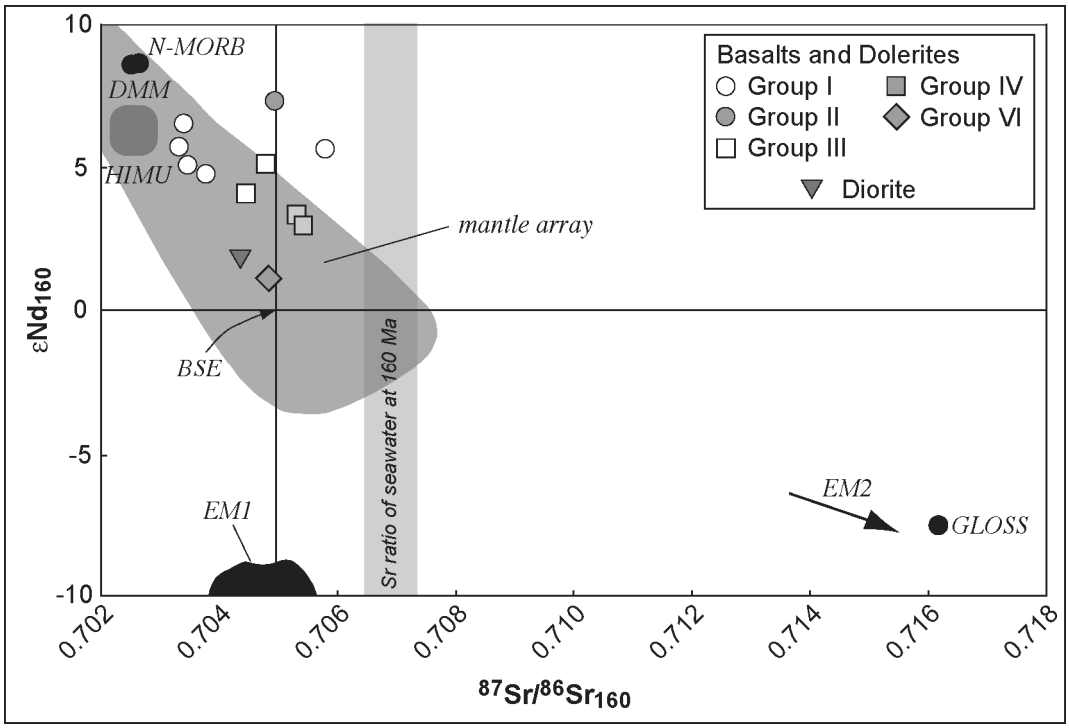

Fig. 2-9: εNd_{160} vs. $^{87}Sr/^{86}Sr_{160}$ for the different geochemical groups of the Samothraki ophiolitic basalts and dolerites. Data sources and abbreviations of terms as in captions to Fig. 2-4 and 2-6. Additional data sources: Mantle array (White, 1998); HIMU, BSE, EM1 and EM2 (Zindler & Hart, 1986); Sr Seawater (Burke et al., 1982). Additional abbreviations: HIMU: high-μ mantle reservoir; BSE: bulk silicate earth; EM: enriched mantle. All reference values are recalculated to 160 Ma.

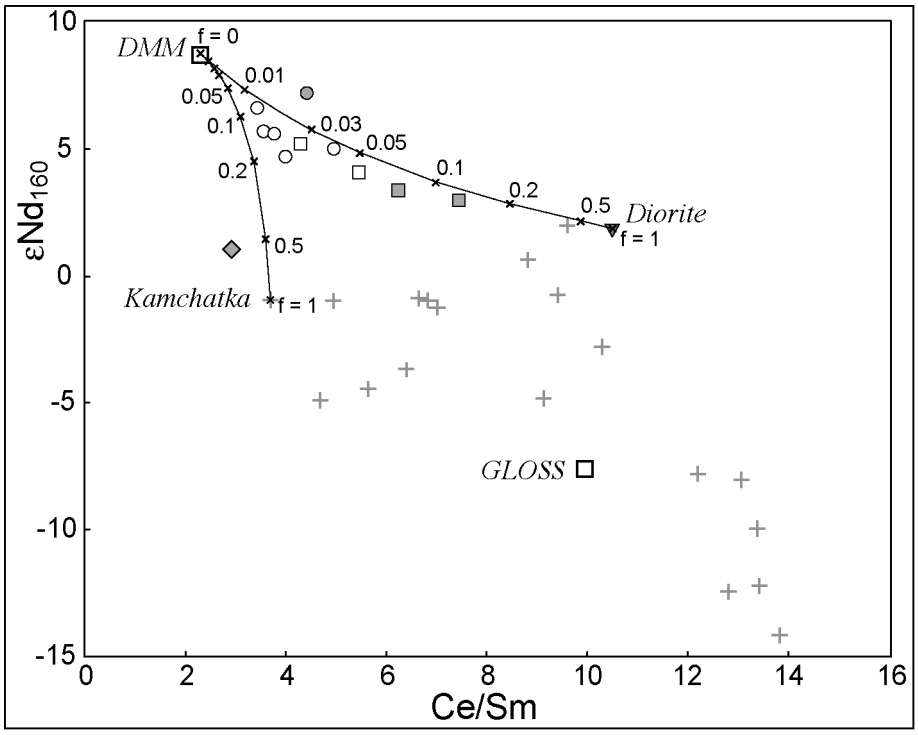

Fig. 2-10: εNd_{160} vs. Ce/Sm for the different geochemical groups of the Samothraki ophiolitic basalts and dolerites. Mixing lines between DMM and diorite SA46 and DMM and sediments from the Kamchatka Trench (Plank & Langmuir, 1998) are indicated. Numbers next to the tic marks on the lines indicate amount of melt fraction of sediment added to the mixture. See caption to figure 2-9 for symbols and data sources. Additional data sources: Grey crosses: bulk compositions of different sediment columns subducting at trenches (Plank & Langmuir, 1998). All reference values are recalculated to 160 Ma.

6. Zircon geochronology

For the purpose of the age determination of the Samothraki ophiolite, zircon crystals have been separated from a gabbro and analysed by SHRIMP II. The gabbro was collected from the plutonic complex in the northern part of the island in the vicinity of Therma village (sample SA08; see Fig. 2-2).

The zircons of gabbro SA08 have prismatic to long-prismatic habit and are mostly idiomorphic; their size varies between 150-200 μm. Cathodoluminescence imaging revealed homogeneous growth (Fig. 2-11) and the stereoscope pictures display several inclusions (Fig. 2-11A, B bottom row). The Th/U ratio of the zircons is greater than 0.5 suggesting a clear magmatic origin (Appendix E-3). On a Tera-Wasserburg diagram they are low in common Pb (Fig. 2-12). Most of the zircon ages are consistent with a $^{238}U/^{206}Pb$ weighted mean age of

159.9 ± 4.5 Ma (Upper Jurassic) (Fig. 2-12). This age is interpreted as the crystallisation age of the gabbro.

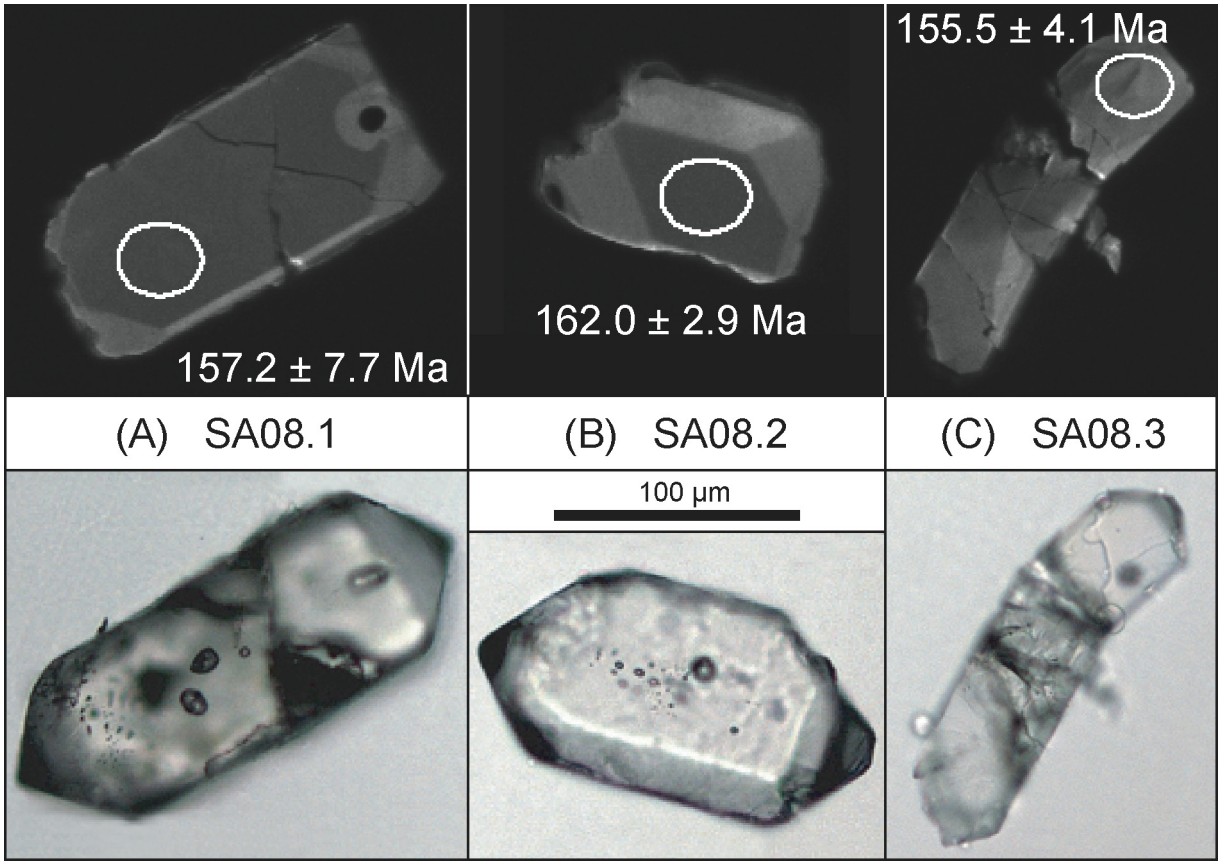

Fig. 2-11: Cathodoluminescence (CL; top row) and stereoscope (bottom row) images of zircon crystals from gabbro SA08. The euhedral shape is well visible. Furthermore, several inclusions (A, B, bottom row) are observable. White ovals indicate the points analysed by SHRIMP. $^{238}U/^{206}Pb$ ages are given with 1σ errors.

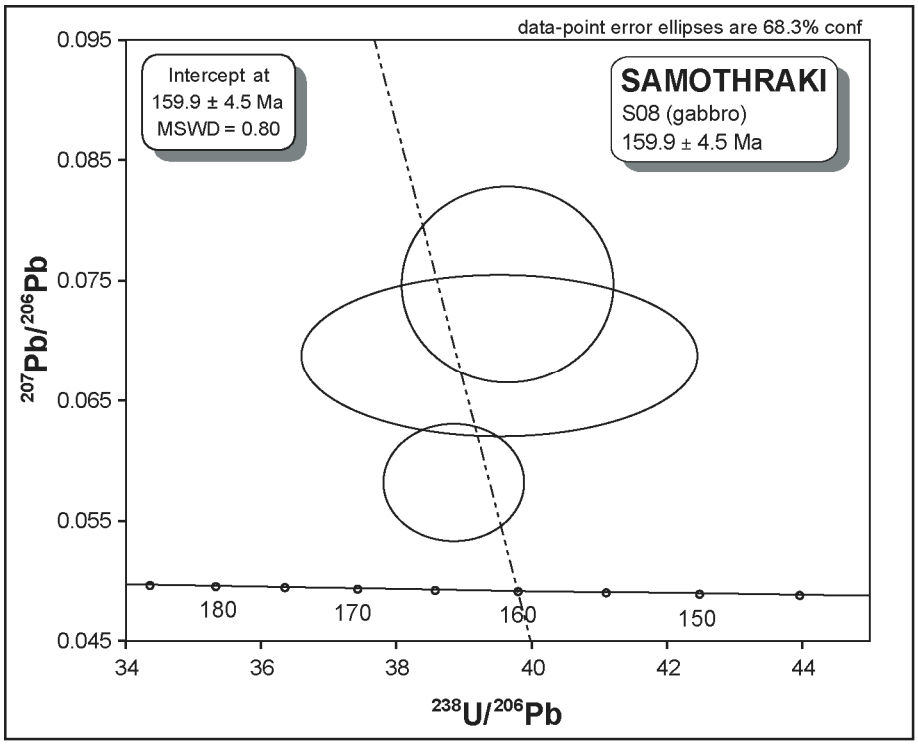

Fig. 2-12: Tera-Wasserburg diagram for measured zircons from gabbro sample SA08. The measured spots yield an intercept on the concordia at 159.9 ± 4.5 Ma that is interpreted as the crystallisation age of the gabbro. Errors of the ellipses are 2σ.

7. Discussion and conclusions

The Samothraki Island ophiolite in the northeastern Aegean Sea, Greece, is regarded as ensialic back-arc basin crust formed in response to northeastward subduction of the Vardar Ocean beneath the Rhodope Massif in late Upper Jurassic (Tsikouras & Hatzipanagiotou, 1998b). The idea of ensialic back-arc basins originated from Bébien et al. (1986) to explain the petrological and structural features of the Guevgueli and Chalkidiki ophiolites (see Introduction & Fig. 2-1). These authors proposed that the above ophiolites were emplaced in a wrench zone located in continental crust; owing to Late Jurassic tectonic activity the process of ocean-basin formation was arrested at the beginning of its development and an ensialic stage of opening was thus preserved. Recently, however, Bonev & Stampfli (2007) favoured southward intra-oceanic subduction of the Meliata–Maliac Ocean under the Vardar Ocean with the inception of an Early Jurassic fore-arc/proto-arc (Evros ophiolite) in the north, followed by Middle–Late Jurassic back-arc spreading (Samothraki ophiolite) in the south. The above, in conjunction with the reported:

- total absence of pillow lavas in the Samothraki complex

- ultrahigh Th abundance (26-44 ppm) of massive basalts and dolerites otherwise interpreted as MORB, occasionally with a subduction-zone imprint
- direct comparison of the complex with the so-called 'Lesvos ophiolite' further south (Tsikouras & Hatzipanagiotou, 1998a, b)

have prompted us to revisit the island and undertake a detailed study of this controversial ophiolitic body.

Our field observations comply with those of previous workers in that the ophiolite is basically in situ (no evidence of thrusting, absence of metamorphic sole, absence of underlying mélange, absence of layered cumulates and mantle sequence). However, our new high-quality trace-element and isotope geochemical analyses of lavas and dolerites have allowed us to distinguish several components involved in the genesis of the ophiolite that in turn help to elucidate its precise geotectonic position.

On the basis of trace-element and isotopic characteristics six distinct geochemical groups have been recognised among the basalts and dolerites of the Samothraki ophiolite:

Group I comprises basalts similar to E-MORB and mixtures of E-MORB with N2-MORB compositions. They are consistent with derivation from deep melting of spinel-lherzolite by small (to moderate) degrees of partial melting. Their Sm/La, Th/La, Hf-Th-Ta, $(Ce/Sm)_N$, $(Sm/Nd)_N$ and $\varepsilon Nd_{(i)}$ systematics suggest mixing of mainly long-term depleted with long-term enriched mantle reservoirs (Fig. 2-13). Some samples show additional enrichment in K, Rb and Ba which, coupled with variable but low Ce/Pb and Nb/U ratios (see also Appendix B-3) at comparable $\varepsilon Nd_{(i)}$ suggest influence from subduction-zone hydrous fluids that also carried Pb and U (Kessel et al., 2005; Spandler et al., 2007).

Group II comprises basalts similar to mixtures of E-MORB with N2-MORB compositions. They are the most enriched of all the Samothraki rocks examined in radiogenic Nd, which, coupled with their $(Ce/Sm)_N \geq 1$ and $(Sm/Nd)_N \leq 1$, requires slight recent enrichment of a long-term depleted source (Fig. 2-13). They are consistent with derivation from deep melting of spinel-lherzolite by small (to moderate) degrees of partial melting. The source was contaminated by hydrous fluids carrying subduction-mobile elements such as K, Rb, Ba and Pb attested to by selective enrichment in K, Rb and Ba and low Ce/Pb ratios.

Group III comprises basalts and dolerites similar to E-MORB but with somewhat lower absolute abundances of all trace elements. Their steeper multi-element patterns (crossing at Ce) and lower P, Y and HREE contents compared to Group I and II rocks suggest

deeper melting in the garnet-lherzolite stability field. The rocks are characterised by $(Ce/Sm)_N$ >1, $(Sm/Nd)_N$ ≤1 and moderate to low $\varepsilon Nd_{(i)}$ values suggesting derivation from long-term enriched mantle (Fig. 2-13). Low Ce/Pb and Nb/U ratios further imply that source enrichment was due to recycled crust or subducted sediments.

Group IV comprises basalts and dolerites bearing great similarities to global subducting sediment or upper continental crust. Their variable but high Th/La at nearly constant but low Sm/La and their variable but high Th/Yb at nearly constant but high Ta/Yb suggest mixing between an enriched source derived by contamination of DMM with a small percentage of an E-MORB/OIB component and variable amounts of melts from subducted sediments or upper continental crust. The nature of the latter contaminant is difficult to assess but it is inferred to have been crust on the basis of sample disposition in the Th-Ta-Hf space. Their larger than unity $(Ce/Sm)_N$ ratio in conjunction with low $\varepsilon Nd_{(i)}$ values suggest a long-term enriched source (Fig. 2-13), whereas their very low Ce/Pb and Nb/U ratios further suggest the additional influence of subduction-zone hydrous fluids (see also Appendix B-3). One of the samples is characterised by (Ce/Nd)>2 and (Sm/Yb) <1 and is best explained by invoking melting of a highly depleted (i.e. harzburgitic) source contaminated by very small amounts of an enriched OIB-like component.

Group V is represented by a single finding of a dyke compositionally transitional between IAT and boninites, similar to Group II of the Upper Pillow Lavas of the Troodos ophiolite, Cyprus. Its chemistry is in accord with derivation from a highly depleted mantle source (spinel harzburgite) metasomatised by an enriched OIB-like melt component and with additional influence of subduction-zone hydrous fluids.

Finally, ***Group VI*** is represented by a single finding of a dolerite dyke. It shows lower than N-MORB Ta/Yb and Sm/La values pointing to a depleted mantle source. However, specific geochemical features such as $(Ce/Sm)_N$<1 in conjunction with nearly chondritic $\varepsilon Nd_{(i)}$ and a hump in Sr, K, Rb and Ba coupled with a low Ce/Pb ratio suggest recent LREE depletion of a long-term enriched source to which a subduction-related hydrous fluid carrying alkali metals, alkaline earths and lead has been added (Fig. 2-13).

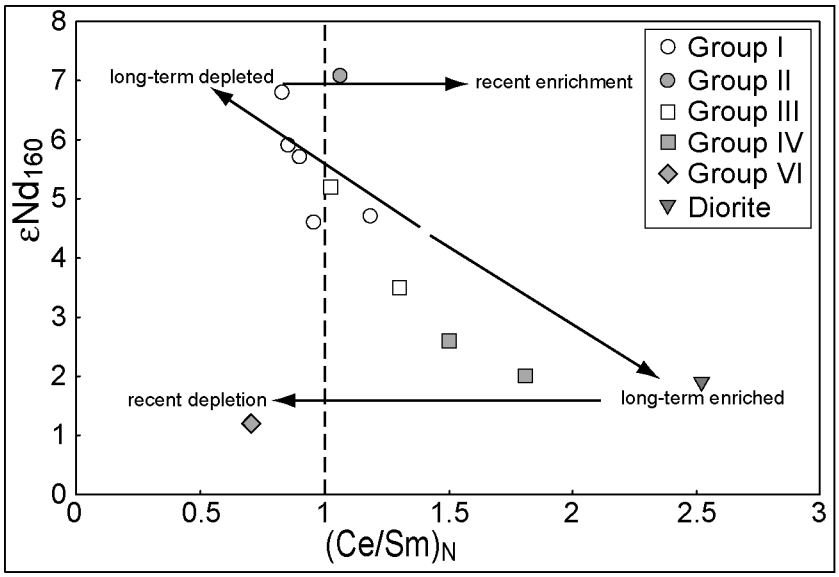

Fig. 2-13: εNd_{160} vs. chondrite-normalised Ce/Sm ratio for the Samothraki extrusives and diorite.

In back-arc basins, the slab-edge ridge segments are generally fed by more fertile mantle (E-MORB) than the segments in the centre of the basins (N-MORB). At the edges, segments furthest from the trench have small subduction components while those nearer to the trench have larger subduction components and slightly more depleted mantle (see, for example, Leat et al., 2004 for the South Sandwich arc-basin system; also Sinton et al., 2003; McConachy et al., 2005; Pearce & Stern, 2006). Moreover, edges of subducting slabs are subject to anomalous thermal gradients due to inflowing mantle that is hotter than the wedge mantle thus causing sediment melting and promoting melting of hydrated depleted mantle.

In view of the above, the Samothraki ophiolite could represent a slab-edge segment of an evolved back-arc basin near the trench, a situation that satisfies the inflow of fertile mantle, the strong signature of sediment melts and the rare occurrence of boninites. Alternatively, it could represent the embryonic stages of back-arc basin formation either by a propagating rift tip into continental crust or by oblique subduction causing back-arc rifting of continental crust and creation of nascent transtensional basins.

Brun & Sokoutis (2004, 2007) developed a model to explain the exhumation of the Southern Rhodope Core Complex by 30° clockwise rotation of the Serbo-Macedonian Massif (including the Chalkidiki peninsula) from mid-Eocene to mid-Miocene times (Fig. 2-14). Back-rotation of the Chalkidiki block would result in perfect alignment of the ophiolites of the eastern Vardar Zone (so-called IMHOB by Bébien et al., 1986) with Samothraki further south (see Fig. 2-14). This kind of restoration repositions the Kassandra and Sithonia ophiolites to the immediate northwest of the Samothraki ophiolite. Zachariadis (2007)

suggested that the Kassandra ophiolite represents back-arc basin crust formed by rifting of the Paikon protoarc (Fig. 2-15A; see also Anders et al., 2005), while the Sithonia ophiolite and the Chortiatis (Magmatic Suite) calc-alkaline arc represent supra-subduction zone magmatism due to intra-oceanic subduction of the Kassandra back-arc basin (Fig. 2-15B).

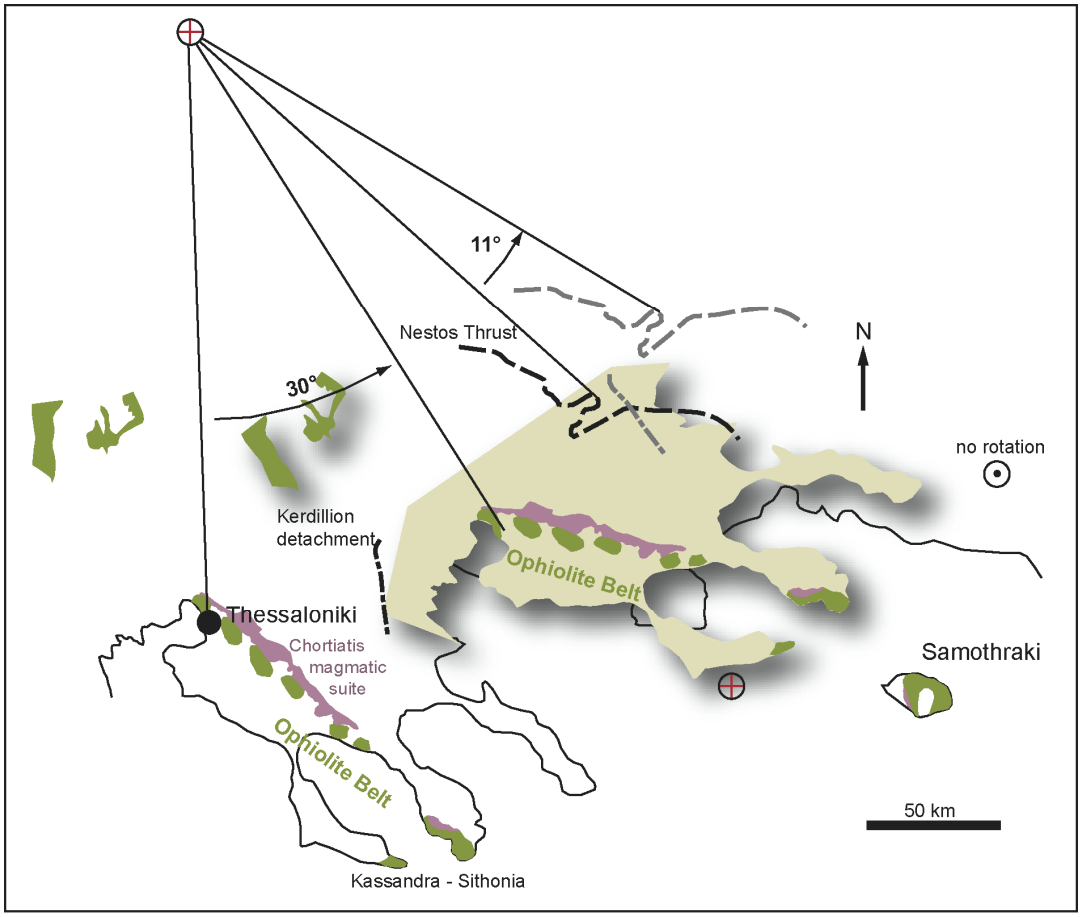

Fig. 2-14: Restoration of block configuration in NE Greece before extensional collapse of the Hellenic hinterland and exhumation of the Rhodope Metamorphic Core Complex (following Brun & Sokoutis, 2004, 2007). Anti-clockwise rotation of the Serbo-Macedonian Massif (including Chalkidiki peninsula) results in a continuous ophiolite belt from Guevgueli to Samothraki, thus assigning the latter to the Innermost Hellenic Ophiolite Belt.

We propose that the Samothraki ophiolite originated at a slab-edge position by rift propagation of the Sithonia spreading ridge into the contemporaneous Chortiatis arc (see Fig. 2-15B). In this position the enriched mantle source of Groups I – III can be explained either by fertile domains residing underneath the basement of the arc or by the inflow of fertile mantle around the edge of the slab, whereas the signature of sediment melts and fluids and the rare occurrences of much depleted material (Groups V and VI) is the result of proximity to

the trench. The strong signature of crust-magma interaction in Group IV is explained by assimilation of arc crust as the Samothraki rift propagates into the Chortiatis Arc.

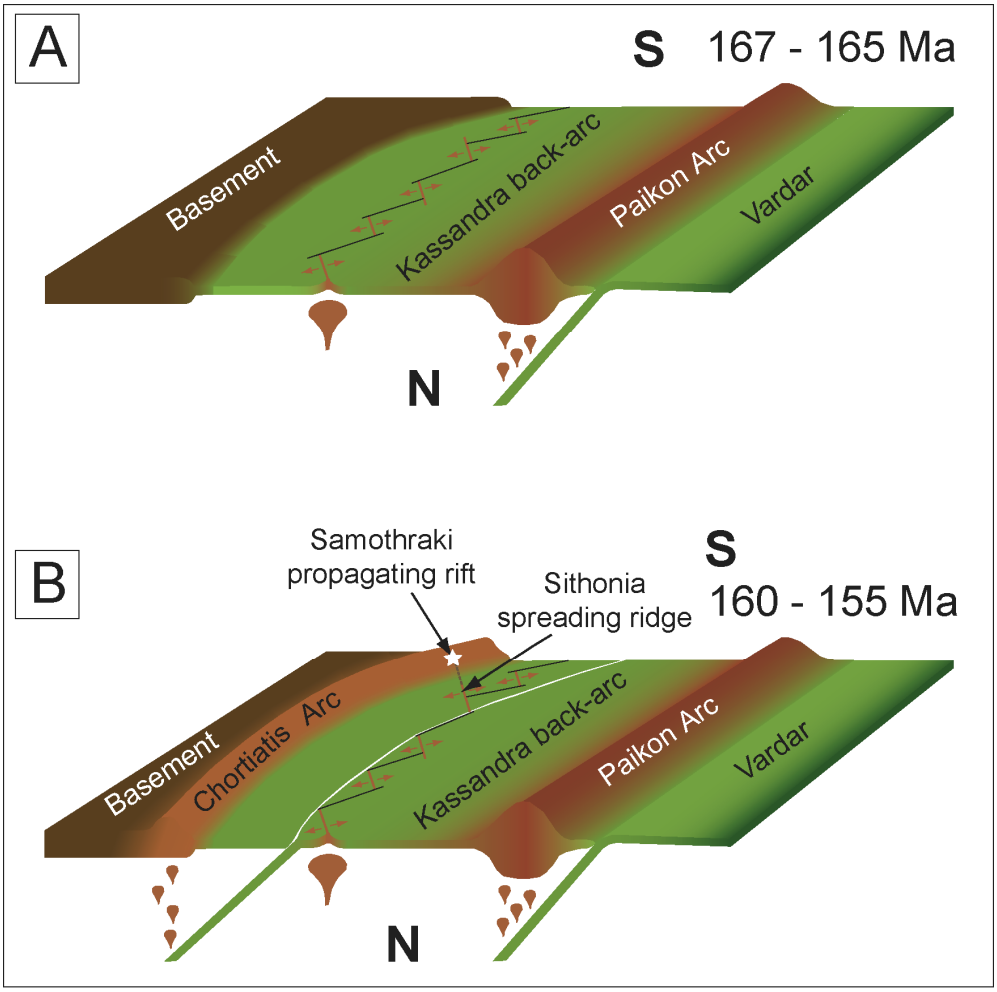

Fig. 2-15: Schematic geotectonic model for the origin of the Samothraki ophiolite (modified after Zachariadis, 2007).

It should be emphasised that the model presented herein for the emplacement of the Samothraki ophiolite by splitting and partial assimilation of the Chortiatis arc, coupled with the presence of a northeastward-directed intra-Rhodope subduction zone in the Jurassic (see Hafkenscheid et al., 2006) responsible for the observed ultrahigh-pressure (UHP) metamorphism (Mposkos & Kostopoulos, 2001) nullify the scenario recently proposed by Bonev & Stampfli (2007).

As a final note we point at the significant differences in age (160 ± 5 vs. 253 ± 6 Ma), geochemistry and tectonic setting between the Samothraki and Lesvos complexes (Koglin et al., submitted) that render a relation between them impossible.

Chapter 3

New constraints on the ophiolitic rocks of the Evros Area, NE Greece: zircon ages, trace-element and isotope geochemistry

Abstract

The ophiolite of the Evros area consists of a plutonic sequence comprising cumulate and non-cumulate gabbros with plagiogranite veins, and an extrusive sequence of basaltic dykes, massive lavas and pillow lavas as well as pyroclastic rocks. Furthermore, in the Rhodope Massif harzburgites and minor dunites can be found as tectonic lenses. All rocks are spatially separated.

The volcanic rocks can be divided into two groups: one group (Group I) containing boninites and island arc tholeiites which are mainly characterised by depleted HFSE and enrichment in LILE, especially in Th, compared to N-MORB and some enrichment in LREE relative to HFSE. The second group (Group II) is made up of calc-alkaline volcanic rocks, which are marked by depleted HFSE and strong enrichments in LILE and LREE relative to N-MORB. The geochemical features of these groups indicate melting of a depleted mantle source above a subduction zone. The island arc character of these rocks is also supported by εNd_{169} values varying from -0.7 to +7.7 what indicates addition of different subduction zone components. Both groups are geochemical similar to volcanic rocks of known oceanic island arcs (e.g. Tonga arc, Mariana arc). The gabbros define two groups as well: Group I is characterised by very low HFSE and LREE and low MREE, HREE and LILE compared to SWIR gabbro but with LILE enrichment relative to HFSE and REE. They represent the plutonic counterpart of the boninites of Group I. This is also supported by low εNd_{169} values (+1.3 - +1.5) pointing to the addition of a subduction zone component enriched in radiogenic Nd like sediment melts. The second group (Group II) contains more LILE, HFSE and REE than Group I, resembling slightly the MOR gabbro from SWIR but they show depletions in HFSE and enriched LILE relative to SWIR gabbro indication depleted mantle and addition of subduction zone fluids. The Evros ophiolitic rocks have been formed in different successive stages of island arc formation in late Middle Jurassic times (169 ± 2 Ma) above the northwards directed intra-oceanic subduction zone of the Vardar Ocean in front of the Thracia

terrane. The obduction of the Evros ophiolite onto the Rhodope basement margin took place during closure of the Vardar ocean basins.

The harzburgites and dunites of the northern Evros area are strongly depleted in Al_2O_3, TiO_2, CaO, REE and HFSE compared to PUM and DMM indicating high degrees of melt extraction (>15%) and, therefore, strongly resembling harzburgites from known oceanic island arcs (e.g. Bismarck (Tabar-Lihir-Tanga-Feni) Arc). This is supported by the low Mg# and high Cr# of Cr-spinels. Enrichments in LILE and the selective enrichment of LREE point to addition of percolating melts and fluids from the subducted slab. The relationship of the peridotites and the Evros ophiolite is still ambiguous, but due to the stratigraphic separation of the peridotites and the ophiolitic rocks it is more likely that they have generated separately. The harzburgites and dunites within the Rhodope Massif most probably represent remnants of the mantle wedge beneath the island arc of the Rhodope terrane and have formed above the subducted slab of the Nestos Ocean. The collision of the Thracia terrane in the south with the Rhodope terrane in the north resulted in thrusting of the Rhodope terrane onto the Thracia terrane whereas the harzburgites and dunites were pushed between the two terranes now cropping out on top of the Thracia terrane within the Rhodope Massif.

1. Introduction

Ophiolites traditionally mark suture zones between crustal blocks that were initially separated by an oceanic tract and eventually collided. Greece is a classical ophiolite country. Typical localities on the Greek mainland include the sizeable Pindos, Vourinos, Othris, Guevgueli, and Evros massifs, whereas smaller outcrops are known from the islands of Crete and Samothraki, just to name a few. Most of these bodies have been studied petrologically and geochemically by several workers for a number of years (see review by Robertson, 2002, and Pe-Piper & Piper, 2002, and references therein).

The Evros mafic and ultramafic rocks are situated in Thrace (NE Greece), within the so-called Evros area (Fig. 3-1) and are described as being part of the Circum-Rhodope Belt (defined by Kauffmann et al., 1976) by several authors (Magganas et al., 1991; Magganas, 2002). The Circum-Rhodope Belt is a NW-SE trending zone along the eastern border of the Vardar Zone and the western border of the Serbo-Macedonian Massif (Fig. 3-1) consisting of alpine limestones, clastic sedimentary and volcanosedimentary sequences, as well as metamafic and granitic rocks. The metamorphic conditions are in the range of greenschist

facies. Within this belt ophiolitic rocks are found, which are mainly mafic and ultramafic cumulates and harzburgitic tectonites.

The Evros complex has been interpreted as an incomplete, dismembered ophiolite of supra-subduction zone origin in a marginal basin – intra oceanic arc setting (Biggazzi et al., 1989; Magganas et al., 1991; Magganas, 2002). Since it is known that the mantle peridotites in this region belong to the Rhodope Massif (Liati et al., 2002; Mposkos & Krohe, 2006) and isotope data as well as age determinations for those rocks are not available the decision was made to re-evaluate the mafic and ultramafic rocks of the Evros area. The geochemical data as well as their petrogenesis and tectonic setting have been newly interpreted and the correlation to ophiolites of the Circum-Rhodope Belt has been established. For this purpose trace-element and isotope geochemistry in conjunction with geochronological analysis were used.

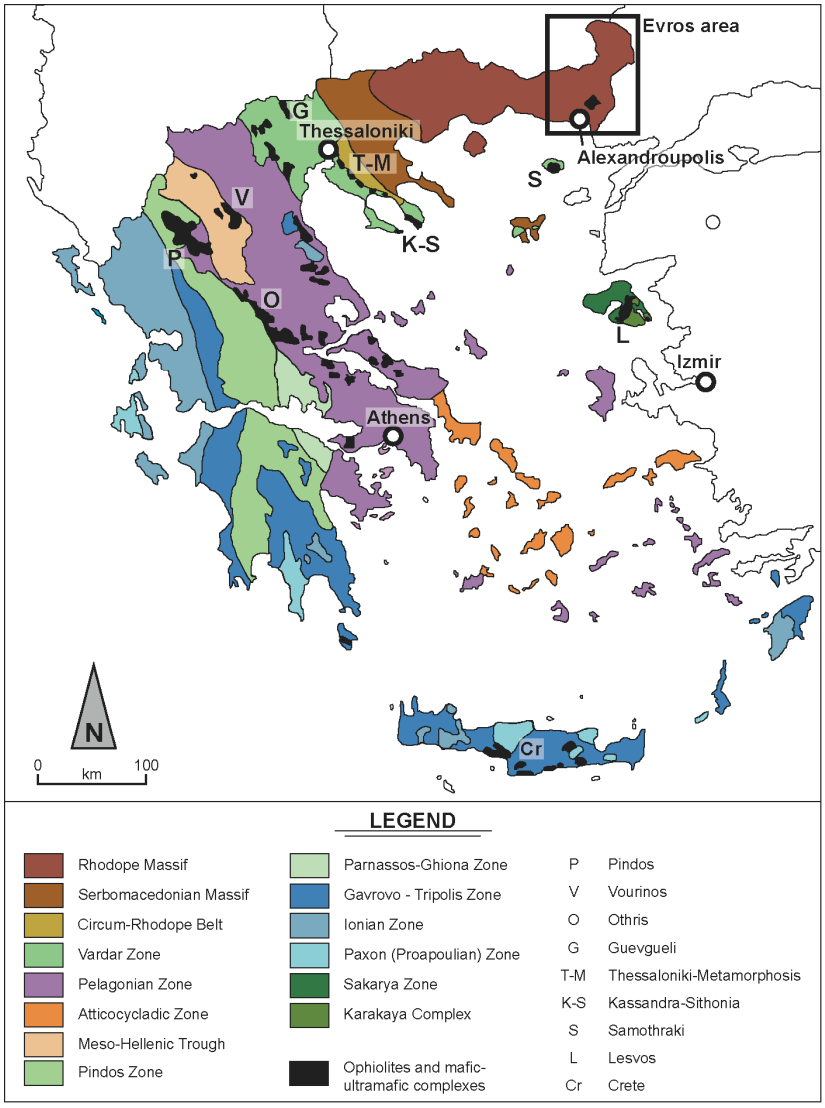

Fig. 3-1: Simplified geological map of Greece (modified after IGME, 1983 and Zachariadis, 2007).

2. Geological setting

In the Evros area different mafic and ultramafic rocks can be found, namely serpentinised mantle peridotites, a plutonic sequence consisting of cumulate and non-cumulate gabbros with plagiogranite veins, and an extrusive sequence of basaltic dykes, massive and pillow lavas as well as pyroclastic rocks. These rocks are spatially separated and can be found in the areas of Petrota, Melia, Metaxades, Didymoticho, Dadia and Smigada (Fig. 3-2).

Gabbros together with few plagiogranite veins as well as massive lavas and dykes crop out around Maronia village. The main gabbro outcrop is located to the south of the village of Petrota, followed by basaltic dykes and massive lavas to the north. Near Krovili village some pyroclastic rocks are exposed but their relationship to the Evros ophiolitic rocks is unclear. North of the villages of Drimos and Melia massive and pillow lavas associated with lava dykes dominate. Around Metaxades village only massive lavas croup out while south of Didymoticho also gabbro can be found. Northwest of the village of Dadia within a separated part of the Thracia terrane (Reischmann & Kostopoulos, 2007; lower high-grade basement unit of Bonev & Stampfli, 2007; Sidironero Complex (Albite-Gneiss Series) of Mposkos & Krohe, 2006) of the Rhodope Massif an elongated, NE-SW striking serpentinised mantle peridotite crops out. Similar rocks can be found southeast of Smigada village where serpentinised mantle peridotites are exposed within Thracia terrane (Reischmann & Kostopoulos, 2007; lower high-grade basement unit of Bonev & Stampfli, 2007; Kechros Unit of Mposkos & Krohe, 2006) of the Rhodope Massif as one large elongated, NE-SW striking body together with smaller outcrops of the same rock type (see Fig. 3-2). Furthermore, Mposkos et al. (1994) mentioned garnet peridotites occuring as tectonic slivers within the lower part of the Rhodope terrane NW of Smigada and SW of Agriani (Fig. 3-2), which have not been studied in this work.

The Rhodope terranes, including the ultramafic rocks of the Dadia and Smigada areas, are unconformably overlain by recrystallised limestone, marble, calc-schists, greenschist and phyllites of the so-called Makri Unit (Magganas et al., 1991; Magganas, 2002; Bonev & Stampfli, 2007) that is equivalent to the Mandrica Group of Bulgaria (Bonev & Stampfli, 2007). On top of this unit the mafic extrusive and intrusive rocks of the areas of Petrota, Melia, Metaxades and Didymoticho are found which are unconformably overlain by a slightly

metamorphosed to non-metamorphosed flysch series. This series crops out associated with turbidite-like sediments and they represent the Drymos-Melia Unit in the Greek part (Magganas et al., 1991; Magganas, 2002; Bonev & Stampfli, 2007) and the Maglenica Unit in Bulgaria (Bonev & Stampfli, 2007).

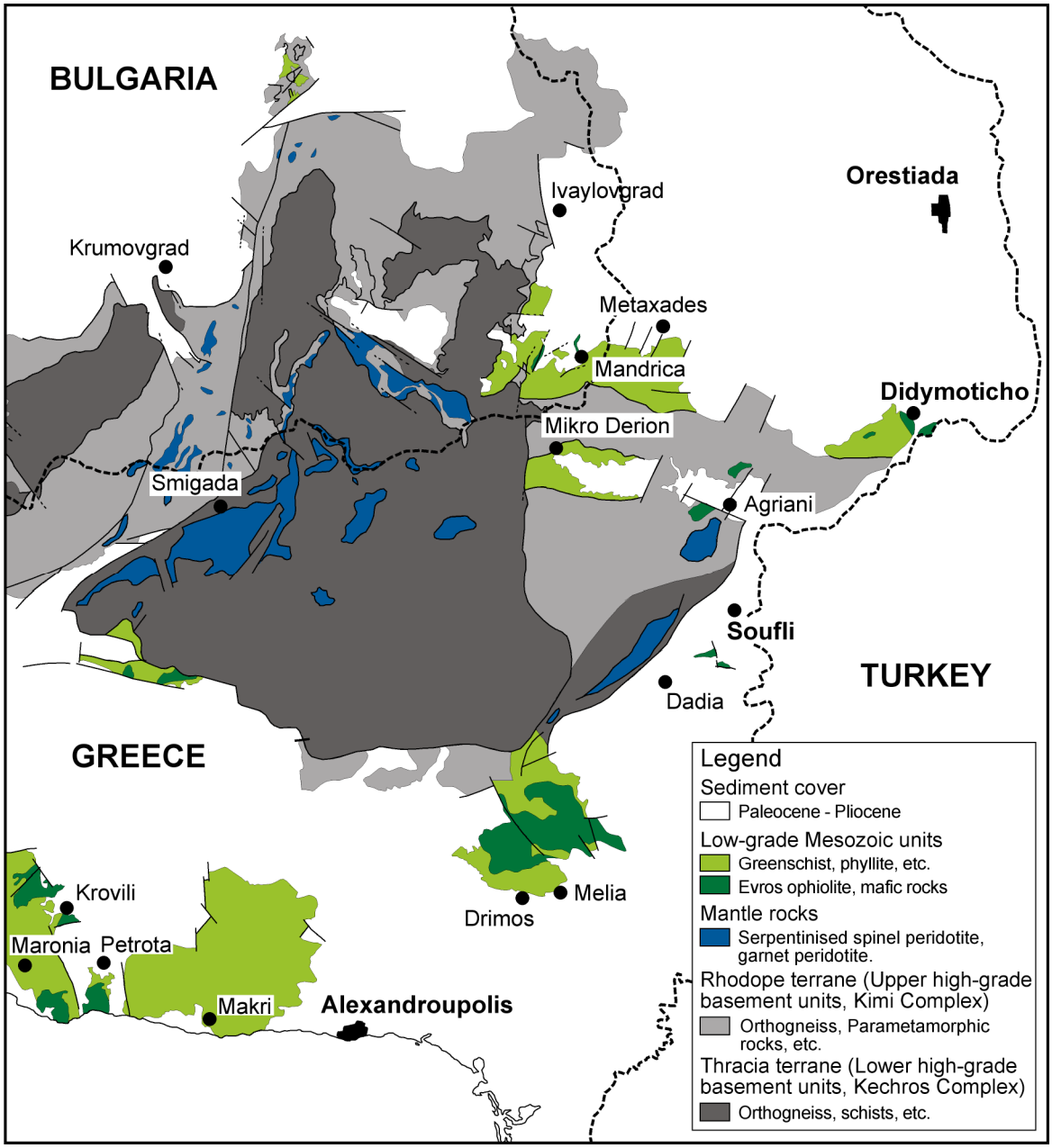

Fig. 3-2: Simplified geological map of the Evros area (after Mposkos, 1989, Papadopoulos & Anastasiadis, 2002 and Bonev & Stampfli, 2007).

3. Analytical methods

3.1. X-ray fluorescence analysis (XRF)

The samples were crushed and milled to a powder with a grain size of less than 50 µm. 6 g sample powder were mixed with Scandiplex A (resin) + B (hardener) and pressed with 7 t to pellets for trace element measurement. For major element measurement 0.8 g of sample powder were mixed with 4.8 g flux material ($LiBO_4$). This mixture was molten in platinum pots and cooled down to glass pellets in a platinum platter. The glass and powder pellets were measured in a Philips PW1404 XRF spectrometer with an Rh X-ray tube with a maximum stimulation of 100kV (3kW) at the Johannes Gutenberg-University, Mainz, Germany. AGV-1, BCR-1, BHVO-1, JP-1 and others were used as standard materials.

3.2. Laser ablation with inductively coupled plasma mass spectrometry (LA-ICPMS)

The rare-earth element measurements were carried out using LA-ICPMS at the Max Planck Institute for Chemistry in Mainz, Germany. 40 mg of sample powder were molten for 10 seconds on an Ir-strip at 1500°C and by rapid cooling homogeneous glass chips were produced for measurement. A solid-state New Wave UP213 Nd:YAG laser operating at a wavelength of 213 nm and a frequency of 10 Hz was used to produce ablation pits of 120 µm in diameter. The ablated material was carried by Helium and measured on a ThermoFinnigan Element2 sectorfield ICPMS in the low-resolution mode. Three laser spots were set on every sample with a measuring time of 20 s on the background and 110 to 130 s on the sample. NIST612, KL2G, BHVO-2 and JP-1 were used as standard materials.

3.3. Thermal ionisation mass spectrometry (TIMS)

The isotope measurements were performed at the Max Planck Institute for Chemistry in Mainz, Germany. Strontium and Nd ratios were determined on a Finnigan MAT 261 thermal ionisation mass spectrometer (TIMS) equipped with a multicollector. Strontium was loaded with TaF_5 on a single W filament, while Nd was loaded on double Re filaments. Both elements were analysed as metals. Two hundred ratios were measured on average for each sample. Mass fractionations were corrected to $^{86}Sr/^{88}Sr = 0.1194$ and $^{146}Nd/^{144}Nd = 0.7219$.

Measurements for the NBS 987 Sr and La Jolla Nd standards gave $^{87}Sr/^{86}Sr = 0.710289 \pm 11$ (n=17, 2σ) and $^{144}Nd/^{143}Nd = 0.511840 \pm 6$ (n=33, 2σ), respectively.

3.4. Sensitive high resolution ion microprobe (SHRIMP)

The U-Th-Pb SHRIMP (Sensitive High Resolution Ion Microprobe) technique allows in-situ spot dating of individual domains within single zircon grains. Combined with a thorough cathodoluminescence imaging study, it permits the dating of zircons with complex structure.

The U-Pb ion microprobe data were obtained using the SHRIMP II instrument at the Centre of Isotopic Research (VSEGEI) in St. Petersburg, Russian Federation. Five scans over the critical mass were carried out using a spot size of 20 μm. The intensity of the primary beam was set at 4 nA. Temora 1 was used as a standard zircon (Black et al., 2003). The data were reduced and visualised using the SQUID and Isoplot/Ex add-in for Excel (Ludwig 2005a, 2005b).

3.5. Scanning electron microprobe (EMS)

Mineral analyses were carried out on polished thin sections using a Jeol JXA 8900 RL electron microprobe at the University in Mainz, Germany. The mineral measurements run at an accelerating voltage of 20kV and a beam current of 12 nA with a beam diameter of 2 μm. Natural and synthetic materials were used as standards. To calculate the concentration units the PRZ correction procedure was used. Cations of chromium spinel, pyroxenes and amphiboles were calculated stoichiometrically based on 4, 6 and 23 oxygens per formula unit, respectively.

4. Whole rock major and trace element geochemistry

4.1. Volcanic rocks

Whole-rock geochemical analyses for the Evros volcanic rocks are given in Appendix B-4. In order to assess the effect of alteration on whole-rock geochemistry each element analysed was plotted against Zr, the latter having long been established as an immobile element during hydrothermal alteration (Kostopoulos 1988 and references therein). These

plots are available in Appendix F-3. It is evident from these plots that most of the major elements are more or less disturbed by alteration as are some of the trace elements. Certain trace elements however (e.g. Nb, Ta, Hf, Th, Y, REE) are immobile and only they are used for rigorous petrogenetic modelling. The covariation diagrams furthermore demonstrate that the extrusive rocks of the Maronia and Makri area are characterised by similar major and trace element contents and, therefore, they will be discussed as one group. However, the volcanic rocks form two groups on the basis of their light to middle rare earth elements (e.g. La and Nd, Appendix F-3): one group (Group I) with low contents of La and Nd (1.1 – 3.9 ppm and 3.5 – 9.1 ppm, respectively) and a second group (Group II) with higher contents of these elements (6.2 – 13.9 ppm and 15.4 – 31.6 ppm, respectively). Furthermore, some volcanic rocks of both groups show high MgO and SiO_2 contents associated with low amounts of TiO_2 and Zr indicating that they are boninites. Plotting the Evros volcanic rocks in the SiO_2 – TiO_2*100 – MgO*10 diagram after Reischmann (1986) four samples can be identified as boninites (E48, E50, E51 and E78) while most of the samples plot in the field of island arc calc-alkaline and tholeiitic volcanic rocks (Fig. 3-3). Few samples (E20, E29) are transitional between boninitic and calk-alkaline – tholeiitic.

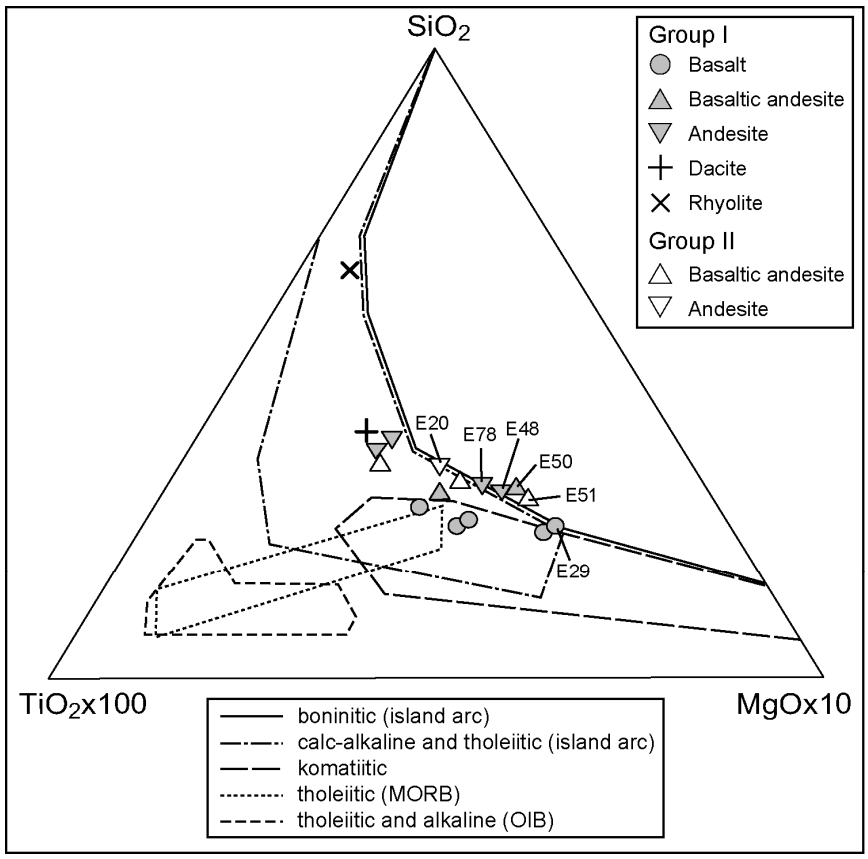

Fig. 3-3: STM-diagram to classify boninitic volcanic rocks after Reischmann (1986). Abbreviations: MORB: mid-ocean ridge basalt; OIB: ocean island basalt.

Chondrite-normalised REE patterns for the volcanic rocks of the Evros area are shown in Fig. 3-4. The patterns of Group I of the extrusive rocks of Evros are almost flat (La_N/Yb_N = 1.0 – 2.0). A slight enrichment in LREE (La_N/Gd_N = 1.0 – 2.0) and in parts some slight enrichment in HREE (Yb_N/Gd_N = 0.8 – 1.4) relative to the MREE results in a U-shaped pattern for some volcanic rocks. This is typical for boninites, which were already identified in Fig. 3-3. In some cases negative or positive Eu anomalies are developed pointing to plagioclase fractionation and accumulation, respectively (Fig. 3-4A). Sample E17 shows a flat pattern in MREE and HREE (Sm_N/Yb_N = 1.0) but it is strongly depleted in LREE (La_N/Sm_N = 0.4) (Fig. 3-4B). The enrichment in LREE can be attributed to the addition of a subduction zone component.

The Group II volcanic rocks are flat in HREE (Yb_N/Ho_N = ~1.0) but they show progressive enrichment from Er towards La (La_N/Er_N = 2.5 – 4.0). The pattern of sample E65 is parallel to those of the other Group II rocks but more elevated in all REE compared to them suggesting fractionation from the same source (Fig. 3-4C). Compared to those of Group I the volcanic rocks of Group II are more enriched in all REE and show a progressive enrichment from HREE towards LREE.

Compared to the ophiolites of the eastern Vardar Zone (Zachariadis, 2007) and the mafic lavas of the Mandrica Unit of Bulgaria (Bonev & Stampfli, 2007) (Fig. 3-4D) the REE pattern of both, Group I and Group II volcanic rocks of the Evros area resemble mostly the pattern of the Thessaloniki ophiolite, which is interpreted as supra-subduction zone ophiolite (Zachariadis, 2007). The Thessaloniki ophiolite contains flat REE pattern similar to the Group I volcanics as well as pattern with strong enrichment in LREE and MREE what can be compared with the Group II volcanic rocks of Evros.

Compared to REE pattern of known oceanic and continental island arc volcanic rocks (Appendix F-5) it is evident that only the oceanic island arc volcanic rocks comprise both, flat and LREE-MREE enriched pattern, whereas the continental island arc volcanic rocks show strong enrichments in LREE and MREE. Therefore, the REE pattern of both, the island arc tholeiitic rocks of Group I and calc-alkaline rocks of Group II resemble most those of oceanic island arcs, e.g. South Sandwich Arc or Mariana Arc (for references see Appendix F-5).

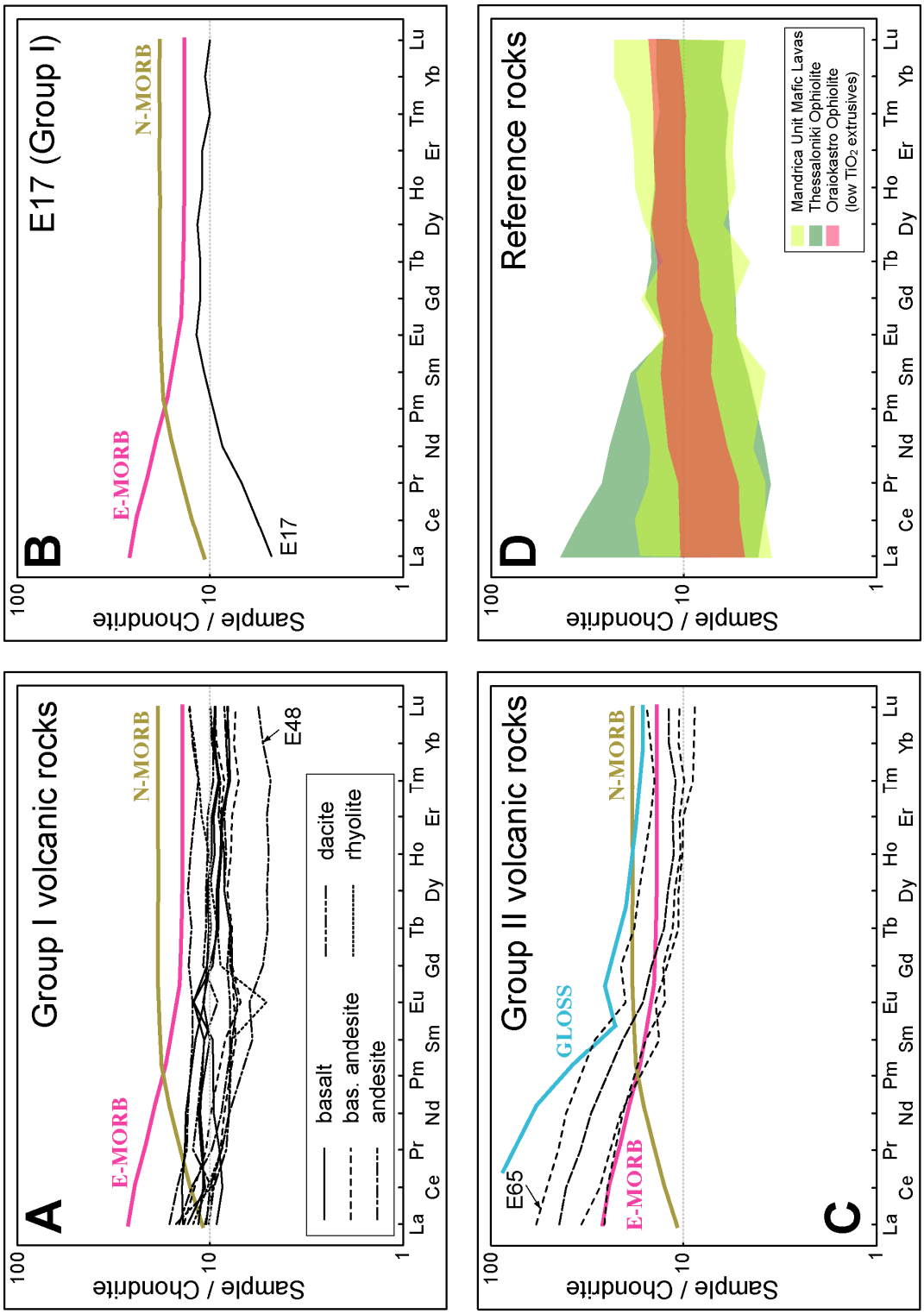

Fig. 3-4: Chondrite-normalised REE profiles for the volcanic rocks of the Evros area (A-C) and reference rocks (D). Data sources: Chondrite (normalising values; Sun & McDonough, 1989); E-MORB and N-MORB (Sun & McDonough, 1989); GLOSS (Plank & Langmuir, 1998); Mandrica Unit Mafic Lavas (Bonev & Stampfli, 2007); Thessaloniki and Oraeokastro ophiolites (Zachariadis, 2007). Abbreviations: N-MORB: normal mid-ocean ridge basalt; E-MORB: enriched mid-ocean ridge basalt; GLOSS: global oceanic subducted sediment.

Normal mid-ocean ridge basalt (N-MORB) normalised multi-element patterns for the Evros extrusive rocks are depicted in Fig. 3-5. Group I is characterised by a distinct negative Nb-Ta and P anomaly (Th_N/Nb_N = 16.7 – 25.1; Ce_N/P_N = 1.1 – 3.8) as well as a variable enrichment in LILE (e.g. Rb_N = 1.5 – 32.8; see also Fig. 3-5A). Such patterns are typical for volcanic rocks generated by melting of a depleted mantle source in a young intra-oceanic island arc setting (Hamilton, 1995). The enrichment in LILE is a result of the mobility of these elements during dehydration and therefore they have been added by fluids derived in a subduction zone setting. Moreover, the basalts are more depleted in Nb and Ta than the more evolved rock types suggesting fractionation. This group resembles strongly the island arc tholeiites (IAT) of Pearce (1982) but with a more distinct Nb-Ta and P anomaly. Sample E17 (Fig. 3-5B) displays the largest Nb-Ta anomaly and is more depleted in La and Ce than the other volcanic rocks in Group I, possibly representing the most primitive volcanic rocks of the Evros series.

Most of the volcanic rocks of Group II are depleted in HFSE (e.g. Nb_N = 0.3 – 0.8) compared to N-MORB but they are more enriched in LREE compared to N-MORB (see also Fig. 3-4C) and IAT thus resembling island arc calc-alkaline basalts (CAB) of Pearce (1982) (Fig. 3-5C). The Nb-Ta anomaly is well pronounced (Th_N/Nb_N = 14.3 – 30.2) and more strongly developed than in CAB and resembles rather IAT. The pattern of sample E65 is more enriched in HFSE (e.g. Nb_N = 2.0) and LILE (e.g. Rb_N = 287) than the other Group II samples but also with a well-developed Nb-Ta anomaly (Th_N/Nb_N = 42.2). This pattern is lying between CAB and GLOSS suggesting strong influence of melts from subducted sediments carrying LILE and LREE. The patterns of this group are more or less parallel to those of Group I but with more elevated LILE and HFSE suggesting a supplementary addition of sediment melt.

Compared to different ophiolites in the eastern Vardar Zone (e.g. Thessaloniki, Oraeokastro; Zachariadis, 2007) as well as mafic lavas in the Mandrica Unit in Bulgaria (Bonev & Stampfli, 2007) (Fig. 3-5D) it is evident that the Group I volcanic rocks of the Evros area are geochemical similar to the low-TiO_2 mafic rocks of the Oraeokastro SSZ ophiolite. They show similar variable enrichments in LILE and comparable depletions in HFSE. The volcanic rocks of Group II can be compared to the volcanic rocks of the supra-subduction zone ophiolite of Thessaloniki (Fig. 3-5D) because they are similar in their Th, HFSE and LREE contents. The Evros volcanic rocks also display similarities to the mafic lavas from the Mandrica Unit of Bulgaria, which is described by Bonev & Stampfli (2003) as

being equivalent to the Makri Unit of the Evros area. The similarities are shown in the variable amount of LILE and a distinct Nb-Ta anomaly. However, the Nb-Ta content of the Evros lavas is much lower than that of the Mandrica Unit.

Furthermore, in Appendix F-6 N-MORB-normalised pattern of different volcanic rocks of oceanic and continental island arcs are plotted. It is clearly visible that all oceanic island arc volcanic rocks (Appendix F-6, A-E) show patterns to which both groups of the Evros volcanic rocks are similar: depleted patterns like those of island arc tholeiitic volcanic rocks of Group I as well as LILE and LREE enriched patterns to which those of calc-alkaline volcanic rocks of Group II can be compared. Moreover, it is evident that N-MORB-normalised patterns of continental island arc volcanic rocks are more enriched in LREE and only the patterns of the Group II volcanic rocks of the Evros area slightly resemble these patterns (see Appendix F-6, F-G).

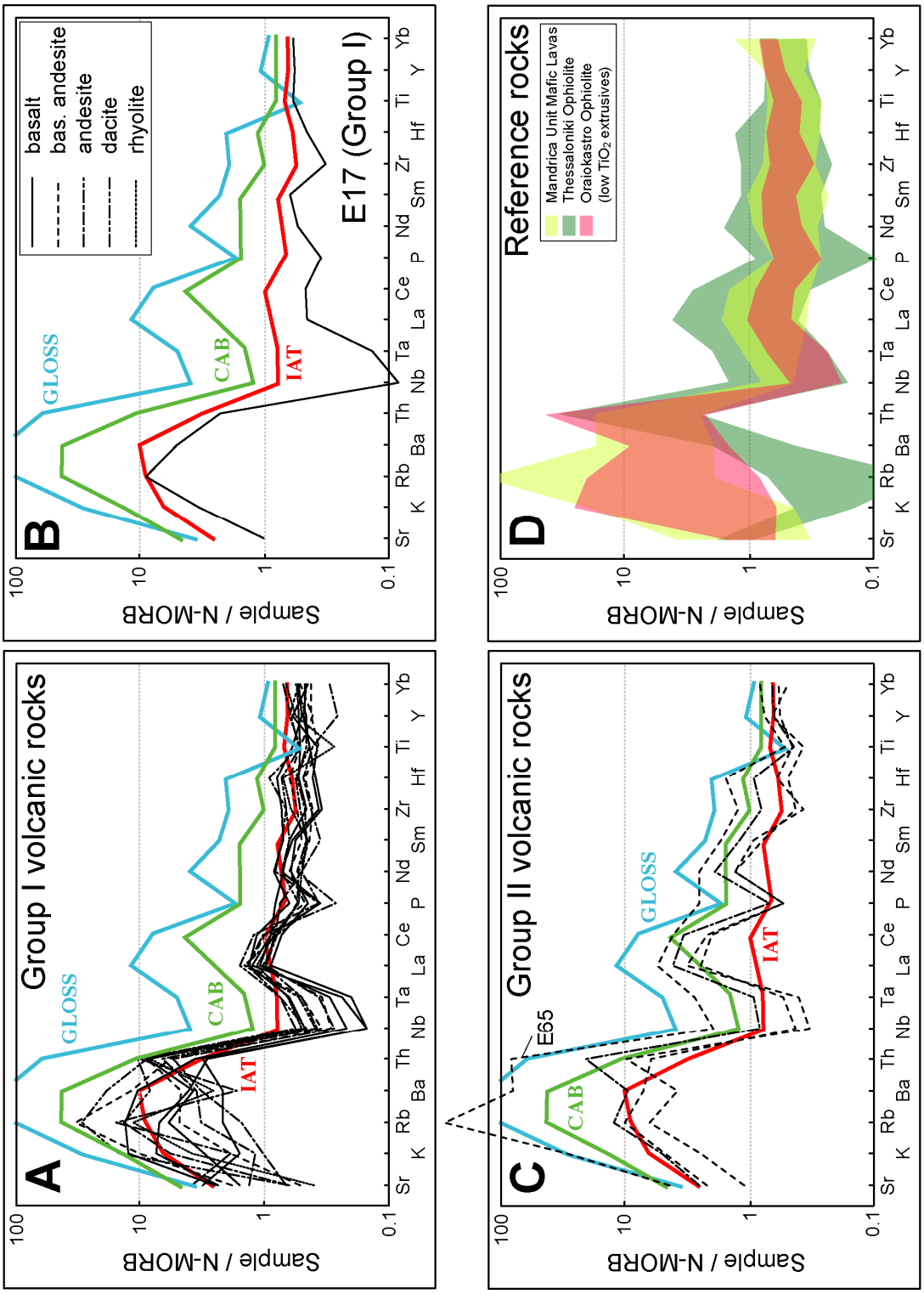

Fig. 3-5: N-MORB-normalised multi-element profiles for the Evros volcanic rocks (A-C) and reference rocks (D). For data sources and abbreviations of terms see captions of Fig. 3-4. Additional data sources: IAT and CAB (Pearce, 1982). Additional abbreviations: IAT: island arc tholeiite; CAB: calc-alkaline basalt.

Hawkesworth et al. (1991, 1993) proposed that island arc magmas could be subdivided into two groups by virtue of their Ce/Yb ratio: one group with low Ce/Yb ratio (<15) where Ce and Yb covary, and a second group with higher Ce/Yb (>15) where the Ce content varies at similar Yb abundances. The first group represents the oceanic island arc magmas, because their low Ce/Yb ratio is less than accepted estimates for the bulk continental crust (BCC = 22.63; Rudnick & Gao, 2003). Furthermore, they show lower Rb/Sr and Th/U ratios than the bulk continental crust (Rb/Sr = 0.153; Rudnick & Gao, 2003; Th/U = 3.82; McLennan, 2001). The high Ce/Yb group represents the continental island arc magmas. They contain higher amounts of incompatible trace elements and more restricted in their HREE. This can be attributed to both, contributions from the subducted slab and old, trace element enriched mantle wedge (Hawkesworth et al., 1993).

The volcanic rocks of Group I of the Evros area show generally low Ce/Yb (1.9 – 6.8), variable Rb/Sr (0.004 – 0.296) and Th/U values (0.85 – 3.50). In the Ce vs. Yb diagram of Hawkesworth et al. (1993) (Fig. 3-6) they plot into the range of oceanic island arc magmas (e.g. Izu-Bonin Arc [e.g. Tamura et al., 2005], Lesser Antilles [after Hawkesworth et al., 1993], Tonga-Kermadec Arc [e.g. Turner et al., 1997; Hergt & Woodhead, 2007], South Sandwich Islands [after Hawkesworth et al., 1993]).

The volcanic rocks of Group II display generally higher Ce/Yb ratios than those of Group I (8.5 – 12.5) but are still below the estimated boundary between the oceanic and continental island arcs (~15). Their Rb/Sr ratios are, except for sample E65 (0.402) very low (0.029 – 0.035) but their Th/U ratios are very high (2.08 – 6.12). In Fig. 3-6 they plot transitional between the oceanic and continental island arc magmas within the lower Ce/Yb part of the continental island arc (e.g. Kamchatka [e.g. Dorendorf et al., 2000], Cascades [e.g. Reagan et al., 2003], Philippines [after Hawkesworth et al., 1993]) but also oceanic island arcs show in some cases higher Ce/Yb ratios like the rocks of the Tonga-Kermadec Arc (e.g. Turner et al., 1997; Hergt & Woodhead, 2007). The low Rb/Sr ratios might be attributed to the addition of Sr by fluids. The Rb/Sr and Th/U ratios in both groups have to be treated critically since they are mobile.

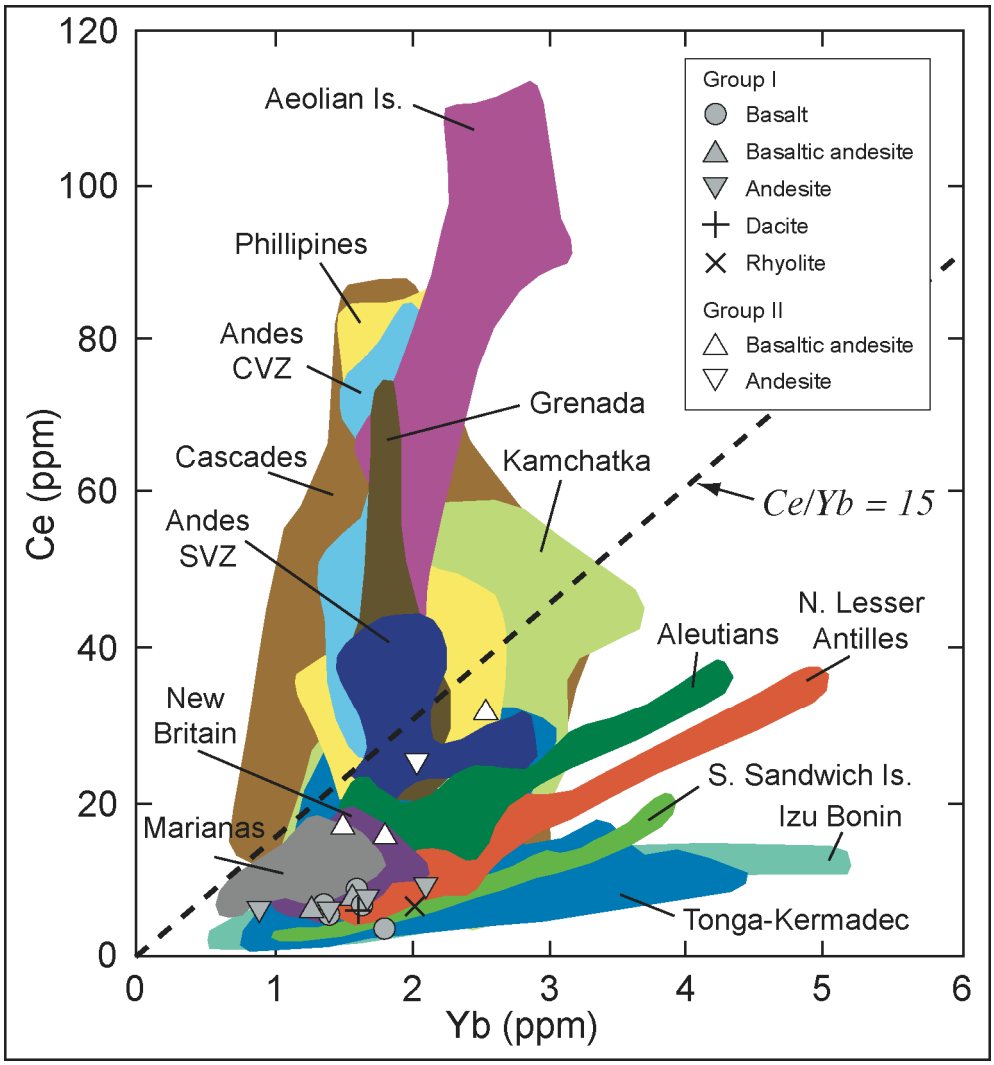

Fig. 3-6: Ce vs. Yb diagram after Hawkesworth et al. (1993) for the Evros volcanic rocks. With low Ce/Yb ratios the rocks of Group I fall into the range of oceanic island arc magmas while the Group II basalts are transitional between oceanic and continental island arc magmas. Data sources: Aeolian Islands, Philippines, Andes CVZ, Andes SVZ, Grenada, New Britain, Marianas, Aleutians, Northern Lesser Antilles, South Sandwich Islands (adapted from Hawkesworth et al., 1993); Tonga-Kermadec Arc (e.g. Turner et al., 1997; Hergt & Woodhead, 2007); Izu-Bonin Arc (e.g. Tamura et al., 2005); Kamchatka (e.g. Dorendorf et al., 2000); Cascades (e.g. Reagan et al., 2003).

The widely used tectonomagmatic discriminant diagram of Wood (1980) that employs the elements Th, Ta and Hf is shown in Fig. 3-7. Thorium is a good indicator of subduction-zone enrichment and is known for its immobility up to 600°C (Wood 1979) and its mobility in melts.

The Evros volcanics are depleted in Ta and show addition of subduction zone components such as Th, which is shown in Fig. 3-7. Due to the high Th and low Ta values the

volcanic rocks follow the trend of "subduction zone enrichment". The Group II volcanic rocks are more enriched in Th than those of Group I. Sample E65 displays the highest enrichment in Th as already seen in Fig. 3-5 while sample E17 is the most depleted rock. Furthermore, the more evolved rock types contain more Th than the basalts (Fig. 3-7). The Evros volcanic rocks resemble the volcanic rocks of the South Sandwich Islands (e.g. Pearce et al., 1995; Barry et al., 2006) and the Tonga oceanic island arc (e.g. Turner et al., 1997; Hergt & Woodhead, 2007). Therefore, they can be interpreted as oceanic island arc. The enrichment of Th can be attributed to subduction zone processes.

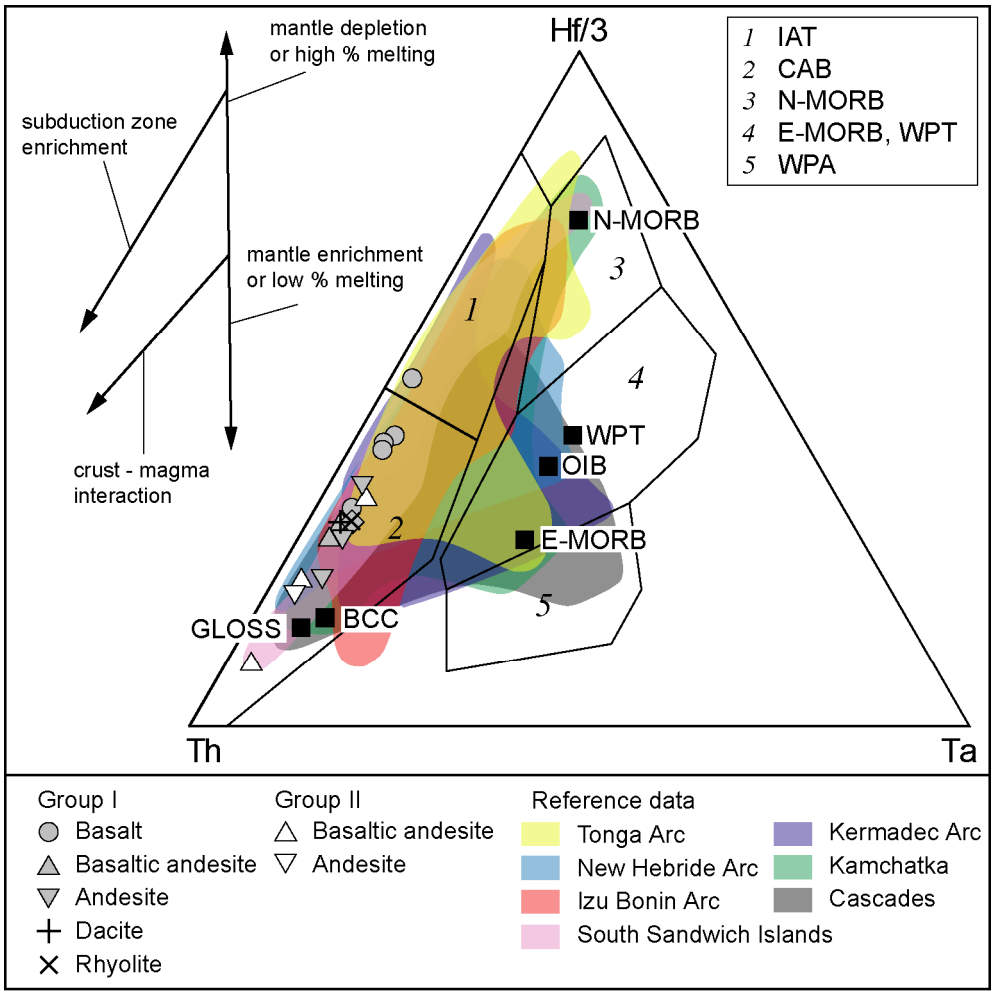

Fig. 3-7: Hf/3-Th-Ta tectonomagmatic discriminant diagram for the Evros volcanic rocks (Wood 1980, with modifications after Pearce [unpublished]). Data sources as in caption to Fig. 3-6. Additional data sources: OIB (Sun & McDonough, 1989); WPT (Pearce, 1982); BCC (Rudnick & Gao, 2003); South Sandwich Islands (e.g. Barry et al., 2006); New Hebrides Arc (e.g. Peate et al., 1997). Additional abbreviations: IAT: island arc tholeiite; CAB: calc-alkaline basalt; OIB: ocean island basalt; WPT: within-plate tholeiite; WPA: within-plate alkalic.

The enrichment or depletion of the mantle source is shown by a high or low Ta/Yb ratio, respectively, while the addition of a siliceous subduction melt is indicated only by high Th/Yb ratios as depicted in the Th/Yb against Ta/Yb diagram of Pearce (1982) in Fig. 3-8. Moreover, a contemporaneous enrichment in Th/Yb and Ta/Yb can be attributed to fractionation or different degrees of melting (Fig. 3-8). The volcanics of the Evros area plot in the range of tholeiitic to calc-alkaline basalts parallel to the MORB array but with elevated Th/Yb ratios. The displacement towards high Th/Yb ratios compared to the MORB array indicates an enrichment of a MORB mantle or more depleted mantle source by subduction zone components like sediment melts or fluids. Fractionation or lower degrees of melting can explain the trend towards higher Th/Yb and Ta/Yb. As shown in Fig. 3-7, the Group II volcanic rocks display higher Th/Yb ratios compared to the Group I rocks while samples E65 and E17 are the most enriched and most depleted samples, respectively, of the Evros volcanic rocks. The higher enrichment in Th is a result of addition of sediment melts. Similar to Fig. 3-6 the Group I basalts are the most depleted rocks of the Evros volcanics while the other rock types in Group I show similar enrichment in Th (Fig. 3-8).

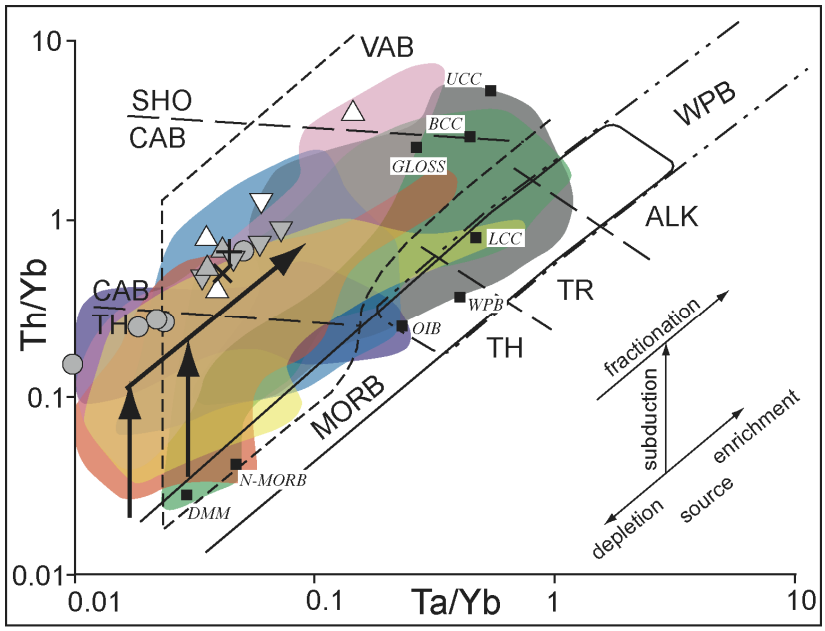

Fig. 3-8: The diagram Th/Yb against Ta/Yb after Pearce (1982) indicates a modification of a depleted mantle source for the Evros volcanic rocks. Group II volcanic rocks are more enriched in Th than Group I, which is caused by larger addition of a Th-rich component (subduction zone fluids or melts). Sample signatures, reference data signatures, data sources and abbreviations of terms as in captions to Fig. 3-6 and 3-7. Additional data sources: DMM (Workman & Hart, 2005). Additional abbreviations: DMM: depleted MORB mantle; SHO: shoshonitic; TH: tholeiitic; TR: transitional; ALK: alkaline.

Sediment input can be estimated by the Th/La vs. Sm/La diagram introduced by Plank (2005), which identifies sediment recycling at subduction zones and quantifies mantle-sediment mixing calculations. In general, mantle-derived melts do not have high Th/La, except when sediment subduction/crustal contamination is independently implicated (Plank 2005). Otherwise, the Sm/La ratio is a measure of the extent of LREE depletion or enrichment. When considered together with the Th/La ratio the proportion of sedimentary/crustal components and the extent of depletion of the mantle source can be evaluated using the geochemical signature of basalt.

The Th/La vs. Sm/La systematics for the Evros extrusive rocks is shown in Fig. 3-9. The basalts of Group I are low in Th/La (0.49 – 0.67) and in Sm/La (0.12 – 0.16) similar to those of the South Sandwich Islands (e.g. Barry et al., 2006) and partly to the Tonga Arc (e.g. Hergt & Woodhead, 2007; see Fig. 3-9). Sample E17 shows high Sm/La value (1.45) at moderate Th/La value (0.24) indicating addition of a Th-rich component to very depleted mantle source. The more evolved rocks of Group I plot into Sm/La range of 0.35 – 0.50 and display Th/La values of 0.27 – 0.35. The enrichment in Th resulting in a high Th/La ratio can be ascribed to mixing with less than 1% of crustal material or melts from subducted sediments to a depleted mantle source (DMM; see also Mixing line DMM – Atlantic Ocean Sediment (orange field) in Fig. 3-9).

The Group II volcanic rocks show similar Th/La ratios (0.12 – 0.27) than the Group I extrusive rocks (Fig. 3-9) but at slightly lower Sm/La values (0.26 – 0.45). This might be either the result of mixing of a depleted mantle source with different amounts (up to 10%) of an enriched component (e.g. E-MORB, GLOSS) or the result of adding an enriched component (e.g. Atlantic Ocean Sediment) to an already enriched mantle source (e.g. OIB, E-MORB). Sample E65 displays a very high Th/La ratio (0.72) and low Sm/La value (0.32). The very high Th contents can be ascribed to the addition of a sedimentary of crustal component extremely rich in Th to a depleted mantle source.

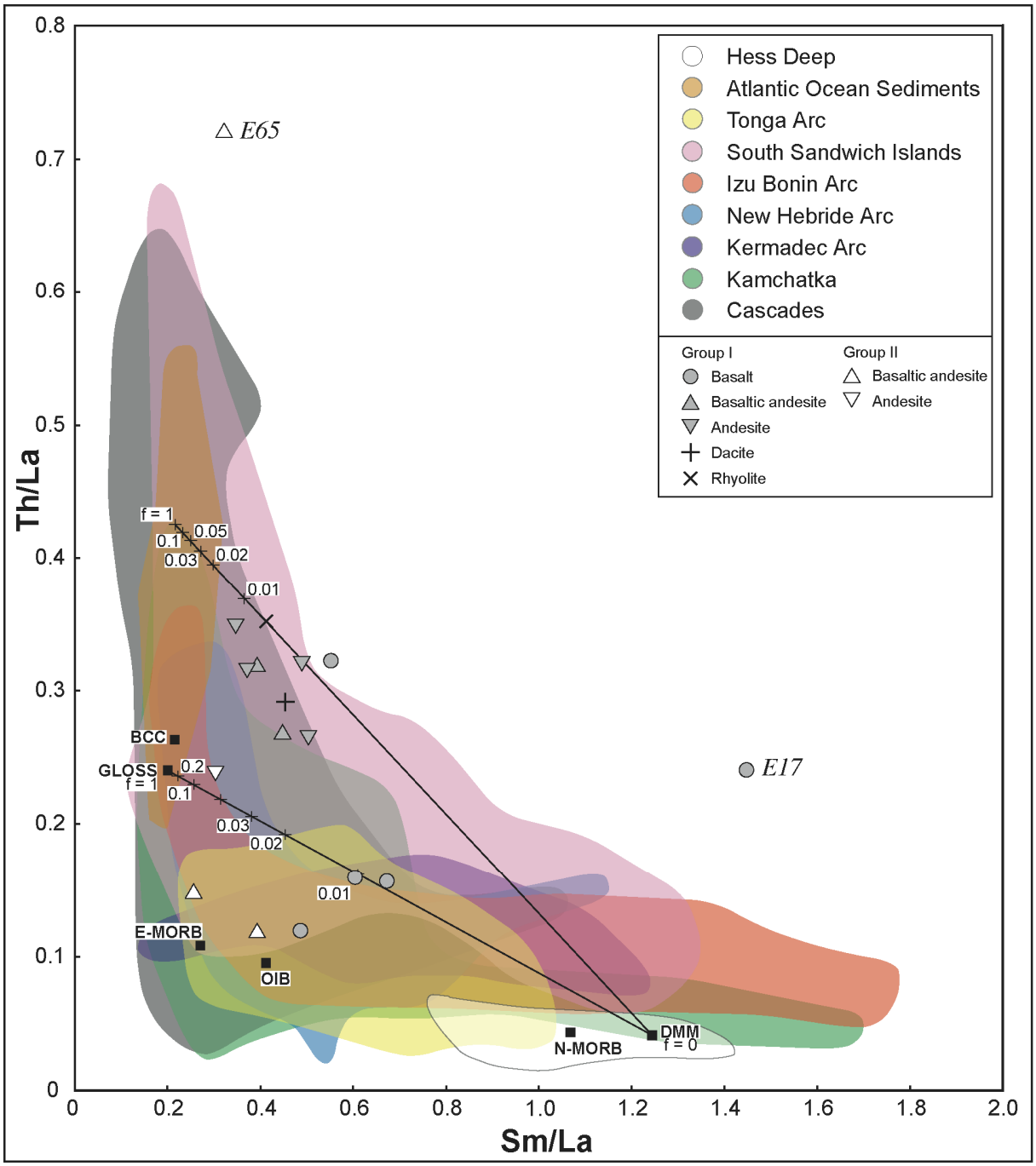

Fig. 3-9: Th/La against Sm/La for the Evros volcanic rocks (after Plank, 2005). Mixing lines are given for DMM – Atlantic Ocean Sediment and DMM – GLOSS. Numbers next to the tic marks on the lines indicate amount of melt fraction of sediment melt added to the mixture. Sample signatures, data sources and abbreviations of terms as in captions to Fig. 3-6 and 3-7. Additional data sources: Hess Deep (Stewart et al., 2002); Atlantic Ocean sediments (Ben Othman et al., 1989).

It has long been established that plotting a compatible element against an incompatible element is a useful technique to determine the processes responsible for the geochemical variations in a certain lava suite (Pearce, 1975, 1980, 1982; Pearce et al., 1984, 1986; Kostopoulos, 1988). In such plots, partial melting trends will be subparallel to the incompatible element axis because partial melting will rapidly extract the incompatible element from the source (Kostopoulos, 1988). By contrast, fractional crystallisation trends will initially be almost vertical to the incompatible element axis because early precipitation of mafic minerals (e.g. Ol, Cr-Sp) will cause rapid depletion of the compatible element in the derivative melts (Kostopoulos, 1988).

Figure 3-10 is a plot of Ti (incompatible element) vs. Cr (compatible element) for the Evros volcanic rocks (a) with partial melting and crystallisation vectors (b) taken from Kostopoulos (1988) and Kostopoulos & Murton (1992). Assuming that a Fertile Spinel Lherzolite (FSL), compositionally equivalent to DMM, is the source peridotite, the Evros volcanic rocks of both groups would require 20 – 30% melting (Fig. 3-10a) followed by ~20% fractionation of clinopyroxene (Fig. 3-10b, vector Cpx_{20}). This is supported by the mineral assemblage of the volcanic rocks, which contain clinopyroxene and plagioclase. Assuming that the mantle source is more depleted (Depleted Spinel Lherzolite; DSL), it would require less than 10% melting of this depleted source to produce this melt. The low Ti content of sample E46 (rhyolite of Group I; Fig. 3-10a) indicates fractionation of Fe-Ti oxides.

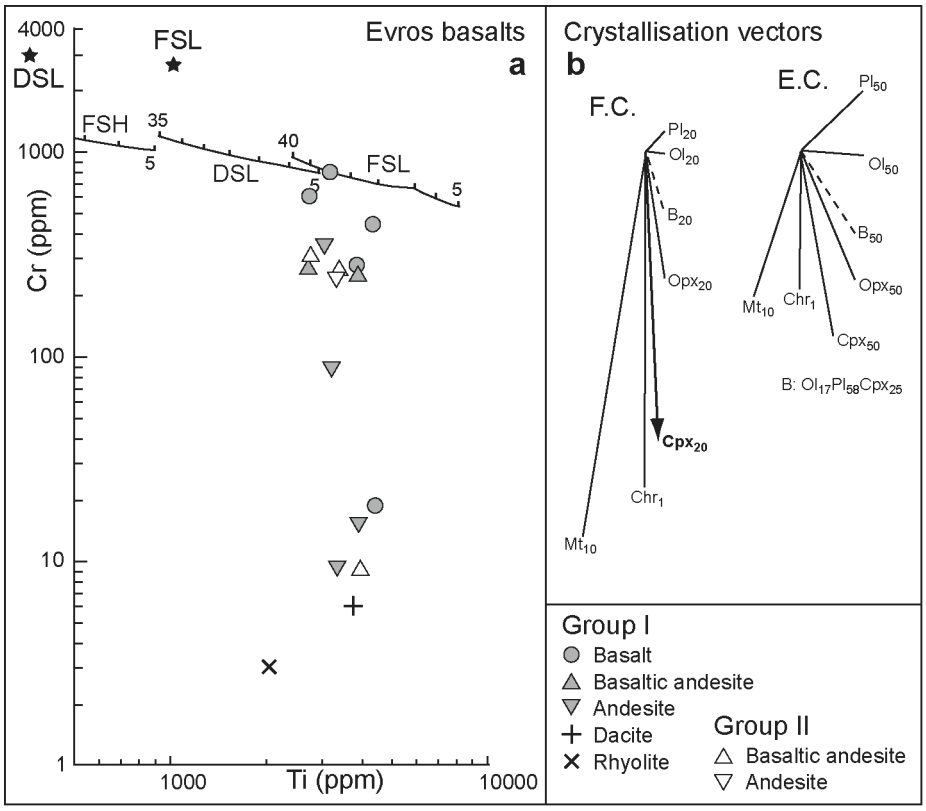

Fig. 3-10: Ti-Cr diagram with melting trends after Kostopoulos & Murton (1992). Crystallisation vectors after Kostopoulos (1988). Sample signatures as in Fig. 3-6. Abbreviations: E.C.: Equilibrium crystallisation; F.C.: Fractional crystallisation; FSL: fertile spinel lherzolite; DSL: depleted spinel lherzolite; FSH: fertile spinel harzburgite. Melts of FSL, DSL and FSH are accumulated.

4.2. Gabbros

Whole-rock major and trace element analyses for the Evros gabbros are given in Appendix B-4. In order to assess the effect of alteration each element analysed by whole-rock geochemistry was plotted against Zr as it was done for the volcanic rocks. These plots are available in Appendix F-4. It is evident from these plots that, except for TiO_2 and Fe_2O_3, most of the major elements are more or less disturbed by alteration as are some of the trace elements. Furthermore, the covariation diagrams demonstrate that the gabbros of the Maronia area can be divided by their major and trace element contents into two groups. Plotting these diagrams in a logarithmic scale the grouping is better visible (Fig. 3-11). One group, here called Group I, is characterised by generally primitive compositions shown by low Zr, Ti, Na and K and high Mg, Cr and Ni contents and high Mg#. Moreover, this group is low in LILE, HFSE and REE as well as in Pb and U (Fig. 3-11, 3-13A and 3-14A, see also Appendix F-4). The second group, in the following named as Group II, displays more evolved characteristics

such as high Zr, Ti, Na, K, Pb and U as well as high LILE, HFSE and REE. The contents of Mg, Cr and Ni and the Mg# are low (Fig. 3-11, 3-13A and 3-14A, see also Appendix F-4). The grouping can also be traced by the spatial distribution of the samples. While the primitive Group I can be found in the so-called Main Facies of the gabbro complex (see Fig. 3-12), the more evolved Group II is located in the so-called Cumulatic Suite of the gabbro complex (Fig. 3-12) and one gabbro sample of this group (E77) is located WSW of Agriani (see Fig. 3-2).

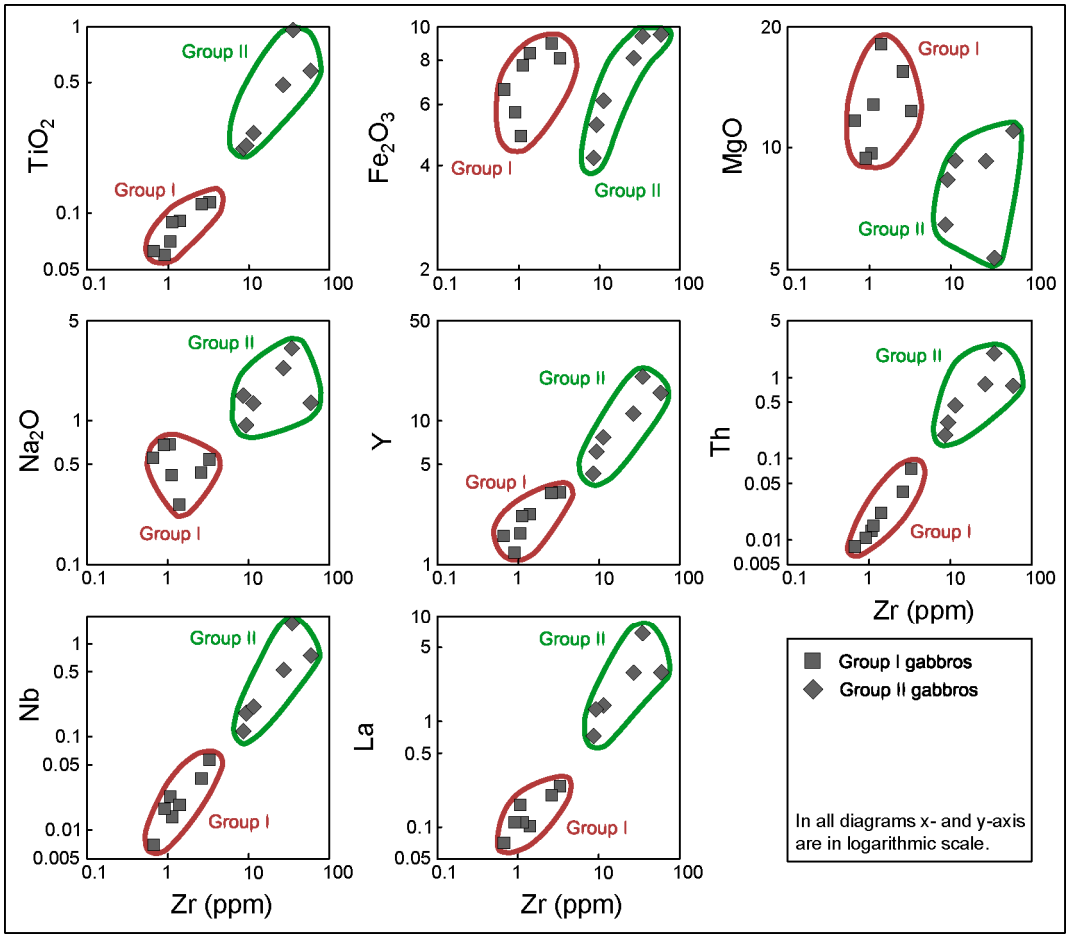

Fig. 3-11: Logarithmic covariation diagrams of Zr (in ppm) versus major (in wt%) and trace elements (in ppm) of the gabbros of the Evros area. The gabbros can be divided into a primitive Group I (grey squares) and a more evolved Group II (grey diamonds).

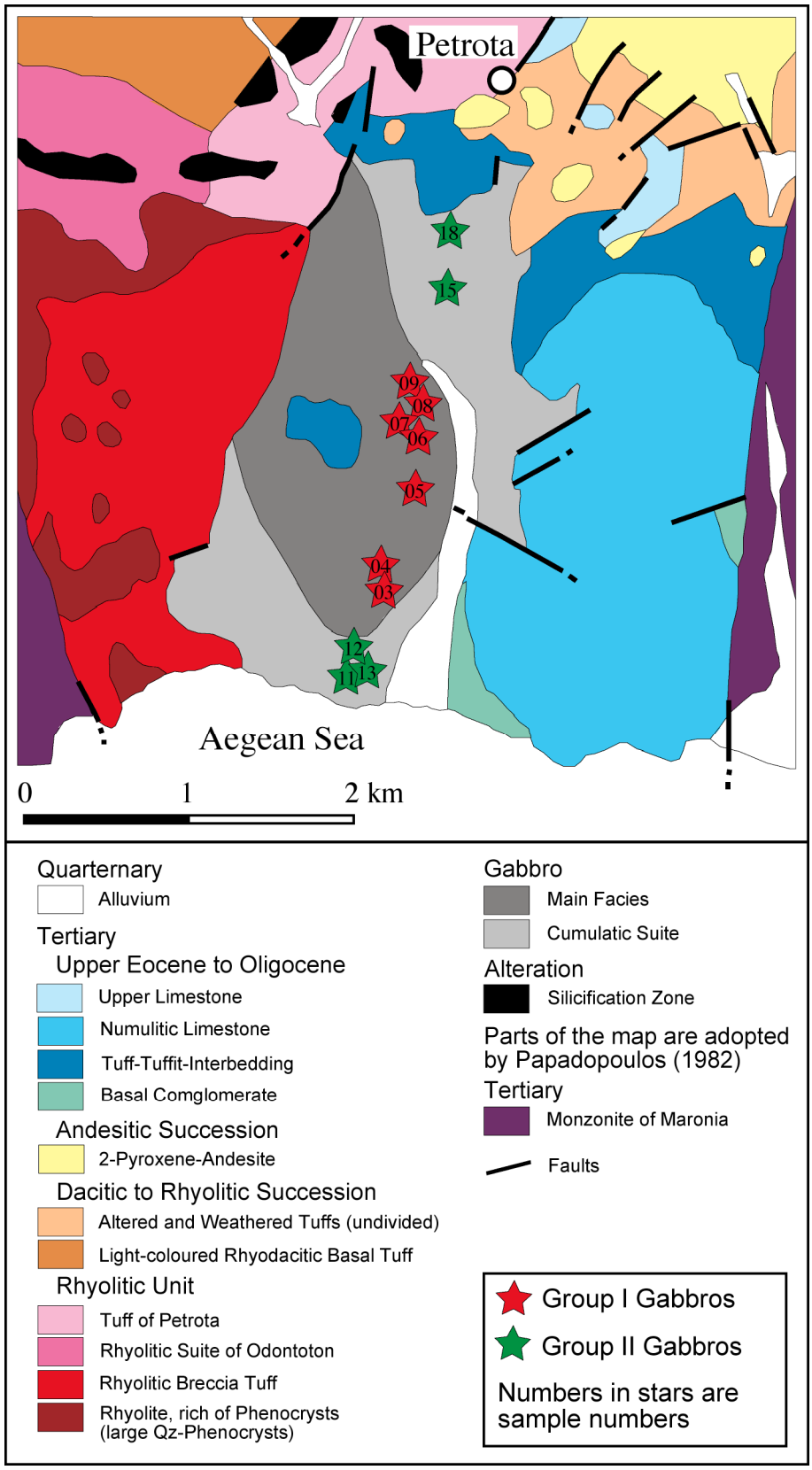

Fig. 3-12: Map of the area south of Petrota village (adapted from Frass et al., 1990). The localities of the gabbros samples are marked with different-coloured stars (see legend).

Chondrite-normalized REE patterns for the Evros gabbros are shown in Fig. 3-13. The REE patterns of Group I gabbros are flat in LREE (La_N/Nd_N = 0.8 – 1.2) and show a depletion from HREE towards LREE (Nd_N/Lu_N = 0.27 – 0.44) (see Fig. 3-13A). In many cases a well-pronounced positive Eu anomaly is visible indicating accumulation of plagioclase. Compared to different gabbros from oceanic and continental island arcs (Fig. 3-13B) the Group I gabbros are more depleted in LREE and MREE than most of the given references. They resemble the single gabbro from the Central American Volcanic Belt (Hauff et al, 2000), which shows the same depletion from HREE towards LREE. There are also similarities to the most depleted gabbros from the Greater Antilles (e.g. Marchesi et al., 2006) with low concentrations of REE but the LREE contents of the Group I gabbros is much lower and the Eu anomaly is less than that of the Greater Antilles gabbros (Fig. 3-13B).

The REE pattern of the Group II gabbros are almost flat (La_N/Yb_N = 1.0 – 1.7) while gabbro E13 displays an enrichment from MREE towards LREE (La_N/Ho_N = 2.1) strongly resembling the average MOR gabbro from the SWIR (Fig. 3-13A). Mainly positive Eu anomalies are developed suggesting accumulation of plagioclase. The gabbros of Group II resemble gabbros from both, oceanic (Scotia Arc [e.g. Willan & Kelley, 1999]; Greater Antilles [e.g. Marchesi et al., 2006]) and continental island arcs (e.g. Aleutian Arc [e.g. Nye et al., 1994]; Cascades [Tepper, 1996]). Both, oceanic and continental island arc gabbros have flat REE patterns with some slight enrichment in LREE to which the Evros gabbros of Group II are similar.

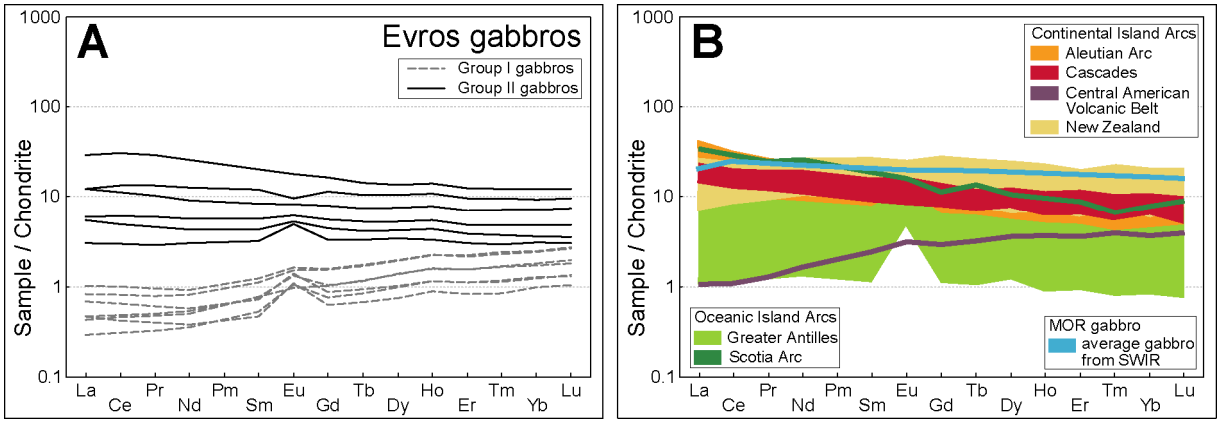

Fig. 3-13: Chondrite-normalised REE profiles for the Evros gabbros (A) and different gabbros from mid ocean ridge and oceanic and continental island arcs (B). Data sources: Aleutian Arc (e.g. Nye et al., 1994); Cascades (Tepper, 1996); Central America Volcanic Belt (Hauff et al, 2000); New Zealand (e.g. Cole et al., 2001); Greater Antilles (e.g. Marchesi et al., 2006); Scotia Arc (e.g. Machado et al., 2005). Abbreviations: SWIR: Southwest Indian Ridge.

The multi-element patterns for the gabbros have been normalised by an average MOR gabbro from the Southwest Indian Ridge (SWIR; ODP176; Hart et al., 1999). The patterns of Group I display are strongly depleted in HFSE compared to SWIR gabbro with depletion from Yb towards La (La_N/Yb_N = 0.4 – 0.9) and well-pronounced negative Nb and Zr anomalies. The LIL elements are enriched relative to the HFS elements, but except of Rb, more depleted than the average MOR gabbro from SWIR (Fig. 3-14A). Compared to different gabbros from oceanic and continental island arcs (Fig. 3-14B), the Group I gabbros display similar LILE concentrations but are more depleted in HFSE than most of the given reference gabbros. They slightly resemble one gabbro of the Central American Volcanic Belt (Hauff et al, 2000) and the most depleted gabbros from the Greater Antilles (e.g. Marchesi et al., 2006). The strongly depleted character of the Group I gabbros indicates a similar parental melt as for the boninites of the Evros area and, therefore, a forearc position of both rocks types.

The Group II gabbros are flat to slightly depleted in HFSE (La_N/Yb_N = 1.7 – 2.9) with a well-developed Nb-Ta anomaly and a slight negative Zr anomaly (Fig. 3-14A). Gabbro E13 displays a slight enrichment in HFSE from Yb towards La (La_N/Yb_N = 4.1). The HFSE pattern of this most enriched gabbro resembles the average MOR gabbro of the SWIR while the other samples are parallel but more depleted in HFSE. The LIL elements are enriched compared to the HFS elements. The more HFSE-enriched patterns resemble gabbros from both, oceanic (e.g. Scotia Arc [e.g. Willan & Kelley, 1999]) and continental island arcs (e.g. Cascades [Tepper, 1996]).

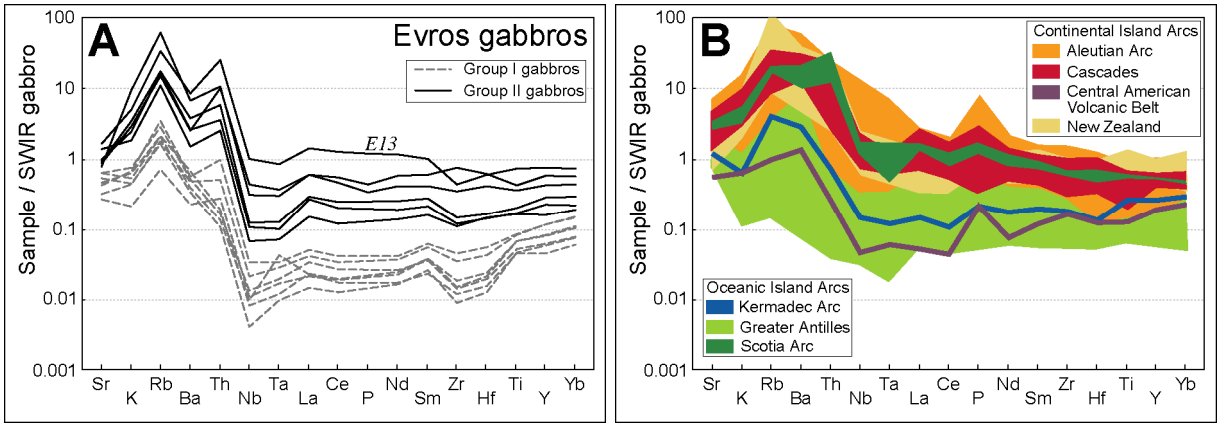

Fig. 3-14: Multi-element profiles for the Evros gabbros (A) and different oceanic and continental island arc gabbros (B) normalised by an average MOR gabbro of the Southwest Indian Ridge (SWIR; ODP176; Hart et al., 1999). See caption of Fig. 3-5 and 3-13 for data sources and abbreviations of terms. Additional data sources: Kermadec Arc (Turner et al., 1997).

4.3. Mantle peridotites

Whole rock geochemical data are available in Appendix B-5. The peridotites of the Evros area have been classified using the Ol – Opx – Cpx ternary diagram (Fig. 3-15). The calculated amounts of olivine (Ol), clinopyroxene (Cpx) and orthopyroxene (Opx) were determined following Hutchinson (1975). According to Fig. 3-15, the majority of the ultramafic rocks classify as harzburgites with varying amounts of Opx and Ol. Only one peridotite plots in the field of dunites.

On bivariate diagrams of element vs. MgO (recalculated volatile-free; Fig. 3-16) the concentration of the different major and trace elements varies with relative stable MgO concentration. The peridotites are much lower in TiO_2, Al_2O_3, CaO and Y than the published estimates of the composition of the primitive upper mantle (PUM) indicating high degrees of melting what is also depicted in the partial melting trends in figure 3-16. Therefore, the peridotites of the Evros region represent harzburgitic residues after high degrees of melt extractions (> 15%).

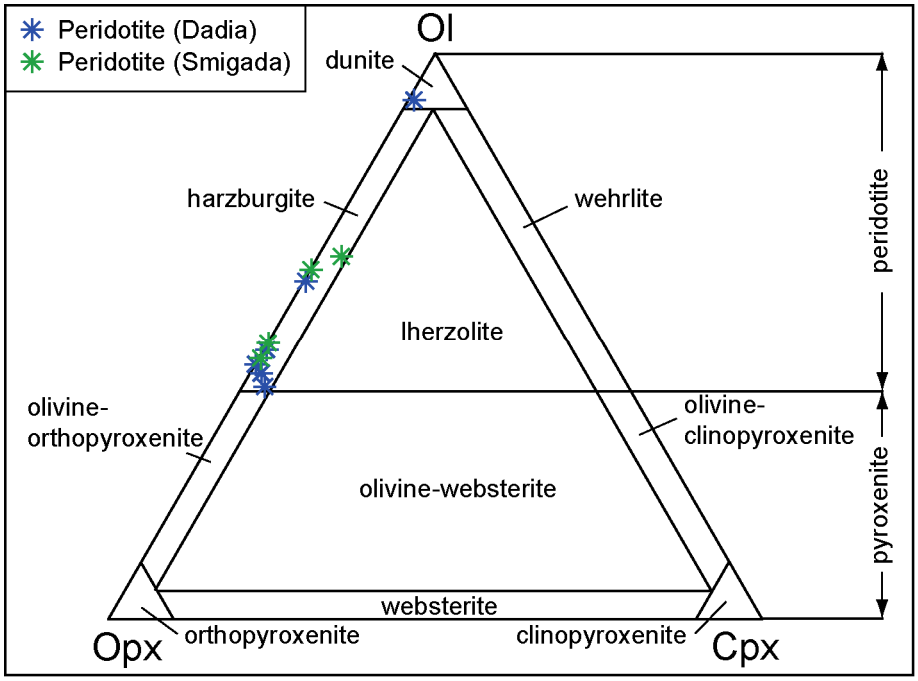

Fig. 3-15: Ol – Opx – Cpx ternary diagram. Mineral modal abundances calculated following Hutchinson (1975). Ol: olivine; Opx: orthopyroxene; Cpx: clinopyroxene.

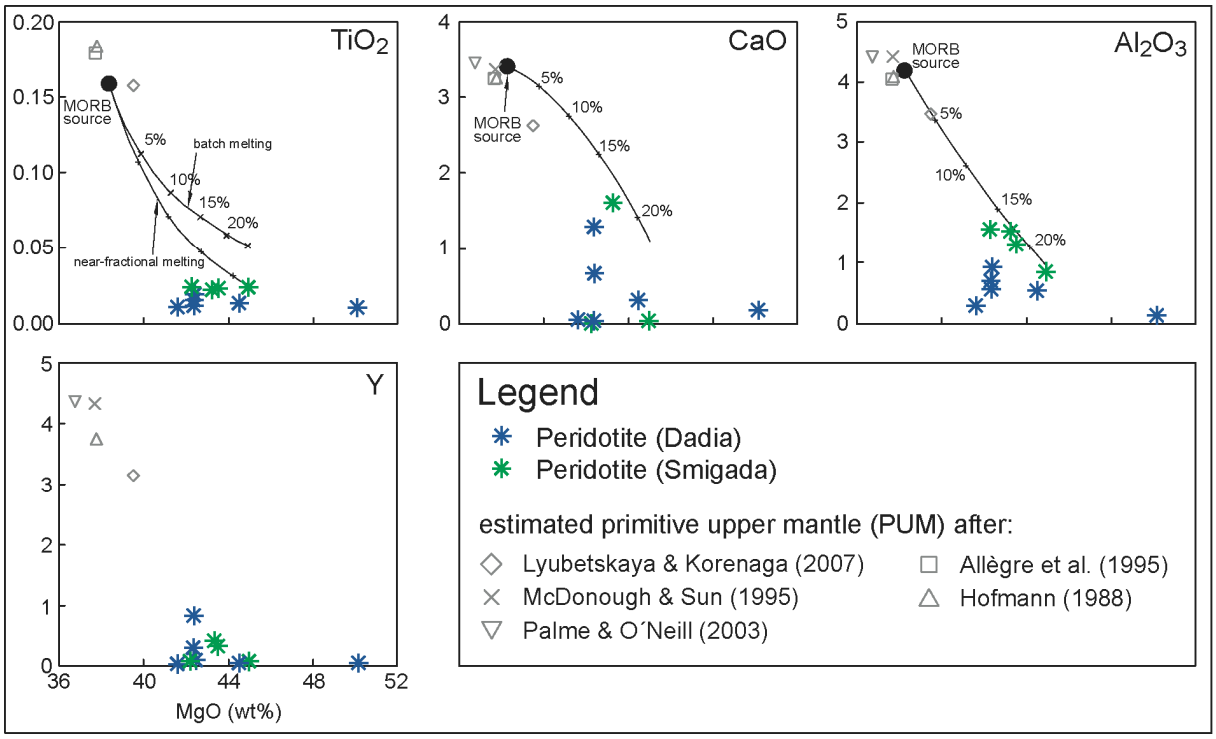

Fig. 3-16: Element vs. MgO bivariate plots for the peridotites of the Evros area (major elements in wt.%; trace elements in ppm). Primitive upper mantle estimates from the literature are given for comparison. Polybaric near-fractional and isobaric batch partial melting trends after Barth et al. (2007).

In chondrite-normalised REE plots, the peridotites show a depletion of MREE relative to HREE (Dy_N/Yb_N = 0.2 – 0.9) and variable amounts of LREE, mainly resulting in typical spoon- or dish-shaped patterns (Fig. 3-17A). Such patterns can be produced by contamination of the depleted peridotites by percolating melts (e.g. OIB) as demonstrated by Kostopoulos & Murton (1992). The pattern with a negative Ce anomaly indicates an additional source for La, probably from a subduction-related hydrous fluid (Cameron, 1985; Taylor & Nesbitt, 1988; Kostopoulos, 1988). The peridotite patterns are strongly similar to those of harzburgites from the Bismarck (Tabar-Lihir-Tanga-Feni) oceanic island arc (Fig. 3-17B), which are explained by an early partial melting depletion event with high degrees of melting. This refractory mantle was overprinted by oxidation and enrichments related to percolation of slab-derived hydrous melts after plate movement away from the ridge to an island arc setting (Gregoire et al., 2001).

Samples E52 and E55 exhibit flat depleted REE patterns (Ce_N/Yb_N = 0.7 – 1.3) with a marked positive Eu anomaly and some depletion in HREE (Fig. 3-17A). These patterns are generally more enriched compared to those of the Evros peridotites. They slightly resemble

the most depleted patterns of the continental island arc peridotites of the Andean Arc (3-17B) but they differ in the concentration of Nb and Sm.

It is clearly evident from Fig. 3-17B that the Evros peridotites are more depleted in REE than the peridotites from continental island arcs and, therefore, differ significantly.

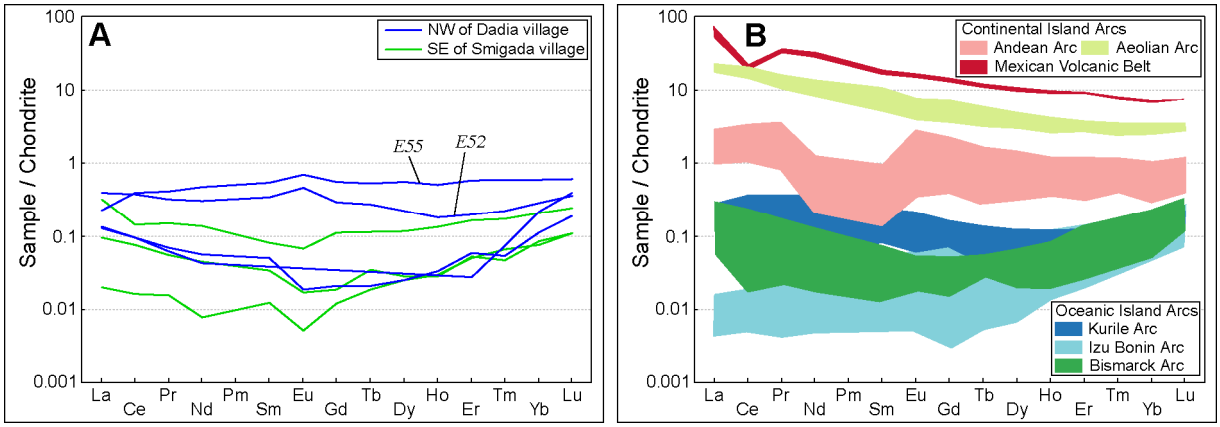

Fig. 3-17: Chondrite normalized REE patterns of the Evros peridotites (A) and different oceanic and continental island arc peridotites (B). Normalizing values after Sun & McDonough (1989). Data sources: Andean Arc (2005 Conceicao et al., 2005); Aeolian Arc (Laiolo & Cigolini, 2006); Mexican Volcanic Belt (Mukasa et al., 2007); Kurile Arc (Takazawa et al., 2000); Izu-Bonin Arc (Parkinson & Pearce, 1998); Bismarck (Tabar-Lihir-Tanga-Feni) Arc (Gregoire et al., 2001).

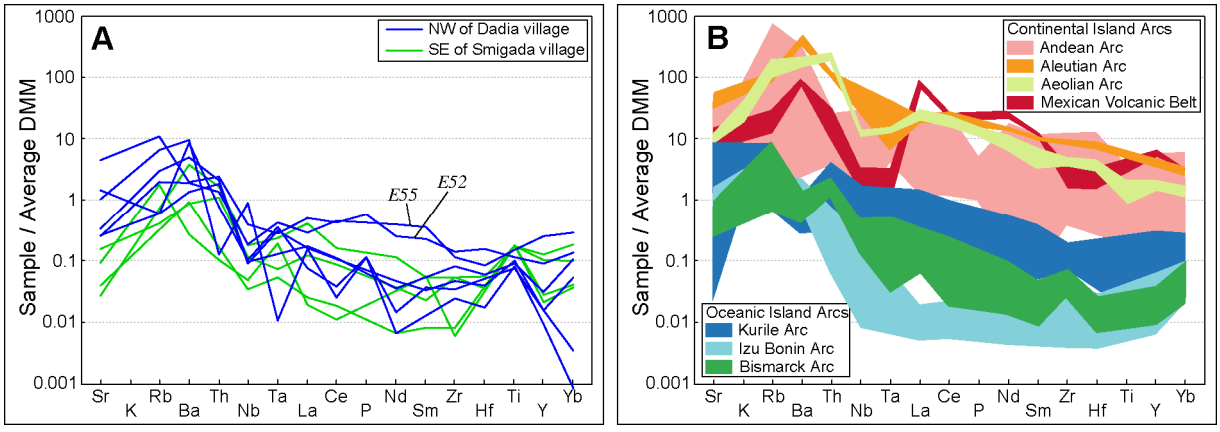

Fig. 3-18: DMM normalized multi-element diagrams for the Evros peridotites (A) and different oceanic and continental island arc peridotites (B). It is clearly evident that the peridotites of the Evros area resemble the peridotites of oceanic island arcs. Normalizing values after Workman & Hart (2005). Data sources as in captions to Fig. 3-17. Additional data sources: Aleutian Arc (Debari et al., 1987).

DMM-normalized patterns for the Evros peridotites and for different examples of oceanic and continental island arc peridotites (see figure captions for references) are shown in Fig. 3-18. The patterns of the Evros peridotites show a well-developed hump at their LILE part and a variably strong developed trough over their HFSE part with a positive Ti anomaly (Fig. 3-18A). With these properties they resemble harzburgites and in parts dunites from the oceanic island arc of Izu-Bonin (Parkinson & Pearce, 1998), and harzburgites of the Bismarck (Tabar-Lihir-Tanga-Feni) (Gregoire et al., 2001) and the Kurile oceanic island arc (Takazawa et al., 2000) (Fig. 3-18B). Two peridotites NW of Dadia village (E52, E55) show similar pattern to the other peridotites of the Evros area but are more enriched in LREE and some HFSE (La to Zr) (Fig. 3-18A) suggesting either lower degrees of melting or refertilisation in LREE by addition of a percolating component. These rocks can be compared to dunites from the Kurile oceanic island arc (Takazawa et al., 2000), which show a comparable enrichment in LREE (Fig. 3-18B). It is clearly evident from Fig. 3-18B that peridotites from continental island arcs are more enriched in LILE, LREE and HFSE and therefore differ significantly from the Evros peridotites.

5. Mineral chemistry

5.1. Pyroxenes of the gabbros

Pyroxenes form a major constituent of the gabbros of the Evros area. Within Group I gabbros clinopyroxene and orthopyroxene are found. The clinopyroxenes have mainly diopside composition (Fig. 3-19). Their average composition is $Wo_{39-47}En_{44-49}Fs_{8-11}$, the Mg# ranges from 0.82 – 0.85 and their TiO_2 content is very low (0.05 – 0.24 wt%). Temperature was calculated using the method of Bertrand & Mercier (1985) and assumed pressures of 2 to 10kbar. Since the difference between the calculated temperatures for 2 and 10 kbar is only 10°C in the following temperature estimations are given for 5kbar. Temperature calculations for the clinopyroxenes yield temperatures of 754 - 1066°C. These values agree with the temperatures received from the diagram after Lindsley (1983) (T = 500-1000°C; see also Fig. 3-19). The orthopyroxenes show mainly enstatite composition (Fig. 3-19) with an average composition of $Wo_{1-9}En_{71-78}Fs_{20-23}$ and Mg# of 0.77 – 0.80. According to the diagram after Lindsley (1983) they yield slightly higher temperatures than the clinopyroxenes ranging from 700 – 1100°C (Fig. 3-19).

The Group II gabbros contain only clinopyroxene. While the clinopyroxenes of

sample E13 (S Petrota) were mainly converted to amphibole, the clinopyroxenes of sample E77 (WSW Agriani) remained fresh. The clinopyroxene found in E13 displays typical augite composition with $Wo_{27}En_{45}Fs_{28}$. It has high TiO_2 content of 2.62 wt% and low Mg# of 0.62. According to the diagram after Lindsley (1983), it yield a temperature of 1200°C (Fig. 3-19) which is in good agreement with the calculated temperature after Bertrand & Mercier (1985) of 1255°C. The clinopyroxenes of sample E77 are diopsidic in composition with $Wo_{44-50}En_{41-45}Fs_{6-11}$. Their Mg# range from 0.80 – 0.89 and their TiO_2 contents is low (0.03 – 0.39 wt%). The temperature calculated after the geothermometer of Bertrand & Mercier (1985) gave temperatures ranging from 602 - 739°C. The estimated temperatures of maximum 700°C according to the diagram after Lindsley (1983) are slightly lower than the calculated one but comparable (Fig. 3-19). The chemical data of the pyroxenes are given in Appendices C-2 and C-3.

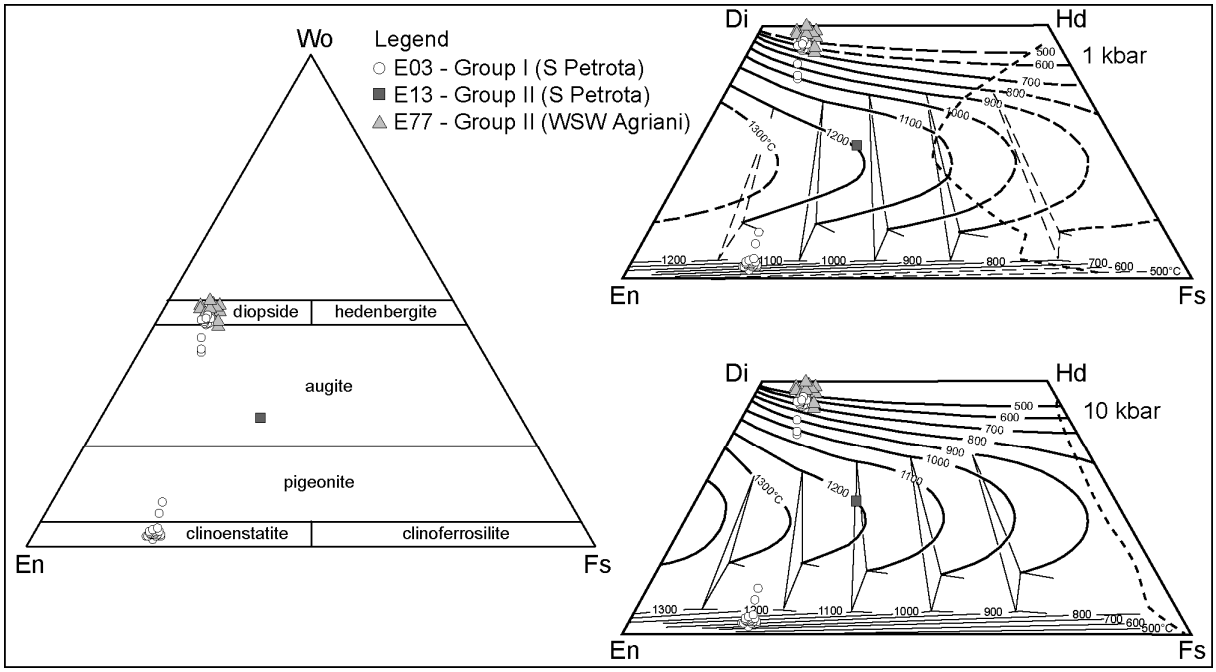

Fig. 3-19: Classification triangle of pyroxenes after Morimoto et al. (1988) (left) and parts of it with the isotherms of 1 kbar and 10 kbar proposed by Lindsley (1983) (right).

5.2. Amphiboles of the gabbros

Amphiboles are common in the gabbros of the Evros area, belonging to the secondary mineral assemblage. The amphiboles are in both groups of calcic composition (Ca_B = 1.73 – 2.01; $(Na+K)_A$ = 0.02 – 0.33) with Mg# (Mg/[Mg+Fe^{2+}]) > 0.5. The Si in formula vs. Mg/(Mg+Fe^{2+}) diagram after Leake et al. (1997) shows actinolitic to magnesiohornblende

amphiboles for both, Group I and II gabbros S of Petrota village. The Group II gabbros WSW of Agriani contain mainly magnesiohornblende (Fig. 3-20). Temperature estimations after Holland & Blundy (1994) using hornblende and plagioclase yield maximum overprint temperatures of 874 - 895°C at assumed pressures of 2 – 4 kbar for sample E77. Estimations of the formation temperatures of the amphiboles of the Group I gabbro S of Petrota village (E03) after Holland & Blundy (1994) yield 824 – 848°C. The temperatures for the formation of the Group II gabbro in this area (E13) are slightly lower (794 – 809°C). The compositions of the amphiboles are available in Appendix C-4. The very high formation temperatures of the amphiboles and their large grain size in all gabbros indicate hydration during cooling of the gabbros.

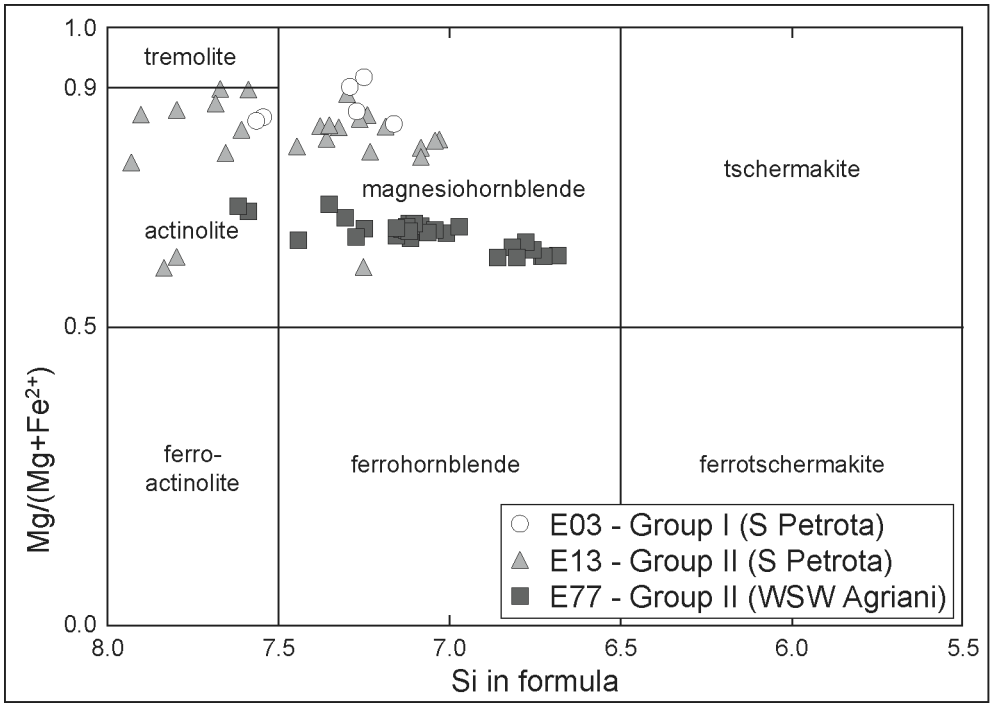

Fig. 3-20: Classification diagram for calcic amphiboles with $Ca_B \geq 1.50$ and $(Na+K)_A < 0.50$ after Leake et al. (1997) for the amphiboles of the gabbros of the Evros area.

5.3. Spinels of the mantle peridotites

In a pioneering paper, Dick & Bullen (1984) used spinel chemistry [Cr/(Cr+Al)) vs. $Mg/(Mg+Fe^{2+})$ or Cr# vs. Mg#] to classify spinel peridotites from different settings. In such a diagram (Fig. 3-21) spinels from abyssal (i.e. MORB-type) and a significant population of Alpine-type peridotites are characterized by high Al and Mg and low Cr and Fe^{2+} contents.

This results in low Cr# and high Mg# values while higher depletions of mantle rocks is characterised by low Al and Mg and high Cr and Fe^{2+}, resulting in high Cr# and low Mg#.

The Evros peridotite Cr-spinels are rich in Fe^{2+}, low in Al and Mg and contain moderate amounts of Cr (see Appendix C-5). They exhibit high Cr# values (0.75 – 0.99) and low Mg# (0.02 – 0.32) (Fig. 21), indicating high depletion. They are similar to the spinels of Type III peridotite after Dick & Bullen (1984), which have melted in the presence of water, suggesting a subduction-zone setting. Hellebrand et al. (2001) used the Cr# of spinel to calculate the degree of melting of spinel peridotites using the formula F = 10ln(Cr#)+24. Upon application of the above formula to the Cr-spinels of the Evros peridotites, degrees of melting between 21 and 24% can be calculated.

Kamenetsky et al. (2001) used TiO_2 vs. Al_2O_3 content of spinel to discriminate between peridotites from different tectonic settings (Fig. 3-22). The Cr-spinels from the Evros peridotites plot at medium to high TiO_2 and low Al_2O_3 values, indicating a depleted island arc character.

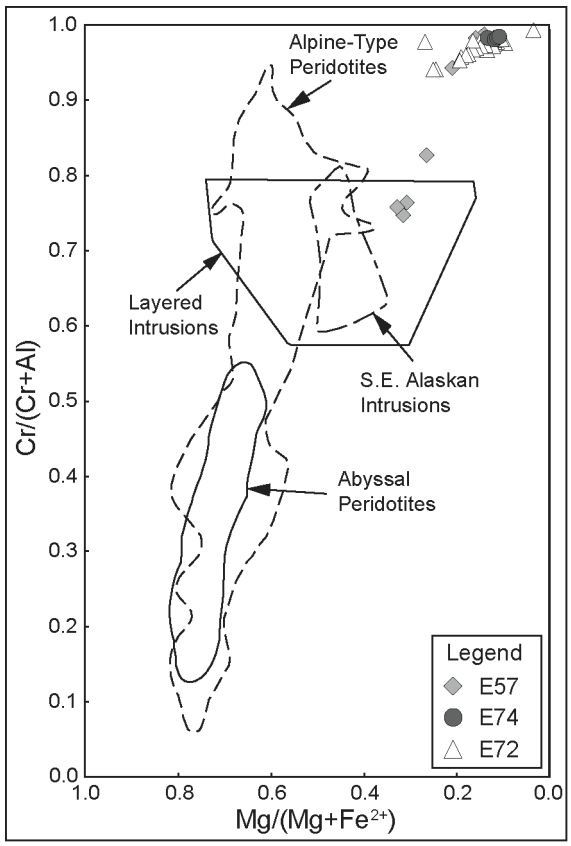

Fig. 3-21: Cr# against Mg# for spinels from the Evros peridotites (after Dick & Bullen 1984).

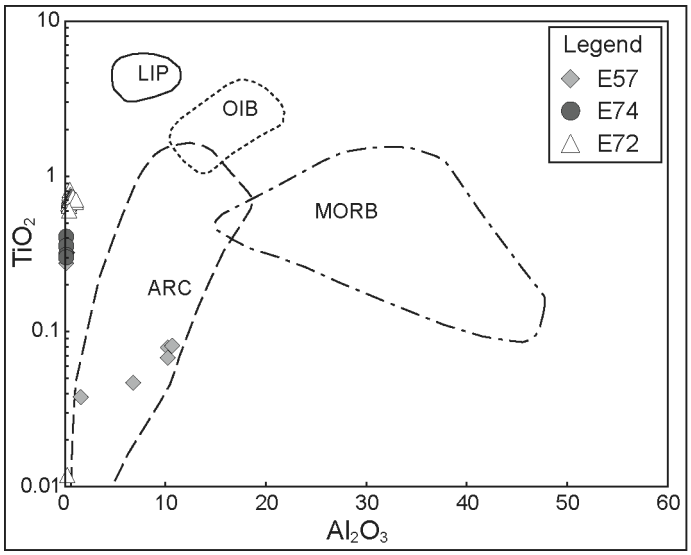

Fig. 3-22: TiO_2 against Al_2O_3 content of spinel from peridotite after Kamenetsky et al. (2001). Medium to high TiO_2 and low Al_2O_3 indicate a depleted character for the peridotites. LIP: large igneous provinces.

6. Sr and Nd isotopic ratios

In this section the Sr and Nd isotopic results for the rocks of the Evros area are presented. Sr initial ratios and epsilon Nd values are calculated for an age of 169 Ma, which is the age obtained from zircon geochronology of the gabbros (see Section 7).

6.1. Volcanic rocks

The volcanic rocks of both groups of the Evros area show huge variations in their εNd_{169} values. The Group I rocks range from –0.7 to +7.7 while the Group II rocks fall into that range with εNd_{169} values from +4.7 to +7.7. The initial Sr ratios of both groups are similar (Group I: 0.7039 – 0.7048; Group II: 0.7037 – 0.7047; see also Appendix D-3). Most of the Evros volcanic rocks plot within the mantle array (Fig. 3-23) suggesting that metamorphism has slightly affected the isotopic systems considered, especially that of Sr which is much more susceptible to alteration than Nd. However, some samples are affected by seawater alteration as evident from the shifts to higher initial $^{87}Sr/^{86}Sr$ values.

It is evident from Fig. 3-24 that there are two different components involved. The first component causes enrichment in LREE, which is also responsible for a slight enrichment in radiogenic Nd (low εNd_{169}) similar to the subducted sediments at the Alaskan trench. The second component causes a larger enrichment in radiogenic Nd but with lower contents of

LREE similar to the Tonga trench sediments (Fig. 3-24). The high-LREE samples can be explained by addition of different amounts (up to 10%) of a component similar to the Alaskan trench sediments to the DMM. The low-LREE samples are a result of mixing depleted mantle with up to 2% of a component similar to the sediments subducted at the Tonga trench (Fig. 3-24). Sample E17 displays εNd_{169} and Ce/Sm values similar to DMM.

6.2. Gabbros

The grouping of the gabbros is also reflected by the isotopic composition. While the gabbros of Group I show low εNd_{169} values of +1.3 – +1.5 and high $^{87}Sr/^{86}Sr_{169}$ ratio values of 0.7049 – 0.7052 (Fig. 3-23 and Appendix D-3), the Group II gabbros are characterised by high values of εNd_{169} (+3.8 - +5.2) and low initial Sr ratios (0.7040 – 0.7045). Both groups plot amongst the volcanic rocks within the mantle array (Fig. 3-23).

In Fig. 3-24 the grouping of the gabbros is also well observable. The Group II gabbros fall amongst those volcanic rocks with high enrichment of LREE and can be a result of mixing the depleted mantle source with 2 – 7% of a component similar to the Alaskan trench sediments. The gabbros of Group I plot within the field of the volcanic rocks containing high amounts of radiogenic Nd and can be explained by addition of less than 1% of melts similar to that of Tonga trench sediments (Fig. 3-24).

6.3. Mantle peridotites

The mantle peridotites display low to intermediate initial εNd values of +2.8 – +4.8 and initial Sr ratios of 0.7060 – 0.7094 (Fig. 3-23 and Appendix D-3). While the peridotite of Dadia village still plots within the mantle array, the peridotite of Smigada village plots outside the mantle array (Fig. 3-23). If one assumes alteration by Sr-bearing fluids or seawater, then one can explain the slight horizontal shift of the Dadia peridotite towards higher Sr initial ratios. In the case of the Smigada peridotite however, seawater cannot be the reason for the high $^{87}Sr/^{86}Sr_{253}$ value because seawater has a lower, time-corrected, Sr initial ratio value than that of the Smigada peridotite. It is then plausible, according to Fig. 3-23, that some other enrichment process has played a role in the isotopic shift of this peridotite sample. Most probably the serpentinisation of this rock could have caused this shift but also an enriched melt (e.g. OIB) with an inherent recycled sedimentary component could have been the enrichment component.

In Fig. 3-24 the Dadia peridotite plots at lower εNd_{169} value and low Ce/Sm ratio together with the volcanic rocks and gabbros with high amounts of radiogenic Nd. The peridotite of Smigada shows higher values of εNd_{169} and Ce/Sm therefore falling into the range of the high-LREE volcanic rocks and gabbros.

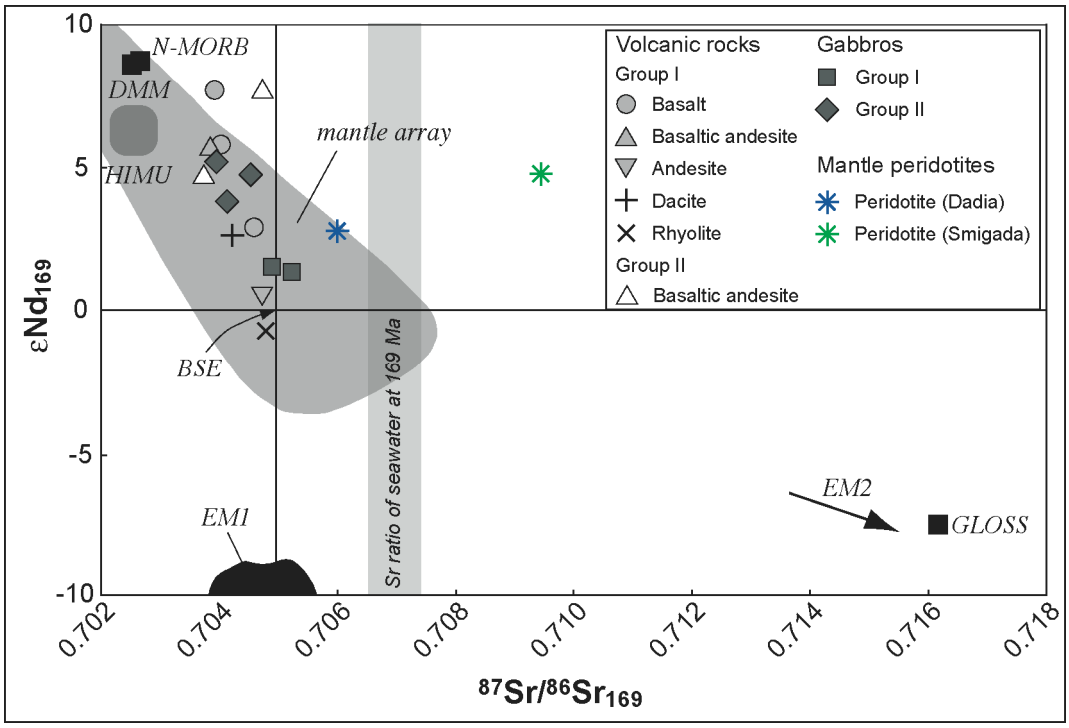

Fig. 3-23: εNd_{169} vs. $^{87}Sr/^{86}Sr_{169}$ for the different rock types of the Evros area. Data sources and abbreviations of terms as in caption to figures 3-5 and 3-7. Additional data sources: Mantle array (White, 1998); HIMU, BSE, EM1 and EM2 (Zindler & Hart, 1986); Sr isotopic ratio seawater (Burke et al., 1982). Additional abbreviations: HIMU: high-μ mantle reservoir; BSE: bulk silicate earth; EM: enriched mantle. All reference values are recalculated to 169 Ma.

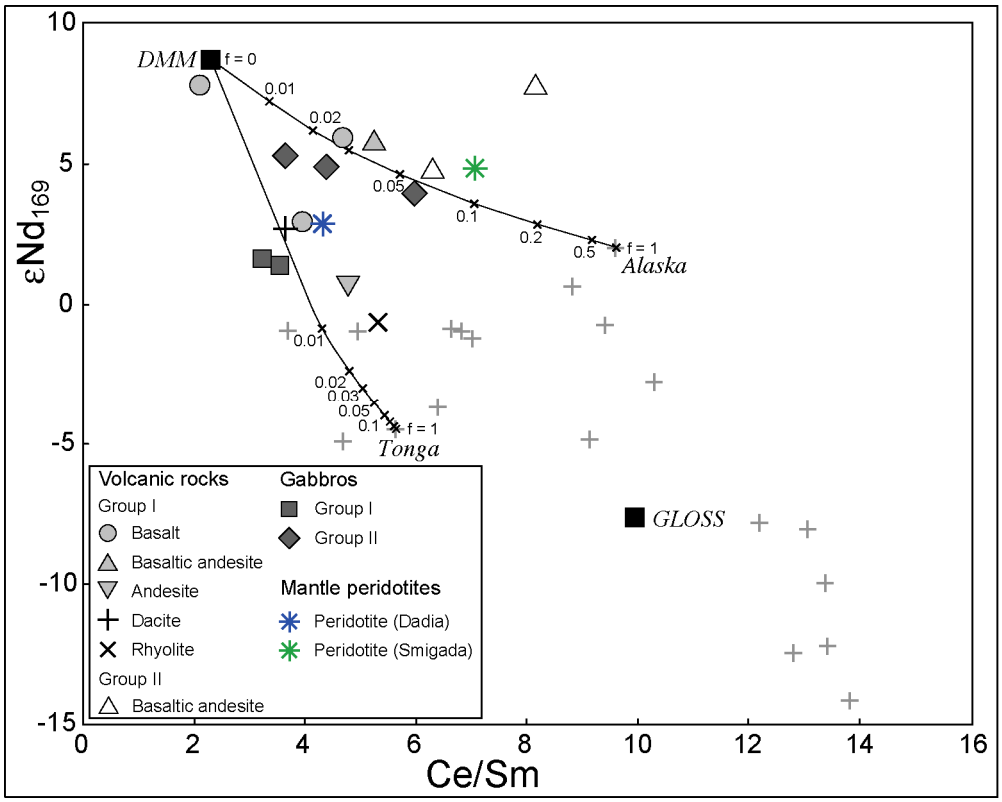

Fig. 3-24: Ce/Sm versus εNd_{169} for the different rock types from the Evros area. It is evident that the enrichment of LREE together with variable decreasing εNd_{169} values possibly derived from two different sources: one LREE-rich, radiogenic Nd-poor source (Alaskan trench sediments), and a LREE-poor, radiogenic Nd-rich source (Tonga trench sediments). Mixing lines between DMM – Alaskan trench sediments and DMM – Tonga trench sediments are indicated. Numbers next to the tic marks on the lines indicate amount of melt fraction of sediment added to the mixture. See captions to figure 3-23 for sample signatures and data sources. Additional data sources: Grey crosses: bulk compositions of different sediment columns subducting at trenches (Plank & Langmuir, 1998); Tonga and Alaskan trench sediments (Plank & Langmuir, 1998). All reference values are recalculated to 169 Ma.

7. Geochronological results

For the purpose of the age determination of the Evros ophiolite, zircons have been separated from a gabbro and analysed by SHRIMP II. The gabbro was collected from the so-called Cumulate Suite south of Petrota village and belongs to the Group II gabbros (sample E13, see Fig. 3-12) which are best suited for dating the ophiolite because the Group I gabbros are related to the boninites and, therefore, could be earlier in the forearc of the subduction zone.

The zircons of gabbro E13 have prismatic and mostly idiomorphic shape and their size varies between 120 and 200 μm. Cathodoluminescence imaging revealed homogeneous growth and well- developed oscillatory zoning (Fig. 3-25). The Th/U ratio of the zircons ranges between 0.5 and 1.6, suggesting a clear magmatic origin (Appendix E-4). Most of the zircon ages are consistent with a $^{206}Pb/^{238}U$ concordia age of 168.6 ± 1.8 Ma (Middle Jurassic) (Fig. 3-26). This age is interpreted as the crystallization age of the gabbro and is slightly older than the Late Jurassic to Early Cretaceous age (140 – 161 Ma) obtained by Biggazzi et al. (1989) using fission track on apatite from gabbros.

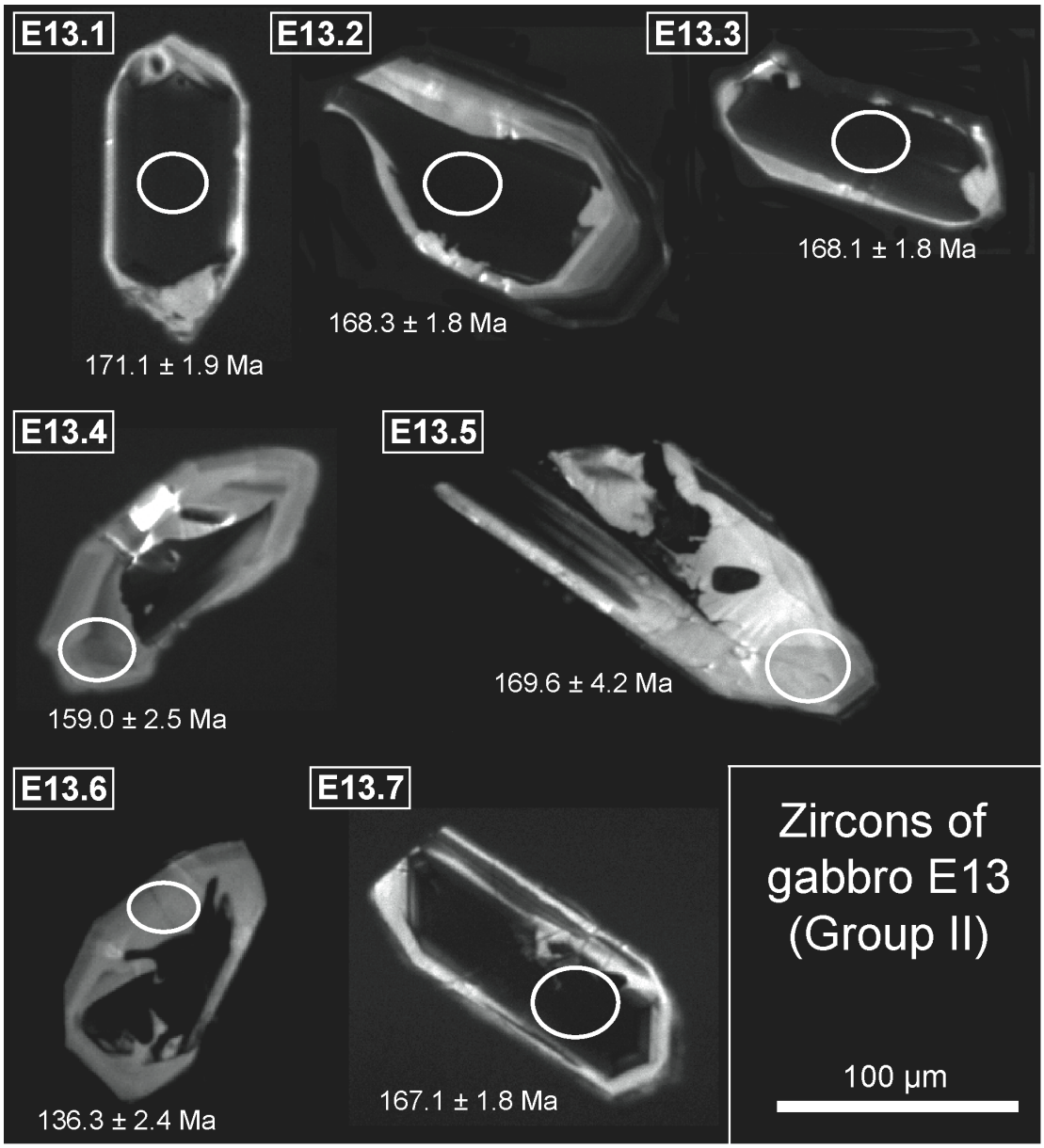

Fig. 3-25: Cathodoluminescence (CL) images of zircon crystals from gabbro E13. The euhedral shape and the oscillatory zoning are visible in some grains (E13.2; E13.4). White ovals indicate the points analysed by SHRIMP. $^{206}Pb/^{238}U$ ages are given with 1σ errors.

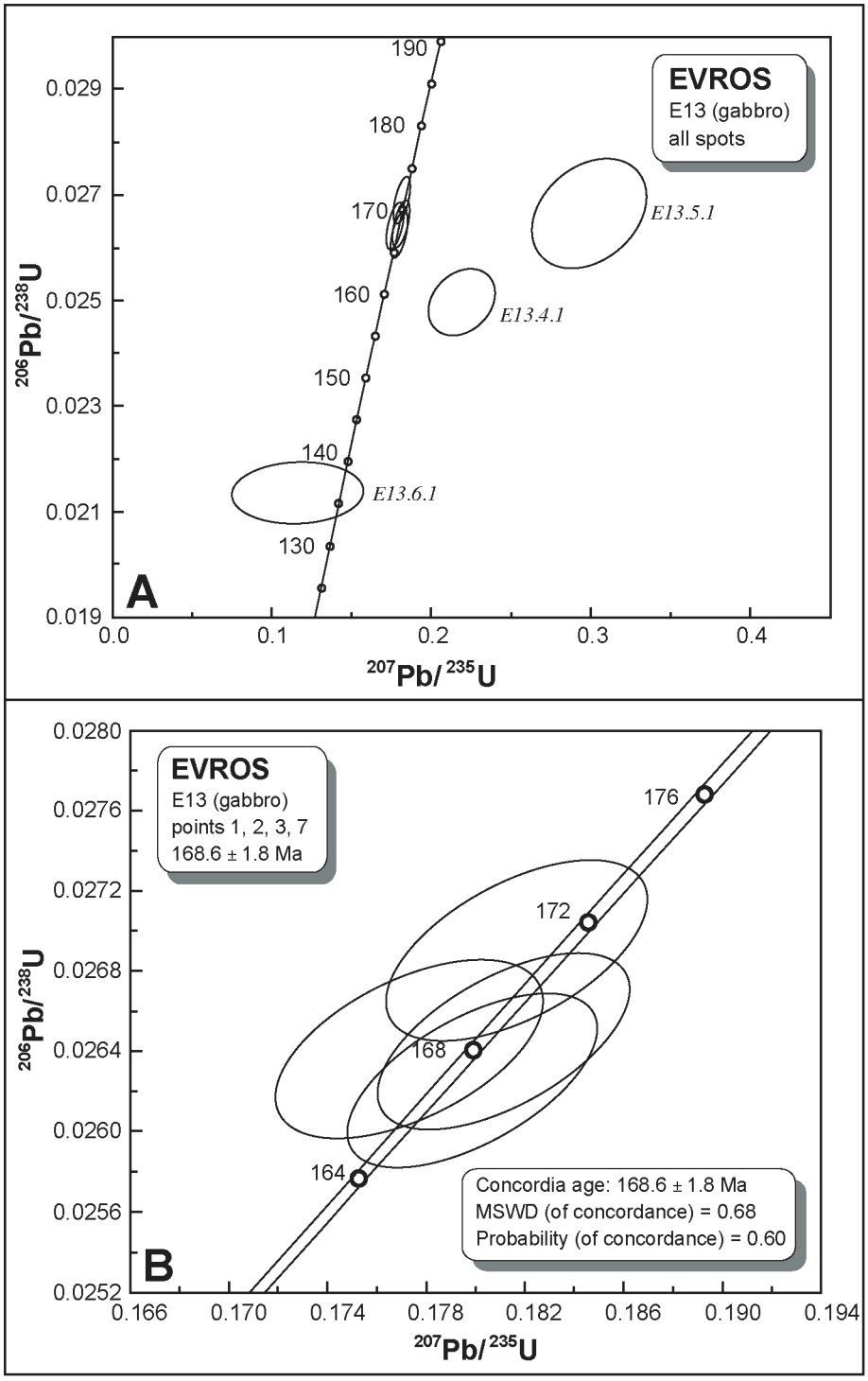

Fig. 3-26: Concordia diagram for all measured zircons (A) and the concordant zircons (B) from gabbro sample E13. The measured spots in B yield an intercept on the concordia at 168.6 ± 1.8 Ma, which is interpreted as the crystallisation age of the gabbro. Errors of the ellipses are 2σ.

8. Discussion

8.1. Volcanic rocks

The volcanic rocks of the Evros area can be found as massive lavas, pillow lavas and sheeted dyke complexes and their compositions range from basalt to rhyolite. They underwent greenschist facies metamorphism that is visible in alteration of the primary mineral assemblage to the typical greenschist facies assemblage, namely albite, chlorite, epidote, actinolite, quartz and titanite.

The geochemistry of the volcanic rocks shows typical features of island arc magmatism such as depleted HFSE, enriched LREE and LILE (see also Section 3) as well as moderate to low εNd_{169} (see also Section 6) (e.g. Shervais, 2001; Pearce et al., 2005). The depletion in HFSE is the result of hydrous melting of a depleted mantle source, which represents the residuum after extraction of mid-ocean ridge basalt melts. The various additions of LILE and LREE can be attributed to fluids and melts from the subducted slab (e.g. Hawkins, 2003; Pearce et al., 2005). Moreover, the typical rock types occurring in island arcs like boninites, island arc tholeiites and calc-alkaline volcanic rocks as described by Taylor et al. (1992), Shervais (2001) and Hawkins (2003) are represented in the Evros ophiolite. Flat to slightly U-shaped REE patterns are typical for the Group I volcanic rocks thus resembling island arc tholeiites and boninites. The Group II volcanic rocks are more enriched in LREE and LILE and therefore are best described as calc-alkaline volcanic rocks. Sample E17 (Group I) differs from the Group I volcanic rocks in the depletion of LREE. Its REE pattern is parallel to N-MORB but with lower values in all REE. This feature and the enrichment in Th indicate a depleted source similar to that of the other Group I volcanic rocks but only LILE have been added from the subducted slab. Sample 48 (Group I) shows a U shaped REE pattern with MREE depletion relative to the LREE and HREE. It represents the most typical member of the boninites of the Evros ophiolite, also displayed in its high SiO_2, MgO, Ni and Cr contents and low TiO_2 value. Moreover, this sample refers to a very depleted mantle source, enriched in LREE and LILE by fluids and melts of the subducted slab (e.g. Hawkins, 2003; Pearce et al., 2005).

Both groups show geochemical similarities with volcanic rocks of recent oceanic island arcs, e.g. Izu-Bonin Arc while Group II also shows similarities to the more depleted rock types of continental island arcs, e.g. Kamchatka. Initial Sr and Nd isotopic composition are similar in both groups and show a negative correlation. The εNd_{169} values range from –0.7

up to +7.7 with mainly moderate values of around +4.2. This is typical for island arc volcanic rocks (Shervais, 2001). The $^{87}Sr/^{86}Sr_{169}$ ratios are between 0.7037 and 0.7048. Correlated with the REE contents it is shown in Section 6 that at least two additional components played a role in the evolution of the volcanic rocks: a first component carrying LREE and little radiogenic Nd, and a second group bearing mainly radiogenic Nd.

Petrogenetic modelling indicates 20 – 30% melting of a FSL source or less than 10% melting of a DSL source, based on compatible versus incompatible element non-modal equilibrium melting modelling. Such high degrees of melting are found in young arcs built on oceanic lithosphere, e.g. Tonga, Scotia, Kermadec (Pearce & Parkinson, 1993).

Geochemically and petrographically similar ophiolitic rocks can be found NE of Thessaloniki within a new exposed outcrop and within the Oraeokastro ophiolite (low-TiO_2 volcanic rocks), both having formed in a supra-subduction zone setting. These ophiolites are described in detail by Zachariadis (2007).

In summary the volcanic rocks of Group I of the Evros region can be described as forearc boninites and oceanic island arc tholeiites while the Group II volcanic rocks represent calc-alkaline volcanic rocks generated in an oceanic island arc setting.

8.2. Gabbros

The gabbros of the Evros area can be divided spatially and geochemically in two groups: Group I with high Mg and low Ti, LILE, HFSE and REE, and Group II with low Mg and high Ti, LILE, HFSE and REE. While Group I is located in the middle part of the gabbroic complex south of Petrota village within the so-called Main Facies (Frass et al., 1990), the gabbros of Group II are found in the southern and northern part of that complex within the so-called Cumulate Suite (Frass et al., 1990) which is surrounding the Main Facies (see also Fig. 3-11).

Both groups show typical characteristics of island arc magmatism like depletion in HFSE and enrichment in LILE indicating a depleted mantle source fluxed by fluids and melts from the subducted slab. In Group I LILE are enriched relative to HFSE but, except for Rb, do not exceed the concentrations of the average MOR gabbro from the SWIR. Furthermore, this group is characterised by low LREE. The very strong depletion of HFSE and LREE indicate similar parental melts for the Group I gabbros and the boninites of the Group I volcanic rocks. The Group II gabbros show, in contrast to the gabbros of Group I, flat REE patterns and higher amounts of LILE and HFSE, whereas the HFSE are depleted relative to

the LILE. The general enrichment of the Group II gabbros relative to the gabbros of Group I indicates a more fertile mantle source for the gabbros of Group II. Both groups can also be distinguished by their Nd and Sr isotopic characteristics. Group I is low in εNd_{169} (+1.3 - +1.5) with high initial Sr ratios (0.7049 – 0.7052) and Group II has initial εNd values ranging from +3.8 - +5.2 and $^{87}Sr/^{86}Sr_{169}$ ratios between 0.7040 – 0.7046.

Clinopyroxene thermometry after Bertrand & Mercier (1985) and Lindsley (1983) yield temperatures of 749 – 1066°C for the Group I gabbros. Within the Group II gabbros clinopyroxenes are found which yield temperatures of 602 – 739°C for sample E77 (WSW Agriani) and 1255°C for sample E13 (S Petrota). The high Mg# combined with low TiO_2 contents are typical for clinopyroxenes formed in an island arc setting. Amphiboles of mainly magnesiohornblende composition are found within both groups. Estimating the formation temperatures for these amphiboles after Holland & Blundy (1994), both groups yield temperatures in the range of 794 – 895°C.

Zircons collected from gabbro E13 (Group II) and measured by SHRIMP yield $^{206}Pb/^{238}U$ concordia ages of 169 ± 2 Ma, which are interpreted as intrusion ages of this gabbro.

Summarizing, it can be said that the two groups of gabbros of the Evros region were formed in an island arc setting. Group I gabbros are the result of melting a strongly depleted mantle source and possibly represent the plutonic counterpart of the forearc boninites. The gabbros of Group II were the result of melting a less depleted mantle in an island arc setting. LILE-bearing components derived from the subducted slab were added to both groups (e.g. Hawkins, 2003; Pearce et al., 2005).

8.3. Mantle peridotites

The peridotites of the northern Evros region can be characterised as harzburgites and minor dunites. Polybaric near-fractional and isobaric batch partial melting trends after Barth et al. (2007) suggest melting degrees higher than 15%. This is supported by calculated high melting degrees of 21-24 % from Cr-spinels after Hellebrand et al. (2001). Such high degrees of melting are known from young oceanic island arcs (Pearce & Parkinson, 1993). The harzburgites are strongly depleted in Al_2O_3, TiO_2, CaO and Y compared to PUM. They also characterized by enriched LILE forming a “hump” and depletion in HFSE forming a “trough”. The dish-shaped REE pattern can be explained by the addition of percolation melts (e.g. OIB) to a depleted harzburgite. Two harzburgites show enrichments in LREE what is

also seen in the REE pattern. That point to a process that led to the addition of a REE-bearing component. In their REE and multi-element pattern the harzburgites of the Evros area strongly resemble harzburgites and dunites of recent oceanic island arcs (e.g. Bismarck (Tabar-Lihir-Tanga-Feni) Arc, Kurile Arc).

The spinels of the harzburgites are Fe- and Cr-rich with Mg# of 0.02 – 0.32 and Cr# ranging from 0.75 – 0.99. The calculated melting degree (after Hellebrand et al., 2001) ranges from 21 – 24%.

The initial Nd value of the Dadia harzburgite is +2.8 with high initial Sr ratio of 0.7060. The harzburgite of Smigada is characterised by a higher εNd_{169} (+4.8) but with very high initial Sr ratio of 0.7094 what might be caused either by percolating melts (e.g. OIB) or by serpentinisation of the rock.

In summary the harzburgites and dunite within the Rhodope Massif can be described as being residues after high degrees of melt extraction derived in an island arc setting.

9. Conclusion

9.1. The mafic complex of the Evros area (Evros ophiolite)

The volcanic rocks and gabbros of the Evros region were formed by melting a depleted mantle source in an oceanic island arc setting. This setting explains the strong depletions in HFSE, the enrichment in LILE and the selective enrichments in LREE. The results of fieldwork and geochemical analyses converge towards the following scenario that represents a plausible solution.

Concerning the evolution of a supra-subduction zone ophiolite Shervais (2001) described five stages: (1) Birth, (2) Youth, (3) Maturity, (4) Death, and (5) Resurrection. The first three stages describe the development of the oceanic island arc what is represented by the Evros ophiolite and will be explained in the following.

(1) The birth of the island arc is characterised by inflow of MORB source asthenosphere and only slight contributions from the subducted slab. The generated melts are similar to MORB with depletion in LREE but also with HFSE depletion, slight LILE enrichment, especially in Th, and low Ti (Shervais, 2001). Sample E17 (Group I) best represents the volcanic rocks of this earliest stage of island arc formation.

(2) The youth stage of the island arc is marked by melting the previously molten asthenosphere by increasing flux of fluids and melts from the subducted slab. This results in primitive melts like boninites, high-Mg andesites and island arc tholeiites (Shervais, 2001; Hawkins, 2003) which are strongly depleted in HFSE and show enrichment in LILE and LREE added by melts and fluids from the subducted slab (e.g. Hawkins, 2003; Pearce et al., 2005). The plutonic rocks of that stage intrude the older plutons from stage 1. This stage of island arc formation is best represented by the boninites and the depleted gabbros of Group I generated within a forearc setting and the island arc tholeiites of Group I originated within the ocean island arc.

(3) If the subduction zone is stable and the rate of crustal spreading slows, then the stage of maturity of an island arc is reached. The melts tend to be more silica rich and they are more enriched in LILE but still with depletion in HFSE pointing to a depleted mantle source underneath. The volcanic rocks consist of basaltic andesites to rhyolites with calc-alkaline or transitional to calc-alkaline character (Shervais, 2001). The Evros calc-alkaline volcanic rocks of Group II as well as the Group II gabbros best represent this stage of island arc development. Since maturity stage (3) is developed in the Evros ophiolite inferences can be made about the size of the subducted ocean basin. In order to preserve the stage of maturity, the ocean basin being subducted must be large enough to complete the first two stages without disappearing, but not so large that the ophiolite evolves into the basement of a long-lived arc complex.

(4) and (5) the stage of death is reached when the magmatic activity stopped. Resurrection is the emplacement of the ophiolite onto a passive continental margin or is otherwise uplifted or exposed. Both stages can be simultaneously but also with a time gap of several million years (Shervais, 2001).

A possible scenario for the genesis of the Evros ophiolitic rocks in the context of the Tethyan realm is described in the following. In Mid-Jurassic time, prior to the extensional collapse of the Hellenic Hinterland and exhumation of the Rhodope Core Complex, an intra-oceanic subduction zone developed due to the subduction of the Vardar Ocean towards north in front of the Thracia terrane. With proceeding subduction an intra-oceanic island arc formed during late Middle Jurassic (see Fig. 3-27) starting with the formation of volcanic rocks represented by sample E17 (Group I) and proceeding with boninites (e.g. E48) and Group I gabbros in the forearc and the island arc tholeiites of Group I in the arc. When reaching maturity the island arc produced calc-alkaline volcanic rocks and gabbros, both of Group II.

The northwards movement of the African plate caused closure of the ocean basin what resulted in the obduction of the Evros ophiolite onto the passive margin of the Thracia terrane (Fig. 3-27).

9.2. The mantle peridotites of the Rhodope Massif

The peridotites of the Rhodope Massif represent mainly harzburgites and minor dunites, which report high degrees of melting (>15%). The strong geochemical similarity to harzburgites from oceanic island arcs indicates a comparable setting for the peridotites of the Evros region. Further arguments for this setting are the composition of the Cr-spinels (low Mg#, high Cr#), the depletion in HFSE, the enrichment in LILE and the selective enrichment of LREE caused by addition of fluids and melts from the subducted slab and percolating melts.

Both, the mafic complex of the Evros area as well as the peridotites of the Rhodope Massif show geochemical, isotopic and mineral chemical evidence for a genesis in an oceanic island arc setting. Therefore, they could have generated within the same arc and belong to one ophiolite as indicated by Ricou et al. (1998). The problem is the stratigraphic separation of these rocks. The peridotites are part of the Rhodope Massif (Liati et al., 2002; Mposkos & Krohe, 2006) and are stratigraphically located between the Rhodope and the Thracia terrane. The Evros ophiolite is situated between the Makri and Drymos-Melia Units, which unconformably overlie the Rhodope Massif. Moreover, the presence of a suture zone within the Rhodope Massif (Rodope Ocean of Van Hinsbergen, 2005; Nestos Suture of Reischmann & Kostopoulos, 2007) as well as the absence of clear evidence for the connection of the peridotites and the Evros ophiolite (e.g. ages of the peridotites) lead to a treatment as separate units. Nevertheless, the question about the relationship of both, the Evros ophiolite and the peridotites, still remains open. Further investigations are necessary to shed light on the genesis of the peridotites within the Rhodope Massif in the northern Evros area. In the following the most probable scenario of a Rhodope island arc origin for the peridotites is described.

Reischmann & Kostopoulos (2007) divided the Rhodope Massif into two different terranes, the Rhodope terrane (Upper high-grade basement unit of Bonev & Stampfli, 2007; Kimi Complex of Mposkos & Krohe, 2006) and the Thracia terrane (Lower high-grade

basement unit of Bonev & Stampfli, 2007; Kechros Complex of Mposkos & Krohe, 2006), which were separated by an ocean in Late Triassic – Early Jurassic times (Rodope ocean of Van Hinsbergen, 2005; Nestos Suture of Reischmann & Kostopoulos, 2007; Fig. 3-27A). During subduction of the Nestos Ocean beneath the Rhodope terrane during Late Jurassic times island arc magmas were formed leaving behind depleted rocks of the mantle wedge (harzburgites and dunites; Fig. 3-27B). The collision of the two terranes in Late Jurassic – Early Cretaceous (Van Hinsbergen, 2005) resulted in thrusting of the Rhodope terrane onto the Thracia terrane whereas the harzburgites and dunites were squeezed between the two terranes now cropping out on top of the Thracia terrane of the Rhodope Massif (Fig. 3-27C).

The ages of the Rhodope Massif terranes were detected by several members and colleagues of the DFG research training group, Mainz. Geochronological analyses yielded late Middle Jurassic – Early Cretaceous ages (Central Rhodope Massif: 134 – 163 Ma, Turpaud, 2006; Eastern Rhodope Massif: 145 Ma, Cornelius et al., 2007; Western Rhodope Massif: 164 Ma [unpubl. SHRIMP age], pers. comm. D. Kostopoulos) for the Rhodope terrane and ages of Latest Carboniferous to Early Permian (Central Rhodope Massif: 270 – 291 Ma, Turpaud, 2006; Eastern Rhodope Massif: 275 – 290 Ma, Cornelius et al., 2007) for the Thracia terrane.

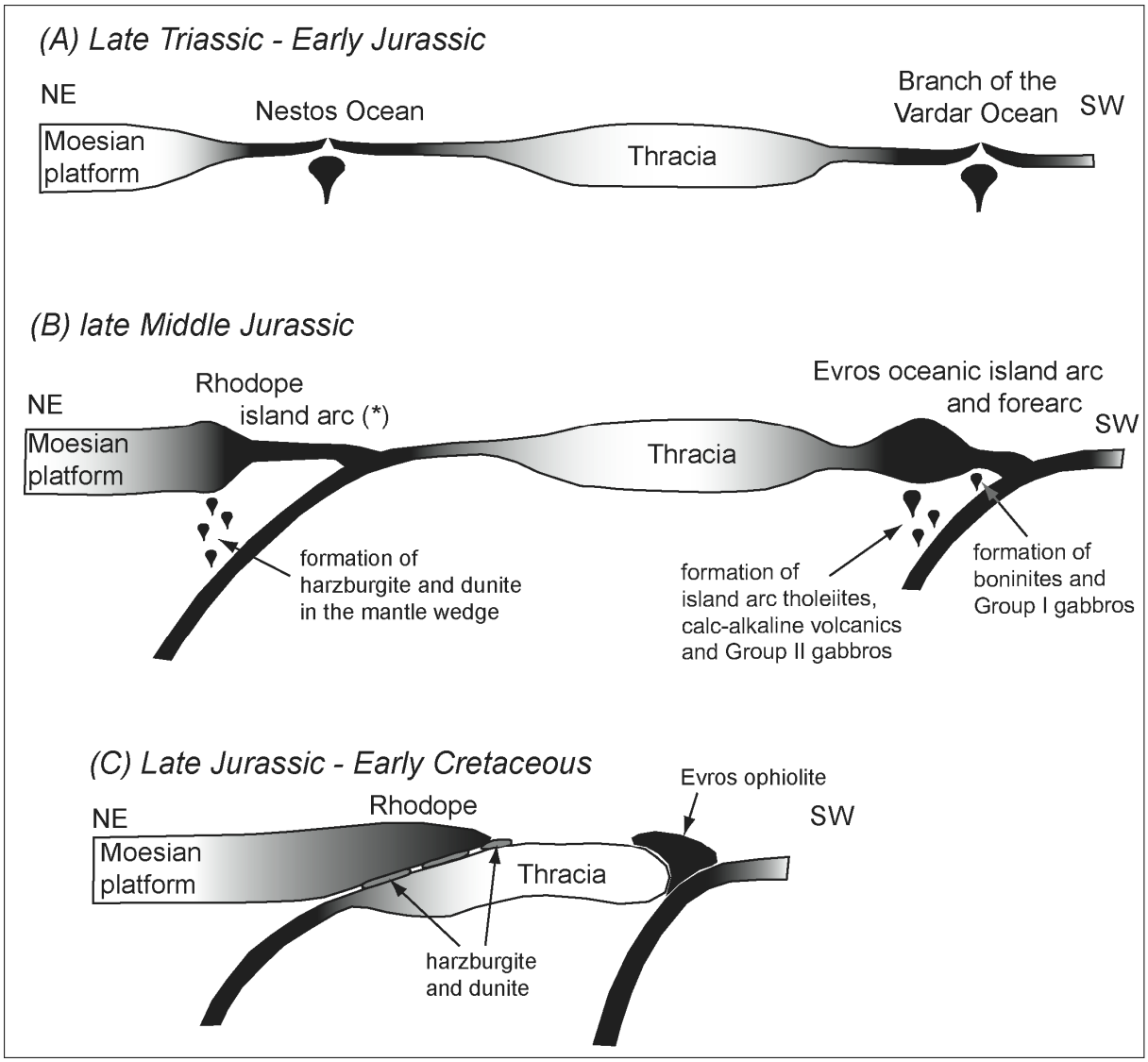

Fig. 3-27: Interpretative model for the evolution of the Evros ophiolite and the peridotites (modified after Turpaud, 2006 and Reischmann & Kostopoulos, 2007; orientations are indicative).

(A) Late Triassic – Early Jurassic: Spreading of the Nestos Ocean and Vardar ocean system.

(B) Late Middle Jurassic: Subduction of the Nestos Ocean beneath the Moesian platform and formation of the Rhodope island arc. Harzburgites and dunites originated in the mantle wedge. Further south: subduction of a branch of the Vardar Ocean beneath the Thracia terrane results in the formation of the Evros island arc. (*) Late Middle Jurassic – Early Cretaceous ages (134 – 164 Ma) of the Rhodope terrane have been verified by several authors (see text for details).

(C) Late Jurassic – Early Cretaceous: Thrusting of the Rhodope terrane over the Thracia terrane creating the Rhodope Massif and dragging of the harzburgites and dunites between the two terranes. Obduction of the Evros ophiolite onto the southern margin of the Rhodope Massif.

Synthesis

The following section highlights the most important results on the petrogenesis and geotectonic setting of the ophiolites and mafic and ultramafic complexes of NE Greece in combination with paleogeographic reconstructions.

The Lesvos Island mafic-ultramafic complex:

This complex consists of thrust sheets of mantle peridotite overriding a tectonic mélange containing metasediments, metabasalts and a few metagabbros. However, the complete absence of a sheeted dyke complex and of a layered cumulate sequence does not support an ophiolite origin.

The basalts of the mélange define a N-MORB type group (Vatera) and a WPB-type group (Mélange) representing rift-related magmas, which is also indicated by low degrees of melting (~10% for Vatera basalts; <5% for Mélange basalt) of spinel (and occasionally garnet) lherzolite that carried small amounts (~3%) of different enriched components (OIB, sediment melt).

The peridotites comprise both spinel lherzolites and harzburgites and can be defined as alpine-type and continental peridotites. The lherzolites have experienced low degrees of melting in the stability field of spinel but also of garnet. The harzburgites also display evidence of melting in the stability field of spinel, but furthermore, they have been contaminated by a percolating component like OIB or sediment melts.

The crystallization of the gabbros took place in Upper Permian (253 ± 6 Ma) with new occasional growth of zircon rims at 236 ± 8 Ma (Middle Triassic) coeval to the widespread rift-related intrusion of A-type granites in the eastern Mediterranean. Gabbro zircon ages of 777, 539 and 338 Ma strongly suggest inheritance from the intruded basement and correspond to ages of distinct terranes recently recognized in the Hellenides (e.g. Florina terrane; Anders et al., 2006).

The paleogeographic location of Lesvos during Permo-Triassic and Late Triassic times (250 – 240 Ma) is within the Meliata-Maliac rift at the northern margin of the Pelagonian basement. With proceeding subduction of the Maliac Ocean in Late Jurassic (155 Ma; Hatzipanagiotou & Pe-Piper 1995) the basalts were obducted together with slivers of lherzolite and harzburgite.

The Lesvos mafic and ultramafic complex best represents an incipient continental rift setting that led to the subsequent formation of the Meliata-Maliac-Vardar branches of Neotethys. Therefore, the term “Lesvos ophiolite” should be abandoned.

The Samothraki ophiolite:

This ophiolite is an ‘in situ’ mafic suite comprising gabbros, sparse dykes and basalt flows as well as pillows cut by late dolerite dykes. The age of the complex has been dated in this study to be 160 ± 5 Ma (i.e. Oxfordian; early Upper Jurassic), which precludes any correlation with the so-called Lesvos ophiolite further south (253 ± 6 Ma; Uppermost Permian; this study).

Six geochemical groups have been identified among the basalts and dolerites of the Samothraki ophiolite on the basis of trace-element and Nd-Sr isotopic characteristics. All groups display the presence of an enriched component in their source region, either a long-term enriched mantle reservoir or an enriched melt. They also invariably show evidence of the addition of subduction-related hydrous fluids. Some groups testify to recent depletion events of long-term enriched mantle, some to the involvement of strongly depleted, recently refertilised mantle, whereas others to significant addition of melts either from subducted sediments or continental crust.

In view of recent advances in back-arc basin geology and the data collected here, the Samothraki ophiolite could represent a slab-edge segment of an evolved back-arc basin near the trench, a situation that satisfies the inflow of fertile mantle, the strong signature of sediment melts and the rare occurrence of boninite-like melts. Alternatively, it could represent the embryonic stages of back-arc basin formation either by a propagating rift tip into continental crust or by oblique subduction causing back-arc rifting of continental crust and creation of nascent transtensional basins.

Restoration of block configuration in NE Greece before extensional collapse of the Hellenic hinterland and exhumation of the Rhodope Metamorphic Core Complex (mid-Eocene to mid-Miocene), results in a continuous ophiolite belt from Guevgueli to Samothraki, thus assigning the latter to the Innermost Hellenic Ophiolite Belt. The proposition of the results is an origin of the Samothraki ophiolite via rift propagation of the Sithonia ophiolite spreading ridge into the Chortiatis calc-alkaline arc (and its basement), which was partly assimilated.

The ophiolitic rocks of the Evros area:

The ophiolite of the Evros area contains a plutonic sequence consisting of cumulate and non-cumulate gabbros with plagiogranite veins, and an extrusive sequence of basalt dykes, massive and pillow lavas as well as pyroclastic rocks. Furthermore, in the Rhodope Massif harzburgites and dunites can be found as tectonic lenses. All rocks are spatially separated and have tectonic contacts to the neighbouring rock units.

The volcanic rocks can be divided into two groups: one group (Group I) containing boninites and island arc tholeiites and a second group (Group II), which is made up of calc-alkaline volcanic rocks. The geochemical and isotopic features of these groups indicate melting of a depleted mantle source above a subduction zone. These rocks show geochemical similarities to volcanic rocks of recent oceanic island arcs (e.g. Tonga arc, Mariana arc). The gabbros define two groups as well, a geochemically depleted Group I, which represents the plutonic counterpart of the boninites of Group I volcanic rocks, an a second group (Group II), which is less depleted than Group I gabbros. The depletion in HFSE and enriched LILE relative to SWIR gabbro is an indication for a less depleted mantle and addition of subduction zone fluids for Group II. The Evros ophiolitic rocks have been formed in different successive stages of island arc formation in late Middle Jurassic times (169 ± 2 Ma) above the northwards directed intra-oceanic subduction zone of the Vardar Ocean (Ricou et al., 1998; Van Hinsbergen, 2005) in front of the Thracia terrane. The obduction of the Evros ophiolite onto the Rhodope basement margin took place during closure of the Vardar ocean basins.

The harzburgites and dunites of the northern Evros area are geochemically strongly depleted compared to PUM and DMM indicating high degrees of melt extraction (>15%) and, therefore, are similar to harzburgites from recent oceanic island arcs (e.g. Bismarck (Tabar-Lihir-Tanga-Feni) Arc). This is also supported by the low Mg# and high Cr# of Cr-spinels as well as the compositions of the clinopyroxenes. The slight enrichment in LILE and in some LREE points to addition of percolating melts and fluids from the subducted slab. Since the peridotites have generated in an oceanic island arc setting similar to the Evros ophiolite, their root could be located within the same ocean (Vardar Ocean; Ricou et al., 1998) but the stratigraphic separation of the peridotites and the ophiolitic rocks (see also Section 2 and 9.2) indicate a separate generation for the peridotites within the Nestos Suture, which is part of the Rhodope Massif (Van Hinsbergen; Reischmann & Kostopoulos, 2007). This relationship between the Evros ophiolite and the peridotites remains questionable. Therefore, further investigations are necessary to shed light on the origin of the peridotites. The present study indicates that the harzburgites and dunites within the Rhodope Massif most probably

represent remnants of the mantle wedge beneath the island arc of the Rhodope terrane and thus might have formed above the northwards directed subducted slab (Van Hinsbergen, 2005; Turpaud, 2006) of the Nestos Ocean. The collision of the Thracia terrane with the Rhodope terrane and the thrusting of the Rhodope terrane took place while the harzburgites and dunites were pushed between the two terranes now cropping out on top of the Thracia terrane within the Rhodope Massif.

Paleogeographic implications: Due to the opening of the Neotethyan Ocean in the south and movement of the Cimmerian blocks towards the north, the closure of the Paleotethys took place with a northwards directed subduction zone during the Latest Permian – Early Triassic (~ 250 Ma). At the same time rifting of the Meliata-Maliac ocean system started north of the Paleotethyan subduction zone due to slab rollback, which gave birth to the Lesvos mafic-ultramafic rift complex at the northern margin of Pelagonia (Fig. 2A). Further east the closure of the Paleotethys gave birth to the Karakaya accretionary complex (NW Turkey). With continuous spreading of the Meliata and Maliac oceans also a rift opened between the Moesian platform, Thracia terrane and the Serbomacedonian Massif, forming the Nestos Ocean (Fig. 2B). During this time the Thracia terrane and the Serbomacedonian Massif were separated by a basin called Athos-Volvi Zone (Himmerkus et al., 2005). The northwards movement of the African plate caused compression and resulted in the formation of a northwards directed subduction zone in Middle Jurassic times (180 Ma) in the northern part of the Maliac-Vardar ocean system (Fig. 2C and D). Slightly later (Fig. 2E) another subduction zone developed north of the Nestos Ocean. Due to subduction of the Maliac-Vardar ocean system the Paikon Arc formed southwest of the Thracia terrane. In Middle Jurassic times (~170 Ma) magma production in the subduction zones built up the Rhodope and Evros island arcs (Fig. 2E). Within the area between the Paikon Arc in the SW and the Thracia terrane in the NE (Paionias Sea; Zachariadis, 2007) the ophiolites of the eastern Vardar Zone (Guevgueli, Oraeokastro, Thessaloniki-Metamorphosis, Kassandra-Sithonia) generated at the same time and continued until 155 Ma. In Late Jurassic times (160 – 155 Ma; Fig. 2F) the Kassandra back-arc basin started to subduct beneath the Thracia terrane forming the Chortiatis Arc. One section of the spreading ridge within the Kassandra backarc basin proceeded in spreading (Sithonia ophiolite spreading ridge). The formation of the Samothraki ophiolite then resulted in rift propagation of the Sithonia spreading ridge into the Chortiatis Arc. During that time thrusting of the Rhodope terrane onto the Thracia terrane already started to form the Rhodope Massif.

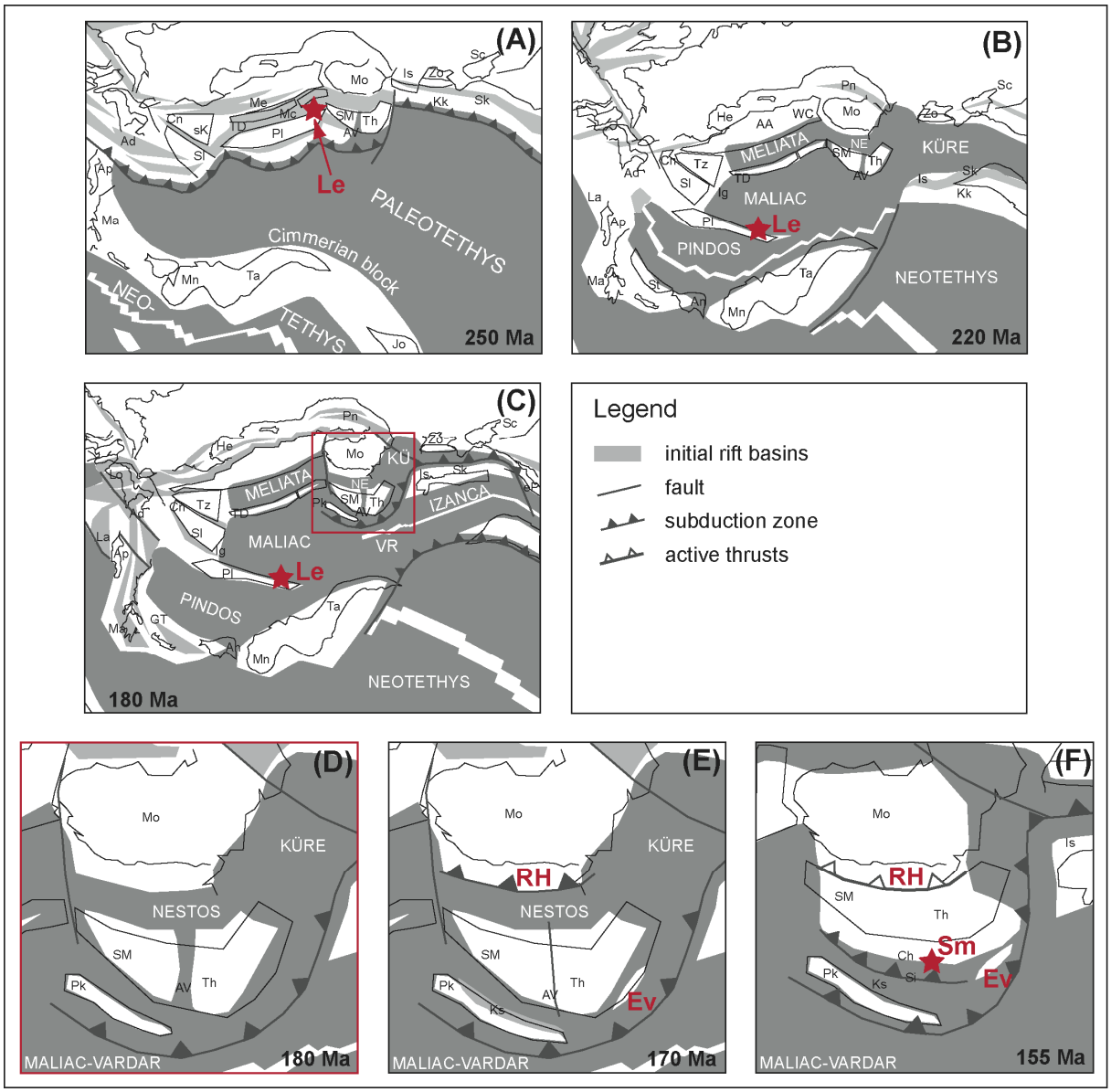

Fig. 2: Paleogeographic reconstructions of the Mediterranean area (modified after Stampfli & Borel, 2002). See text for discussion.

AA, Austro-Alpin; Ad, Adria; An, Antalya Alakir Cay; Ap, Apulia; AV, Athos-Volvi Zone; Ch, Chortiatis Arc; Cn, Carnic-Julian; eP, east Pontides; Ev, Evros island arc and rift; GT, Gavrovo-Tripolitza; He, Helvetic rim basin; Ig, Igal trough; Is, Istanbul; Jo, Jolfa; Kk, Karakaya complex; Ks, Kassandra rift basin; La, Lagonegro; Le, Lesvos rift; Lo, Lombardian; Ma, Mani; Mc, Maliac rift and ocean; Me, Meliata rift and ocean; Mn, Menderes; Mo, Moesia; NE, Nestos ocean; Pk, Paikon Arc; Pl, Pelagonian; Pn, Pienniny rift; RH, Rhodope island arc and terrane; Sc, Scythian platform; Si, Sithonia spreading ridge; Sk, Sakarya; sK, south-Karawanken fore arc; Sl, Slavonia; SM, Serbo-Macedonian; Sm, Samothraki ophiolite; St, Sitia-E-Crete; Ta, Taurus; TD, Transdanubian; Th, Thracia terrane; Tz, Tizia; VR, Vardar ocean; WC, West-Carpathian; Zo, Zonguldak.

References

Allègre, C.J., Poirier, J.-P., Humler, E., Hofmann, A.W., 1995. The chemical composition of the Earth. Earth and Planetary Science Letters 134, 515 – 526.

Anders, B., Reischmann, T., Kostopoulos, D., Poller, U., 2006. The oldest rocks of Greece: first evidence for a Precambrian terrane within the Pelagonian Zone. Geological Magazine 143, 1, 41 – 58.

Anders, B., Reischmann, T., Poller, U., Kostopoulos, D., 2005 . Age and origin of granitic rocks of the eastern Vardar Zone, Greece: new constraints on the evolution of the Internal Hellenides. Journal of the Geological Society 162, 857 – 870.

Anonymous, 1972. Penrose field conference on ophiolites. Geotimes 17, 24-25.

Ballhaus, C.G., Berry, R.F., Green, D.H., 1990. Oxygen fugacity controls in the Earth's upper mantle. Nature 348, 437 – 440.

Ballhaus, C.G., Berry, R.F., Green, D.H., 1991. High pressure experimental calibration of the olivine-orthopyroxene-spinel oxygen geobarometer; implications for the oxidation state of the upper mantle. Contribution to Mineralogy and Petrology 107, 1, 27 – 40.

Barr, S.R., Temperley, S., Tarney, J., 1999. Lateral growth of the continental crust through deep level subduction-accretion: a re-evaluation of central Greek Rhodope. Lithos 46, 69 – 94.

Barry, T.L., Pearce, J.A., Leat, P.T., Millar, I.L., Le Roex, A.P., 2006. Hf isotope evidence for selective mobility of high-field strength elements in a subduction setting: South Sandwich Islands. Earth and Planetary Science Letters 252, 223 – 244.

Barth, M.G., Mason, P.R.D., Davies, G.R., Drury, M.R., 2007. The Othris Ophiolite, Greece: A snapshot of subduction initiation at a mid-ocean ridge. Lithos, doi: 10.1016/j.lithos.2007.06.018.

Bébien, J., Dubois, R., Gauthier, A., 1986. Example of ensialic ophiolites emplaced in a wrench zone: Innermost Hellenic ophiolite belt (Greek Macedonia). Geology 14, 1016 – 1019.

Beccaletto, L., Jenny, C., 2004. Geology and Correlation of the Enzine Zone: A Rhodope Fragment in NW Turkey? Turkish Journal of Earth Sciences 13, 145 – 176.

Ben Othman, D., White, W.M., Patchett, J., 1989. The geochemistry of marine sediments, island arc magma genesis, and crust-mantle recycling. Earth and Planetary Science Letters 94, 1 – 21.

Bertrand, P., Mercier, J.C.C., 1985. The mutual solubility of coexisting ortho- and clinopyroxene; toward an absolute geothermometer for the natural system? Earth and Planetary Science Letters 76, 109 – 122.

Biggazzi, G., Del Moro, A., Innocenti, F., Kyriakopoulos, K., Manetti, P., Papadopoulos, P., Norelli, P., Magganas, A., 1989. The magmatic intrusive complex of Petrota, West Thrace: age and geodynamic significance. Geologica Rhodopica 1, 290– 297.

Black, L.P., Kamo, S.L., Allen, C.M., Aleinikoff, J.N., Davis, D.W., Korsch, R.J., Foudoulis, C., 2003. Temora 1: a new zircon standard for Phanerozoic U-Pb geochronology. Chemical Geology 200, 155 – 170.

Bonev, N., Stampfli, G., 2003. New structural and petrologic data on Mesozoic schists in the Rhodope (Bulgaria): geodynamic implications. C. R. Geoscience 335, 691 – 699.

Bonev, N., Stampfli, G., 2007. Petrology, geochemistry and geodynamic implications of Jurassic island arc magmatism as revealed by mafic volcanic rocks in the Mesozoic low-grade sequence, eastern Rhodope, Bulgaria. Lithos, doi: 10.1016/j.lithos.2007.06.019.

Brongniart, A., 1827. Classification et caractères mineralogiques des roches homogènes et hétérogènes. Levrault, Paris, 144 pp.

Brun, J.-P., Sokoutis, D., 2004. North Aegean extension: from the Rhodope core complex to Neogene basins. In: Proceedings of the 5th International Symposium on Eastern Mediterranean Geology, Thessaloniki, Greece, 1, 49 – 52.

Brun, J.-P., Sokoutis, D., 2007. Kinematics of the Southern Rhodope Core Complex (North Greece). International Journal of Earth Sciences (Geologische Rundschau) 96, 1079 – 1099.

Burke, W.H., Denison, R.E., Hetherington, E.A., Koepnick, R.B., Nelson, H.F., Otto, J.B., 1982. Variation of seawater $^{87}Sr/^{86}Sr$ throughout Phanerozoic time. Geology 10, 516 – 519.

Cakir, Ü., Genc, Y., Paktunc, D., 2006. Intrusive lherzolites within the basalts of Küre ophiolite (Turkey): an occurrence in the Tethyan suprasubduction marginal basin. Geological Journal 41, 123 – 143.

Cameron, W.E., 1985. Petrology and origin of primitive lavas from the Troodos ophiolite, Cyprus. Contributions to Mineralogy and Petrology 89, 239 – 255.

Celik, Ö.F., Delaloye, M.F., 2003. Origin of metamorphic soles and their post-kinematic mafic dyke swarms in the Antalya and Lycian ophiolites, SW Turkey. Geological Journal 38, 235 – 256.

Christofides, G., Eleftheriadis, G., Esson, J., Soldatos, T., Koroneos, A., Bröcker, M., 2000. The evolution of the Samothraki granitic pluton (N. Aegean sea, Greece): geochronology, chemical and isotopic constraints for AFC modelling. In: Proceedings of the Third International Conference of the Geology of the Eastern Mediterranean, Panayides, I., Xenophontos, C., Malpas, J. (eds.), 193 – 209.

Cole, J.W., Gamble, J.A., Burt, D.M., Carroll, L.D., Shelley, D., 2001. Mixing and mingling in the evolution of andesite-dacite magmas: evidence from co-magmatic plutonic enclaves, Taupo Volcanic Zone, New Zealand. Lithos 59, 25 – 46.

Collins, A.S., Robertson, A.H.F., 1999. Evolution of the Lycian Allochthon, western Turkey, as a north-facing Late Paleozoic to Mesozoic rift and passive continental margin. Geological Journal 34, 107 – 138.

Conceicao, R.V., Mallmann, G., Koester, E., Schilling, M., Bertotto, G.W., Rodriguez-Vargas, A., 2005. Andean subduction-related mantle xenoliths: Isotopic evidence of Sr-Nd decoupling during metasomatism. Lithos 82, 273 – 287.

Cornelius, N.K., Reischmann, T., Frei, D., Kostopoulos, D., 2007. Geochronology, geochemistry and isotopes of orthogneisses from the Greek Rhodope. Goldschmidt Conference Abstracts 2007, A190.

Dannat, C., Reischmann, T., 1997. A geochemical, isotopic and geochronological study of granitoid gneisses of the Menderes Massif, SW Turkey. Terra Nova, 9, 404.

Dannat, C., Reischmann, T., 1998. Geochronological, geochemical and isotopic data on granitic gneisses from of the Menderes Massif, SW Turkey. Third International Turkish Geology Symposium, Middle East Technical University, Ankara, Conference Abstracts, 282.

De Bono, A., 1998. Pelagonian Margins in Central Evia Island (Greece). Stratigraphy and Geodynamic Evolution. PhD, Université de Lausanne, 134 pp.

Debari, S.M., Mahlburg Kay, K.S., Kay, R.W., 1987. Ultramafic xenoliths from Adagdak Volcano, Adak, Aleutian Islands, Alaska: Deformed igneous cumulates from the MOHO of an island arc. Journal of Geology 95. 329 – 341.

Dick, H.J.B., Bullen, T., 1984. Chromian spinel as a petrogenetic indicator in abyssal and alpine-type peridotites and spatial associated lavas. Contributions to Mineralogy and Petrology 86, 54 – 76.

Donnelly K.E., Goldstein, S.L., Langmuir, C.H., Spiegelman, M., 2004. Origin of enriched ocean ridge basalts and implications for mantle dynamics. Earth and Planetary Science Letters 226, 347 – 366.

Dorendorf, F., Wiechert, U., Wörner, G., 2000. Hydrated sub-arc mantle: a source for the Kluchevskoy volcano, Kamchatka/Russia. Earth and Planetary Science Letters 175, 69 – 86.

Eleftheriadis, G., Pe-Piper, G., Christofides, G., Soldatos, T., Esson, J., 1994. K-Ar dating of the Samothraki volcanic rocks, Thrace, northeastern Aegean (Greece). Bulletin of the Geological Society of Greece 30, 205 – 212.

Esson, J., Christofides, G., Eleftheriadis, G., 1990. Ferromagnesian minerals as indicators of the conditions of evolution of the lavas of Samothraki island (N. Greece). Geologica Rhodopica 2, 263 – 279.

Fallon, T.J., Danyushevsky, L.V., Crawford, T.J., Maas, R., Woodhead, J.D., Eggins, S.M., Bloomer, S.H., Wright, D.J., Zlobin, S.K., Stacey, A.R., 2007. Multiple mantle plume components involved in the petrogenesis of subduction-related lavas from the northern termination of the Tonga Arc and northern Lau Basin: Evidence from the geochemistry of arc and backarc submarine volcanics. Geochemistry, Geophysics, Geosystems 8, Q09003, doi: 10.1029/2007GC001619.

Frass, A., Hegewald, S., Kloos, R.M., Tesch, C., Arikas, K., 1990. The geology of the Graben of Petrota (Thrace, NE Greece). Geologica Rhodopica 2, 50 – 63.

Fretzdorff, S., Livermore, R.A., Devey, C.W., Leat, P.T., Stoffers, P., 2002. Petrogenesis of the back-arc East Scotia Ridge, South Atlantic Ocean. Journal of Petrology 43, 1435 – 1467.

Fretzdorff, S., Schwarz-Schampera, U., Gibson, H.L., Garbe-Schönberg, C.D., Hauff, F., Stoffers, P., 2006. Hydrothermal activity and magma genesis along a propagating back-arc basin: Valu Fa Ridge (southern Lau Basin). Journal of Geophysical Research 111, B08205, doi: 10.1029/2005JB003967.

Gökten, E., Floyd, P.A., 2007. Stratigraphy and geochemistry of pillow basalts within the ophiolitic mélange of the Izmir-Ankara-Erzincan suture zone: implications for the geotectonic character of the northern branch of Neotethys. International Journal of Earth Sciences (Geologische Rundschau) 96, 725 – 741.

Göncüoglu, M.C., Kuwahara, K., Tekin, U.K., Turhan, N., 2004. Upper Permian (Changxingian) Radiolarian Cherts within the Clastic Successions of the "Karakaya Complex" in NW Anatolia. Turkish Journal of Earth Sciences 13, 201 – 213.

Gregoire, D.C., McInnes, B.I.A., O´Reilly, S.Y., 2001. Hydrous metasomatism of oceanic sub-arc mantle, Lihir, Papua New Guinea Part 2. Trace element characteristics of slab-derived fluids. Lithos 59, 91 – 108.

Hafkenscheid, E., Wortel, M.J.R., Spakman, W., 2006. Subduction history of the Tethyan region derived from seismic tomography and tectonic reconstructions. Journal of Geophysical Research, 111, B08401, doi:10.1029/2005JB003791.

Hamilton, W.B., 1995. Subduction systems and magmatism. In: Smellie, J.L. (ed.), Volcanism Associated with Extension at Consuming Plate Margins. Geological Society Special Publication 81, 3 – 28.

Hart, S.R., Blusztajn, J., Dick, H.J.B., Meyer, P.S., Muehlenbachs, K., 1999. The fingerprint of seawater circulation in a 500-meter section of ocean crust gabbros. Geochimica et Cosmochimica Acta 63, 4059 – 4080.

Hatzipanagiotou, K., Pe-Piper, G., 1995. Ophiolitic and sub-ophiolitic metamorphic rocks of the Vatera area, southern Lesbos (Greece): Geochemistry and geochronology. Ofioliti 20, 17 – 29.

Hauff, F., Hoernle, K., van den Bogaard, P., Alvarado, G., Garbe-Schönberg, D., 2000. Age and geochemistry of basaltic complexes in western Costa Rica: Contributions to the geotectonic evolution of Central America. Geochemistry, Geophysics, Geosystems 1, doi: 1999GC000020.

Hawkesworth, C.J., Hergt, J.M., McDermott, F., Ellam, R.M., 1991. Destructive margin magmatism and the contributions from the mantle wedge and subducted crust. Australian Journal of Earth Sciences 38, 577 – 594.

Hawkesworth, C.J., Gallagher, K., Hergt, J.M., McDermott, F., 1993. Mantle and Slab Contributions in Arc Magmas. Annual Reviews of the Earth and Planetary Sciences 21, 175 – 204.

Hawkins, J.W., 2003. Geology of supra-subduction zones – Implications for the origin of ophiolites. In: Ophiolite concept and the evolution of geological thought. Dilek, Y., Newcomb, S. (eds.). Geological Society of America Special Paper 373, 227 – 268.

Hecht, J., 1970. Zur Geologie von Südost-Lesbos (Griechenland). PhD thesis, University of Munich, 64 S.

Hecht, J., 1972. Geological map of Greece, 1:50.000, Lesbos Island - Plomari/Mytilene.

Hecht, J., 1972. Zur Geologie von Südost-Lesbos (Griechenland). Zeitschrift der Deutschen Geologischen Gesellschaft 123, 423-432.

Hecht, J., 1974. Geological map of Greece, 1:50.000, Lesbos Island - Polychnitos.

Heimann, K., Lebküchner, H., Kretzler, W., 1972. Geological Map of Greece, 1:50.000, Samothraki sheet.

Hellebrand, E., Snow, J.E., Dick, H.J.B., Hofmann, A.W., 2001. Coupled major and trace elements as indicators of the extend of melting in mid-ocean-ridge peridotites. Nature 410, 677 – 681.

Hémond, C., Hofmann, A.W., Vlastélic, I., Nauret, F., 2006. Origin of MORB enrichment and relative trace element compatibilities along the Mid-Atlantic Ridge between 10° and 24°N. Geochemistry, Geophysics, Geosystems 7, Q12010, doi:10.1029/ 2006GC001317.

Hergt, J.M., Woodhead, J.D., 2007. A critical evaluation of recent models for Lau-Tonga arc-backarc basin magmatic evolution. Chemical Geology 245, 9 – 44.

Himmerkus, F., Reischmann, T., Kostopoulos, D.K., 2004. Triassic rifting recorded in Gondwana derived Tethyan terranes, Serbo-Macedonian Massif, northern Greece. Berichte der Deutschen Mineralogischen Gesellschaft, Beihefte zum European Journal of Mineralogy 16, 57.

Himmerkus, F., Zachariadis, P., Reischmann, T., Kostopoulos, D., 2005. The mafic complexes of the Athos-Volvi-Zone – a suture zone between the Serbo-Macedonian Massif and the Rhodope Massif? Geophysical Research Abstracts, Vol. 7, 10240.

Hochstaedter, A.G., Gill, J.B., Peters, R., Broughton, P., Holden, P., 2001. Across arc geochemical trends in the Izu-Bonin Arc: contributions from the subducting slab. Geochemistry, Geophysics, Geosystems 2, 2000GC000105.

Hofmann, A.W., 1988. Chemical differentiation of the Earth: the relationship between mantle, continental crust and oceanic crust. Earth and Planetary Science Letters 90, 297-314.

Holland, T., Blundy, J., 1994. Non-ideal interactions in calcite amphiboles and their bearing on amphibole-plagioclase thermometry. Contributions to Mineralogy and Petrology 116, 433 – 447.

Hutchinson, C.S., 1975. The norm, its variations, their calculation and relationships. Bulletin Suisse de Mineralogie et Petrographie 55, 243 – 256.

IGME, 1983. Geological Map of Greece, scale 1:500.000, Institute of Geology and Mineral Exploration, Athens.

Ishimaru, S., Arai, S., Ishida, Y., Shirasaka, M., Okrugin, V.M., 2007. Melting and Multi-stage Metasomatism in the Mantle Wedge beneath a Frontal Arc Inferred from Highly Depleted Peridotite Xenoliths from the AvachaVolcano, Southern Kamchatka. Journal of Petrology 48, 395 – 433.

Jacobshagen, V., 1986. Geologie von Griechenland. In: Beiträge zur regionalen Geologie der Erde. Borntraeger, Berlin, 363 pp.

Kamenetsky, V.S., Crawford, A.J., Meffre, S., 2001. Factors controlling chemistry of magmatic spinel: an empirical study of associated olivine, Cr-spinel and melt inclusions from primitive rocks. Journal of Petrology 42, 655 – 671.

Katsikatsos, G., Migiros, G., Triantaphyllis, M., Mettos, A., 1986. Geological structure of internal Hellenides (E. Thessaly – SW. Macedonia, Euboea – Attica – Northern Cyclades islands and Lesvos). Geological and Geophysical Research, Special issue, 191 – 212.

Katzir, Y., Avigad, D., Matthews, A., Garfunkel, Z., Evans, B.W., 2000. Origin, HP/LT metamorphism and cooling of ophiolitic mélanges in southern Evia (NW Cyclades), Greece. Journal of metamorphic Geology 18, 699 – 718.

Kauffmann, G., Kockel, F., Mollat, H., 1976. Notes on the stratigraphic and paleogeographic position of the Svoula Formation in the innermost zone of the Hellenides (northern Greece). Bulletin de la Société Géologique de France 18, 225 – 230.

Kessel, R., Schmidt, M.W., Ulmer, P., Pettke, T., 2005. Trace element signature of subduction-zone fluids, melts and supercritical liquids at 120-180 km depth. Nature 437, 724 – 727.

Koglin, N., Kostopoulos, D., Reischmann, T.: The Lesvos mafic-ultramafic complex, Greece: ophiolite or incipient rift? Lithos Special Issue: Balkan Ophiolites (submitted).

Koglin, N., Reischmann, T., Kostopoulos, D., Matukov, D., Sergeev, S., 2007. Zircon SHRIMP ages and the origin of ophiolitic rocks from the NE Aegean region, Greece. Geophysical Research Abstracts, Vol. 9, 06848.

Koralay, O.E., Satir, M., Dora, O.Ö., 2001. Geochemical and geochronological evidence for Early Triassic calc-alkaline magmatism in the Menderes Massif, western Turkey. International Journal of Earth Sciences 89, 822 – 835.

Kostopoulos, D.K., 1988. Geochemistry, petrogenesis and tectonic setting of the Pindos ophiolite, NW Greece. PhD Thesis, University of Newcastle-upon-Tyne, U.K., p. 528.

Kostopoulos, D.K., James, S.D., 1992. Parameterization of the melting regime of the shallow upper mantle and the effect of variable lithospheric stretching in mantle modal stratification and trace-element concentrations in magmas. Journal of Petrology 33, 665 – 691.

Kostopoulos, D.K., Murton, B.J., 1992. Origin and distribution of components in boninite genesis: significance of the OIB component. In: Parson, L.M., Murton, B.J., Browning, P. (eds.), Ophiolites and Their Modern Oceanic Analogues, Geological Society Special Publication 60, 133-154.

Kotopouli, C.N., Hatzipanagiotou, K., Tsikouras, B., 1989. Petrographic and geochemical characteristics of the ophiolitic rocks in northern Samothrace, Greece. Geologica Balcanica 19, 61 – 67.

Kozur, H., Kaya, O., Mostler, H., 1996. First evidence of lower to middle Scythian (Dienerian-lower Olenekian) radiolarians from the Karakaya Zone of northwestern Turkey. Geologisch-Palaeontologische Mitteilungen Innsbruck 4, 271 – 285.

Laiolo, M., Cigolini, C., 2006. Mafic and ultramafic xenoliths in San Bartolo lava field: New insights on the ascent and storage of Stromboli magmas. Bulletin of Volcanology 68, 653 – 670.

Lapierre, H., Bosch, D., Narros, A., Mascle, G.H., Tardy, M., Demant, A., 2007. The Mamonia Complex (SW Cyprus) revisited: remnant of Late Triassic intra-oceanic volcanism along the Tethyan southwestern passive margin. Geological Magazine 144, 1 – 19.

Leake, B.E., Woolley, A.R., Arps, C.E.S., Birch, W.D., Gilbert, M.C., Grice, J.D., Hawthorne, F.C., Kato, A., Kisch, H.J., Krivovichev, V.G., Linthout, K., Laird, J., Mandarino, J.A., Maresch, W.V., Nickel, E.H., Rock, N.M.S. Schumacher, J.C., Smith, D.C., Stephenson, N.C.N., Ungaretti, L., Whittaker, E.J.W., Youzhi, G., 1997. Nomenclature of Amphiboles: Report of the Subcommittee on Amphiboles of the International Mineralogical Association, Commission on new Minerals and Mineral Names. The Canadian Mineralogist 35, 219 – 246.

Leat, P.T., Livermore, R.A., Millar, I.L., Pearce, J.A., 2000. Magma Supply in Back-arc Spreading Centre Segment E2, East Scotia Ridge. Journal of Petrology 41, 845-866.

Leat, P.T., Pearce, J.A., Barker, P.F., Millar, I.L., Barry, T.L., Larter, R.D., 2004. Magma genesis and mantle flow at a subducting slab edge: the South Sandwich arc-basin system. Earth and Planetary Science Letters 227, 17-35.

Liati, A., Gebauer, D., Wysoczanski, R., 2002. U–Pb SHRIMP-dating of zircon domains from UHP garnet-rich mafic rocks and late pegmatoids in the Rhodope zone (N Greece): evidence for Early Cretaceous crystallization and Late Cretaceous metamorphism. Chemical Geology 184, 281 – 299.

Lindsley, D.H., 1983. Pyroxene thermometry. American Mineralogist 68, 477 – 493.

Loss, S., Reischmann, T., 1999. The evolution of the southern Menderes Massif in SW Turkey as revealed by zircon dating. Journal of the Geological Society of London 156, 1021 – 1030.

Ludwig, K.R., 2005a. User's manual for Isoplot/Ex 3.22. A Geochronological Toolkit for Microsoft Excel. Berkeley Geochronological Center Special Publication, 71 pp.

Ludwig, K.R., 2005b. SQUID 1.12 User´s Manual. A Geochronological Toolkit for Microsoft Excel. Berkeley Geochronological Center Special Publication, 71 pp.

Lyubetskaya, T., Korenaga, J., 2007. Chemical composition of Earth's primitive mantle and its variance: 1. Method and results. Journal of Geophysical Research, 112, B03211, doi:10.1029/2005JB004223.

Machado, A., Lima, E.F., Chemale Jr., F., Morata, D., Oteiza, O., Almeida, D.P.M., Figueiredo, A.M.G., Alexandre, F.M., Urrutia, J.L., 2005. Chemistry constraints of Mesozoic. Cenozoic calc-alkaline magmatism in the South Shetland arc, Antarctica. Journal of South American Earth Sciences 18, 407 – 425.

Magganas, A., Sideris, C., Kokkinakis, A., 1991. Marginal Basin Volcanic Arc Origin of Metabasic Rocks of the Circum-Rhodope Belt, Thrace, Greece. Mineralogy and Petrology 44, 235 – 252.

Magganas, A.C., 2002. Constraints on the petrogenesis of Evros ophiolite extrusives, NE Greece. Lithos 65, 165 – 182.

Marchesi, C., Garrido, C.J., Godard, M., Proenza, J.A., Gervilla, F., Blanco-Moreno, J., 2006. Petrogenesis of highly depleted peridotites and gabbroic rocks from the Mayarí-Baracoa Ophiolitic Belt (eastern Cuba). Contributions to Mineralogy and Petrology 151, 717 – 736.

McConachy, T.F., Arculus, R.J., Yeats, C.J., Binns, R.A., Barriga, F.J.A.S., McInnes, B.I.A., Sestak, S., Sharpe, R., Rakau, B., Tevi, T., 2005. New hydrothermal activity and alkalic volcanism in the backarc Coriolis Troughs, Vanuatu. Geology 33, 61 – 64.

McDonough, W.F., Sun, S.-s., 1995. The composition of the Earth. Chemical Geology 120, 223 – 253.

McLennan, S.M., 2001. Relationships between the trace element composition of sedimentary rocks and upper continental crust. Geochemistry, Geophysics, Geosystems 2, doi: 2000GC000109.

Moores, E.M., 1969. Petrology and Structure of the Vourinos ophiolitic complex of northern Greece. Special Paper – Geological Society of America 118, 65pp.

Moores, E.M., Vine, F.J., 1971. The Troodos massif, Cyprus and other ophiolites as oceanic crust: evaluation and implications. Philosophical Transactions of the Royal Society of London, Series A: Mathematical and Physical Sciences 268, 443-466.

Moores, E.M., 1982. Origin and emplacement of ophiolites. Reviews of Geophysics and Space Physics 20, 735 – 766.

Morimoto, N., Fabries, J., Ferguson, A.K., Ginzburg, I.V., Ross, M., Seifert, F.A., Zussman, J., Aoki, K., Gottardi, G., 1988. Nomenclature of Pyroxenes. Mineralogy and Petrology 39, 55 – 76.

Mposkos, E., Perdikatsis, V., Iliadis, A., 1994. Petrology of ultramafic rocks in the upper tectonic unit of eastern Rhodopes: contributions to the metamorphic evolution of the Rhodopes zone. Bulletin of the Geological Society of Greece 30, 241 – 254.

Mposkos, E., 1989. High-Pressure Metamorphism in Gneisses and Pelitic Schists in the Eastern Rhodope Zone (N. Greece). Mineralogy and Petrology 41, 25 – 39.

Mposkos, E.D., Kostopoulos, D.K., 2001. Diamond, former coesite and supersilicic garnet in metasedimentary rocks from the Greek Rhodope: A new ultrahigh-pressure metamorphic province established. Earth and Planetary Science Letters, 192, 497 – 506.

Mposkos, E., Krohe, A., 2006. Pressure-temperature-deformation paths of closely associated ultra-high-pressure (diamond-bearing) crustal and mantle rocks of the Kimi complex: implications for the tectonic history of the Rhodope Mountains, northern Greece. Canadian Journal of Earth Sciences 43, 1755 – 1776.

Mukasa, S.B., Blatter, D.L., Andronikov, A.V., 2007. Mantle peridotite xenoliths in andesite lava at El Penon, Central Mexican Volcanic Belt: Isotopic and trace element evidence for melting and metasomatism in the mantle wedge beneath an active arc. Earth and Planetary Science Letters 260, 37 – 55.

Nohara, M., Hirose, K., Eissen, J.P., Urabe, T., Joshima, M., 1994. The North Fiji Basin basalts and their magma sources: Part II. Sr-Nd isotopic and trace element constraints. Marine Geology 116, 179 – 195.

Nye, C.J., Swanson, S.E., Avery, V.F., Miller, T.P., 1994. Geochemistry of the 1989-1990 eruption of Redoubt Volcano: Part I. Whole-rock major- and trace-element chemistry. Journal of Volcanology and Geothermal Research 62, 429 – 452.

O´Neill, H.S.C., Wall, V.J., 1987. The olivine-orthopyroxene-spinel oxygen geobarometer, the nickel precipitation curve, and the oxygen fugacity of the Earth's upper mantle. Journal of Petrology 28, 1169 – 1191.

Okay, A.I., Satir, M., Maluski, H., Siyako, M., Monié, P., Metzger, R., Akyüz, S., 1996. Paleo- and Neo-Tethyan events in northwest Turkey: geological and geochronological

constraints. In: Yin, A., Harrison, M. (eds.), Tectonics of Asia. Cambridge University Press, 420 – 441.

Okay, A.I., Monod, O., Monié, P., 2002. Triassic blueschists and eclogites from northwest Turkey: vestiges of the Paleo-Tethyan subduction. Lithos 64, 155 – 178.

Okay, A.I., Göncüoglu, M.C., 2004. The Karakaya Complex: A Review of Data and Concepts. Turkish Journal of Earth Sciences 13, 77 – 95.

Önen, A.P., 2003. Neotethyan ophiolitic rocks of the Anatolides of NW Turkey and comparison with Tauride ophiolites. Journal of the Geological Society 160, 947 – 962.

Palme, H., O´Neill, H.S.C., 2003. Cosmochemical Estimates of Mantle Composition. Treatise on Geochemistry 2, 1 – 38, doi: 10.1016/B0-08-043751-6/02177-0.

Papadopoulos, P., Anastasiadis, I., 2002. Geological map of Greece, scale 1:200 000, sheet Rhodopi-Thrace. IGME, Xanthi.

Papanikolaou, D., 1986. Late Cretaceous paleogeography of the metamorphic Hellenides. Geological and Geophysical Research, Special issue, 315-328.

Papanikolaou, D., 1999. The Triassic Ophiolites of Lesvos Island within the Cimmeride Orogene Event. In: European Union of Geosciences conference abstracts; EUG 10. Journal of Conference Abstracts 4, 315.

Parkinson, I.J., Pearce, J.A., 1998. Peridotites from the Izu-Bonin-Mariana Forearc (ODP Leg 125): Evidence for mantle melting and melt-mantle interaction in a supra-subduction zone setting. Journal of Petrology 39, 1577 – 1618.

Pearce, J.A., 1975. Basalt geochemistry used to investigate past tectonic environments on Cyprus. Tectonophysics 25, 41-67.

Pearce, J.A., 1980. Geochemical evidence for the genesis and eruptive setting of lavas from Tethyan ophiolites. In: Panayiotou, A. (ed.), Ophiolites, 261-272, Geol. Surv. Dept. Cyprus.

Pearce, J.A., 1982. Trace element characteristics of lavas from destructive plate boundaries. In: Thorpe, R.S. (ed.), Andesites: Orogenic andesites and related rocks, 252-548, John Wiley and Sons.

Pearce, J.A., Lippard, S.J., Roberts, S., 1984. Characteristics and tectonic significance of supra-subduction zone ophiolites. In: Kokelaar, B.P., Howells, M.F. (eds.), Marginal basin geology, Geological Society Special Publications 16, 77-94.

Pearce, J.A., Rogers, N., Tindle, A.J., Watson, J.S., 1986. Geochemistry and petrogenesis of basalts from Deep-Sea Drilling Project Leg 92, Eastern Pacific. Initial Reports DSDP 92, 435-457, doi: 10.2973/dsdp.proc.92.126.1986.

Pearce, J.A., Parkinson, I.J., 1993. Trace element models for mantle melting: application to volcanic arc petrogenesis. In: Magmatic Processes and Plate Tectonics. Prichard, H.M., Alabaster, T., Harris, N.B.W., Neary, C.R. (eds.). Geological Society Special Publication 76, 373 – 403.

Pearce, J.A., Baker, B.E., Harvey, P.K., Luff, I.W., 1995. Geochemical Evidence for Subduction Fluxes, Mantle Melting and Fractional Crystallization Beneath the South Sandwich Island Arc. Journal of Petrology 36, 1073 – 1109.

Pearce, J.A., Ernewein, M., Bloomer, S.H., Parson, L.M., Murton, B.J., Johnson, L.E., 1995. Geochemistry of Lau Basin volcanic rocks: influence of ridge segmentation and arc proximity. Geological Society of London, Special Publication 81, 53 – 75.

Pearce, J.A., Kempton, P.D., Nowell, G.M., Noble, S.R., 1999. Hf-Nd Element and Isotope Perspective on the Nature and Provenance of Mantle and Subduction Components in Western Pacific Arc-Basin Systems. Journal of Petrology 40, 1579 – 1611.

Pearce, J.A., Barker, B.F., Edwards, S.J., Parkinson, I.J., Leat, P.T., 2000. Geochemistry and tectonic significance of peridotites from the South Sandwich arc-basin system, South Atlantic. Contributions to Mineralogy and Petrology 139, 36 - 53.

Pearce, J.A., Stern, R.J., Bloomer, S.H., Fryer, P., 2005. Geochemical mapping of the Mariana arc-basin system: Implications for the nature and distribution of subduction components. Geochemistry, Geophysics, Geosystems 6, Q07006, doi:10.1029/ 2004GC000895.

Pearce, J.A., Stern, R.J., 2006. Origin of back-arc basin magmas: trace element and isotope perspectives. In: Back-arc spreading systems: geological, biological, chemical, and physical interactions. Christie, D.M., Fisher, C.R., Lee, S.M., Givens, S. (eds.). Geophysical Monograph 166, 63 – 86.

Peate, D.W., Pearce, J.A., Hawkesworth, C.J., Colley, H., Edwards, C.M.H., Hirose, K., 1997. Geochemical Variations in Vanuatu Arc Lavas: the Role of Subducted Material and a Variable Mantle Wedge Composition. Journal of Petrology 38, 1331 – 1358.

Pe-Piper, G., 1980. The Cenozoic volcanic sequence of Lesbos, Greece. Zeitschrift der Deutschen Geologischen Gesellschaft 131, 889-901.

Pe-Piper, G., Piper, D.J.W., 1992. Geochemical variation with time in the Cenozoic high-K volcanic rocks of the island of Lesbos, Greece: significance for shoshonite petrogenesis. Journal of Volcanology and Geothermermal Research 53, 371-387.

Pe-Piper, G., Piper, D.J.W., Matarangas, D., Varti-Matarangas, M., 2001. The sub-ophiolitic melange of the island of Lesbos, Greece. Neues Jahrbuch für Mineralogie, Monatshefte 2001 (6), 241-260.

Pe-Piper, G., Piper, D.J.W., 2002: The igneous rock of Greece: the anatomy of an orogen. Borntraeger, Berlin, 573 pp.

Pickett, E.A., Robertson, A.H.F., 1996. Formation of the Late Palaeozoic-Early Mesozoic Karakaya Complex and related ophiolites in NW Turkey by Palaeotethyan subduction-accretion. Journal of the Geological Society 153, 995 – 1009.

Pickett, E.A., Robertson, A.H.F., 2004. Significance of the Volcanogenic Nilüfer Unit and Related Components of the Triassic Karakaya Complex for Tethyan Subduction/Accretion Processes in NW Turkey. Turkish Journal of Earth Sciences 13, 97 – 143.

Plank, T., 2005. Constraints from Thorium/Lanthanum on Sediment Recycling at Subduction Zones and the Evolution of the Continents. Journal of Petrology 46, 921-944.

Plank, T., Langmuir, C.H., 1998. The chemical composition of subducting sediment and its consequences for the crust and mantle. In: Albarede, F., Blichert, T.J., Staudigel, H., White, W.M. (eds.), Geochemical Earth Reference Model (GERM), Chemical Geology 145, 325-394.

Pollock, M.A., Klein, E.M., Karson, J.A., Tivey, M.A., 2005. Temporal and spatial variability in the composition of lavas exposed along the Western Blanco Transform Fault. Geochemistry, Geophysics, Geosystems 6, Q11009, doi:10.1029/2005GC001026.

Rampone, E., Bottazzi, P., Ottolini, L., 1991. Complementary Ti and Zr anomalies in orthopyroxene and clinopyroxene from mantle peridotites. Nature 354, 518 – 520.

Rampone, E., Hofmann, A.W., Piccardo, G.B., Vannucci, R., Bottazzi, P., Ottolini, L., 1996. Trace element and isotope geochemistry of depleted peridotites from an N-MORB type ophiolite (Internal Liguride, N. Italy). Contributions to Mineralogy and Petrology 123, 61 – 76.

Reagan, M.K., Sims, K.W.W., Erich, J., Thomas, R.B., Cheng, H., Edwards, R.L., Layne, G., Ball, L., 2003. Time-scales of Differentiation from Mafic Parents to Rhyolite in North American Continental Arcs. Journal of Petrology 44, 1703 – 1726.

Reischmann, T., 1986. Geologie und Genese spätproterozoischer Vulkanite der Red Sea Hills, Sudan. Unpubl. PhD thesis, Johannes Gutenberg University, Mainz, 257 pp.

Reischmann, T., 1998. Pre-Alpine origin of tectonic units from the metamorphic complex of Naxos, Greece, identified by single zircon Pb/Pb dating. Bulletin of the Geological Society of Greece, 22, 101 – 111.

Reischmann, T., Kostopoulos, D., 2007. Terrane accretion in the Internal Hellenides. Geophysical Research Abstracts, Vol. 9, 05337.

Richard, P., Allegre, C.J., 1980. Neodymium and strontium isotope study of ophiolite and orogenic lherzolite petrogenesis. Earth and Planetary Science Letters 47, 65 – 74.

Ricou, L.E., Burg, J.P., Godfriaux, I., Ivanov, Z., 1998. Rhodope and Vardar: the metamorphic and the olistostromic paired belts related to the Cretaceous subduction under Europe. Geodinamica Acta 11, 285 – 309.

Robertson, A.H.F., 2002. Overview of the genesis and emplacement of Mesozoic ophiolites in the Eastern Mediterranean Tethyan region. Lithos 65, 1 – 67.

Rojay, B., Yaliniz, K.M., Altiner, D., 2001. Tectonic Implications of Some Cretaceous Pillow Basalts from the North Anatolian Ophiolite Mélange (Central Anatolia-Turkey) to the Evolution of Neotethys. Turkish Journal of Earth Sciences 10, 93 – 102.

Rudnick, R.L., Gao, S., 2003. Composition of the Continental Crust. Treatise on Geochemistry 3, 1-64, doi:10.1016/B0-08-043751-6/03016-4.

Sack, R.O., Ghiorso, M.S., 1991. Chromian spinels as petrogenetic indicators: Thermodynamics and petrological applications. American Mineralogist 76, 827 – 847.

Schünemann, M., 1985. Contributions to the geology, geochemistry and tectonics of the Chortiatis series metamorphic calc-alkaline suite, Chalkidiki, northern Greece. Unpubl. PhD Thesis, University of Hamburg, Germany, 167 pp.

Seymour, K.S., Tsikouras, V., Kotopouli, K., Hatzipanagiotou, K., Pe-Piper, G., 1996. A window to the operation of microplate tectonics in the Tethys Ocean; the geochemistry of the Samothrace granite, Aegean Sea. Mineralogy and Petrology 56, 251 – 272.

Shervais, J.W., 2001. Birth, death, and resurrection: The life cycle of suprasubduction zone ophiolites. Geochemistry, Geophysics, Geosystems 2, doi: 2000GC000080.

Shinjo, R., Chung, S.L., Kato, Y., Kimura, M., 1999. Geochemical and Sr-Nd isotopic characteristics of volcanic rocks from the Okinawa Trough and Ryukyu Arc: implications for the evolution of a young intracontinental back arc basin. Journal of Geophysical Research 104, 10591 – 10608.

Sinton, J.M., Lori, L.F., Chappell, B., McCulloch, M.T., 2003. Magma genesis and mantle heterogeneity in the Manus back-arc basin, Papua New Guinea. Journal of Petrology 44, 159 – 195.

Spandler, C., Mavrogenes, J., Hermann, J., 2007. Experimental constraints on element mobility from subducted sediments using high-P synthetic fluid/melt inclusions. Chemical Geology 239, 228 – 249.

Stampfli, G., Marcoux, J., Baud, A., 1991. Tethyan margins in space and time. Palaeogeography, Palaeoclimatology, Palaeoecology 87, 373 – 409.

Stampfli, GM., Borel, G.D., 2002. A plate tectonic model for the Paleozoic and Mesozoic constrained by dynamic plate boundaries and restored synthetic oceanic isochrones. Earth and Planetary Science Letters 196, 17 – 23.

Steinmann, G., 1927. Die ophiolithischen Zonen in den mediterranen Kettengebirgen. Compte Rendus XIV. Congrés Geologique International, Madrid.

Stewart, M.A., Klein, E.M., Karson, J.A., 2002. Geochemistry of dikes and lavas from the north wall of the Hess Deep Rift; insights into the four-dimensional character of crustal construction at fast spreading mid-ocean ridges. Journal of Geophysical Research 107, (B10), 2238, doi:10.1029/2001JB000545.

Sun, S.s., McDonough, W.F., 1989.Chemical and isotopic systematics of oceanic basalts: implications for mantle composition and processes. In: Saunders, A.D., Norry, M.J. (eds.), Magmatism in the Ocean Basins, Geological Society Special Publication 42, 313 – 345.

Takazawa, E., Frey, F.A., Shimizu, N., Obata, M., 2000. Whole rock compositional variations in an upper mantle peridotite (Horoman, Hokkaido, Japan): Are they consistent with a partial melting process? Geochimica et Cosmochimica Acta 64, 695 – 716.

Tamura, Y., Tani, K., Ishizuka, O., Chang, Q., Shukuno, H., Fiske, R.S., 2005. Are Arc Basalts Dry, Wet, or Both? Evidence from the Sumisu Caldera Volcano, Izu-Bonin Arc, Japan. Journal of Petrology 46, 1769 – 1803.

Tankut, A., Dilek, Y., Önen, P., 1998. Petrology and geochemistry of the Neo-Tethyan volcanics as revealed in the Ankara melange, Turkey. Journal of Volcanology and Geothermal Research 85, 265 – 284.

Taylor, R.N. Nesbitt, R.W., 1988. Light rare-earth enrichment of supra-subduction zone mantle: evidence from the Troodos ophiolite, Cyprus. Geology 16, 448 – 451.

Taylor, R.N., Murton, B.J., Nesbitt, R.W., 1992. Chemical transects across intra-oceanic arcs: implications for the tectonic setting of ophiolites. In: Ophiolites and their modern

oceanic analogues. Parson, L.M., Murton, B.J., Browning, P. (eds.). Geological Society Special Publication 60, 117 – 132.

Teipel, U., Eichhorn, R., Loth, G., Rohrmüller, J., Höll, R., Kennedy, A., 2004. U-Pb SHRIMP and Nd isotopic data from the western Bohemian Massif (Bayerischer Wald, Germany): Implications for Upper Vendian and Lower Ordovician magmatism. International Journal of Earth Sciences (Geologische Rundschau) 93, 782 – 801.

Tepper, J.H., 1996. Petrology of Mafic Plutons Associated with Calc-Alkaline Granitoids, Chilliwack Batholith, North Cascades, Washington. Journal of Petrology 37, 1409 – 1436.

Tomaschek, F., Kennedy, A., Keay, S., Ballhaus, C., 2001. Geochronological constraints on Carboniferous and Triassic magmatism in the Cyclades: SHRIMP U-Pb ages of zircons from Syros, Greece. Journal of Conference Abstracts 6, 315.

Tsikouras, B., 1992. The ophiolites of the island of Samothrace. Unpubl. PhD Thesis, University of Patras, Greece, 262 pp.

Tsikouras, B., Pe-Piper, G., Hatzipanagiotou, K., 1990. A new date for an ophiolite on the northeastern margin of the Vardar Zone, Samothraki, Greece. Neues Jahrbuch der Mineralogie, Monatshefte, 11, 521 – 527.

Tsikouras, B., Hatzipanagiotou, K., 1998a. Petrogenetic evolution of an ophiolite fragment in an ensialic marginal basin, northern Aegean Sea (Samothraki Island, Greece). European Journal of Mineralogy 10, 551 – 567.

Tsikouras, B., Hatzipanagiotou, K., 1998b. Two alternative solutions for the development of a marginal basin in NE Greece. Ofioliti 23, 83 – 92.

Turner, S., Hawkesworth, C., Rogers, N., Bartlett, J., Worthington, T., Hergt, J., Pearce, J., Smith, I., 1997. ^{238}U-^{230}Th disequilibria, magma petrogenesis, and flux rates beneath the depleted Tonga-Kermadec island arc. Geochimica et Cosmochimica Acta 61, 4855 – 4884.

Turpaud, P., 2006. Characterization of igneous terranes by zircon dating: implications for the UHP relicts occurrences and suture identification in the Central Rhodope, Northern Greece. Unpubl. PhD thesis, Johannes Gutenberg University, Mainz, 107 pp.

Van Hinsbergen, D.J.J., Hafkenscheid, E., Spakman, W., Meulenkamp, J.E., Wortel, R., 2005. Nappe stacking resulting from subduction of oceanic and continental lithosphere below Greece. Geology 33, 325 – 328.

Viereck, L.G., Flower, M.F.J., Hertogen, J., Schmincke, H.-U., Jenner, G.A., 1989. The genesis and significance of N-MORB sub-types. Contributions to Mineralogy and Petrology 102, 112 – 126.

Vlahou, M., Christofides, G., Eleftheriadis, G., Pinarelli, L., Koroneos, A., 2006. Tertiary volcanic rocks from Samothraki island (north Aegean, Greece): Sr and Nd isotope constraints on their evolution. In: Postcollisional tectonics and magmatism in the Mediterranean region and Asia. Geological Society of America Special Paper 409, Dilek, Y., Pavlides, S., (eds.), 283 – 304.

White, W.M., 1998. Geochemistry. An on-line textbook. http://www.geo.cornell.edu/geology/classes/geo455/Chapters.html

Willan, R.C.R., Kelley, S.P., 1999. Mafic dike swarms in the South Shetland Islands volcanic arc: Unravelling multiepisodic magmatism related to subduction and continental rifting. Journal of Geophysical Research 104 (B10) 23051 – 23068.

Winchester, J.A., Floyd, P.A., 1977. Geochemical discrimination of different magma series and their differentiation products using immobile elements. Chemical Geology 20, 325-343.

Wood, D.A., 1979. Dynamic partial melting: Its application to the petrogenesis of basalts erupted in Iceland, the Faeroe Islands, the Isle of Sky (Scotland) and the Troodos massif (Cyprus). Geochimica et Cosmochimica Acta 43, 1031-1046.

Wood, D.A., 1980. The application of a Th-Hf-Ta diagram to problems of tectonomagmatic classification and to establishing the nature of crustal contamination of basaltic lavas of the British Tertiary Volcanic Province. Earth and Planetary Science Letters 50, 11-30.

Workman, R.K., Hart, S.R., 2005. Major and trace element composition of the depleted MORB mantle (DMM). Earth and Planetary Science Letters 231, 53-72.

Zachariadis, P., 2007. Ophiolites of the eastern Vardar Zone, N. Greece. Unpubl. PhD thesis, Johannes Gutenberg University, Mainz, 131 pp.

Zidarov, N., Peytcheva, I., von Quadt, A., Tarasova, E., Andreichev, V., 2004. Timing and magma sources of Igralishte pluton (SW Bulgaria): Preliminary isotope-geochronological and geochemical data. Bulgarian Geological Society, Annual Scientific Conference “Geology 2004” 16 – 17.12.2004, 4 pp.

Zindler, A., Hart, S., 1986. Chemical Geodynamics. Annual Review of Earth and Planetary Sciences 14, 493 – 571.

Appendices

Appendix A – Sample lists
- Appendix A-1: Lesvos Island
- Appendix A-2: Samothraki Island
- Appendix A-3: Evros Area

Appendix B – Whole rock major and trace element geochemical data
- Appendix B-1: Basalts of Lesvos Island
- Appendix B-2: Mantle peridotites of Lesvos Island
- Appendix B-3: Basalts, dolerites and diorite of Samothraki Island
- Appendix B-4: Volcanic rocks and gabbros of the Evros area
- Appendix B-5: Mantle Peridotites of the Evros area

Appendix C – Mineral chemical data
- Appendix C-1: Spinels from Lesvos Island lherzolites
- Appendix C-2: Orthopyroxenes from gabbros of the Evros area
- Appendix C-3: Clinopyroxenes from gabbros of the Evros area
- Appendix C-4: Amphiboles from gabbros of the Evros area
- Appendix C-5: Spinels from harzburgites of the Evros area

Appendix D – Sr and Nd isotopic geochemical data
- Appendix D-1: Lesvos Island mafic and ultramafic rocks
- Appendix D-2: Samothraki Island basalts, dolerites and diorite
- Appendix D-3: Mafic and ultramafic rocks of the Evros area

Appendix E – U-Pb SHRIMP zircon data
- Appendix E-1: Sample L02 – Lesvos Island gabbro
- Appendix E-2: Sample L40 – Lesvos Island gabbro
- Appendix E-3: Sample SA08 – Samothraki Island gabbro
- Appendix E-4: Sample E13 – Gabbro of the Evros area

Appendix F – Photos and diagrams
- Appendix F-1: Pillow lavas on Samothraki Island
- Appendix F-2: Zr vs. major and trace elements for the Samothraki Island basalts and dolerites
- Appendix F-3: Zr vs. major and trace elements for the volcanic rocks of the Evros area
- Appendix F-4: Zr vs. major and trace elements for the gabbros of the Evros area
- Appendix F-5: N-MORB-normalised multi-element profiles for different oceanic and continental island arc and back-arc basin volcanic rocks
- Appendix F-6: Chondrite-normalised REE profiles for different oceanic and continental island arc and back-arc basin volcanic rocks

Appendix A – Sample lists

Appendix A-1: Lesvos Island

Sample name	Rock type	Locality	Latitude	Longitude
L05	Harzburgite	SE Loutra	39°00'47.5"	26°36'23.2"
L08	Lherzolite	Komi	39°11'41.8"	26°23'56.5"
L12	Harzburgite	SW of Komi	39°08'39.3"	26°24'00.8"
L13	Lherzolite	SW of Komi	39°08'37.8"	26°23'29.4"
L14	Lherzolite	SW of Komi	39°08'49.7"	26°23'33.7"
L20	Lherzolite	SW of Komi	39°10'57.4"	26°20'51.1"
L21	Lherzolite	SW of Komi	39°11'05.9"	26°20'11.3"
L23	Pillow-Basalt	W of Vatera	39°01'05.7"	26°10'05.8"
L24	Pillow-Basalt	W of Vatera	39°01'05.7"	26°10'05.8"
L29	Pillow-Basalt	W of Vatera	39°00'26.3"	26°10'08.7"
L30	Pillow-Basalt	W of Vatera	39°00'26.5"	26°10'08.8"
L31	Pillow-Basalt	W of Vatera	39°00'26.8"	26°10'08.9"
L33	Basalt	W of Plomari	38°58'41.4"	26°19'37.4"
L36	Pillow-Basalt	W of Plomari	38°58'37.5"	26°20'57.2"
L37	Basalt	W of Plomari	38°58'34.0"	26°21'07.8"
L45	Lherzolite	NE of Ambeliko	39°06'28.9"	26°19'00.9"
L46	Lherzolite	NW of Ambeliko	39°06'04.1"	26°19'36.4"
L51	Lherzolite	N of Ambeliko	39°04'50.3"	26°18'56.2"
L54	Lherzolite	N of Ambeliko	39°03'59.0"	26°18'16.3"
L55	Lherzolite	N of Ambeliko	39°03'40.7"	26°18.448'
L59	Harzburgite	SE of Loutra	39°00'48.7"	26°35'54.0"
L61	Lherzolite	SE of Loutra	39°01'57.1"	26°34'56.7"
L62	Lherzolite	SE of Loutra	39°02'21.3"	26°34'16.1"
L63	Lherzolite	SE of Loutra	39°03'09.4"	26°33'37.3"

For coordinate specification the Hellenic Geodetic Reference System 87 (HGRS87) was used.

Appendix A-2: Samothraki Island

Sample name	Rock type	Locality	Latitude	Longitude
SA01	Pillow-Basalt	Paleopoli	40°30'17.2"	25°32'20.1"
SA02	Basalt-Dyke	Paleopoli	40°30'17.0"	25°32'19.4"
SA03	Pillow-Basalt	Paleopoli	40°30'17.2"	25°32'20.1"
SA04	Basalt-Dyke	W of Therma	40°29'41.8"	25°35'59.2"
SA08	Gabbro	W of Therma	40°29'43.8"	25°35'58.1"
SA10	Dolerite-Dyke	W of Therma	40°29'46.3"	25°36'07.5"
SA14	Pillow-Basalt	Paleopoli	40°30'17.0"	25°32'19.4"
SA15	Pillow-Basalt	Paleopoli	40°30'17.0"	25°32'20.5"
SA17	Basalt-Dyke	W of Therma	40°29'45.8"	25°36'04.4"
SA20	Pillow-Basalt	Kipos beach	40°25'18.1"	25°41'13.5"
SA21	Basalt-Dyke	Kipos beach	40°25'18.1"	25°41'13.5"
SA22	Pillow-Basalt	Kipos beach	40°25'17.9"	25°41'13.5"
SA23	Basalt	Aghios Georgios	40°27'41.7"	25°32'13.2"
SA27	Basalt	SE Dafnes	40°24'36.3"	25°34'03.9"
SA29	Basalt	SE Dafnes	40°24'44.7"	25°33'28.7"
SA30	Dolerite	SE Dafnes	40°24'45.9"	25°33'19.1"
SA31	Dolerite	SE Dafnes	40°24'59.2"	25°32'58.2"
SA33	Dolerite-Dyke	Profitis Ilias	40°26'03.2"	25°32'06.7"
SA35	Dolerite	Profitis Ilias	40°26'05.7"	25°32'24.1"
SA37	Basalt	Profitis Ilias	40°26'08.0"	25°32'37.3"
SA46	Diorite	Profitis Ilias	40°25'58.9"	25°32'03.4"

For coordinate specification the Hellenic Geodetic Reference System 87 (HGRS87) was used.

Appendix A-3: Evros area

Sample name	Rock type	Locality	Latitude	Longitude
E03	Gabbro	S of Petrota	40°52'16.7"	25°36'21.1"
E04	Gabbro	S of Petrota	40°52'16.7"	25°36'21.1"
E05	Gabbro	S of Petrota	40°52'31.6"	25°36'28.0"
E06	Gabbro	S of Petrota	40°52'36.6"	25°36'26.7"
E07	Gabbro, fine grained	S of Petrota	40°52'39.4"	25°36'27.1"
E08	Gabbro	S of Petrota	40°52'39.5"	25°36'27.2"
E09	Gabbro	S of Petrota	40°52'39.7"	25°36'27.5"
E11	Gabbro, fine grained	S of Petrota	40°52'04.6"	25°36'25.0"
E12	Gabbro	S of Petrota	40°52'04.8"	25°36'25.3"
E13	Gabbro, fine grained	S of Petrota	40°52'04.9"	25°36'25.4"
E15	Gabbro	S of Petrota	40°53'17.8"	25°36'29.5"
E16	Basalt-Dyke	S of Petrota	40°53'27.6"	25°36'26.5"
E17	Basalt-Dyke	S of Petrota	40°53'27.6"	25°36'26.5"
E18	Gabbro	S of Petrota	40°53'27.6"	25°36'26.5"
E20	Basalt-Dyke	S of Petrota	40°53'27.5"	25°36'26.6"
E25	Basalt	N of Melia	40°59'31.6"	26°03'51.4"
E26	Basalt	N of Melia	40°59'30.7"	26°03'54.7"
E29	Basalt-Dyke	N of Melia	40°59'46.9"	26°03'30.8"
E32	Basalt-Dyke	N of Melia	41°00'10.6"	26°03'19.7"
E34	Basalt	N of Melia	41°00'14.2"	26°03'39.9"
E36	Basalt	N of Melia	41°00'21.4"	26°03'51.1"
E37	Basalt	N of Melia	41°00'36.7"	26°03'44.9"
E46	Basalt-Dyke	N of Melia	40°59'46.9"	26°03'30.8"
E48	Basalt-Dyke	N of Melia	40°59'46.7"	26°03'30.8"
E51	Basalt-Dyke	N of Melia	40°59'46.7"	26°03'30.7"
E52	Harzburgite, serpent.	NW of Dadia	41°05'43.3"	26°05'43.6"
E55	Harzburgite, serpent.	NW of Dadia	41°09'37.2"	26°12'56.0"
E57	Harzburgite, serpent.	NW of Dadia	41°07'29.2"	26°09'29.6"
E59	Harzburgite, serpent.	NW of Dadia	41°05'49.2"	26°06'04.9"
E60	Dunite, serpent.	NW of Dadia	41°06'01.7"	26°06'31.6"
E61	Harzburgite, serpent.	NW of Dadia	41°07'26.5"	26°09'14.3"
E63	Basalt	Metaxades	41°08'56.8"	26°17'24.0"
E65	Basalt	S of Petrota	40°54'47.7"	25°36'56.6"
E70	Harzburgite, serpent.	SE of Smigada	41°15'36.2"	25°42'12.3"
E71	Harzburgite, serpent.	SE of Smigada	41°16'49.0"	25°45'13.4"
E72	Harzburgite, serpent.	SE of Smigada	41°16'43.5"	25°46'30.3"
E73	Harzburgite, serpent.	SE of Smigada	41°16'33.0"	25°46'40.9"
E77	Gabbro	WSW of Agriani	41°16'45.7"	26°16'34.2"

For coordinate specification the Hellenic Geodetic Reference System 87 (HGRS87) was used.

Appendix B – Whole rock major and trace element data

Appendix B-1: Basalts of Lesvos Island

Sample	L23	L24	L29	L30	L31	L33	L36	L37	L69
SiO_2	48.8	46.7	49.9	49.3	50.5	51.9	50.4	51.5	49.1
TiO_2	1.26	1.17	1.38	1.84	1.22	1.42	1.64	1.49	1.80
Al_2O_3	17.9	19.0	18.2	15.4	17.1	20.5	16.4	14.8	14.9
Fe_2O_3	9.6	8.6	8.5	11.3	9.1	9.1	11.7	11.1	12.7
MnO	0.13	0.14	0.18	0.18	0.15	0.13	0.16	0.15	0.18
MgO	7.03	5.21	6.13	6.62	7.82	5.94	6.07	6.42	6.65
CaO	12.3	16.5	11.2	11.1	9.7	5.3	8.9	10.1	10.9
Na_2O	2.74	2.55	4.04	3.96	4.03	4.62	4.09	3.90	3.30
K_2O	0.032	0.021	0.356	0.125	0.198	0.818	0.415	0.247	0.145
P_2O_5	0.097	0.085	0.105	0.156	0.094	0.220	0.239	0.206	0.229
LOI	7.09	5.66	4.06	2.87	4.10	4.00	2.98	2.36	2.81
Sum	99.8	99.6	99.5	98.7	99.9	99.4	99.4	99.7	99.0
Sc	38	46	40	43	35	30	37	38	31
V	194	215	224	296	206	306	230	236	244
Cr	295	346	276	214	300	100	240	264	218
Co	44	37	38	45	42	32	44	44	37
Ni	127	95	88	75	66	44	100	104	56
Cu	81	82	91	76	115	155	66	63	79
Zn	68	63	59	83	69	96	100	94	101
Ga	13	16	16	17	13	18	17	14	18
Rb	*0.57*	*0.45*	*4.20*	*1.26*	*1.85*	*12.46*	*7.69*	*4.88*	*2.51*
Sr	*100*	*120*	*204*	*155*	*208*	*122*	*182*	*215*	*311*
Y	*20.9*	*19.3*	*21.2*	*36.6*	*20.6*	*22.5*	*30.3*	*29.6*	*23.3*
Zr	*79*	*65*	*80*	*134*	*64*	*102*	*136*	*129*	*118*
Nb	*2.4*	*1.8*	*2.9*	*4.1*	*1.8*	*8.4*	*9.9*	*9.3*	*19.8*
Cs	*4.85*	*1.60*	*2.54*	*1.13*	*2.93*	*0.98*	*0.58*	*0.32*	*0.10*
Ba	*23*	*123*	*84*	*32*	*36*	*112*	*37*	*23*	*29*
La	*3.3*	*2.8*	*4.0*	*5.5*	*2.6*	*12.9*	*3.9*	*6.4*	*14.6*
Ce	*9.5*	*8.6*	*11.6*	*15.5*	*8.1*	*28.3*	*11.2*	*15.7*	*32.4*
Pr	*1.59*	*1.43*	*1.81*	*2.57*	*1.38*	*3.61*	*1.83*	*2.33*	*3.91*
Nd	*8.2*	*7.6*	*9.3*	*13.8*	*7.5*	*16.0*	*9.8*	*11.4*	*16.5*
Sm	*2.61*	*2.46*	*2.86*	*4.36*	*2.51*	*3.84*	*3.51*	*3.54*	*4.03*
Eu	*1.05*	*1.11*	*1.22*	*1.60*	*1.04*	*1.23*	*1.25*	*1.30*	*1.48*
Gd	*3.35*	*3.05*	*3.47*	*5.68*	*3.24*	*4.28*	*4.52*	*4.47*	*4.45*
Tb	*0.59*	*0.53*	*0.59*	*0.97*	*0.57*	*0.68*	*0.80*	*0.78*	*0.71*
Dy	*4.02*	*3.58*	*3.98*	*6.58*	*3.86*	*4.39*	*5.54*	*5.36*	*4.43*
Ho	*0.83*	*0.73*	*0.82*	*1.37*	*0.79*	*0.89*	*1.15*	*1.11*	*0.87*
Er	*2.41*	*2.12*	*2.31*	*3.99*	*2.26*	*2.53*	*3.38*	*3.27*	*2.39*
Tm	*0.34*	*0.30*	*0.33*	*0.57*	*0.32*	*0.35*	*0.49*	*0.48*	*0.33*
Yb	*2.39*	*2.12*	*2.38*	*3.85*	*2.23*	*2.42*	*3.42*	*3.34*	*2.21*
Lu	*0.34*	*0.30*	*0.34*	*0.57*	*0.32*	*0.35*	*0.49*	*0.49*	*0.31*
Hf	*2.02*	*1.64*	*2.01*	*3.32*	*1.76*	*2.49*	*3.37*	*3.25*	*2.87*
Ta	*0.17*	*0.12*	*0.20*	*0.29*	*0.12*	*0.50*	*0.57*	*0.54*	*1.17*
Pb	*1.82*	*1.17*	*1.34*	*1.43*	*0.40*	*1.68*	*2.24*	*2.86*	*1.94*
Th	*0.18*	*0.13*	*0.20*	*0.35*	*0.13*	*2.48*	*1.01*	*0.96*	*2.18*
U	*0.22*	*0.05*	*0.07*	*0.11*	*0.04*	*0.58*	*0.49*	*0.36*	*0.50*
Mg#	0.63	0.59	0.63	0.58	0.67	0.60	0.55	0.57	0.55

LOI: loss of ignition; total iron quoted as Fe_2O_3; Mg# = $Mg/(Mg+Fe^{2+})$. Data analysed by LA-ICPMS are signed in italics. Oxides in wt%, elements in ppm.

Appendix B-2: Mantle peridotites of Lesvos Island

Sample	L13	L20	L21	L45	L51	L55	L62	L63	L05	L12	L59
Material	Lherzolite								Harzburgite		
SiO_2	43.7	45.5	43.6	44.6	44.9	46.3	44.0	46.1	45.4	45.5	46.0
TiO_2	0.06	0.09	0.04	0.08	0.09	0.11	0.07	0.09	0.03	0.02	0.05
Al_2O_3	2.0	3.2	2.3	3.5	3.0	3.4	2.4	4.1	1.3	1.3	2.0
Fe_2O_3	9.3	8.4	9.2	10.1	8.9	8.1	9.3	8.3	9.2	9.7	8.9
MnO	0.15	0.13	0.16	0.15	0.13	0.14	0.13	0.14	0.11	0.08	0.14
MgO	40.3	38.5	41.1	37.0	39.3	35.5	40.9	35.3	43.2	42.5	41.0
CaO	3.8	3.5	2.8	3.8	2.7	5.8	2.4	5.2	0.1	0.2	1.2
Na_2O	b.d.	0.09	b.d.	0.12	0.28	0.01	0.14	0.04	0.06	b.d.	b.d.
K_2O	0.010	0.021	b.d.	0.031	0.041	0.021	0.020	0.011	b.d.	0.011	0.011
P_2O_5	b.d.	b.d.	b.d.	b.d.	b.d.	b.d.	b.d.	b.d.	b.d.	b.d.	b.d.
LOI	3.90	6.49	5.61	4.85	2.35	5.86	1.70	8.87	12.63	12.42	12.99
Sum	100.3	100.1	99.8	101.1	100.0	99.4	99.8	100.2	100.6	100.3	100.7
Sc	14	16	12	15	14	23	11	16	11	11	13
V	58	72	61	92	73	128	60	94	49	50	66
Cr	2572	2725	2836	2233	2623	3329	2264	3447	2767	2990	2703
Co	108	98	105	108	107	87	113	89	110	105	102
Ni	2024	1772	1988	1815	1964	1612	2091	1614	2047	2241	2006
Zn	46	45	47	54	45	41	49	52	38	29	43
Ga	2	3	3	4	3	3	2	3	1	1	1
Rb	*0.09*	*0.32*	*0.06*	*0.33*	*0.52*	*1.02*	*0.21*	*0.28*	*0.13*	*0.08*	*0.82*
Sr	*0.8*	*2.5*	*2.7*	*4.2*	*5.4*	*9.5*	*6.9*	*3.6*	*2.2*	*0.9*	*3.0*
Y	*0.9*	*2.4*	*1.4*	*2.9*	*2.3*	*3.8*	*1.7*	*3.0*	*0.7*	*0.5*	*1.0*
Zr	*0.18*	*0.60*	*0.10*	*0.36*	*0.85*	*0.97*	*0.57*	*0.27*	*0.09*	*0.23*	*2.87*
Nb	*0.014*	*0.008*	*0.007*	*0.015*	*0.019*	*0.010*	b.d.	*0.005*	*0.028*	*0.065*	*0.017*
Cs	*0.021*	*0.020*	*0.003*	*0.013*	*0.063*	*0.214*	*0.020*	*0.186*	*0.034*	*0.012*	*0.033*
Ba	*0.3*	*0.4*	*0.4*	*0.9*	*1.1*	*2.4*	*0.4*	*2.1*	*1.4*	*3.9*	*7.3*
La	*0.011*	*0.012*	*0.015*	*0.018*	*0.018*	*0.018*	*0.008*	*0.012*	*0.035*	*0.096*	*0.068*
Ce	*0.025*	*0.031*	*0.030*	*0.034*	*0.058*	*0.044*	*0.037*	*0.019*	*0.107*	*0.154*	*0.097*
Pr	*0.005*	*0.011*	*0.005*	*0.010*	*0.018*	*0.014*	*0.011*	*0.005*	*0.020*	*0.016*	*0.013*
Nd	*0.044*	*0.125*	*0.044*	*0.110*	*0.154*	*0.144*	*0.106*	*0.078*	*0.097*	*0.063*	*0.058*
Sm	*0.04*	*0.11*	*0.04*	*0.12*	*0.12*	*0.15*	*0.07*	*0.10*	*0.03*	*0.01*	*0.02*
Eu	*0.018*	*0.051*	*0.020*	*0.053*	*0.056*	*0.065*	*0.038*	*0.045*	*0.013*	*0.006*	*0.015*
Gd	*0.09*	*0.25*	*0.11*	*0.28*	*0.23*	*0.36*	*0.17*	*0.26*	*0.06*	*0.03*	*0.08*
Tb	*0.019*	*0.049*	*0.026*	*0.057*	*0.048*	*0.077*	*0.036*	*0.058*	*0.012*	*0.007*	*0.016*
Dy	*0.15*	*0.40*	*0.21*	*0.45*	*0.36*	*0.62*	*0.26*	*0.47*	*0.09*	*0.07*	*0.14*
Ho	*0.034*	*0.090*	*0.053*	*0.108*	*0.084*	*0.139*	*0.061*	*0.112*	*0.023*	*0.018*	*0.037*
Er	*0.11*	*0.28*	*0.16*	*0.33*	*0.26*	*0.44*	*0.19*	*0.36*	*0.08*	*0.07*	*0.12*
Tm	*0.017*	*0.043*	*0.024*	*0.050*	*0.040*	*0.066*	*0.031*	*0.055*	*0.014*	*0.013*	*0.019*
Yb	*0.13*	*0.32*	*0.21*	*0.35*	*0.28*	*0.46*	*0.21*	*0.40*	*0.10*	*0.11*	*0.16*
Lu	*0.022*	*0.049*	*0.037*	*0.058*	*0.050*	*0.070*	*0.037*	*0.065*	*0.018*	*0.020*	*0.027*
Hf	*0.016*	*0.056*	*0.017*	*0.048*	*0.065*	*0.066*	*0.046*	*0.047*	*0.010*	*0.005*	*0.074*
Ta	b.d.	b.d.	b.d.	b.d.	b.d.	b.d.	b.d.	b.d.	b.d.	b.d.	b.d.
Pb	*0.027*	*0.028*	*0.033*	*0.024*	*0.046*	*0.042*	*0.029*	*0.013*	*0.077*	*0.091*	*0.233*
Th	b.d.	b.d.	b.d.	*0.006*	b.d.	*0.006*	b.d.	*0.006*	*0.006*	*0.028*	*0.016*
U	b.d.	b.d.	b.d.	b.d.	b.d.	b.d.	b.d.	b.d.	b.d.	b.d.	*0.007*
Mg#	0.91	0.91	0.91	0.90	0.91	0.91	0.91	0.91	0.92	0.91	0.91

LOI: loss of ignition; total iron quoted as Fe_2O_3; Mg# = $Mg/(Mg+Fe^{2+})$; b.d. = below detection limit. Data analysed by LA-ICPMS are signed in italics. Oxides in wt%, elements in ppm.

Appendix B-3: Basalts, dolerites and diorite of Samothraki Island

Sample	SA01	SA02	SA03	SA04	SA14	SA15	SA17	SA20	SA21	SA22
Material	Basalt									
Group	I	I	I	III	I	I	V	I	II	I
SiO_2	51.8	51.1	50.0	50.4	49.8	49.4	48.8	49.9	49.9	49.8
TiO_2	1.49	1.71	1.54	0.91	1.57	1.45	0.60	1.28	1.28	1.41
Al_2O_3	14.2	14.6	14.3	15.6	14.9	14.9	15.9	15.5	16.0	14.8
Fe_2O_3	11.0	10.8	11.8	7.0	11.9	11.9	9.3	11.0	10.0	11.2
MnO	0.16	0.16	0.17	0.08	0.19	0.18	0.17	0.20	0.19	0.16
MgO	7.3	6.8	7.6	9.9	7.6	7.3	11.2	6.3	7.2	5.9
CaO	11.2	12.5	12.3	13.7	11.3	12.8	10.7	12.0	12.5	11.6
Na_2O	2.58	1.90	1.91	2.09	2.58	1.75	2.92	3.28	2.08	4.35
K_2O	0.144	0.123	0.177	0.061	0.113	0.124	0.205	0.374	0.735	0.493
P_2O_5	0.133	0.195	0.146	0.092	0.144	0.124	0.031	0.114	0.114	0.146
LOI	1.82	1.95	2.65	1.18	2.02	2.53	2.02	3.26	2.52	9.81
Sum	99.3	99.2	98.6	99.4	99.3	99.5	99.7	99.6	99.1	99.0
Sc	37	38	38	43	40	38	36	43	40	42
V	304	305	311	224	317	302	211	289	271	278
Cr	188	152	182	479	199	219	654	286	274	143
Co	40	36	39	40	44	44	41	43	42	42
Ni	76	63	80	140	82	90	210	81	93	57
Cu	57	59	58	9	57	59	76	150	61	39
Zn	84	81	90	27	93	94	68	98	84	83
Ga	17	16	17	13	17	17	12	15	15	14
Rb	*2.5*	*1.9*	*3.8*	*0.6*	*2.0*	*2.2*	*6.0*	*8.3*	*24.4*	*15.5*
Sr	*107*	*210*	*131*	*279*	*120*	*129*	*124*	*128*	*152*	*78*
Y	*36.6*	*33.3*	*30.6*	*20.6*	*36.0*	*29.4*	*15.2*	*29.1*	*24.5*	*30.1*
Zr	*88*	*105*	*76*	*50*	*90*	*74*	*16*	*79*	*67*	*75*
Nb	*5.0*	*9.9*	*5.0*	*3.9*	*5.3*	*4.6*	*2.0*	*4.7*	*4.6*	*5.8*
Cs	*0.73*	*0.30*	*0.47*	*0.34*	*0.76*	*0.38*	*1.68*	*0.24*	*0.49*	*0.76*
Ba	*24*	*32*	*26*	*18*	*29*	*19*	*19*	*56*	*183*	*39*
La	*4.7*	*7.9*	*4.5*	*3.6*	*5.1*	*4.1*	*1.4*	*4.4*	*4.0*	*5.5*
Ce	*12.6*	*19.7*	*12.8*	*9.4*	*13.8*	*12.0*	*3.4*	*11.4*	*11.3*	*13.0*
Pr	*2.01*	*2.77*	*1.96*	*1.35*	*2.21*	*1.85*	*0.48*	*1.78*	*1.70*	*2.09*
Nd	*10.7*	*13.3*	*10.0*	*6.7*	*11.8*	*9.6*	*2.6*	*9.2*	*8.6*	*10.37*
Sm	*3.61*	*3.99*	*3.31*	*2.19*	*4.00*	*3.19*	*1.10*	*3.01*	*2.75*	*3.26*
Eu	*1.27*	*1.43*	*1.28*	*0.76*	*1.44*	*1.19*	*0.59*	*1.09*	*1.06*	*1.21*
Gd	*5.16*	*5.11*	*4.45*	*2.89*	*5.55*	*4.21*	*1.88*	*4.19*	*3.61*	*4.30*
Tb	*0.90*	*0.88*	*0.79*	*0.52*	*1.01*	*0.74*	*0.36*	*0.74*	*0.64*	*0.76*
Dy	*6.36*	*5.98*	*5.44*	*3.60*	*7.04*	*5.15*	*2.58*	*5.05*	*4.36*	*5.29*
Ho	*1.35*	*1.25*	*1.16*	*0.77*	*1.49*	*1.08*	*0.57*	*1.08*	*0.92*	*1.13*
Er	*3.99*	*3.64*	*3.39*	*2.23*	*4.18*	*3.18*	*1.67*	*3.14*	*2.65*	*3.25*
Tm	*0.57*	*0.52*	*0.49*	*0.33*	*0.61*	*0.46*	*0.24*	*0.46*	*0.39*	*0.47*
Yb	*3.93*	*3.61*	*3.42*	*2.26*	*4.27*	*3.23*	*1.70*	*3.07*	*2.68*	*3.29*
Lu	*0.58*	*0.53*	*0.50*	*0.32*	*0.63*	*0.46*	*0.25*	*0.46*	*0.39*	*0.47*
Hf	*2.56*	*2.87*	*2.20*	*1.43*	*2.93*	*2.07*	*0.58*	*2.16*	*1.84*	*2.04*
Ta	*0.33*	*0.63*	*0.31*	*0.23*	*0.38*	*0.28*	*0.12*	*0.31*	*0.29*	*0.36*
Pb	*0.56*	*0.67*	*0.50*	*1.29*	*0.67*	*0.57*	*1.80*	*2.01*	*2.28*	*1.58*
Th	*0.45*	*1.00*	*0.41*	*0.38*	*0.51*	*0.36*	*0.17*	*0.42*	*0.36*	*0.47*
U	*0.18*	*0.27*	*0.17*	*0.17*	*0.17*	*0.19*	*0.05*	*0.24*	*0.11*	*0.25*
Mg#	0.61	0.60	0.60	0.77	0.60	0.59	0.74	0.57	0.63	0.55
Ce/Pb	22.71	29.41	25.28	7.30	20.60	20.99	1.89	5.69	4.96	8.25
Nb/U	28.18	36.55	29.88	22.81	32.22	24.42	40.70	20.07	40.18	23.31
$(Ce/Sm)_N$	0.87	1.24	0.96	1.08	0.86	0.94	0.77	0.95	1.03	1.00
$(Sm/Nd)_N$	1.03	0.91	1.01	1.01	1.03	1.01	1.28	1.00	0.98	0.96

LOI: loss of ignition; total iron quoted as Fe_2O_3; Mg# = $Mg/(Mg+Fe^{2+})$. Data analysed by LA-ICPMS are signed in italics. Oxides in wt%, elements in ppm. Normalised values are normalised with chondrite values (after Sun & McDonough, 1989).

Appendix B-3: Continued.

Sample	SA23	SA27	SA29	SA37	SA10	SA30	SA31	SA33	SA35	SA46
Material	Basalt				Dolerite					Diorite
Group	II	I	IV	IV	III	IV	IV	IV	VI	
SiO_2	47.7	51.4	53.2	49.8	47.1	57.3	56.9	52.1	42.1	55.5
TiO_2	1.43	1.43	0.73	1.69	0.77	0.93	1.09	2.79	3.26	0.51
Al_2O_3	17.0	14.2	17.2	14.8	13.7	15.7	16.3	14.0	12.9	15.6
Fe_2O_3	11.2	11.4	7.6	12.3	9.7	6.8	7.9	13.8	20.7	6.9
MnO	0.20	0.34	0.32	0.18	0.17	0.13	0.18	0.23	0.21	0.11
MgO	8.7	7.8	6.2	6.1	15.8	5.7	6.0	4.9	7.1	6.6
CaO	9.8	9.7	9.6	10.7	11.1	6.8	5.8	7.6	10.4	10.9
Na_2O	2.71	3.48	4.02	3.52	1.23	5.58	4.38	3.84	2.60	2.66
K_2O	1.056	0.154	1.048	0.802	0.104	0.831	1.374	0.432	0.592	1.129
P_2O_5	0.155	0.143	0.064	0.173	0.083	0.092	0.125	0.360	0.010	0.062
LOI	3.27	1.00	5.00	0.66	3.04	1.53	2.18	1.92	3.15	1.72
Sum	99.9	98.7	99.4	99.1	99.1	99.1	99.0	98.2	99.1	99.5
Sc	35	41	33	39	31	27	30	31	46	43
V	274	309	159	317	184	148	167	337	754	171
Cr	392	94	331	210	991	208	266	48	18	61
Co	43	38	18	36	56	21	31	31	58	30
Ni	132	47	92	74	443	49	63	27	3	105
Cu	63	87	2	49	34	5	38	24	31	105
Zn	93	1250	166	101	74	93	444	112	112	47
Ga	16	15	16	16	12	14	17	21	19	14
Rb	*26.6*	*2.5*	*50.8*	*53.7*	*3.2*	*27.8*	*53.5*	*13.3*	*22.1*	*28.9*
Sr	*105*	*147*	*710*	*755*	*117*	*429*	*316*	*368*	*322*	*608*
Y	*29.8*	*32.9*	*14.1*	*31.3*	*16.8*	*26.1*	*30.8*	*47.4*	*19.9*	*13.1*
Zr	*81*	*79*	*31*	*56*	*49*	*44*	*94*	*195*	*31*	*24*
Nb	*8.5*	*5.0*	*2.8*	*5.2*	*5.8*	*4.5*	*8.0*	*9.2*	*0.8*	*2.2*
Cs	*1.20*	*0.33*	*2.20*	*1.80*	*0.86*	*0.92*	*1.89*	*0.97*	*4.85*	*1.62*
Ba	*165*	*43*	*524*	*370*	*19*	*219*	*682*	*294*	*182*	*494*
La	*5.9*	*4.1*	*5.2*	*13.3*	*5.4*	*18.8*	*16.1*	*18.0*	*2.9*	*14.0*
Ce	*15.2*	*11.2*	*11.2*	*29.7*	*11.9*	*36.5*	*35.2*	*43.3*	*8.5*	*30.0*
Pr	*2.20*	*1.75*	*1.31*	*3.86*	*1.69*	*4.27*	*4.51*	*5.88*	*1.52*	*3.72*
Nd	*10.80*	*9.20*	*5.32*	*16.74*	*7.85*	*17.41*	*19.05*	*26.59*	*8.70*	*14.95*
Sm	*3.43*	*3.13*	*1.38*	*4.33*	*2.19*	*4.04*	*4.69*	*6.94*	*2.90*	*2.87*
Eu	*1.16*	*0.96*	*0.41*	*1.36*	*0.92*	*1.46*	*1.43*	*2.27*	*1.20*	*0.89*
Gd	*4.43*	*4.45*	*1.65*	*4.92*	*2.78*	*4.44*	*5.17*	*7.98*	*3.79*	*2.61*
Tb	*0.79*	*0.80*	*0.32*	*0.83*	*0.49*	*0.72*	*0.85*	*1.32*	*0.63*	*0.39*
Dy	*5.41*	*5.65*	*2.35*	*5.51*	*3.30*	*4.65*	*5.61*	*8.60*	*4.18*	*2.51*
Ho	*1.12*	*1.22*	*0.53*	*1.13*	*0.69*	*0.96*	*1.14*	*1.77*	*0.85*	*0.51*
Er	*3.28*	*3.59*	*1.63*	*3.28*	*1.89*	*2.73*	*3.29*	*5.05*	*2.26*	*1.44*
Tm	*0.48*	*0.52*	*0.25*	*0.47*	*0.27*	*0.39*	*0.47*	*0.72*	*0.31*	*0.20*
Yb	*3.26*	*3.57*	*1.78*	*3.26*	*1.88*	*2.70*	*3.25*	*4.92*	*2.02*	*1.42*
Lu	*0.48*	*0.54*	*0.26*	*0.46*	*0.28*	*0.39*	*0.46*	*0.72*	*0.29*	*0.22*
Hf	*2.29*	*2.31*	*1.19*	*1.91*	*1.40*	*1.56*	*2.78*	*5.00*	*1.25*	*1.13*
Ta	*0.54*	*0.33*	*0.20*	*0.41*	*0.41*	*0.36*	*0.51*	*0.62*	*0.07*	*0.21*
Pb	*2.25*	*120.45*	*74.43*	*39.54*	*1.37*	*30.09*	*72.94*	*4.66*	*0.51*	*3.47*
Th	*0.71*	*0.38*	*1.85*	*5.42*	*0.62*	*9.59*	*5.06*	*3.22*	*0.09*	*10.82*
U	*0.21*	*0.62*	*1.31*	*1.63*	*0.18*	*3.06*	*1.14*	*0.75*	*0.02*	*1.75*
Mg#	0.64	0.61	0.66	0.54	0.79	0.66	0.64	0.45	0.44	0.69
Ce/Pb	6.76	0.09	0.15	0.75	8.71	1.21	0.48	9.29	16.67	8.63
Nb/U	41.02	8.03	2.14	3.17	32.25	1.48	7.01	12.23	32.32	1.24
$(Ce/Sm)_N$	1.11	0.89	2.03	1.72	1.36	2.25	1.87	1.56	0.74	2.61
$(Sm/Nd)_N$	0.97	1.04	0.79	0.79	0.85	0.71	0.75	0.80	1.02	0.59

LOI: loss of ignition; total iron quoted as Fe_2O_3; Mg# = $Mg/(Mg+Fe^{2+})$. Data analysed by LA-ICPMS are signed in italics. Oxides in wt%, elements in ppm. Normalised values are normalised with chondrite values (after Sun & McDonough, 1989).

Appendix B-4: Volcanic rocks and gabbros of the Evros area

Sample	E17	E25	E26	E29	E34	E16	E36	E50	E51	E65
Material	Basalt					Basaltic	andesite			
Group	I	I	I	I	I	II	I	I	II	II
SiO_2	50.2	50.4	50.0	50.6	52.9	56.6	54.8	56.2	55.5	56.5
TiO_2	0.74	0.54	0.65	0.47	0.75	0.57	0.65	0.46	0.47	0.67
Al_2O_3	16.7	14.3	16.1	12.7	17.7	15.8	16.1	13.2	13.8	15.8
Fe_2O_3	8.4	8.4	10.9	11.2	10.4	7.0	9.0	13.0	11.9	9.6
MnO	0.15	0.13	0.29	0.27	0.17	0.12	0.14	0.18	0.17	0.25
MgO	8.6	11.5	8.3	11.2	6.7	6.8	6.7	8.4	9.3	4.3
CaO	12.7	12.3	10.3	11.5	6.1	9.7	7.5	5.4	4.2	8.2
Na_2O	2.21	1.74	2.35	1.90	4.99	2.83	4.90	2.40	4.39	2.15
K_2O	0.249	0.540	0.884	0.114	0.221	0.348	0.132	0.726	0.177	2.133
P_2O_5	0.041	0.052	0.094	0.042	0.074	0.063	0.055	0.062	0.063	0.299
LOI	2.92	3.63	4.01	4.02	3.95	1.87	9.25	3.66	3.93	1.12
Sum	99.4	100.0	100.2	100.2	98.8	96.8	99.9	100.1	99.8	99.3
Sc	40	35	41	30	32	36	40	35	36	5
V	200	192	214	185	260	202	270	194	194	31
Cr	442	796	268	601	18	263	253	274	307	9
Co	37	38	43	43	37	30	31	47	50	9
Ni	100	210	64	184	20	40	57	58	65	7
Cu	76	9	22	11	86	66	101	11	21	2
Zn	61	38	76	76	83	47	77	75	71	13
Ga	14	13	14	14	16	16	13	13	13	15
Rb	*5.1*	*3.9*	*7.2*	*1.2*	*3.2*	*5.7*	*2.7*	*18.4*	*3.6*	*160.7*
Sr	*91*	*208*	*220*	*279*	*139*	*199*	*45*	*164*	*100*	*400*
Y	*16.1*	*13.6*	*14.8*	*16.6*	*13.8*	*16.2*	*11.4*	*11.5*	*18.6*	*21.6*
Zr	*24*	*25*	*33*	*27*	*53*	*28*	*40*	*30*	*32*	*92*
Nb	*0.19*	*0.34*	*0.50*	*0.35*	*1.10*	*1.00*	*0.80*	*0.66*	*0.76*	*4.61*
Cs	*0.47*	*5.26*	*6.73*	*2.18*	*9.64*	*0.71*	*0.41*	*4.58*	*2.51*	*4.27*
Ba	*32*	*26*	*65*	*13*	*24*	*45*	*29*	*74*	*24*	*499*
La	*1.1*	*2.2*	*2.7*	*3.1*	*3.3*	*6.2*	*3.2*	*2.5*	*8.0*	*13.9*
Ce	*3.5*	*5.3*	*6.6*	*6.5*	*8.6*	*15.4*	*7.4*	*5.9*	*16.7*	*31.6*
Pr	*0.65*	*0.85*	*1.03*	*1.06*	*1.29*	*2.15*	*1.00*	*0.84*	*2.28*	*4.24*
Nd	*4.1*	*4.5*	*5.3*	*5.4*	*6.2*	*9.7*	*4.7*	*4.0*	*10.0*	*19.1*
Sm	*1.65*	*1.48*	*1.66*	*1.54*	*1.82*	*2.42*	*1.29*	*1.13*	*2.05*	*4.45*
Eu	*0.69*	*0.71*	*0.71*	*0.63*	*0.63*	*0.72*	*0.40*	*0.44*	*0.82*	*1.16*
Gd	*2.32*	*1.99*	*2.15*	*2.06*	*2.14*	*2.62*	*1.58*	*1.58*	*2.51*	*4.38*
Tb	*0.42*	*0.35*	*0.38*	*0.34*	*0.37*	*0.43*	*0.29*	*0.29*	*0.40*	*0.67*
Dy	*2.98*	*2.37*	*2.64*	*2.30*	*2.58*	*2.85*	*2.16*	*2.07*	*2.71*	*4.35*
Ho	*0.62*	*0.50*	*0.56*	*0.49*	*0.53*	*0.59*	*0.48*	*0.44*	*0.58*	*0.90*
Er	*1.82*	*1.44*	*1.63*	*1.43*	*1.58*	*1.75*	*1.46*	*1.28*	*1.67*	*2.45*
Tm	*0.26*	*0.20*	*0.23*	*0.20*	*0.23*	*0.25*	*0.22*	*0.18*	*0.23*	*0.36*
Yb	*1.80*	*1.40*	*1.64*	*1.36*	*1.61*	*1.82*	*1.57*	*1.28*	*1.51*	*2.53*
Lu	*0.26*	*0.21*	*0.24*	*0.21*	*0.24*	*0.27*	*0.24*	*0.19*	*0.22*	*0.40*
Hf	*0.92*	*0.79*	*1.06*	*0.83*	*1.62*	*1.25*	*1.27*	*0.95*	*1.03*	*3.19*
Ta	*0.02*	*0.03*	*0.04*	*0.03*	*0.08*	*0.07*	*0.06*	*0.05*	*0.05*	*0.37*
Pb	*1.04*	*1.34*	*1.97*	*2.04*	*3.15*	*1.43*	*3.05*	*0.80*	*1.26*	*18.56*
Th	*0.27*	*0.34*	*0.43*	*0.37*	*1.06*	*0.74*	*1.04*	*0.67*	*1.18*	*10.02*
U	*0.09*	*0.40*	*0.23*	*0.24*	*0.40*	*0.17*	*0.45*	*0.38*	*0.19*	*4.81*
Mg#	0.70	0.76	0.64	0.70	0.60	0.69	0.63	0.60	0.64	0.51

LOI: loss of ignition; total iron quoted as Fe_2O_3; Mg# = $Mg/(Mg+Fe^{2+})$. Data analysed by LA-ICPMS are signed in italics. Oxides in wt%, elements in ppm.

Appendix B-4: Continued

Sample	E20	E32	E48	E63	E78	E37	E46	E03	E04	E05
Material	Andesite					Dacite	Rhyolite	Gabbro		
Group	II	I	I	I	I	I	I	I	I	I
SiO_2	58.2	60.0	57.4	60.7	59.2	64.1	77.7	49.1	51.8	50.4
TiO_2	0.56	0.57	0.52	0.66	0.55	0.64	0.35	0.07	0.09	0.11
Al_2O_3	16.4	14.6	15.2	15.8	16.4	16.1	11.1	20.6	9.4	14.2
Fe_2O_3	6.6	11.9	10.2	9.1	8.5	7.7	4.9	4.86	8.40	8.14
MnO	0.12	0.11	0.12	0.14	0.19	0.08	0.11	0.09	0.17	0.16
MgO	5.8	4.0	8.3	4.0	7.8	3.5	0.8	9.7	18.1	12.4
CaO	8.7	5.6	3.6	5.3	2.1	0.7	0.2	14.7	11.5	13.9
Na_2O	3.10	3.16	4.44	3.92	5.16	6.12	4.49	0.69	0.26	0.54
K_2O	0.369	0.135	0.086	0.409	0.074	1.051	0.274	0.07	0.02	0.06
P_2O_5	0.082	0.031	0.086	0.042	0.042	0.062	0.061	b.d.	b.d.	b.d.
LOI	2.86	3.77	6.59	3.52	9.85	2.75	1.44	1.17	0.79	0.79
Sum	100.5	100.0	99.7	98.9	99.4	99.8	99.8	100.0	99.8	96.6
Sc	31	37	33	27	28	21	14	35	51	55
V	167	423	197	279	207	239	12	102	163	195
Cr	236	9	345	15	86	6	3	721	1766	631
Co	24	33	36	27	31	24	2	29	54	49
Ni	50	7	71	15	38	13	1	99	201	115
Cu	60	111	28	63	71	29	31	84	7	21
Zn	49	79	107	72	117	55	54	30	49	46
Ga	17	18	11	13	16	13	10	12	7	10
Rb	*6.9*	*8.7*	*1.8*	*7.7*	*0.8*	*16.5*	*6.4*	*1.0*	*0.3*	*1.2*
Sr	*227*	*338*	*119*	*55*	*59*	*56*	*35*	*99*	*42*	*67*
Y	*17.8*	*12.9*	*7.2*	*16.7*	*13.1*	*17.3*	*15.8*	*1.66*	*2.26*	*3.18*
Zr	*61*	*35*	*31*	*50*	*37*	*49*	*44*	*1.12*	*1.46*	*3.48*
Nb	*1.94*	*1.29*	*0.87*	*1.07*	*0.63*	*0.89*	*1.15*	*0.023*	*0.019*	*0.057*
Cs	*0.75*	*7.46*	*2.59*	*0.25*	*0.05*	*1.28*	*0.77*	*0.130*	*0.071*	*0.193*
Ba	*60*	*10*	*22*	*52*	*20*	*115*	*16*	*5.02*	*2.13*	*5.40*
La	*10.5*	*3.4*	*2.5*	*3.9*	*2.4*	*3.6*	*2.9*	*0.162*	*0.102*	*0.241*
Ce	*25.1*	*7.7*	*6.1*	*9.1*	*5.9*	*5.9*	*6.3*	*0.400*	*0.285*	*0.614*
Pr	*3.27*	*0.93*	*0.82*	*1.27*	*0.78*	*1.16*	*0.82*	*0.057*	*0.046*	*0.090*
Nd	*14.2*	*4.1*	*3.7*	*6.1*	*3.7*	*5.4*	*3.7*	*0.270*	*0.235*	*0.431*
Sm	*3.17*	*1.19*	*0.92*	*1.90*	*1.21*	*1.62*	*1.18*	*0.110*	*0.118*	*0.190*
Eu	*0.94*	*0.42*	*0.36*	*0.71*	*0.46*	*0.52*	*0.29*	*0.081*	*0.056*	*0.094*
Gd	*3.02*	*1.62*	*1.09*	*2.65*	*1.68*	*2.22*	*1.79*	*0.181*	*0.210*	*0.324*
Tb	*0.47*	*0.30*	*0.19*	*0.47*	*0.30*	*0.39*	*0.34*	*0.035*	*0.044*	*0.065*
Dy	*3.06*	*2.16*	*1.28*	*3.31*	*2.14*	*2.66*	*2.46*	*0.258*	*0.350*	*0.499*
Ho	*0.64*	*0.48*	*0.28*	*0.72*	*0.47*	*0.58*	*0.57*	*0.066*	*0.090*	*0.128*
Er	*1.90*	*1.51*	*0.83*	*1.99*	*1.40*	*1.70*	*1.82*	*0.183*	*0.256*	*0.356*
Tm	*0.28*	*0.23*	*0.12*	*0.29*	*0.21*	*0.24*	*0.29*	*0.030*	*0.043*	*0.058*
Yb	*2.04*	*1.68*	*0.89*	*2.11*	*1.41*	*1.61*	*2.03*	*0.217*	*0.309*	*0.410*
Lu	*0.30*	*0.26*	*0.14*	*0.33*	*0.22*	*0.25*	*0.33*	*0.033*	*0.050*	*0.067*
Hf	*1.91*	*1.11*	*0.98*	*1.85*	*1.14*	*1.47*	*1.42*	*0.042*	*0.052*	*0.118*
Ta	*0.12*	*0.10*	*0.07*	*0.10*	*0.05*	*0.07*	*0.08*	*0.003*	*0.003*	*0.006*
Pb	*3.71*	*2.24*	*3.41*	*4.77*	*6.51*	*2.70*	*1.42*	*0.705*	*0.328*	*0.897*
Th	*2.50*	*1.20*	*0.78*	*1.24*	*0.64*	*1.04*	*1.00*	*0.013*	*0.022*	*0.076*
U	*0.70*	*0.41*	*0.22*	*0.54*	*0.37*	*0.30*	*0.47*	*0.006*	*0.013*	*0.036*
Mg#	0.67	0.44	0.65	0.51	0.68	0.51	0.27	0.82	0.83	0.78

LOI: loss of ignition; total iron quoted as Fe_2O_3; Mg# = $Mg/(Mg+Fe^{2+})$; b.d. = below detection limit. Data analysed by LA-ICPMS are signed in italics. Oxides in wt%, elements in ppm.

Appendix B-4: Continued

Sample	E06	E07	E08	E09	E11	E12	E13	E15	E18	E77
Material	Gabbro									
Group	I	I	I	I	II	II	II	II	II	II
SiO_2	50.2	48.7	51.4	48.6	53.2	49.9	53.9	49.2	50.5	49.0
TiO_2	0.09	0.06	0.11	0.06	0.49	0.58	0.98	0.23	0.27	0.22
Al_2O_3	14.5	21.3	10.9	17.3	14.8	14.3	17.2	19.5	17.5	22.9
Fe_2O_3	7.77	5.69	8.94	6.61	8.15	9.57	9.40	5.25	6.15	4.19
MnO	0.15	0.11	0.17	0.14	0.15	0.14	0.13	0.08	0.11	0.08
MgO	12.8	9.4	15.5	11.7	9.3	11.1	5.3	8.4	9.3	6.5
CaO	13.9	13.9	12.2	14.9	10.6	12.8	9.2	16.1	14.5	15.5
Na_2O	0.42	0.69	0.44	0.56	2.35	1.34	3.23	0.94	1.34	1.51
K_2O	0.06	0.05	0.04	0.04	0.89	0.28	0.48	0.23	0.32	0.17
P_2O_5	b.d.	b.d.	b.d.	b.d.	0.031	0.041	0.112	b.d.	b.d.	b.d.
LOI	0.49	0.66	0.55	0.96	2.06	1.84	1.65	2.23	3.32	12.12
Sum	100.0	99.9	98.5	96.3	98.2	100.0	100.2	98.2	99.7	99.4
Sc	49	34	53	45	46	52	36	43	43	34
V	172	98	196	133	243	246	299	139	226	111
Cr	704	450	1427	589	561	124	26	428	488	30
Co	44	34	52	40	42	57	33	32	36	24
Ni	129	117	216	118	155	72	24	106	101	34
Cu	27	9	16	22	19	19	58	13	78	82
Zn	44	31	50	35	57	44	51	26	60	20
Ga	10	12	9	11	14	12	18	12	14	16
Rb	*0.8*	*0.7*	*0.6*	*0.6*	*21.8*	*5.3*	*11.7*	*6.0*	*6.0*	*3.9*
Sr	*73*	*101*	*51*	*85*	*123*	*140*	*257*	*156*	*147*	*222*
Y	*2.19*	*1.22*	*3.16*	*1.58*	*11.37*	*15.74*	*20.33*	*6.16*	*7.78*	*4.35*
Zr	*1.19*	*0.95*	*2.72*	*0.70*	*27.08*	*59.18*	*34.47*	*9.29*	*11.39*	*8.53*
Nb	*0.014*	*0.017*	*0.036*	*0.007*	*0.530*	*0.755*	*1.695*	*0.181*	*0.213*	*0.115*
Cs	*0.091*	*0.167*	*0.196*	*0.246*	*0.768*	*0.341*	*0.846*	*12.59*	*1.061*	*2.388*
Ba	*6.35*	*3.71*	*4.58*	*3.25*	*63.47*	*23.95*	*80.23*	*25.00*	*36.37*	*14.41*
La	*0.111*	*0.111*	*0.198*	*0.070*	*2.914*	*2.885*	*6.899*	*1.300*	*1.415*	*0.718*
Ce	*0.296*	*0.260*	*0.503*	*0.189*	*6.905*	*8.180*	*18.761*	*3.024*	*3.694*	*1.815*
Pr	*0.048*	*0.038*	*0.075*	*0.031*	*0.973*	*1.271*	*2.767*	*0.432*	*0.565*	*0.274*
Nd	*0.254*	*0.179*	*0.380*	*0.168*	*4.298*	*5.946*	*11.96*	*1.980*	*2.628*	*1.420*
Sm	*0.116*	*0.072*	*0.170*	*0.082*	*1.278*	*1.849*	*3.115*	*0.660*	*0.864*	*0.490*
Eu	*0.076*	*0.064*	*0.088*	*0.062*	*0.482*	*0.562*	*1.043*	*0.304*	*0.354*	*0.286*
Gd	*0.212*	*0.130*	*0.320*	*0.156*	*1.631*	*2.356*	*3.395*	*0.908*	*1.140*	*0.684*
Tb	*0.043*	*0.025*	*0.063*	*0.032*	*0.279*	*0.391*	*0.537*	*0.155*	*0.196*	*0.123*
Dy	*0.351*	*0.191*	*0.491*	*0.252*	*1.909*	*2.650*	*3.465*	*1.062*	*1.345*	*0.871*
Ho	*0.090*	*0.051*	*0.127*	*0.065*	*0.443*	*0.613*	*0.789*	*0.245*	*0.311*	*0.185*
Er	*0.256*	*0.138*	*0.365*	*0.183*	*1.173*	*1.602*	*2.047*	*0.640*	*0.806*	*0.505*
Tm	*0.042*	*0.022*	*0.061*	*0.029*	*0.184*	*0.247*	*0.314*	*0.096*	*0.123*	*0.074*
Yb	*0.291*	*0.167*	*0.422*	*0.210*	*1.225*	*1.588*	*2.070*	*0.614*	*0.814*	*0.522*
Lu	*0.046*	*0.026*	*0.069*	*0.034*	*0.188*	*0.243*	*0.314*	*0.090*	*0.122*	*0.076*
Hf	*0.046*	*0.033*	*0.091*	*0.027*	*0.880*	*1.309*	*1.269*	*0.301*	*0.353*	*0.312*
Ta	*0.002*	*0.007*	*0.005*	*0.002*	*0.050*	*0.060*	*0.138*	*0.017*	*0.021*	*0.012*
Pb	*0.329*	*0.405*	*0.627*	*0.243*	*5.632*	*1.940*	*5.262*	*1.746*	*1.850*	*0.475*
Th	*0.015*	*0.011*	*0.039*	*0.008*	*0.835*	*0.796*	*2.006*	*0.283*	*0.462*	*0.197*
U	*0.007*	*0.007*	*0.020*	*0.004*	*0.249*	*0.321*	*0.412*	*0.093*	*0.087*	*0.065*
Mg#	0.79	0.79	0.80	0.81	0.73	0.73	0.57	0.79	0.78	0.78

LOI: loss of ignition; total iron quoted as Fe_2O_3; Mg# = $Mg/(Mg+Fe^{2+})$; b.d. = below detection limit. Data analysed by LA-ICPMS are signed in italics. Oxides in wt%, elements in ppm.

Appendix B-5: Mantle Peridotites of the Evros area

Sample	E70	E71	E72	E73	E52	E55	E57	E59	E61	E60
Material	Harzburgite									Dunite
SiO_2	43.8	46.2	45.8	43.7	47.6	49.2	45.6	44.5	45.5	39.8
TiO_2	0.02	0.02	0.02	0.02	0.01	0.02	0.01	0.01	0.01	0.01
Al_2O_3	0.85	1.32	1.55	1.53	0.70	0.93	0.31	0.56	0.54	0.12
Fe_2O_3	9.6	8.1	9.6	9.0	7.9	5.4	11.6	9.2	10.6	8.9
MnO	0.06	0.10	0.10	0.13	0.10	0.06	0.21	0.14	0.19	0.12
MgO	45.0	43.5	42.3	43.3	42.4	42.4	41.6	44.5	42.4	50.2
CaO	0.03	b.d.	0.01	1.60	0.66	1.30	0.06	0.32	0.05	0.19
Na_2O	b.d.	b.d.	b.d.	b.d.	b.d.	b.d.	b.d.	b.d.	b.d.	b.d.
K_2O	b.d.	b.d.	b.d.	b.d.	b.d.	b.d.	b.d.	b.d.	b.d.	b.d.
P_2O_5	b.d.	b.d.	b.d.	b.d.	0.0057	b.d.	0.0012	b.d.	b.d.	0.0012
LOI	1.5	4.4	2.3	4.6	12.2	11.8	14.4	22.2	12.6	20.4
Sum	100.5	100.4	100.1	100.6	100.5	100.3	100.5	101.3	100.6	101.3
Sc	36	28	29	39	4	29	2	8	8	2
V	112	209	216	133	33	64	18	30	28	13
Cr	2741	3141	2729	2818	2941	4226	2374	2172	3203	2441
Co	24	28	28	90	92	58	145	96	121	121
Ni	3020	2505	2543	2411	1605	1404	3016	2807	2719	3045
Cu	86	76	56	1	9	b.d.	b.d.	b.d.	b.d.	b.d.
Zn	23	117	70	60	45	31	65	78	57	32
Ga	15	16	16	4	4	2	1	1	2	b.d.
Rb	*0.02*	*0.004*	*0.004*	*0.09*	*0.55*	*0.10*	*0.33*	*0.03*	*0.15*	*0.03*
Sr	*1.2*	*0.2*	*0.3*	*0.7*	*35.3*	*1.9*	*7.9*	*2.0*	*2.5*	*11.2*
Y	*0.09*	*0.34*	*0.07*	*0.41*	*0.30*	*0.82*	*0.03*	*0.05*	*0.10*	*0.05*
Zr	*0.27*	*0.27*	*0.04*	*0.03*	*0.70*	*0.58*	*0.12*	*0.23*	*0.40*	*0.17*
Nb	*0.017*	*0.026*	*0.005*	*0.007*	*0.058*	*0.027*	*0.132*	*0.013*	*0.014*	*0.015*
Cs	*0.216*	*0.001*	*0.001*	*0.037*	*0.547*	*0.028*	*0.177*	*0.004*	*0.074*	*0.001*
Ba	*0.48*	*2.17*	*0.53*	*0.15*	*1.11*	*1.07*	*5.38*	*0.75*	*2.82*	*4.98*
La	*0.0230*	*0.0780*	*0.0048*	*0.0036*	*0.0952*	*0.0544*	*0.0300*	*0.0306*	*0.0323*	*0.0145*
Ce	*0.0470*	*0.0889*	*0.0100*	*0.0059*	*0.2338*	*0.2442*	*0.0135*	*0.0589*	*0.0596*	*0.0206*
Pr	*0.0053*	*0.0145*	*0.0015*	*0.0006*	*0.0309*	*0.0403*	*0.0034*	*0.0067*	*0.0059*	*0.0040*
Nd	*0.0212*	*0.0647*	*0.0037*	b.d.	*0.1470*	*0.2276*	*0.0037*	*0.0263*	*0.0200*	*0.0083*
Sm	*0.0053*	*0.0126*	*0.0019*	*0.0132*	*0.0542*	*0.0847*	b.d.	*0.0078*	b.d.	*0.0087*
Eu	*0.0010*	*0.0040*	*0.0003*	*0.0018*	*0.0277*	*0.0412*	b.d.	*0.0011*	b.d.	b.d.
Gd	*0.0039*	*0.0233*	*0.0025*	*0.0209*	*0.0614*	*0.1156*	b.d.	*0.0044*	b.d.	b.d.
Tb	*0.0013*	*0.0043*	*0.0007*	*0.0046*	*0.0103*	*0.0204*	b.d.	*0.0008*	b.d.	b.d.
Dy	*0.0073*	*0.0301*	*0.0064*	*0.0448*	*0.0575*	*0.1457*	b.d.	*0.0064*	b.d.	b.d.
Ho	*0.0016*	*0.0077*	*0.0017*	*0.0124*	*0.0103*	*0.0295*	b.d.	*0.0019*	b.d.	b.d.
Er	*0.0088*	*0.0277*	*0.0084*	*0.0496*	*0.0333*	*0.0995*	b.d.	*0.0098*	*0.0046*	b.d.
Tm	*0.0012*	*0.0045*	*0.0017*	*0.0082*	*0.0058*	*0.0154*	*0.0031*	*0.0014*	*0.0019*	*0.0021*
Yb	*0.0146*	*0.0360*	*0.0131*	*0.0668*	*0.0497*	*0.1040*	*0.0003*	*0.0191*	*0.0379*	*0.0012*
Lu	*0.0028*	*0.0063*	*0.0028*	*0.0129*	*0.0093*	*0.0157*	*0.0022*	*0.0049*	*0.0101*	*0.0041*
Hf	*0.0055*	*0.0087*	*0.0000*	b.d.	*0.0240*	*0.0129*	*0.0027*	*0.0060*	*0.0092*	b.d.
Ta	*0.0007*	*0.0022*	*0.0005*	*0.0018*	*0.0027*	*0.0040*	*0.0001*	*0.0029*	b.d.	*0.0034*
Pb	*0.0129*	*0.0079*	*0.0136*	*0.0105*	*0.2928*	*0.0143*	*0.0656*	*0.0402*	*0.2441*	*0.1645*
Th	*0.0086*	*0.0131*	*0.0013*	*0.0008*	*0.0195*	*0.0107*	*0.0010*	*0.0148*	*0.0170*	*0.0061*
U	*0.0040*	*0.0035*	*0.0008*	b.d.	*0.0212*	*0.0082*	*0.0055*	*0.0034*	*0.0035*	*0.1759*
Mg#	0.92	0.93	0.91	0.92	0.93	0.95	0.89	0.92	0.90	0.93

LOI: loss of ignition; total iron quoted as Fe_2O_3; Mg# = $Mg/(Mg+Fe^{2+})$; b.d. = below detection limit. Data analysed by LA-ICPMS are signed in italics. Oxides in wt%, elements in ppm.

Appendix C – Mineral chemical data

Appendix C-1: Spinels from Lesvos Island lherzolites

Sample	TiO_2	Al_2O_3	Cr_2O_3	Fe_2O_3	FeO	MnO	MgO	Total	Mg#	Cr#	F
L08-Sp01	0.11	45.0	21.6	2.35	13.7	0.17	16.3	99.7	0.68	0.24	9.9
L08-Sp02	0.12	44.8	20.7	3.05	14.1	0.17	16.0	99.4	0.67	0.24	9.6
L08-Sp04	0.15	43.9	22.3	2.25	13.8	0.15	16.1	99.2	0.67	0.25	10.3
L08-Sp05	0.12	44.1	21.0	3.07	14.3	0.16	15.7	99.0	0.66	0.24	9.8
L08-Sp08	0.13	45.0	21.0	2.67	14.5	0.12	15.8	99.9	0.66	0.24	9.7
L08-Sp11	0.10	42.5	23.8	2.51	15.0	0.13	15.3	99.9	0.65	0.27	11.0
L14-Sp02	0.05	54.7	13.2	1.41	11.2	0.06	19.0	100.1	0.75	0.14	4.3
L14-Sp06	0.02	55.7	12.3	1.60	12.3	0.06	18.5	101.2	0.73	0.13	3.5
L14-Sp09	0.07	54.7	12.8	1.89	11.3	0.12	18.9	100.5	0.75	0.14	4.0
L14-Sp13	0.09	53.5	15.0	1.45	11.8	0.16	18.7	101.2	0.74	0.16	5.6
L14-Sp14	0.08	53.4	14.9	1.71	11.5	0.09	18.9	101.1	0.75	0.16	5.5
L14-Sp20A	0.08	53.7	14.0	1.67	11.4	0.11	18.8	100.3	0.75	0.15	4.9
L14-Sp21	0.03	54.6	12.8	1.38	11.1	0.12	18.9	99.6	0.75	0.14	4.0
L14-Sp26-dark	0.04	53.3	15.0	1.51	10.8	0.10	19.2	100.5	0.76	0.16	5.6
L14-Sp26-light	0.08	52.4	15.4	1.54	11.0	0.07	18.9	99.9	0.75	0.16	5.9
L14-Sp-28	0.08	53.9	13.4	1.61	11.3	0.12	18.8	99.7	0.75	0.14	4.5
L46-Sp01	0.22	38.7	28.6	3.31	14.5	0.11	15.7	101.6	0.66	0.33	13.0
L46-Sp02A	0.17	41.5	25.6	3.52	13.7	0.11	16.5	101.4	0.68	0.29	11.7
L46-Sp04	0.26	37.4	29.4	3.08	15.3	0.21	15.0	101.2	0.64	0.34	13.4
L46-Sp05A	0.22	37.8	28.5	4.38	15.3	0.14	15.1	101.9	0.64	0.34	13.1
L46-Sp06	0.15	36.7	31.3	2.88	14.8	0.15	15.3	101.7	0.65	0.36	13.9
L46-Sp08	0.20	36.1	30.3	3.35	15.8	0.16	14.5	101.0	0.62	0.36	13.8
L46-Sp11A	0.22	37.9	29.1	3.73	14.9	0.10	15.5	101.8	0.65	0.34	13.2
L46-Sp12	0.21	39.9	27.5	3.15	14.8	0.14	15.6	101.8	0.65	0.32	12.5
L46-Sp13	0.23	39.4	27.3	3.36	14.7	0.21	15.4	101.1	0.65	0.32	12.5
L46-Sp15A	0.21	36.4	30.0	3.67	15.3	0.19	14.8	101.0	0.63	0.36	13.7
L46-Sp16A	0.19	39.2	27.5	3.89	14.2	0.19	15.8	101.4	0.67	0.32	12.6
L46-Sp17	0.24	37.9	29.3	3.62	14.9	0.20	15.4	102.0	0.65	0.34	13.2
L46-Sp18A	0.18	38.6	28.1	3.42	15.0	0.16	15.2	101.2	0.64	0.33	12.8
L46-Sp19	0.21	38.0	29.1	3.55	15.3	0.10	15.2	101.9	0.64	0.34	13.2
L46-Sp20	0.21	38.5	28.1	3.30	15.3	0.16	15.1	101.1	0.64	0.33	12.9
L46-Sp23	0.22	36.6	29.9	3.65	15.3	0.19	14.8	101.1	0.63	0.35	13.6
L46-Sp24	0.21	36.7	29.3	3.96	15.5	0.15	14.7	100.9	0.63	0.35	13.4
L46-Sp25	0.23	36.1	30.2	3.42	15.7	0.20	14.5	100.9	0.62	0.36	13.8
L46-Sp26	0.24	38.5	27.6	4.15	15.2	0.14	15.2	101.7	0.64	0.32	12.7
L46-Sp27A	0.24	35.0	30.6	4.13	16.6	0.15	13.9	101.1	0.60	0.37	14.0
L46-Sp29	0.23	39.0	27.6	3.85	15.2	0.20	15.3	101.8	0.64	0.32	12.7
L46-Sp30	0.22	42.7	24.5	3.32	13.1	0.13	17.0	101.4	0.70	0.28	11.2
L46-Sp31	0.19	37.6	28.5	3.73	14.7	0.21	15.2	100.5	0.65	0.34	13.1
L46-Sp32	0.22	37.6	29.4	3.65	15.2	0.20	15.1	101.9	0.64	0.34	13.3
L46-Sp34	0.20	37.3	29.9	3.39	15.2	0.22	15.1	101.8	0.64	0.35	13.5
L46-Sp36A	0.21	42.6	24.2	3.28	12.9	0.17	16.9	100.6	0.70	0.28	11.1
L46-Sp36B	0.20	43.8	23.3	3.34	12.7	0.06	17.3	101.3	0.71	0.26	10.6
L46-Sp36C	0.25	42.2	24.4	3.68	13.7	0.20	16.5	101.3	0.68	0.28	11.3
L46-Sp37A	0.19	38.0	29.0	3.35	15.0	0.19	15.3	101.4	0.64	0.34	13.2
L46-Sp37B	0.25	39.0	27.7	3.84	14.0	0.13	16.0	101.4	0.67	0.32	12.7
L46-Sp37C	0.22	36.7	30.0	3.36	15.5	0.16	14.8	101.1	0.63	0.35	13.6
L46-Sp38	0.18	37.7	29.3	3.63	14.3	0.13	15.7	101.3	0.66	0.34	13.3
L46-Sp39	0.26	38.9	28.1	3.55	14.8	0.21	15.5	101.8	0.65	0.33	12.8
L51-Sp01A	0.14	40.1	28.1	1.79	15.7	0.14	14.9	101.5	0.63	0.32	12.6
L51-Sp03	0.15	41.0	25.8	3.11	15.3	0.15	15.3	101.2	0.64	0.30	11.8
L51-Sp04	0.13	45.3	21.3	2.88	13.7	0.09	16.5	100.5	0.68	0.24	9.7

Mg#: magnesium number ($Mg/(Mg+Fe^{2+})$); Cr#: chromium number (Cr/(Cr+Al)); F: degree of melting (10ln(Cr#)+24) (in %); Oxides in wt%.

Appendix C-1: Continued

Sample	TiO_2	Al_2O_3	Cr_2O_3	Fe_2O_3	FeO	MnO	MgO	Total	Mg#	Cr#	F
L51-Sp05A	0.26	40.7	25.0	3.80	15.4	0.19	15.1	100.9	0.63	0.29	11.7
L51-Sp05B	0.19	44.1	21.8	3.06	14.2	0.09	16.0	99.9	0.67	0.25	10.1
L51-Sp06	0.17	44.0	22.2	3.63	13.1	0.11	16.8	100.5	0.70	0.25	10.2
L51-Sp08	0.17	39.8	26.5	3.40	15.4	0.19	14.9	100.9	0.63	0.31	12.2
L51-Sp09	0.13	44.2	22.2	3.70	14.3	0.16	16.2	101.3	0.67	0.25	10.2
L51-Sp11	0.08	43.8	22.4	2.92	14.1	0.13	16.0	99.9	0.67	0.26	10.3
L51-Sp12A	0.14	41.7	24.8	3.13	15.1	0.14	15.4	100.9	0.64	0.28	11.4
L51-Sp12B	0.15	41.2	25.7	2.63	15.4	0.13	15.1	101.0	0.64	0.29	11.8
L51-Sp14	0.06	46.4	20.3	3.10	13.7	0.12	16.7	101.0	0.68	0.23	9.2
L51-Sp15	0.07	46.3	20.3	3.06	13.8	0.16	16.6	100.7	0.68	0.23	9.2
L51-Sp18	0.12	42.5	24.4	3.28	14.6	0.16	15.9	101.4	0.66	0.28	11.2
L51-Sp24	0.13	38.5	28.1	2.70	17.9	0.18	13.2	101.4	0.57	0.33	12.9
L54-Sp01	0.03	54.4	13.7	2.49	11.2	0.12	19.2	101.8	0.75	0.14	4.7
L54-Sp02	0.06	54.9	13.1	2.57	11.1	0.08	19.4	101.8	0.76	0.14	4.2
L54-Sp03A	0.08	53.8	14.3	2.39	11.9	0.13	18.8	101.9	0.74	0.15	5.1
L54-Sp04	0.01	54.2	13.0	1.95	11.1	0.10	19.0	99.9	0.75	0.14	4.2
L54-Sp05	0.03	55.0	13.8	1.90	11.1	0.10	19.5	101.9	0.76	0.14	4.6
L54-Sp06A	0.07	53.9	13.8	2.11	11.1	0.08	19.2	100.6	0.76	0.15	4.8
L54-Sp06B	0.07	53.6	14.5	2.54	11.3	0.06	19.2	101.9	0.75	0.15	5.3
L54-Sp06C	0.05	53.3	14.3	2.00	11.4	0.13	18.8	100.5	0.75	0.15	5.2
L54-Sp07A	0.01	55.2	13.0	2.01	11.0	0.11	19.4	101.3	0.76	0.14	4.1
L54-Sp08A	0.05	53.2	14.4	2.42	11.5	0.07	18.8	100.9	0.74	0.15	5.3
L54-Sp11B	0.03	54.3	13.2	2.16	11.1	0.10	19.0	100.5	0.75	0.14	4.3
L54-Sp13	0.04	53.5	13.7	2.40	11.7	0.11	18.5	100.5	0.74	0.15	4.8
L54-Sp14B	0.04	53.8	13.1	3.07	11.4	0.15	18.9	101.0	0.75	0.14	4.4
L54-Sp15	0.03	54.2	13.1	2.32	10.7	0.11	19.2	100.3	0.76	0.14	4.3
L54-Sp18	0.05	54.6	12.7	2.48	10.5	0.13	19.5	100.4	0.77	0.13	3.9
L54-Sp21	0.03	55.3	12.7	2.16	10.9	0.10	19.4	101.2	0.76	0.13	3.8
L54-Sp22D	0.04	54.7	13.6	2.17	10.7	0.07	19.6	101.4	0.77	0.14	4.5
L54-Sp24	0.01	54.5	13.3	2.13	11.3	0.07	19.1	100.9	0.75	0.14	4.4
L54-Sp26C	0.04	53.5	14.7	2.34	10.7	0.09	19.4	101.3	0.76	0.16	5.4
L54-Sp31	0.03	49.5	18.5	2.09	12.0	0.07	18.1	101.0	0.73	0.20	7.9
L61-Sp01	0.10	42.9	22.7	4.14	14.6	0.12	15.8	100.8	0.66	0.26	10.6
L61-Sp02	0.12	40.8	26.3	3.48	13.8	0.14	16.2	101.3	0.68	0.30	12.0
L61-Sp03	0.09	42.4	23.7	3.15	14.3	0.15	15.7	99.9	0.66	0.27	11.0
L61-Sp04	0.07	43.1	23.1	3.97	13.9	0.18	16.2	101.0	0.67	0.26	10.7
L61-Sp06A	0.03	48.0	18.8	2.82	13.2	0.14	17.1	100.7	0.70	0.21	8.3
L61-Sp07	0.11	42.4	23.7	3.29	14.1	0.14	15.9	100.1	0.67	0.27	11.0
L61-Sp08	0.08	46.6	19.8	2.63	13.1	0.14	16.9	99.8	0.70	0.22	8.9
L61-Sp09A	0.03	54.9	10.5	3.76	11.6	0.10	18.6	100.2	0.74	0.11	2.3
L61-Sp12	0.05	50.6	16.6	2.01	12.1	0.12	18.0	100.0	0.73	0.18	6.9
L61-Sp14	0.03	48.7	18.1	3.15	12.4	0.18	17.7	100.8	0.72	0.20	7.9
L61-Sp15	0.03	52.5	14.7	2.39	12.8	0.08	17.8	101.1	0.71	0.16	5.6
L61-Sp16	0.07	45.9	21.6	3.16	13.6	0.11	16.9	101.8	0.69	0.24	9.7
L61-Sp17	0.05	47.7	19.3	2.98	13.0	0.12	17.3	100.8	0.70	0.21	8.6
L61-Sp18	0.06	45.8	20.9	2.09	12.9	0.10	16.9	99.5	0.70	0.23	9.5
L61-Sp20	0.05	49.0	15.5	4.62	13.6	0.12	16.8	100.2	0.69	0.17	6.6
L61-Sp21	0.09	46.1	20.9	2.84	13.5	0.10	16.8	100.9	0.69	0.23	9.4
L61-Sp22	0.10	49.7	17.7	2.60	12.8	0.15	17.7	101.5	0.71	0.19	7.5
L61-Sp24	0.05	48.8	18.7	2.73	13.6	0.10	17.2	101.7	0.69	0.20	8.1
L61-Sp25	0.08	46.0	20.2	2.86	13.4	0.08	16.7	99.9	0.69	0.23	9.2
L61-Sp26	0.08	43.1	22.5	2.42	13.8	0.12	15.8	99.4	0.67	0.26	10.5
L61-Sp27	0.10	43.5	22.9	4.15	13.8	0.17	16.4	101.5	0.68	0.26	10.6
L61-Sp28	0.03	47.8	18.8	3.08	11.4	0.11	18.0	100.1	0.74	0.21	8.3

Mg#: magnesium number ($Mg/(Mg+Fe^{2+})$); Cr#: chromium number (Cr/(Cr+Al)); F: degree of melting (10ln(Cr#)+24) (in %); Oxides in wt%.

Appendix C-1: Continued

Sample	TiO_2	Al_2O_3	Cr_2O_3	Fe_2O_3	FeO	MnO	MgO	Total	Mg#	Cr#	F
L61-Sp29	0.06	44.2	21.8	3.48	13.5	0.12	16.4	100.1	0.68	0.25	10.1
L61-Sp30	0.03	46.7	19.3	3.13	13.4	0.11	16.7	100.0	0.69	0.22	8.7
L61-Sp32	0.08	42.7	24.8	2.85	14.1	0.16	16.1	101.5	0.67	0.28	11.3
L61-Sp33	0.08	46.7	19.4	3.68	13.9	0.15	16.6	101.0	0.68	0.22	8.7
L61-Sp34A	0.12	39.8	26.7	3.41	14.7	0.16	15.4	100.5	0.65	0.31	12.3
L61-Sp34B	0.13	42.3	24.6	3.11	14.4	0.14	15.9	101.0	0.66	0.28	11.3
L61-Sp34C	0.14	42.3	24.5	3.39	14.5	0.16	15.9	101.3	0.66	0.28	11.2
L61-Sp35	0.10	42.8	24.4	2.72	14.4	0.19	15.9	101.1	0.66	0.28	11.1
L61-Sp37	0.04	55.1	12.7	2.22	11.2	0.13	19.0	101.4	0.75	0.13	3.9
L61-Sp39	0.12	39.9	25.9	3.15	13.8	0.13	15.7	99.1	0.67	0.30	12.1
L61-Sp40	0.11	43.6	22.5	2.98	14.0	0.06	16.1	99.8	0.67	0.26	10.4
L61-Sp41	0.15	40.6	25.5	3.31	14.0	0.15	15.8	99.8	0.67	0.30	11.8

Mg#: magnesium number ($Mg/(Mg+Fe^{2+})$); Cr#: chromium number (Cr/(Cr+Al)); F: degree of melting (10ln(Cr#)+24) (in %); Oxides in wt%.

Appendix C-2: Orthopyroxenes from gabbros of the Evros area

Sample	SiO_2	Al_2O_3	Cr_2O_3	FeO*	MnO	MgO	CaO	Na_2O	K_2O	Total	Mg#
E03-px08	55.9	1.28	0.22	14.8	0.25	28.0	1.12	0.05	0.01	101.7	0.77
E03-px11	55.5	1.36	0.23	14.1	0.30	27.4	1.55	0.02	b.d.	100.7	0.78
E03-px12	55.8	1.41	0.18	14.0	0.29	28.4	1.26	0.04	b.d.	101.5	0.78
E03-px13	55.1	1.39	0.18	13.2	0.30	28.4	1.58	0.03	b.d.	100.3	0.80
E03-px13A	55.5	1.33	0.14	13.8	0.23	28.3	1.19	b.d.	b.d.	100.7	0.78
E03-px15	55.4	1.29	0.21	14.0	0.29	28.0	1.52	0.03	b.d.	101.0	0.78
E03-px16	55.9	1.27	0.24	13.7	0.29	28.5	1.18	0.02	b.d.	101.2	0.79
E03-px16B	55.8	1.31	0.19	14.2	0.32	28.6	0.74	0.01	b.d.	101.3	0.78
E03-px17	55.5	1.30	0.20	13.0	0.25	28.8	1.12	b.d.	b.d.	100.4	0.80
E03-px18	55.4	1.31	0.20	14.6	0.33	27.8	1.18	0.04	b.d.	101.1	0.77
E03-px19	54.8	1.28	0.23	13.4	0.32	28.4	1.38	b.d.	b.d.	99.9	0.80
E03-px19A	55.2	1.28	0.21	13.2	0.36	28.7	0.98	0.05	b.d.	100.2	0.80
E03-px22	55.1	1.24	0.18	13.5	0.30	28.1	1.79	0.03	b.d.	100.4	0.79
E03-px23	54.6	1.24	0.19	12.4	0.24	25.7	4.56	0.06	b.d.	99.1	0.79
E03-px24	54.8	1.20	0.17	13.9	0.28	27.8	1.91	0.01	b.d.	100.2	0.79
E03-px26	54.7	1.28	0.18	14.0	0.29	28.0	1.44	0.01	b.d.	100.1	0.79
E03-px28	54.8	1.27	0.17	14.3	0.29	27.9	1.11	0.02	0.01	99.9	0.78
E03-px29	55.0	1.35	0.26	13.9	0.27	28.3	1.33	0.02	b.d.	100.7	0.79
E03-px30	55.5	1.18	0.14	13.3	0.26	28.6	1.14	0.01	b.d.	100.3	0.79
E03-px34	55.8	1.27	0.22	14.4	0.29	27.8	0.97	b.d.	b.d.	100.9	0.77
E03-px35	56.0	1.26	0.18	14.2	0.29	28.2	1.13	0.01	b.d.	101.5	0.78
E03-px38	56.0	1.33	0.24	14.2	0.27	27.9	1.22	0.01	0.01	101.3	0.78
E03-px41	55.8	1.30	0.21	13.6	0.28	28.2	1.31	0.05	b.d.	100.9	0.79
E03-px41A	55.3	1.31	0.18	13.3	0.28	27.4	3.54	b.d.	b.d.	101.5	0.80

Mg#: magnesium number ($Mg/(Mg+Fe^{2+})$); FeO* = total iron expressed as FeO; b.d. = below detection limit; Oxides in wt%.

Appendix C-3: Clinopyroxenes from gabbros of the Evros area

Sample	SiO_2	Al_2O_3	Cr_2O_3	FeO*	MnO	MgO	CaO	Na_2O	K_2O	Total	Mg#
E03-px01	53.3	1.24	0.26	5.9	0.15	15.6	22.85	0.16	0.02	99.7	0.83
E03-px02	54.3	1.61	0.29	5.5	0.14	15.8	22.78	0.21	b.d.	100.8	0.84
E03-px03	54.1	1.54	0.30	5.7	0.16	15.9	22.21	0.21	0.01	100.3	0.83
E03-px04	53.4	1.99	0.55	6.7	0.19	17.3	19.66	0.19	b.d.	100.2	0.82
E03-px05	53.1	2.09	0.52	6.9	0.21	17.4	19.27	0.26	0.01	99.9	0.83
E03-px06	53.2	1.94	0.37	6.1	0.12	16.8	20.63	0.21	b.d.	99.6	0.83
E03-px07	53.3	1.46	0.34	5.0	0.13	16.4	22.68	0.10	0.01	99.6	0.85
E03-px09	53.0	1.57	0.29	5.5	0.16	15.9	22.62	0.19	0.01	99.4	0.85
E03-px10	53.9	1.44	0.32	5.9	0.20	15.7	22.15	0.24	b.d.	100.2	0.83
E03-px14	54.4	1.15	0.11	5.4	0.16	16.1	23.09	0.15	b.d.	100.7	0.84
E03-px16A	53.8	1.31	0.31	5.4	0.15	15.7	23.07	0.14	0.01	99.9	0.84
E03-px1A	53.5	1.83	0.29	5.4	0.12	15.9	22.72	0.20	0.01	100.2	0.84
E03-px20	53.1	1.90	0.36	5.5	0.13	16.1	22.23	0.23	0.01	99.8	0.85
E03-px21	53.0	1.73	0.24	5.8	0.18	16.1	22.07	0.18	b.d.	99.5	0.84
E03-px32	54.0	1.87	0.29	5.4	0.15	16.2	22.42	0.18	b.d.	100.7	0.84
E13-px01	48.3	6.07	0.10	15.1	0.35	14.1	11.35	0.69	0.30	99.1	0.62
E77-px01	53.6	0.93	0.46	4.6	0.16	15.2	24.77	0.09	b.d.	99.9	0.86
E77-px10	53.1	0.97	0.04	6.8	0.20	15.4	22.62	0.26	b.d.	99.7	0.82
E77-px12	54.4	0.38	0.09	5.0	0.23	15.6	24.16	0.04	b.d.	100.1	0.85
E77-px13	53.9	2.12	0.06	5.5	0.20	15.2	22.51	0.97	0.01	100.7	0.87
E77-px14	53.8	1.13	0.04	4.9	0.15	16.1	23.56	0.15	b.d.	100.1	0.86
E77-px14B	54.1	0.71	0.04	4.0	0.21	16.5	24.56	0.02	b.d.	100.2	0.89
E77-px03	54.9	0.66	0.05	5.6	0.21	15.2	24.34	0.23	0.01	101.2	0.83
E77-px04	53.2	1.62	0.09	6.9	0.18	15.4	21.95	0.26	b.d.	100.1	0.80
E77-px05	54.8	0.67	0.04	5.5	0.22	15.4	24.49	0.11	b.d.	101.3	0.83
E77-px07	54.8	0.25	0.15	5.2	0.18	15.4	25.01	0.07	0.02	101.1	0.84
E77-px08	54.9	0.47	0.02	3.9	0.21	16.4	24.85	0.01	b.d.	100.9	0.88
E77-px09A	53.0	0.62	0.27	6.4	0.23	15.0	23.62	0.17	0.01	99.4	0.83
E77-px09B	53.9	0.28	0.02	6.1	0.26	14.9	24.54	0.14	b.d.	100.2	0.83

Mg#: magnesium number ($Mg/(Mg+Fe^{2+})$); FeO* = total iron expressed as FeO; b.d. = below detection limit; Oxides in wt%.

Appendix C-4: Amphiboles from gabbros of the Evros area

Sample	SiO_2	TiO_2	Al_2O_3	Cr_2O_3	FeO*	MnO	MgO	CaO	Na_2O	K_2O	Total
E03-am04	53.13	0.17	3.72	0.31	7.78	0.13	18.82	11.98	0.34	0.03	96.5
E03-am7B	50.93	0.26	5.42	0.64	6.73	0.10	18.91	12.07	0.75	0.01	96.0
E03-am8D	50.86	0.17	4.97	0.27	7.63	0.11	18.56	12.13	0.66	0.05	95.6
E03-am9B	50.03	0.26	6.95	0.29	8.36	0.09	17.26	11.94	1.10	0.06	96.5
E03-am11	54.15	0.27	4.24	0.09	7.30	0.14	19.33	11.69	0.51	0.05	97.9
E03-am15	50.97	0.22	6.07	0.39	7.70	0.14	17.77	12.21	0.70	0.03	96.4
E13-am01	45.97	2.13	7.97	0.03	15.99	0.33	12.26	11.37	0.97	0.40	97.5
E13-am02	45.43	1.65	8.85	0.03	16.21	0.32	11.63	11.65	1.08	0.34	97.3
E13-am04	47.77	1.43	7.16	0.02	14.87	0.38	13.21	11.59	1.05	0.24	97.9
E13-am05	52.59	0.52	3.52	0.06	12.85	0.35	15.34	11.69	0.43	0.13	97.6
E13-am06	48.63	0.95	6.56	0.06	14.75	0.36	13.49	11.11	0.80	0.26	97.2
E13-am07	48.86	1.00	6.51	0.03	14.77	0.35	13.40	11.38	0.88	0.31	97.7
E13-am08	48.54	0.96	6.38	0.29	14.29	0.30	13.26	11.66	0.75	0.33	96.8
E13-am09	45.78	1.55	8.59	0.03	16.19	0.29	11.97	11.51	1.10	0.49	97.6
E13-am11	53.02	0.46	3.23	0.04	12.77	0.34	15.69	11.76	0.35	0.12	97.9
E13-am12	46.44	1.55	8.64	0.06	16.32	0.37	11.81	11.58	1.01	0.46	98.4
E13-am13	49.12	0.76	6.59	0.04	14.67	0.26	13.34	11.73	0.68	0.33	97.6
E13-am14	45.44	2.01	8.59	0.04	16.46	0.30	11.67	11.43	1.01	0.41	97.4
E13-am15	48.83	1.05	6.54	0.01	14.80	0.35	13.26	11.57	0.79	0.33	97.6
E13-am16	50.29	0.44	5.59	0.10	13.87	0.26	14.06	11.88	0.72	0.19	97.5
E13-am18	46.23	1.59	8.23	0.04	15.70	0.28	11.87	11.51	1.02	0.37	97.0
E13-am19	48.77	1.04	6.57	0.10	14.79	0.30	13.40	11.54	0.76	0.28	97.7
E13-am20	48.24	0.79	7.08	0.05	15.14	0.31	13.07	11.75	0.86	0.32	97.7
E13-am21	47.97	1.09	6.53	0.01	14.88	0.33	13.16	11.19	0.91	0.28	96.4
E13-am22	45.00	1.90	9.05	0.04	15.95	0.35	11.65	11.55	1.24	0.32	97.2
E13-am24	50.49	0.58	4.76	0.00	13.67	0.36	14.69	11.58	0.52	0.20	97.0
E13-am26	48.21	1.09	6.40	0.05	14.23	0.36	13.02	11.46	0.84	0.25	96.0
E13-am27	48.51	1.06	6.86	0.06	15.29	0.28	13.10	11.52	0.82	0.40	98.0
E13-am28	51.00	0.41	5.41	0.06	13.43	0.33	13.64	11.99	0.69	0.21	97.3
E13-am29	46.19	1.37	8.41	0.04	15.86	0.29	12.07	11.64	0.96	0.45	97.5
E13-am30	47.48	1.14	6.59	1.09	15.06	0.36	12.79	11.06	1.01	0.32	97.0
E13-am33	50.03	0.59	6.12	0.02	14.20	0.23	13.46	12.13	0.73	0.21	97.8
E13-am34	48.90	0.81	6.78	0.11	14.74	0.36	13.23	11.75	0.87	0.27	97.9
E77-am01	51.45	0.84	5.17	0.02	9.42	0.16	17.97	11.66	0.96	0.10	97.8
E77-am02	53.33	0.39	2.08	1.05	9.14	0.20	17.67	12.68	0.17	0.05	96.9
E77-am04	50.58	1.07	5.62	0.06	9.61	0.12	17.54	11.64	1.02	0.15	97.5
E77-am05	53.42	0.19	2.44	0.21	14.81	0.68	13.30	12.39	0.20	0.03	97.8
E77-am08	56.38	0.16	1.17	0.03	6.19	0.16	20.25	12.70	0.13	0.03	97.3
E77-am10	52.11	0.47	4.88	0.03	9.36	0.19	17.99	11.67	0.94	0.20	97.9
E77-am11	52.43	0.43	4.78	0.04	9.39	0.17	17.47	11.78	0.69	0.20	97.5
E77-am12	49.51	0.09	5.71	0.73	16.60	0.29	12.33	11.69	1.24	0.11	98.4
E77-am14	49.04	1.45	6.22	0.14	10.10	0.13	16.54	11.56	1.19	0.18	96.7
E77-am14B	49.36	1.70	6.50	0.05	9.65	0.10	17.10	11.58	1.38	0.20	97.8
E77-am15	51.31	0.93	4.45	0.06	9.46	0.18	17.44	11.78	0.80	0.25	96.8
E77-am16	54.76	0.41	2.26	0.07	6.80	0.19	20.14	12.24	0.25	0.00	97.2
E77-am19	50.33	1.19	5.44	0.04	9.97	0.20	16.70	12.02	0.81	0.29	97.1
E77-am21	53.57	0.05	2.68	0.08	15.52	0.51	12.92	12.00	0.33	0.07	97.8
E77-am22	54.73	0.18	2.96	0.07	5.36	0.20	20.60	12.07	0.46	0.06	96.8
E77-am23	51.31	0.85	4.89	0.09	8.63	0.14	17.78	12.21	0.67	0.24	97.0
E77-am24	53.87	0.28	2.86	0.07	5.78	0.16	20.04	13.34	0.35	0.02	96.9
E77-am24A	49.34	1.15	7.62	0.08	8.64	0.12	17.01	11.94	1.42	0.17	97.7
E77-am27	52.01	0.79	4.79	0.06	8.53	0.17	18.28	11.42	0.82	0.20	97.2
E77-am27B	55.39	0.23	1.72	0.11	6.37	0.16	20.04	12.59	0.17	0.03	96.9
E77-am28	49.94	0.76	7.94	0.08	8.67	0.11	16.50	12.93	1.17	0.06	98.3
E77-am31	51.11	0.57	6.30	0.06	7.71	0.14	17.89	12.45	0.77	0.03	97.2
E77-am33	53.92	0.29	3.35	0.07	8.32	0.18	18.89	11.65	0.55	0.08	97.4
E77-am34	51.63	0.52	4.91	0.08	8.06	0.14	18.81	11.87	0.75	0.16	97.0
E77-am36	55.65	0.11	0.46	0.07	9.69	0.15	18.20	12.78	0.05	0.01	97.3

FeO* = total iron expressed as FeO; Oxides in wt%.

Appendix C-5: Spinels from harzburgites of the Evros area

Sample	TiO_2	Al_2O_3	Cr_2O_3	Fe_2O_3	FeO	MnO	MgO	Total	Mg#	Cr#	F
E57-Sp01	0.08	10.78	53.6	4.0	23.9	0.49	5.62	99.7	0.30	0.77	21.4
E57-Sp02	0.05	7.32	54.3	7.0	24.7	0.60	4.69	99.7	0.25	0.83	22.2
E57-Sp03	0.04	2.10	58.9	8.2	25.7	0.58	3.55	99.9	0.20	0.95	23.5
E57-Sp04	0.32	0.22	32.5	35.6	26.7	0.42	2.59	99.2	0.15	0.99	23.9
E57-Sp05	0.28	0.13	35.2	32.3	26.9	0.56	2.22	98.4	0.13	0.99	23.9
E57-Sp06	0.08	11.19	53.7	3.2	23.3	0.48	6.03	99.0	0.32	0.76	21.3
E72-Sp01	0.73	0.18	17.6	48.9	26.8	0.39	2.40	97.7	0.14	0.98	23.8
E72-Sp02	0.70	0.17	18.8	48.9	28.3	0.37	1.86	99.9	0.10	0.99	23.9
E72-Sp03	0.71	0.15	17.6	50.3	28.3	0.36	1.87	100.1	0.11	0.99	23.9
E72-Sp06	0.73	0.22	21.6	45.8	27.9	0.50	2.02	99.5	0.11	0.98	23.8
E72-Sp07	0.75	0.24	21.9	45.2	27.9	0.46	2.03	99.3	0.11	0.98	23.8
E72-Sp08	0.69	0.19	19.1	48.5	27.8	0.46	2.00	99.6	0.11	0.99	23.9
E72-Sp09	0.64	0.18	18.2	50.0	26.8	0.42	2.71	99.7	0.15	0.99	23.9
E72-Sp10	0.81	0.27	23.2	44.1	27.7	0.50	2.23	99.6	0.13	0.98	23.8
E72-Sp11	0.81	0.27	21.6	45.8	27.9	0.50	2.05	99.8	0.12	0.98	23.8
E72-Sp12	0.70	0.20	19.9	47.5	27.8	0.42	2.08	99.4	0.12	0.99	23.8
E72-Sp13	0.74	0.23	22.5	44.7	27.7	0.44	2.12	99.3	0.12	0.98	23.8
E72-Sp15	0.68	0.84	22.5	44.2	24.2	0.49	4.12	97.8	0.23	0.95	23.5
E72-Sp16	0.69	0.22	21.1	46.3	27.8	0.48	2.11	99.3	0.12	0.98	23.8
E72-Sp17	0.72	0.34	23.3	43.9	27.2	0.45	2.42	99.1	0.14	0.98	23.8
E72-Sp18	0.70	0.88	23.4	43.5	24.2	0.47	4.24	98.1	0.24	0.95	23.5
E72-Sp19	0.73	0.30	23.5	44.3	27.2	0.48	2.61	99.7	0.15	0.98	23.8
E72-Sp20	0.74	0.37	22.1	44.8	27.0	0.39	2.57	98.7	0.15	0.98	23.8
E72-Sp21	0.76	0.30	21.7	46.1	27.6	0.45	2.29	100.0	0.13	0.98	23.8
E72-Sp22	0.66	0.18	19.6	48.0	28.1	0.33	1.92	99.6	0.11	0.99	23.9
E72-Sp23	0.70	0.38	20.1	47.6	27.9	0.44	2.18	100.1	0.12	0.97	23.7
E72-Sp24	0.78	0.22	21.3	46.1	27.7	0.42	2.19	99.5	0.12	0.99	23.9
E72-Sp25	0.72	0.37	22.1	45.3	26.7	0.61	2.74	99.3	0.15	0.98	23.8
E72-Sp26	0.70	0.19	20.5	46.6	27.3	0.51	2.27	98.7	0.13	0.99	23.9
E72-Sp27	0.73	0.32	21.6	45.4	27.1	0.47	2.39	98.7	0.14	0.98	23.8
E72-Sp28	0.68	0.22	21.0	46.3	27.2	0.47	2.27	99.0	0.13	0.98	23.8
E72-Sp30	0.60	0.19	18.3	49.1	23.3	0.37	4.50	97.2	0.26	0.98	23.8
E72-Sp32	0.73	0.58	20.2	46.8	25.9	0.39	3.22	98.6	0.18	0.96	23.6
E72-Sp33	0.70	0.27	19.4	47.8	27.4	0.51	2.21	99.2	0.13	0.98	23.8
E72-Sp34	0.74	0.27	22.3	45.5	27.3	0.49	2.42	99.9	0.14	0.98	23.8
E72-Sp35	0.66	0.21	19.7	48.3	28.1	0.44	2.07	100.2	0.12	0.98	23.8
E72-Sp36	0.76	0.26	22.5	44.9	27.7	0.51	2.17	99.6	0.12	0.98	23.8
E72-Sp37	0.75	0.20	18.3	49.2	28.3	0.41	1.83	99.6	0.10	0.98	23.8
E72-Sp38	0.70	0.22	18.5	48.8	27.9	0.36	2.00	99.4	0.11	0.98	23.8
E72-Sp39	0.73	0.20	19.6	48.3	28.1	0.49	2.04	100.1	0.11	0.98	23.8
E72-Sp40	0.70	0.22	17.7	50.1	28.3	0.37	1.89	99.9	0.11	0.98	23.8
E72-Sp41	0.67	0.20	19.9	47.3	27.9	0.39	1.98	99.1	0.11	0.99	23.9
E72-Sp42	0.72	0.21	19.7	48.1	28.3	0.45	1.89	100.1	0.11	0.98	23.8
E72-Sp43	0.72	0.23	19.8	47.4	27.6	0.40	2.13	99.0	0.12	0.98	23.8
E72-Sp44	0.71	0.56	22.3	45.3	26.1	0.50	3.17	99.6	0.18	0.96	23.6
E72-Sp47	0.65	0.13	19.5	48.2	28.1	0.39	1.91	99.6	0.11	0.99	23.9
E72-Sp48	0.68	0.46	19.3	47.9	26.2	0.41	2.97	98.7	0.17	0.97	23.7
E72-Sp49	0.70	0.18	17.4	49.5	28.1	0.38	1.77	98.8	0.10	0.98	23.8
E72-Sp51	0.01	0.00	0.0	66.9	28.0	0.55	0.36	96.9	0.02	1.00	24.0
E72-Sp52	0.73	0.27	18.6	48.5	28.0	0.45	1.93	99.2	0.11	0.98	23.8
E72-Sp53	0.74	0.49	22.2	45.3	26.6	0.45	2.90	99.4	0.16	0.97	23.7
E72-Sp55	0.69	0.15	17.1	50.9	28.2	0.43	1.87	100.2	0.11	0.99	23.9
E72-Sp57	0.67	0.12	14.6	52.9	28.5	0.33	1.59	99.6	0.09	0.99	23.9
E74-Sp01	0.30	0.14	15.0	53.2	27.7	0.31	1.84	99.4	0.11	0.99	23.9
E74-Sp03	0.31	0.12	15.7	52.1	27.6	0.38	1.76	98.8	0.10	0.99	23.9
E74-Sp04	0.35	0.16	20.1	48.4	27.4	0.48	2.13	99.8	0.12	0.99	23.9
E74-Sp05	0.40	0.11	17.0	50.9	27.7	0.47	1.68	99.2	0.10	0.99	23.9

Mg#: magnesium number ($Mg/(Mg+Fe^{2+})$); Cr#: chromium number (Cr/(Cr+Al)); F: degree of melting (10ln(Cr#)+24) (in %); Oxides in wt%.

Appendix D – Sr and Nd isotopic geochemical data

Appendix D-1: Lesvos Island mafic and ultramafic rocks

Sample	$^{147}Sm/^{144}Nd$	$^{143}Nd/^{144}Nd$[1]	εNd[2]	$\varepsilon Nd_{(i)}$[2,3]	$^{87}Rb/^{86}Sr$	$^{87}Sr/^{86}Sr$[1]	$^{87}Sr/^{86}Sr_{(i)}$[3]
L29	0.19	0.512888 ± 11	5.3	5.9	0.068	0.704656 ± 10	0.704410
L30	0.20	0.512873 ± 9	4.6	4.6	0.027	0.704619 ± 13	0.704522
L31	0.21	0.512973 ± 8	6.3	6.2	0.029	0.705205 ± 9	0.705099
L36	0.22	0.512870 ± 7	4.5	3.8	0.140	0.705031 ± 9	0.704527
L37	0.19	0.512890 ± 9	4.9	5.1	0.075	0.704849 ± 10	0.704578
L69	0.15	0.512627 ± 10	-0.2	1.3	0.024	0.705723 ± 8	0.705638
L32	0.33	0.512969 ± 13	8.8	2.1	0.218	0.709119 ± 10	0.708335
L50	0.28	0.513091 ± 29	13.8	6.0	0.361	0.706254 ± 13	0.704956
L62	0.42	0.513344 ± 8	6.5	6.6	0.086	0.705656 ± 9	0.705346

1) Uncertainties are given as 2σ.
2) εNd and $\varepsilon Nd_{(i)}$ have been calculated using the chondrite universal reservoir (CHUR) with present-day values: $^{143}Nd/^{144}Nd = 0.512638$ and $^{147}Sm/^{144}Nd = 0.1967$.
3) Initial ratios have been recalculated using Rb and Sr, and Sm and Nd as determined by XRF and LA-ICPMS respectively with $\lambda^{87}Rb = 1.42 \times 10^{-11}$ and $\lambda^{147}Sm = 6.54 \times 10^{-12}$.
The age used for recalculation (253 Ma) is based on SHRIMP zircon dating as described in Chapter 1, Section 6.

Appendix D-2: Samothraki Island basalts, dolerites and diorite

Sample	$^{147}Sm/^{144}Nd$	$^{143}Nd/^{144}Nd$[1]	εNd[2]	$\varepsilon Nd_{(i)}$[2,3]	$^{87}Rb/^{86}Sr$	$^{87}Sr/^{86}Sr$[1]	$^{87}Sr/^{86}Sr_{(i)}$[3]
SA02	0.18	0.512880 ± 9	4.7	5.0	0.026	0.703603 ± 16	0.703544
SA04	0.20	0.512906 ± 1	5.2	5.2	0.006	0.704881 ± 7	0.704867
SA14	0.21	0.512985 ± 9	6.8	6.6	0.048	0.703566 ± 11	0.703458
SA15	0.20	0.512932 ± 6	5.7	5.6	0.050	0.703526 ± 11	0.703412
SA22	0.19	0.512875 ± 10	4.6	4.7	0.576	0.705167 ± 12	0.703856
SA23	0.19	0.513004 ± 7	7.1	7.2	0.736	0.706694 ± 9	0.705020
SA27	0.21	0.512940 ± 8	5.9	5.7	0.049	0.705961 ± 12	0.705849
SA10	0.17	0.512818 ± 15	3.5	4.1	0.079	0.704667 ± 12	0.704486
SA31	0.15	0.512743 ± 11	2.0	3.0	0.490	0.706581 ± 14	0.705466
SA33	0.16	0.512772 ± 8	2.6	3.4	0.105	0.705600 ± 8	0.705362
SA35	0.20	0.512699 ± 8	1.2	1.1	0.199	0.705344 ± 8	0.704892
SA18	0.22	0.512861 ± 13	4.3	3.8	0.082	0.704932 ± 10	0.704745
SA40	0.25	0.512921 ± 16	5.5	4.3	0.054	0.704150 ± 10	0.704026
SA42	0.19	0.512904 ± 9	5.2	5.2	0.031	0.703952 ± 13	0.703883
SA46	0.12	0.512650 ± 10	0.2	1.9	0.138	0.704667 ± 6	0.704353

1) Uncertainties are given as 2σ.
2) εNd and $\varepsilon Nd_{(i)}$ have been calculated using the chondrite universal reservoir (CHUR) with present-day values: $^{143}Nd/^{144}Nd = 0.512638$ and $^{147}Sm/^{144}Nd = 0.1967$.
3) Initial ratios have been recalculated using Rb and Sr, and Sm and Nd as determined by XRF and LA-ICPMS respectively with $\lambda^{87}Rb = 1.42 \times 10^{-11}$ and $\lambda^{147}Sm = 6.54 \times 10^{-12}$.
The age used for recalculation (160 Ma) is based on SHRIMP zircon dating as described in Chapter 2, Section 6.

Appendix D-3: Mafic and ultramafic rocks of the Evros area

Sample	$^{147}Sm/^{144}Nd$	$^{143}Nd/^{144}Nd$[1]	εNd[2]	$\varepsilon Nd_{(i)}$[2,3]	$^{87}Rb/^{86}Sr$	$^{87}Sr/^{86}Sr$[1]	$^{87}Sr/^{86}Sr_{(i)}$[3]
E17	0.25	0.513093 ± 13	7.2	7.7	0.186	0.704384 ± 6	0.703938
E26	0.19	0.512784 ± 11	2.4	2.9	0.109	0.704871 ± 9	0.704608
E34	0.18	0.512914 ± 7	4.5	5.8	0.078	0.704202 ± 12	0.704015
E16	0.15	0.512828 ± 9	4.4	4.7	0.095	0.703967 ± 10	0.703738
E50	0.17	0.512907 ± 8	5.4	5.7	0.371	0.704757 ± 11	0.703866
E51	0.13	0.512953 ± 10	6.4	7.7	0.117	0.705029 ± 9	0.704748
E63	0.25	0.512722 ± 10	0.9	0.5	0.400	0.705674 ± 9	0.704713
E37	0.18	0.512755 ± 12	3.0	2.6	0.857	0.706289 ± 16	0.704229
E46	0.20	0.512599 ± 8	-0.3	-0.7	0.530	0.706042 ± 8	0.704769
E05	0.27	0.512795 ± 19	0.3	1.5	0.052	0.705027 ± 12	0.704902
E07	0.24	0.512759 ± 17	1.8	1.3	0.021	0.705278 ± 24	0.705228
E12	0.19	0.512876 ± 9	3.6	4.8	0.110	0.704816 ± 14	0.704553
E13	0.16	0.512790 ± 10	4.2	3.8	0.132	0.704464 ± 14	0.704147
E77	0.21	0.512920 ± 12	4.2	5.2	0.051	0.704077 ± 9	0.703955
E71	0.12	0.512798 ± 5	4.8	4.8	0.048	0.709545 ± 9	0.709430
E52	0.19	0.512769 ± 8	2.8	2.8	0.045	0.706113 ± 9	0.706005

1) Uncertainties are given as 2σ.

2) εNd and $\varepsilon Nd_{(i)}$ have been calculated using the chondrite universal reservoir (CHUR) with present-day values: $^{143}Nd/^{144}Nd = 0.512638$ and $^{147}Sm/^{144}Nd = 0.1967$.

3) Initial ratios have been recalculated using Rb and Sr, and Sm and Nd as determined by XRF and LA-ICPMS respectively with $\lambda^{87}Rb = 1.42 \times 10^{-11}$ and $\lambda^{147}Sm = 6.54 \times 10^{-12}$.

The age used for recalculation (169 Ma) is based on SHRIMP zircon dating as described in Chapter 3, Section 7.

Appendix E - U-Pb SHRIMP zircon data

Appendix E-1: Sample L02 - Lesvos Island gabbro

Sample	U (ppm)	Th (ppm)	Th/U	$^{206}Pb^*$ (ppm)	$^{238}U/^{206}Pb$ (uncorrected)	$^{207}Pb/^{206}Pb$ (uncorrected)	Age (Ma)[1] $^{206}Pb/^{238}U$
Without points 4.2, 6.1, 8.1							
L02.1.1	51	35	0.72	1.7	24.98 ± 3.1	0.0575 ± 0.0007	251.1 ± 6.8
L02.1.2	31	22	0.73	1.1	24.75 ± 3.4	0.0640 ± 0.0008	251.3 ± 10.9
L02.2.1	38	22	0.59	1.4	23.79 ± 5.2	0.0797 ± 0.0007	256.2 ± 8.1
L02.2.2	18	9	0.53	0.6	24.26 ± 4.2	0.0706 ± 0.0011	254.3 ± 8.6
L02.3.1	52	35	0.70	1.8	24.94 ± 2.9	0.0591 ± 0.0006	250.9 ± 7.7
L02.4.1	83	70	0.87	2.9	24.62 ± 2.7	0.0549 ± 0.0005	255.5 ± 6.1
L02.5.1	22	16	0.72	0.7	25.80 ± 3.8	0.0633 ± 0.0010	241.5 ± 6.8
L02.5.2	16	9	0.55	0.6	24.28 ± 4.3	0.0825 ± 0.0011	250.2 ± 7.8
L02.7.1	61	38	0.65	2.2	24.13 ± 3.0	0.0561 ± 0.0006	260.2 ± 9.3
						WM:	253.1 ± 5.6
						MSWD:	0.34
Points 4.2, 6.1, 8.1							
L02.4.2	77	48	0.65	2.4	27.04 ± 2.9	0.0589 ± 0.0006	231.8 ± 7.4
L02.6.1	31	22	0.74	1.0	26.73 ± 3.4	0.0685 ± 0.0011	231.6 ± 10.8
L02.8.1	105	85	0.83	3.5	26.10 ± 2.5	0.0566 ± 0.0005	240.7 ± 13.4
						WM:	235.9 ± 7.7
						MSWD:	0.62

1) corrected for ^{204}Pb; *) radiogenic Pb; WM: weighted mean; error on WM is given at the 68.3% confidence level; Uncertainties are given as 1σ; MSWD: Mean square of weighted deviates.

Appendix E-2: Sample L40 - Lesvos Island gabbro

Sample	U (ppm)	Th (ppm)	Th/U	$^{206}Pb^*$ (ppm)	$^{238}U/^{206}Pb$ (uncorrected)	$^{207}Pb/^{206}Pb$ (uncorrected)	Age (Ma)[1] $^{206}Pb/^{238}U$
L40.1	306	171	0.58	23.0	11.42 ± 1.4	0.05906 ± 0.00002	538.8 ± 7.5
L40.2	164	56	0.35	18.1	7.78 ± 1.5	0.06560 ± 0.00002	776.9 ± 11
L40.3	1447	37	0.03	66.9	18.58 ± 1.4	0.05366 ± 0.00001	337.5 ± 4.5

1) corrected for ^{204}Pb; *) radiogenic Pb; WM: weighted mean; error on WM is given at the 68.3% confidence level; Uncertainties are given as 1σ; MSWD: Mean square of weighted deviates.

Appendix E-3: Sample SA08 - Samothraki Island gabbro

Sample	U (ppm)	Th (ppm)	Th/U	$^{206}Pb^*$ (ppm)	$^{238}U/^{206}Pb$ (uncorrected)	$^{207}Pb/^{206}Pb$ (uncorrected)	Age (Ma)[1] $^{206}Pb/^{238}U$
SA08.1	69	43	0.64	1.5	39.52 ± 4.9	0.0688 ± 0.0006	157.2 ± 7.7
SA08.2	95	77	0.84	2.1	38.85 ± 1.8	0.0582 ± 0.0006	162.0 ± 2.9
SA08.3	45	23	0.52	1.0	39.65 ± 2.6	0.0747 ± 0.0007	155.5 ± 4.1
						WM:	159.9 ± 4.5
						MSWD:	0.80

1) corrected for ^{204}Pb; *) radiogenic Pb; WM: weighted mean; error on WM is given at the 68.3% confidence level; Uncertainties are given as 1σ; MSWD: Mean square of weighted deviates.

Appendix E-4: Sample E13 – Gabbro of the Evros area

Sample	U (ppm)	Th (ppm)	Th/U	$^{206}Pb^*$ (ppm)	$^{207}Pb/^{235}U$[1]	$^{206}Pb/^{238}U$[1]	Age (Ma)[1] $^{206}Pb/^{238}U$
E13.1	3162	2766	0.90	73.1	0.182 ± 0.03	0.0269 ± 0.0003	171.1 ± 1.9
E13.2	5095	7696	1.56	115.9	0.181 ± 0.03	0.0265 ± 0.0003	168.3 ± 1.8
E13.3	4137	5089	1.27	94.1	0.177 ± 0.04	0.0264 ± 0.0003	168.1 ± 1.8
E13.7	3787	3536	0.96	85.5	0.180 ± 0.03	0.0263 ± 0.0003	167.1 ± 1.8
						WM:	168.6 ± 1.8
						MSWD:	0.68
E13.4	343	314	0.94	7.3	0.219 ± 0.014	0.0250 ± 0.0004	159.0 ± 2.5
E13.5	95	45	0.49	2.2	0.299 ± 0.024	0.0267 ± 0.0007	169.6 ± 4.2
E13.6	488	299	0.63	9.2	0.117 ± 0.027	0.0214 ± 0.0004	136.3 ± 2.4

1) corrected for ^{204}Pb; *) radiogenic Pb; WM: weighted mean; error on WM is given at the 68.3% confidence level; Uncertainties are given as 1σ; MSWD: Mean square of weighted deviates.

Appendix F – Photos and diagrams

Appendix F-1: Pillow lavas on Samothraki Island

Pillow-lava outcrops east of Paleopoli (A) at the northern coast and at Kipos beach (B) at the southeastern coast of Samothraki Island.

Appendix F-2: Zr vs. major and trace elements for the Samothraki Island basalts and dolerites. Basalts (white circles); dolerites (grey boxes).

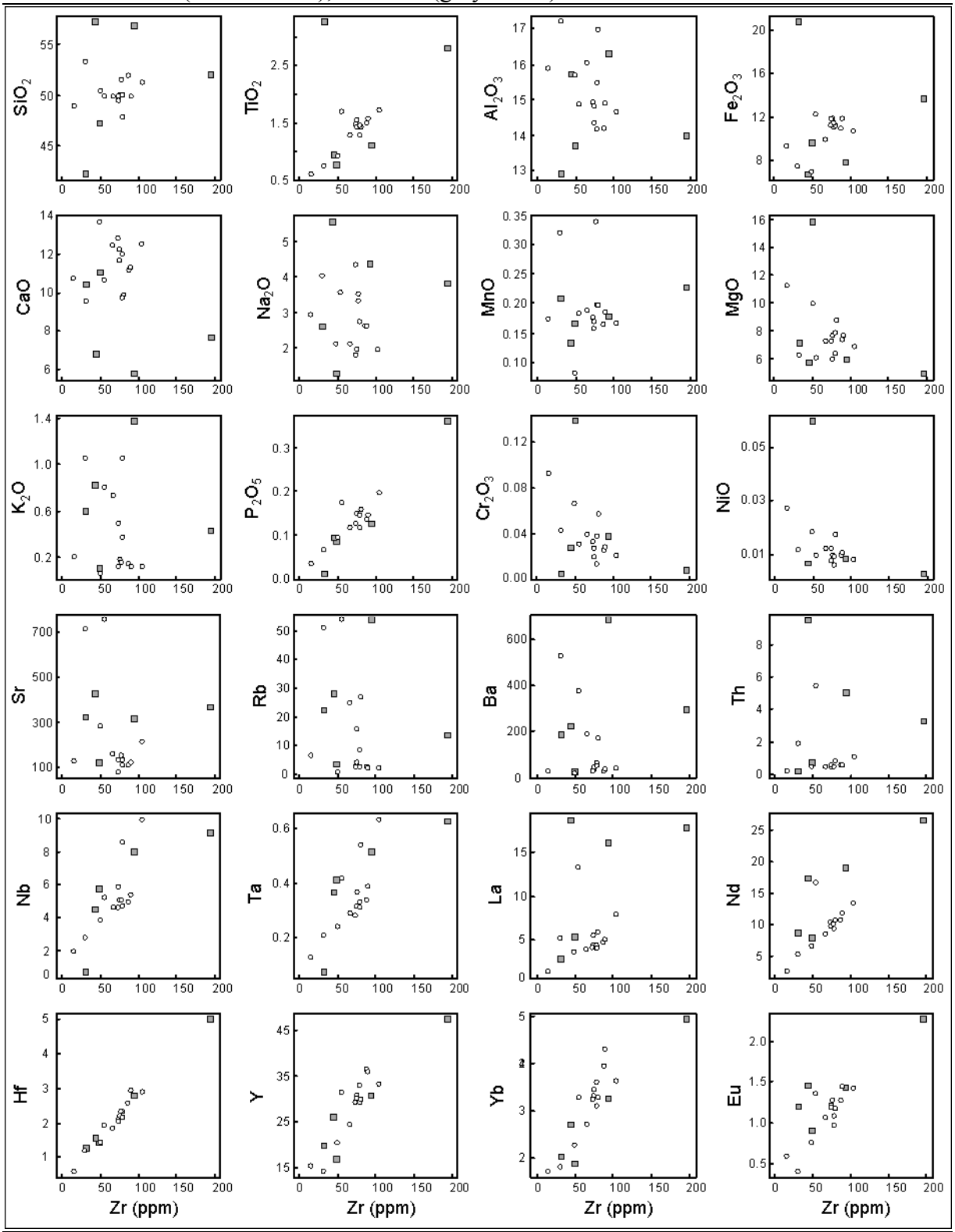

Oxides in wt%; Elements in ppm.

Appendix F-3: Zr vs. major and trace elements for the volcanic rocks of the Evros area. Group I symbols are marked in grey; Group II symbols are marked in white. Basalts (circles); basaltic andesites (triangles); andesites (overturned triangles); dacites (crosses); rhyolites (X).

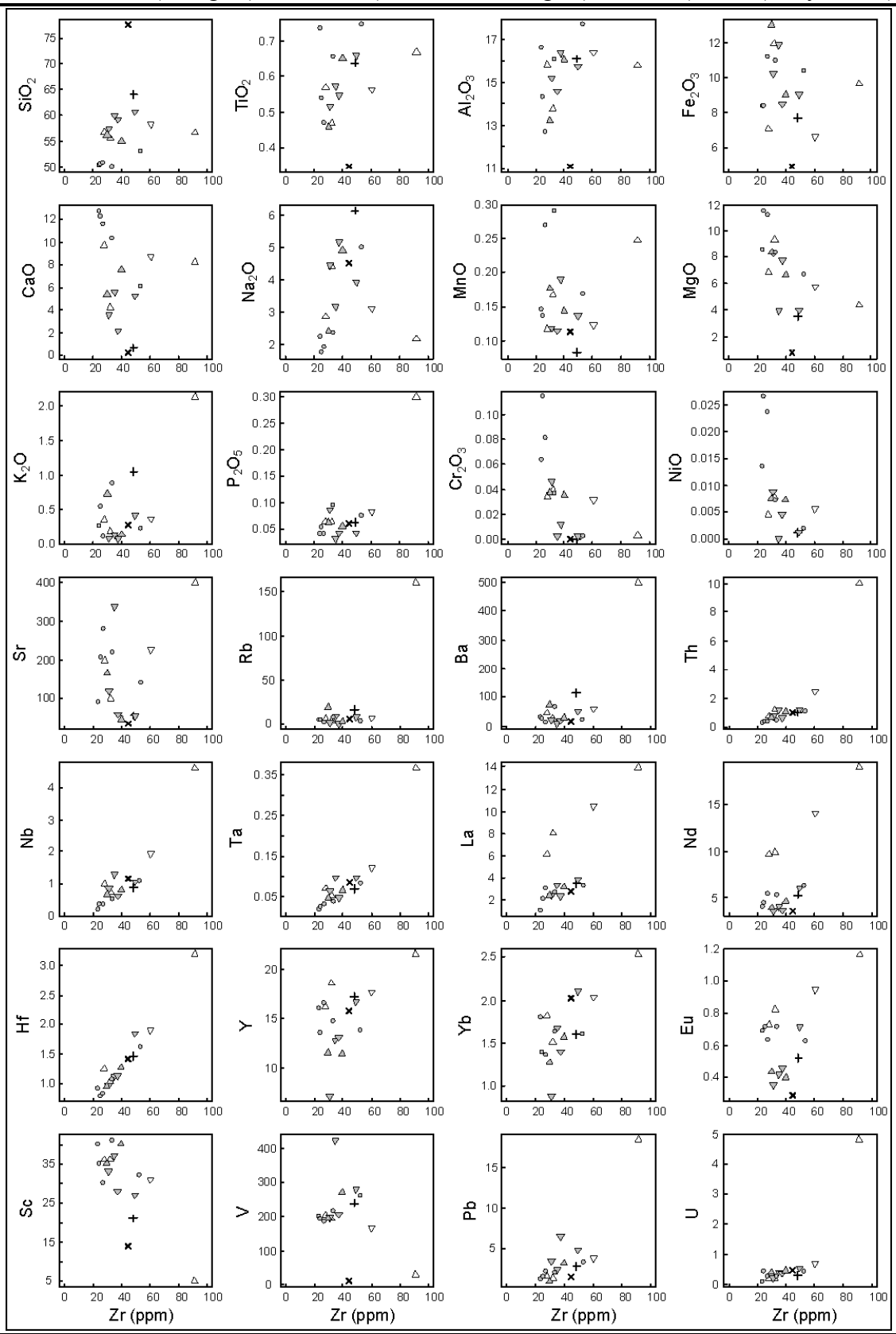

Oxides in wt%; elements in ppm.

Appendix F-4: Zr vs. major and trace elements for the gabbros of the Evros area. Group I (boxes); Group II (diamonds).

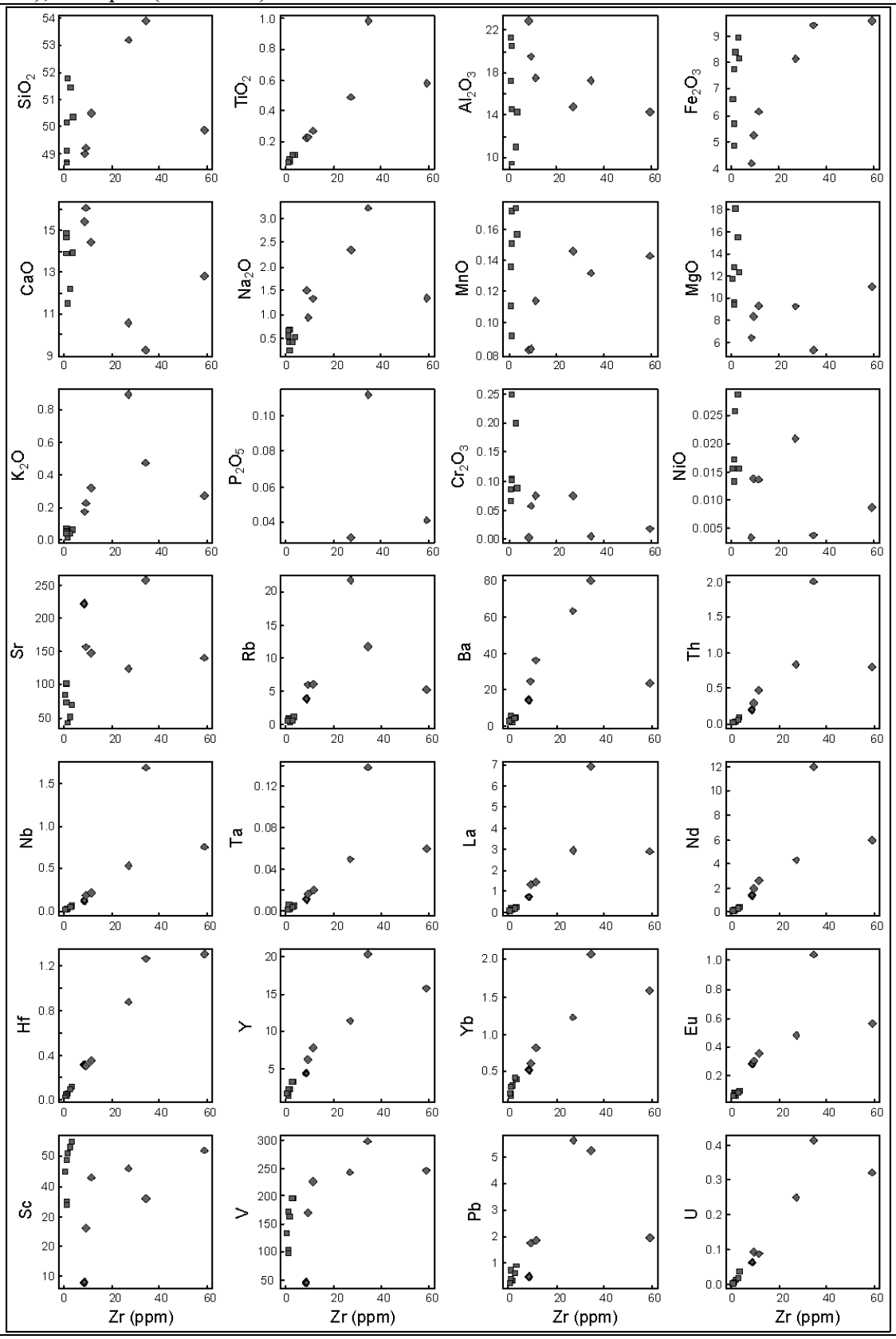

Oxides in wt%; elements in ppm.

Appendix F-5: Chondrite-normalised REE patterns of different oceanic (A-E) and continental island arc volcanic rocks (F-G). Data sources: Tonga Arc (e.g. Turner et al., 1997; Hergt & Woodhead, 2007); South Sandwich Islands (e.g. Barry et al., 2006); Izu-Bonin Arc (e.g. Tamura et al., 2005); Mariana Arc (e.g. Pearce et al., 1999); New Hebrides Arc (e.g. Peate et al., 1997); Kamchatka (e.g. Dorendorf et al., 2000); Cascades (e.g. Reagan et al., 2003).

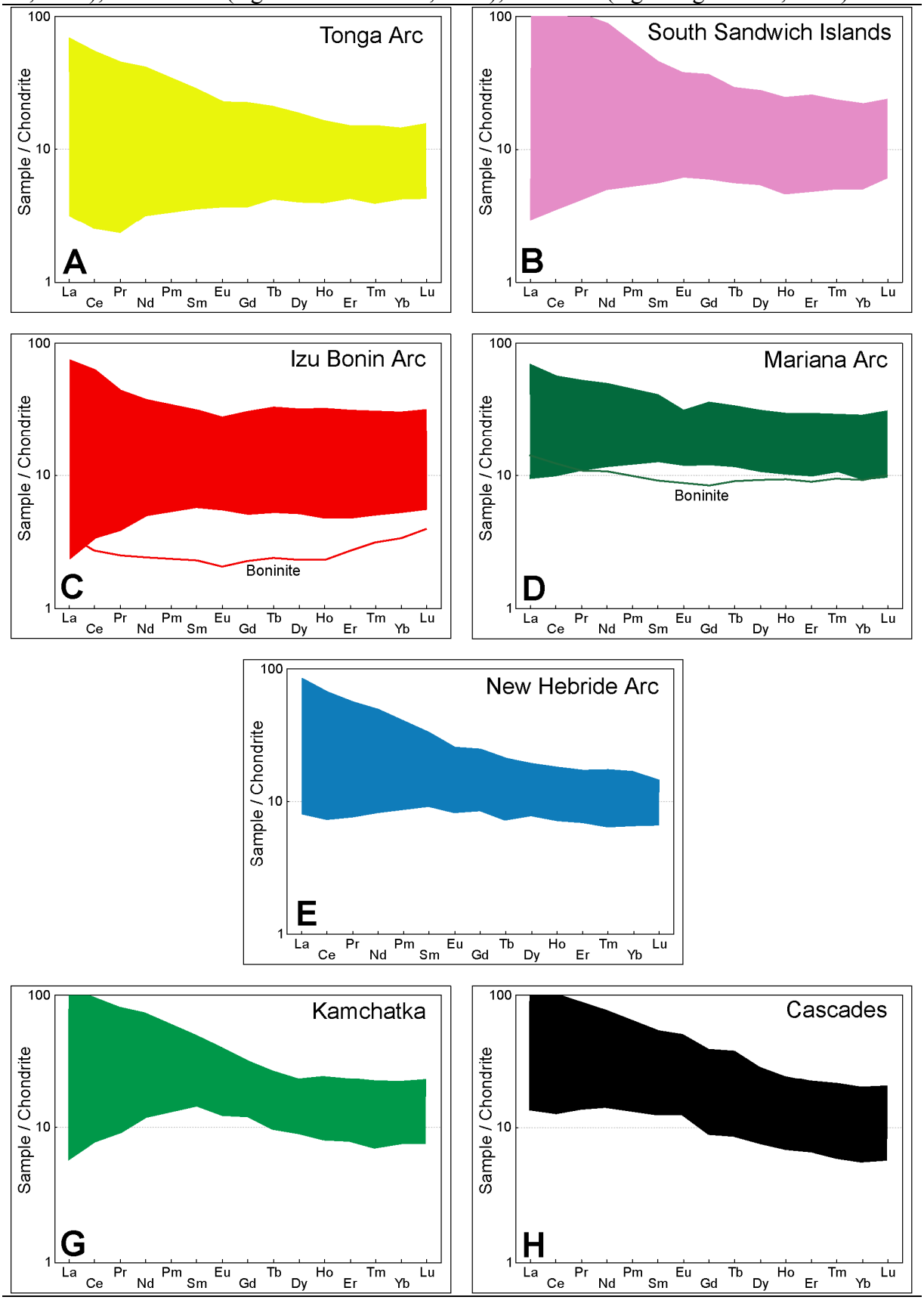
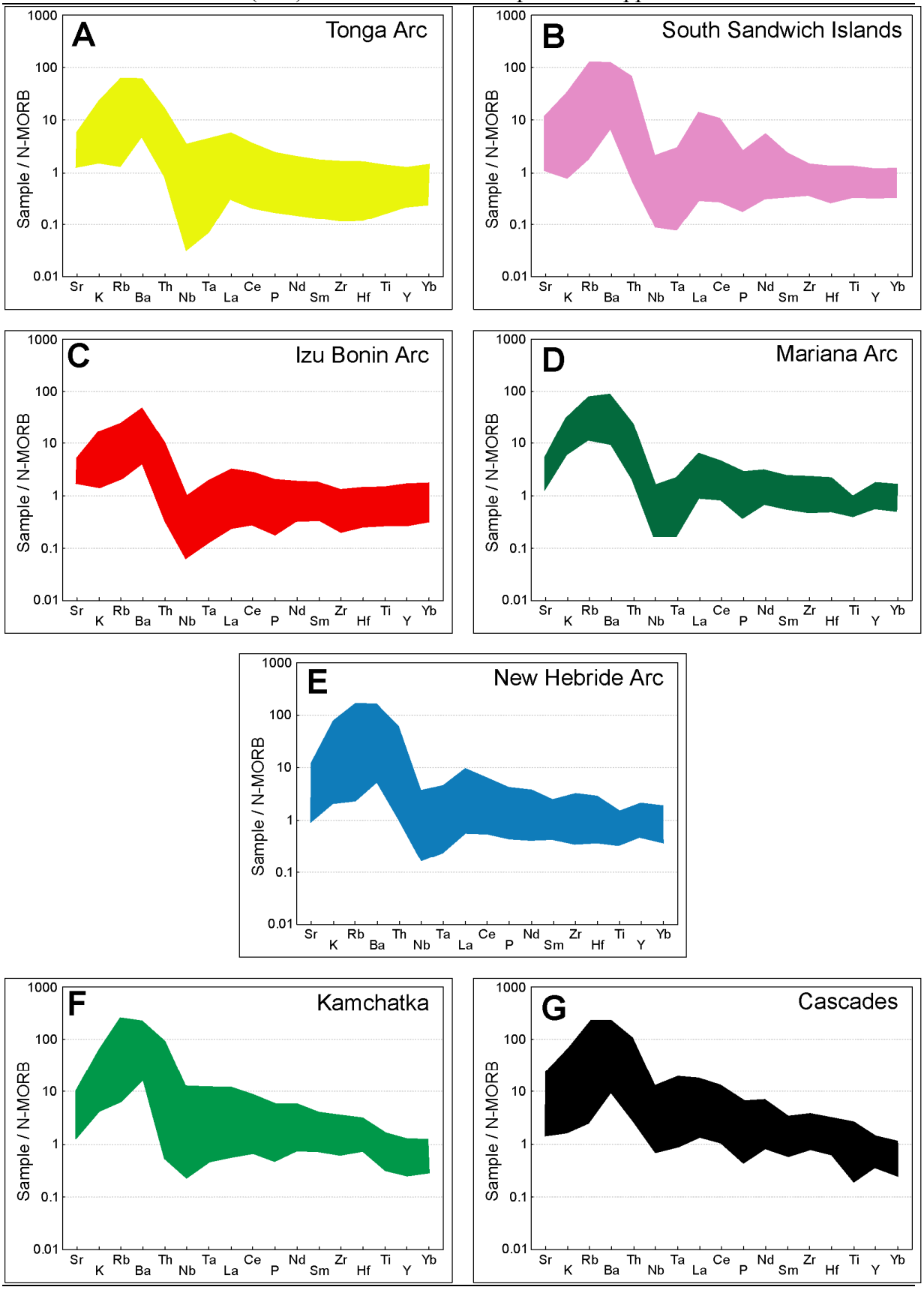
Appendix F-6: N-MORB-normalised patterns of different oceanic (A-E) and continental island arc volcanic rocks (F-G). Data sources as in captions to Appendix F-5.